

ABSTRACT

Damage Accumulation of Bovine Bone Under Chaotic and Variable Amplitude Loading

Marcus A. Hurtado, M.S.B.M.E.

Co-Chairperson: Carolyn Skurla, Ph.D.

Co-Chairperson: Joe Kuehl, Ph.D.

Stress fractures are a common occurrence that can be detrimental to an athlete's career. At present, there is no method for early detection of stress fractures. This study is a continuation of the pilot study to determine if either the Palmgren-Minor rule (PMR) or phase space warping (PSW) could be used to predict fatigue failure of bone tissue. In this study three different experimental set-ups were utilized. The Moon's Beam experimental set-up was used to test chaotic loading conditions. The variable amplitude set-up was utilized to test variable amplitude loading conditions. Lastly, a four-point bend test was used to determine the baseline properties of the bone tissue. Scanning electron microscopy was employed to examine the fracture surface of the bone specimens to determine the fracture type. PSW has shown it is able to identify damage modes of fatigue. Therefore, further investigation into the prediction capabilities of PSW should be pursued.

Damage Accumulation of Bovine Bone
Under Chaotic and Variable Amplitude Loading

by

Marcus A. Hurtado, B.S.B.E.

A Thesis

Approved by the Department of Mechanical Engineering

Paul I. Ro, Ph.D., Chairperson

Submitted to the Graduate Faculty of
Baylor University in Partial Fulfillment of the
Requirements for the Degree
of
Master of Science in Biomedical Engineering

Approved by the Thesis Committee

Carolyn Skurla, Ph.D., Co-Chairperson

Joseph Kuehl, Ph.D., Co-Chairperson

Linda Olafsen, Ph.D.

Accepted by the Graduate School
December 2018

J. Larry Lyon, Ph.D., Dean

Copyright © 2018 by Marcus A. Hurtado

All right reserved

TABLE OF CONTENTS

| | |
|--|-------|
| LIST OF FIGURES | viii |
| LIST OF TABLES | xvii |
| NOMENCLATURE | xviii |
| ACKNOWLEDGMENTS | xix |
| DEDICATION | xx |
| CHAPTER ONE | 1 |
| Introduction | 1 |
| Bone Fatigue and Stress Fractures | 1 |
| Functions of Bone | 3 |
| The Hierarchical Structure of Bone | 4 |
| Mechanical Properties of Bone | 6 |
| Viscoelastic Behavior | 7 |
| Anisotropy | 8 |
| Water Content | 9 |
| Bone Mineral Density | 10 |
| Adaptability | 11 |
| Constitutive Fatigue Model | 12 |
| Fatigue Process | 13 |
| Resistance Mechanisms | 15 |
| Break Classifications | 17 |
| Fatigue Limit - Prediction Methods | 18 |
| Palmgren-Miner Rule | 18 |
| Rainflow Counting | 20 |
| Phase Space Warping | 21 |
| CHAPTER TWO | 30 |
| Methods and Materials | 30 |
| Introduction | 30 |
| Specimen Preparation | 30 |
| Chaotic Loading Test | 33 |
| Hardware | 33 |
| Software | 36 |
| Variable Amplitude Test | 37 |
| Hardware | 37 |
| Software | 37 |
| Four-Point Bend Test | 38 |
| Hardware | 38 |
| Software | 38 |

| | |
|---------------------------------------|--------|
| Specimen and System Preparation..... | 39 |
| Chaotic Loading Test..... | 39 |
| Variable Amplitude Test..... | 40 |
| Four –Point Bend Test | 40 |
| Test Procedure | 41 |
| Chaotic Loading Test..... | 41 |
| Variable Amplitude Test..... | 42 |
| Four-Point Bend Test..... | 43 |
| Analysis..... | 43 |
| ResonantFrequencyLVM.m..... | 43 |
| LaserLabViewCUTv2.m..... | 44 |
| rainflow_bins_mod3.m | 44 |
| rainflow_bins_mod4.m | 44 |
| SpeedPMR.m | 45 |
| PSW_protocol2v2.m..... | 45 |
| Four_Point_Bend_Analysis.m..... | 46 |
| Fracture Surface Classification | 46 |
| Statistical Analysis..... | 47 |
| CHAPTER THREE | 49 |
| Results..... | 49 |
| Chaotic Loading..... | 49 |
| Voltage vs. Time Series | 49 |
| Fracture Surface Classification | 50 |
| Cycles Counts | 50 |
| Palmgren-Miner Rule..... | 53 |
| Phase Space Warping Analysis..... | 54 |
| Variable Amplitude Test..... | 57 |
| Voltage vs. Time Series | 57 |
| Fracture Surface Classification | 58 |
| Cycle Counts..... | 58 |
| Palmgren-Miner Rule..... | 60 |
| Four-Point Bend Test..... | 60 |
| Statistical Analysis..... | 62 |
| CHAPTER FOUR..... | 63 |
| Discussion | 63 |
| Four-point Bend..... | 63 |
| Variable Amplitude Test..... | 64 |
| Chaotic Amplitude Loading..... | 65 |
| Statistical Analysis..... | 69 |
| Conclusion | 69 |
| CHAPTER FIVE | 71 |
| Future Work..... | 71 |
| Improvements – Previous Study | 71 |
| Improvements – Future Study..... | 71 |

| | |
|---|-----|
| APPENDIX A..... | 75 |
| Data Logbook..... | 75 |
| APPENDIX B..... | 77 |
| Specimen photos with 18-megapixel camera | 77 |
| Group 1 | 77 |
| Group 2 | 78 |
| Group 3 | 79 |
| Group 4 | 80 |
| Group 5 | 81 |
| Group 6 | 82 |
| Group 7 | 83 |
| Group 8 | 84 |
| Group 9 | 85 |
| Group 10 | 86 |
| APPENDIX C | 87 |
| Fracture Surface SEM Images | 87 |
| Chaotic Loading Test..... | 87 |
| Variable Amplitude Test..... | 102 |
| APPENDIX D..... | 110 |
| Data Summaries..... | 110 |
| Chaotic Loading Test..... | 110 |
| Variable Amplitude Test..... | 140 |
| Four-Point Bend Test..... | 156 |
| Statistical Analysis..... | 161 |
| APPENDIX E | 168 |
| MATLAB Code | 168 |
| ResonantFrequencyLVM.m..... | 168 |
| LaserLabViewCUTv2.m..... | 169 |
| rainflow_bins_mod3.m..... | 171 |
| rainflow_bins_mod4.m..... | 177 |
| SpeedPMR.m | 183 |
| PSW_protocol2v2.m..... | 185 |
| PSW Code Set..... | 188 |
| Four_Point_Bend_Analysis.m..... | 188 |
| NI LabVIEW VI Programs | 190 |
| WaveGeneration.vi | 190 |
| Variable AmplitudeWaveGeneration-VoltageOutput.vi | 191 |
| LASER-Voltage-ContinuousInput.vi..... | 192 |
| APPENDIX F | 193 |
| Four Point Bend Jig Diagram | 193 |
| APPENDIX G..... | 194 |
| Specifications..... | 194 |

| | |
|----------------------------|-----|
| Amplifier..... | 194 |
| Low-pass filter | 196 |
| Laser Vibrometer | 198 |
| Linear Guide | 199 |
| Shaker | 200 |
| TESTRESOURCE Machine | 201 |
| APPENDIX H..... | 203 |
| Bill of Materials | 203 |
| REFERENCES | 205 |

LIST OF FIGURES

| | |
|---|----|
| Figure 1.1. – A schematic of the hierarchical structure of bone | 4 |
| Figure 1.2. – Stress-strain plot for cortical bone..... | 7 |
| Figure 1.3. – Mechanical properties of cortical bone. | 9 |
| Figure 1.4. – Four-point bending curve for hydrated, dehydrated, and ashed bone. | 10 |
| Figure 1.5. – Illustrated cross-section of femur. | 11 |
| Figure 1.6. – Bone loss and recovery in the femur of astronauts..... | 12 |
| Figure 1.7. – Various fracture prevention mechanisms within bone. | 16 |
| Figure 1.8.b – SEM image of cortical bone of a ductile break. | 19 |
| Figure 1.8.a – SEM image of cortical bone of a brittle break..... | 19 |
| Figure 1.8.c – SEM image of cortical bone of a mixed mode break. | 19 |
| Figure 1.9. – Rainflow counting plot..... | 21 |
| Figure 1.10. – Moon’s beam apparatus set up with components labeled. | 22 |
| Figure 1.11. – Unforced Duffing equation phase space..... | 24 |
| Figure 1.12. – An illustration of false nearest neighbors..... | 27 |
| Figure 1.13. – Phase space warping diagram..... | 28 |
| Figure 2.1. – Schematic of specimens extracted from a left femur. | 31 |
| Figure 2.2. – Moon’s beam apparatus..... | 33 |
| Figure 2.3. – Picture of testing hardware..... | 34 |
| Figure 2.4. – Specimen Pendulum. | 35 |
| Figure 2.5. – Variable Amplitude hardware changes. | 37 |
| Figure 2.6. – TESTRESOURCES apparatus. | 39 |
| Figure 2.7 – Types of motion..... | 41 |

| | |
|---|----|
| Figure 2.8. – Fracture classifications. | 47 |
| Figure 2.9. – Fracture features. | 48 |
| Figure 3.1. – Time series for SP6D..... | 49 |
| Figure 3.2 – Chaotic Loading Test Break Classification Counts..... | 50 |
| Figure 3.3 – Histograms of cycles. | 51 |
| Figure 3.4 – Index of SOC for SP4F | 54 |
| Figure 3.5.b – SOC continuum graphs of SP4F | 55 |
| Figure 3.5.a – SOC graphs of SP4F | 55 |
| Figure 3.6 – Time series of SP8B | 57 |
| Figure 3.7 – Variable Amplitude Test Break Classification Counts | 58 |
| Figure 3.8 – Histogram of SP8B cycles..... | 59 |
| Figure 3.9 – Stress vs. strain plot..... | 61 |
| Figure 3.10 – Scatter plot of total cycles to failure vs. modulus for chaotic loading specimens..... | 62 |
| Figure 4.1 – SOV index for SP7E..... | 67 |
| Figure B.1.a – Specimen 1D: chaotic loading | 77 |
| Figure B.1.b – Specimen 1E: chaotic loading..... | 77 |
| Figure B.1.c – Specimen 1F: chaotic loading..... | 77 |
| Figure B.2.a – Specimen 2D: chaotic loading | 78 |
| Figure B.2.b – Specimen 2E: chaotic loading..... | 78 |
| Figure B.2.c – Specimen 2F: chaotic loading..... | 78 |
| Figure B.3.a – Specimen 3B: variable amplitude loading | 79 |
| Figure B.3.b – Specimen 3C: variable amplitude loading..... | 79 |
| Figure B.3.c – Specimen 3D: chaotic loading | 79 |

| | |
|---|----|
| Figure B.3.d – Specimen 3E: chaotic loading..... | 79 |
| Figure B.3.e – Specimen 3F: chaotic loading..... | 79 |
| Figure B.4.a – Specimen 4B: variable amplitude loading..... | 80 |
| Figure B.4.b – Specimen 4C: variable amplitude loading..... | 80 |
| Figure B.4.c – Specimen 4D: chaotic loading..... | 80 |
| Figure B.4.d – Specimen 4E: chaotic loading..... | 80 |
| Figure B.4.e – Specimen 4F: chaotic loading..... | 80 |
| Figure B.5.a – Specimen 5B: variable amplitude loading..... | 81 |
| Figure B.5.b – Specimen 5C: variable amplitude loading..... | 81 |
| Figure B.5.c – Specimen 5D: chaotic loading..... | 81 |
| Figure B.5.d – Specimen 5E: chaotic loading..... | 81 |
| Figure B.5.e – Specimen 5F: chaotic loading..... | 81 |
| Figure B.6.a – Specimen 6B: variable amplitude loading..... | 82 |
| Figure B.6.b – Specimen 6C: variable amplitude loading..... | 82 |
| Figure B.6.c – Specimen 6D: chaotic loading..... | 82 |
| Figure B.6.d – Specimen 6E: chaotic loading..... | 82 |
| Figure B.4.e – Specimen 6F: chaotic loading..... | 82 |
| Figure B.7.a – Specimen 7B: variable amplitude loading..... | 83 |
| Figure B.7.b – Specimen 7C: variable amplitude loading..... | 83 |
| Figure B.7.c – Specimen 7D: chaotic loading..... | 83 |
| Figure B.7.d – Specimen 7E: chaotic loading..... | 83 |
| Figure B.7.e – Specimen 7F: chaotic loading..... | 83 |
| Figure B.8.a – Specimen 8B: variable amplitude loading..... | 84 |
| Figure B.8.b – Specimen 8C: variable amplitude loading..... | 84 |

| | |
|--|----|
| Figure B.8.c – Specimen 8D: chaotic loading | 84 |
| Figure B.8.d – Specimen 8E: chaotic loading..... | 84 |
| Figure B.9.a – Specimen 9B: variable amplitude loading | 85 |
| Figure B.9.b – Specimen 9C: variable amplitude loading..... | 85 |
| Figure B.9.c – Specimen 9D: chaotic loading | 85 |
| Figure B.9.d – Specimen 9E: chaotic loading..... | 85 |
| Figure B.9.e – Specimen 9F: chaotic loading..... | 85 |
| Figure B.10.a – Specimen 10B: variable amplitude loading | 86 |
| Figure B.10.b – Specimen 10C: variable amplitude loading..... | 86 |
| Figure B.10.c – Specimen 10D: chaotic loading | 86 |
| Figure B.10.d – Specimen 10E: chaotic loading..... | 86 |
| Figure B.10.e – Specimen 10F: chaotic loading..... | 86 |
| Figure C.1 – Specimen 1D: BD break | 87 |
| Figure C.2 – Specimen 1E: BD break..... | 87 |
| Figure C.3 – Specimen 1F: BD break..... | 88 |
| Figure C.4 – Specimen 2D: BD break | 88 |
| Figure C.5 – Specimen 2E: D break | 89 |
| Figure C.6 – Specimen 2F: BD break..... | 89 |
| Figure C.7 – Specimen 3D: D break..... | 90 |
| Figure C.8 – Specimen 3E: BD break..... | 90 |
| Figure C.9 – Specimen 3F: BD break..... | 91 |
| Figure C.10 – Specimen 4D: BD break | 91 |
| Figure C.11 – Specimen 4E: BD break..... | 92 |
| Figure C.12 – Specimen 4F: BD break..... | 92 |

| | |
|--|-----|
| Figure C.13 – Specimen 5D: D break..... | 93 |
| Figure C.14 – Specimen 5E: BD break..... | 93 |
| Figure C.15 – Specimen 5F: BD break..... | 94 |
| Figure C.16 – Specimen 6D: BD break | 94 |
| Figure C.17 – Specimen 6E: D break | 95 |
| Figure C.18 – Specimen 6F: D break..... | 95 |
| Figure C.19 – Specimen 7D: D break..... | 96 |
| Figure C.20 – Specimen 7E: BD break..... | 96 |
| Figure C.21 – Specimen 7F: BD break..... | 97 |
| Figure C.22 – Specimen 8D: BD break | 97 |
| Figure C.23 – Specimen 8E: BD break..... | 98 |
| Figure C.24 – Specimen 8F: BD break..... | 98 |
| Figure C.25 – Specimen 9D: BD break | 99 |
| Figure C.26 – Specimen 9E: BD break..... | 99 |
| Figure C.27 – Specimen 9F: BD break..... | 100 |
| Figure C.28 – Specimen 10D: BD break | 100 |
| Figure C.29 – Specimen 10E: BD break..... | 101 |
| Figure C.30 – Specimen 10F: BD break..... | 101 |
| Figure C.31 – Specimen 3B: B break | 102 |
| Figure C.32 – Specimen 3C: BD break | 102 |
| Figure C.33 – Specimen 4B: BD break | 103 |
| Figure C.34 – Specimen 4C: D break | 103 |
| Figure C.35 – Specimen 5B: BD break | 104 |
| Figure C.36 – Specimen 5C: B break | 104 |

| | |
|--|-----|
| Figure C.37 – Specimen 6B: BD break | 105 |
| Figure C.38 – Specimen 6C: BD break | 105 |
| Figure C.39 – Specimen 7B: BD break | 106 |
| Figure C.40 – Specimen 7C: BD break | 106 |
| Figure C.41 – Specimen 8B: BD break | 107 |
| Figure C.42 – Specimen 8C: BD break | 107 |
| Figure C.43 – Specimen 9B: B break | 108 |
| Figure C.44 – Specimen 9C: BD break | 108 |
| Figure C.45 – Specimen 10B: D break | 109 |
| Figure C.46 – Specimen 10C: BD break | 109 |
| Figure D.1 – Specimen 1D plots..... | 110 |
| Figure D.2 – Specimen 1E plots. | 111 |
| Figure D.3 – Specimen 1F plots. | 112 |
| Figure D.4 – Specimen 2D plots..... | 113 |
| Figure D.5 – Specimen 2E plots | 114 |
| Figure D.6 – Specimen 2F plots | 115 |
| Figure D.7 – Specimen 3D plots..... | 116 |
| Figure D.8 – Specimen 3E plots | 117 |
| Figure D.9 – Specimen 3F plots | 118 |
| Figure D.10 – Specimen 4D plots..... | 119 |
| Figure D.11 – Specimen 4E plots | 120 |
| Figure D.12 – Specimen 4F plots | 121 |
| Figure D.13 – Specimen 5D plots..... | 122 |
| Figure D.14 – Specimen 5E plots | 123 |

| | |
|--|-----|
| Figure D.15 – Specimen 5F plots | 124 |
| Figure D.16 – Specimen 6D plots..... | 125 |
| Figure D.17 – Specimen 6E plots | 126 |
| Figure D.18 – Specimen 6F plots | 127 |
| Figure D.19 – Specimen 7D plots..... | 128 |
| Figure D.20 – Specimen 7E plots | 129 |
| Figure D.21 – Specimen 7F plots | 130 |
| Figure D.22 – Specimen 8D plots..... | 131 |
| Figure D.23 – Specimen 8E plots | 132 |
| Figure D.24 – Specimen 8F plots | 133 |
| Figure D.25 – Specimen 9D plots..... | 134 |
| Figure D.26 – Specimen 9E plots | 135 |
| Figure D.27 – Specimen 9F plots | 136 |
| Figure D.28 – Specimen 10D plots..... | 137 |
| Figure D.29 – Specimen 10E plots | 138 |
| Figure D.30 – Specimen 10F plots | 139 |
| Figure D.31 – Specimen 3B plots..... | 140 |
| Figure D.32 – Specimen 3C plots..... | 141 |
| Figure D.33 – Specimen 4B plots | 142 |
| Figure D.34 – Specimen 4C plots..... | 143 |
| Figure D.35 – Specimen 5B plots | 144 |
| Figure D.36 – Specimen 5C plots..... | 145 |
| Figure D.37 – Specimen 6B plots..... | 146 |
| Figure D.38 – Specimen 6C plots..... | 147 |

| | |
|---|-----|
| Figure D.39 – Specimen 7B plots..... | 148 |
| Figure D.40 – Specimen 7C plots..... | 149 |
| Figure D.41 – Specimen 8B plots..... | 150 |
| Figure D.42 – Specimen 8C plots..... | 151 |
| Figure D.43 – Specimen 9B plots..... | 152 |
| Figure D.44 – Specimen 9C plots..... | 153 |
| Figure D.45 – Specimen 10B plots..... | 154 |
| Figure D.46 – Specimen 10C plots..... | 155 |
| Figure D.47 – Stress vs. Strain plot for specimen 1A..... | 156 |
| Figure D.48 – Stress vs. Strain plot for specimen 2A..... | 156 |
| Figure D.49 – Stress vs. Strain plot for specimen 3A..... | 157 |
| Figure D.50 – Stress vs. Strain plot for specimen 4A..... | 157 |
| Figure D.51 – Stress vs. Strain plot for specimen 5A..... | 158 |
| Figure D.52 – Stress vs. Strain plot for specimen 6A..... | 158 |
| Figure D.53 – Stress vs. Strain plot for specimen 7A..... | 159 |
| Figure D.54 – Stress vs. Strain plot for specimen 8A..... | 159 |
| Figure D.55 – Stress vs. Strain plot for specimen 9A..... | 160 |
| Figure D.56 – Stress vs. Strain plot for specimen 10A..... | 160 |
| Figure D.57 – Chaotic loading total cycles to failure vs. modulus..... | 161 |
| Figure D.58 – Chaotic loading total cycles to failure vs. max stress..... | 161 |
| Figure D.59 – Chaotic loading total cycles to failure vs. strain at max stress..... | 162 |
| Figure D.60 – Chaotic loading total cycles to failure vs. stiffness..... | 162 |
| Figure D.61 – Variable amplitude total cycles to failure vs. modulus..... | 165 |
| Figure D.62 – Variable amplitude total cycles to failure vs. max stress..... | 165 |

| | |
|--|-----|
| Figure D.63 – Variable amplitude total cycles to failure vs. strain at max stress..... | 166 |
| Figure D.64 – Variable amplitude total cycles to failure vs. stiffness..... | 166 |
| Figure E.1. – GUI interface of WaveGeneration.vi | 190 |
| Figure E.2. – Block code of WaveGeneration.vi | 190 |
| Figure E.3. – GUI of VariableAmplitudeWaveGeneration-VoltageOutput.vi | 191 |
| Figure E.4. – Block code of VariableAmplitudeWaveGeneration-VoltageOutput.vi | 191 |
| Figure E.5. – GUI of LASER-Voltage-ContinuousInput.vi | 192 |
| Figure F.1 – Top half of four-point bend jig..... | 193 |
| Figure F.2 – Bottom half of four-point bend jig | 193 |
| Figure G.1 – Amplifier specifications part 1 | 194 |
| Figure G.2 – Amplifier specifications part 2 | 195 |
| Figure G.3 – Low-pass filter specifications part 1 | 196 |
| Figure G.4 – Low-pass filter specifications part 2..... | 197 |
| Figure G.5 – Linear guide specifications..... | 199 |
| Figure G.6 – Shaker specifications | 200 |
| Figure G.7 – TESTRESOURCES specifications part 1 | 201 |
| Figure G.8 – TESTRESOURCES specifications part 1 | 202 |

LIST OF TABLES

| | |
|---|-----|
| Table 3.1 – Cycle count and break classification for chaotic loading test specimens | 51 |
| Table 3.2 – Palmgren-Miner Rule analysis for chaotic loading test specimens | 53 |
| Table 3.3. – SOV values from PSW analysis | 56 |
| Table 3.4 – Cycle count and break classification for variable amplitude test specimens. | 59 |
| Table 3.5. – Palmgren-Miner Rule analysis for variable amplitude test specimens..... | 60 |
| Table 3.6. – Results from four-point bend test | 61 |
| Table A.1 – Chaotic loading test data logbook..... | 75 |
| Table A.2 – Variable amplitude test data logbook | 76 |
| Table A.3 – Four-point bend test data logbook | 76 |
| Table D.1 – Data table from chaotic loading correlations | 163 |
| Table D.2 – Data table from chaotic loading stiffness correlation. | 164 |
| Table D.3 – Data table from variable amplitude correlations..... | 167 |
| Table D.4 – Data table from variable amplitude stiffness correlation..... | 167 |
| Table G.1 – Laser vibrometer specifications | 198 |
| Table H.1 – Bill of Materials | 203 |
| Table H.2 – Bill of Materials continued | 204 |

NOMENCLATURE

| | |
|-----|---------------------------------------|
| B | Brittle fracture |
| D | Ductile fracture |
| BD | Combined brittle and ductile fracture |
| PMR | Palmgren-Miner rule |
| POD | Proper orthogonal decomposition |
| PSW | Phase space warping |
| SOC | Smooth orthogonal coordinates |
| SOD | Smooth orthogonal decomposition |
| SOV | Smooth orthogonal variables |
| VI | Virtual instrument |

ACKNOWLEDGMENTS

I would like to thank Dr. Skurla and Dr. Kuehl for their wonderful support through this study. All of their help and guidance has made this a memorable experience. Thank you to the people involved in the previous studies especially Michelle Cler and Abbey Campbell. All of your hard work has made this study possible.

DEDICATION

To my Alexis, our fur-children, and my family. We did it!

CHAPTER ONE

Introduction

A common bone related injury is a stress fracture. It occurs when an athlete overworks themselves and damages their bones before the body can heal itself. To better understand how stress fractures occur the anatomy, mechanical properties, and fracture mechanics of bone will be examined. Several fatigue prediction methods will also be explored in hopes of developing methods to provide early recognition of damage accumulation prior to the development of a stress fracture.

Bone Fatigue and Stress Fractures

Stress fractures are one of the most serious injuries that a runner can sustain – accounting for about 6% to 20% of all injuries [1–3]. The injury typically occurs within the lower extremities of the person, ranging from metatarsals in the feet to the lower sections of the spine. The tibia accounts for up to 55% of all stress fractures within runners [4]. While the runner demographic experiences stress fractures more frequently, the injury affects various other sports participants, and military recruits. Humans are not alone in experiencing stress fractures. Animals may also experience the injury with race horses and greyhounds being prime examples [5,6].

Stress fractures are an overuse injury. They are caused by repetitive mechanical loading that results in a cumulative strain within the bone. In turn, the aggregate of the load may result in bone damage if the net damage exceeds the body's ability to repair itself [7]. The bone damage reveals itself as small cracks propagating throughout the bone. At first, the damage may go unnoticed as the pain from the crack is undetectable

compared to natural soreness from the activity. As the repetitive loading continues the small cracks grow, leading to a gradual increase in the individual's pain level. At this growing stage, the stress fracture may still be overlooked because the pain will subside with rest and the tenderness in the stress fracture region may be attributed to muscle fatigue. Past this point, if the stress fracture goes unrecognized a final catastrophic mechanical load will cause the bone to completely fracture. Even if the stress fracture is detected early and remedied properly with weeks of rest, there is still a 36% change of a stress fracture reoccurring for that individual [4]. Therefore, it is crucial to understand and predict the accumulated damage in bone that leads to the development of stress fractures in order to halt their progression.

There are intrinsic and extrinsic factors controlling stress fractures. The risk associated with stress fractures is directly influenced by the individual's skeletal properties [8]. By examining the skeletal properties of various groups one can elucidate the main factors that promote stress fractures. Women are at a higher risk of stress fracture than men [3,9]. This distinction could be attributed to differences in bone geometry and bone density varying between the groups. Bone density can also be a sign of other factors that will impact the risk of stress fractures. Bone density decreases with age, extended bed rest or microgravity, and certain diseases. The decreased density indicates an imbalance between the body's natural rates of reabsorption and deposition for the bone remodeling processes. Other intrinsic factors that affect stress fractures are calcium intake and hormonal levels for the individual [10]. Extrinsic factors to be considered are training errors, running mechanics, footwear, frequency and intensity of training. The effects of extrinsic factors are easily seen through people who live a sedentary life style who decide suddenly to begin an intensive exercise program. These

individuals will be more prone to stress fractures because they have not conditioned their body, more specifically bone, to handle such high levels of stress. Understanding these factors will help doctors detect individuals who are the most at risk for stress fractures.

There is no current method to effectively diagnose stress fractures. By the time stress fractures are able to be detected by radiography, magnetic resonance imaging, or triple-phase bone scintigraphy, the bone cracks have grown large enough to be seen by the human eye [9]. Hence, prevention would be the most effective way to combat stress fractures. This avenue of prevention would protect athletes from losing valuable time in their sport and help them live a healthier life. Monitoring the accumulated damage of bone may be the best option.

Functions of Bone

The human skeletal system is highly dynamic. It is composed of bones, ligaments, tendons, and cartilage. The purpose of the skeletal system within organisms is six fold [11].

1. Mineral storage, such as calcium and phosphorus, are essential for cellular activity.
2. Erythrocytes, leukocytes, and thrombocytes are produced in the red marrow of bone.
3. Yellow marrow within bone is responsible for lipid storage.
4. The skeletal system acts as protection for vital organs: such as the cranium for the brain.
5. Bone provides the framework for the body allowing for muscles and other tissue to attach to it.
6. The body utilizes bone as a means of locomotion. The skeletal systems act as a lever system across its various joints to achieve movement.

The Hierarchical Structure of Bone

The hierarchical structure of bone plays into its mechanical properties. A schematic of this structure is seen in Figure 1.1 [10]. The most basic building blocks of bone are seen at the bottom of the figure and are labeled with Roman Numeral I. Each ascending level of the figure depicts a higher order of organization ending with the macroscopic level of a complete bone. The most basic components of bone are mineral carbonated hydroxyapatite, type I collagen, and water. Other components included non-collagenous proteins and proteoglycans [12]. The collagen molecules form a triple helix and are organized into fibrils. At the center of these fibrils, crystals of carbonated hydroxyapatite form. The end product of this junction is the mineralized collagen fibril.

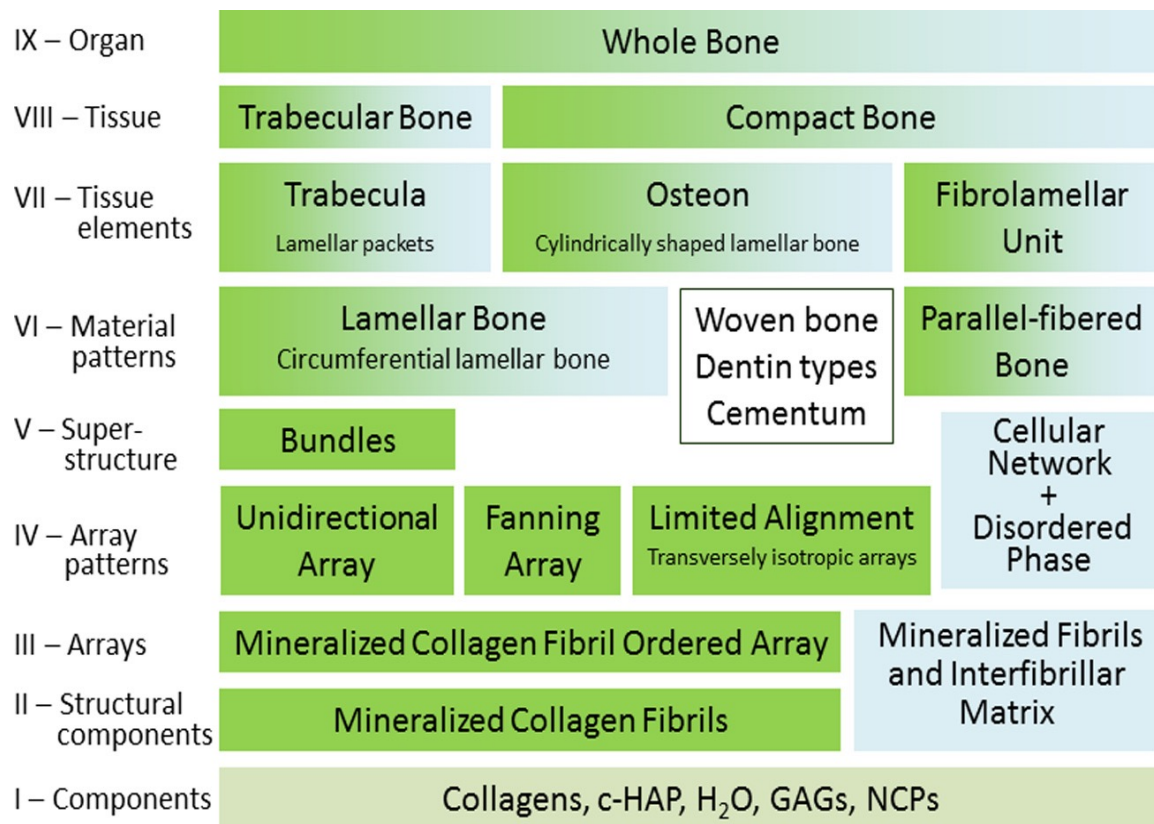


Figure 1.1. – A schematic of the hierarchical structure of bone. Green indicates ordered material while blue indicates disordered material. A gradient of green and blue demonstrate a combination of both ordered and disordered materials [10]. Reprinted with permission from Whipple, T. J., and Eckhardt, R. B., 2011, *The Endurance Paradox: Bone Health for the Endurance Athlete*, Walnut Creek: Taylor and Francis.

The mineralized fibrils self-orient themselves to form arrays: unidirectional, fanning, and limited alignment [13]. Unidirectional collagen fibrils bundle themselves into collagen fiber. The fibers are thought to be oriented to accommodate different kinds of loads, with tension best resisted by fibers aligned longitudinally relative to the load, and compression best resisted by transversely aligned fibers [14]. If the fibers have no discerned orientation, then woven bone is formed. Consequently, woven bone exhibits poor mechanical properties. It is mainly found in immature organisms or injury sites where new bone must be rapidly set. Parallel fibered bone is the antithesis of woven bone. Lamellar bone is an extension of parallel fibered bone. Lamellar bone is formed from lamellae which are composed of both unidirectional and fanning arrays. Lamellae form in layers around the Haversian canals. Lamellar packets alter their orientation around the osteon, like a twisted plywood [15]. The variation of the orientating layers of the lamella promotes bone strength while protecting against torsional forces. Osteocytes are housed by bone lacunas, small cavities within the bone matrix, and form slender canaliculi that radiate and penetrate the adjacent lamellae [16]. The osteon is the basic unit of structure of compact bone comprised of a Haversian canal and its concentrically arranged lamellae. This microstructure of bone is the level at which blood vessels and nerve cells may be located.

Furthermore, four cellular elements of bone are found at the microstructure of bone. Osteoblasts and osteoclasts are essential in the bone remodeling process [17]. Osteoclasts initiate bone remodeling by resorbing and releasing calcium from the bone. Osteoblasts then fill the void and synthesize a collagen matrix. Lastly osteoblasts fill the matrix with hydroxyapatite, producing mineralized bone. From here the osteoblasts may follow one of three pathways. The osteoblasts may remain an active osteoblast, become

an osteocyte, or become a bone lining cell. Osteocytes are osteoblasts that have been encapsulated by bone. It is believed that osteocytes play a role in detecting mechanical loads on the bone and bone remodeling [18]. Bone lining cells are thin, elongated cells that cover the surface of bone and remain relatively inactive. They typically function as a barrier between extracellular fluid and bone.

The macrostructure of bone may be divided into two sections: cortical and cancellous bone. Each may be composed of lamellar, woven, or laminar bone. The main difference between cortical and cancellous bone is the degree of porosity. Human cortical bone, or compact bone, has an apparent density of about 1.9 g/cc while cancellous bone's apparent density is about 0.8 to 1.0 g/cc [19]. Based on the apparent densities, cortical bone displays favorable mechanical properties for supporting loads and resisting bending. Cortical bone comprises the hard outside layer of bones and varies in thickness depending on the bone. Cancellous bone, sometimes called spongy bone, is less mechanically sound than cortical bone and is found within bone, with the epiphyses of long bones being a prime example. From this point, only the mechanical properties of cortical bone will be discussed, examined, and measured. This study performs experimental work on cortical bone from bovine femurs, which are long bones with reinforcing fibers running parallel to the longitudinal axis of the bone.

Mechanical Properties of Bone

Bone is anisotropic, inhomogeneous tissue that evinces elastic, plastic, and viscoelastic properties. A variety of factors that affect the mechanical properties of bone will be discussed.

Viscoelastic Behavior

Figure 1.2 contains multiple stress-strain curves for human cortical bone that illustrate the effect of 5 different strain rates. The linear region of each curve demonstrates the elastic region of the material. The slope of this elastic region is the Young's modulus of the material. Theoretically, this is the region in which the bone may be cyclically loaded indefinitely without concern of permanent damage. The end of the linear range of the curves is the yield point of the material. Past this point, any strain experienced by the material will force the material into its plastic deformation region. Within this region the bone will be permanently altered; the bone will not return to its original shape or exhibit the same mechanical properties when the load is removed. However, within this region, up to six times more energy can be absorbed when compared to the elastic region. This behavior is explained by the mineral crystals undergoing plastic deformation while the fibrous matrix experiences elastic or plastic

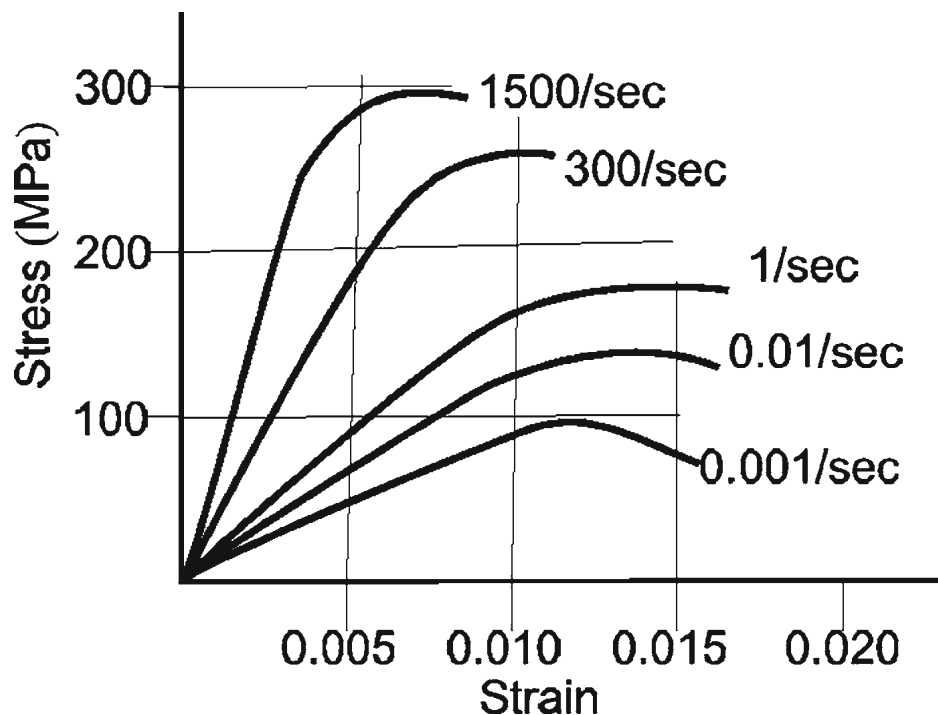


Figure 1.2. – Stress-strain plot for cortical bone. As strain rate increases, the ultimate strength of bone increases while the ultimate strain decreases [19]. Reprinted with permission from Murphy, W., and Black, J., 2016, *Handbook of Biomaterial Properties*, Springer, Boston, MA.

deformation (17). At some point within this plastic zone the bone will fracture. Bone is strain rate sensitive with an optimal strain rate for energy absorption around 0.1-1.0 strain per second [20]. This is optimal because outside of this range there is insufficient time for viscous flow to occur. The material will then behave like an elastic solid. The figure shows that as strain rate decreases the modulus also decreases. This behavior hints at another hallmark property of biological tissue.

The various curves in Figure 1.2 elucidate the viscoelastic properties of bone. When a force is applied to a viscoelastic material, the material will deform and by doing so will demonstrate viscous features. The materials will resist the shear flow and strain linearly with time when stress is applied. Similarly, the material will show elastic properties. The multiple curves in Figure 1.2 reveal that there is no unique modulus of elasticity or fracture stress for a viscoelastic material. As the strain rate increases, Young's modulus and ultimate stress increases, while ultimate strain decreases.

Anisotropy

The mechanical properties of bone will also change with its loading direction. Bone is an anisotropic and inhomogeneous material and as such will express different characteristics under varying load conditions. Figure 1.3 shows how the direction of loading will affect the mechanical properties of human femoral cortical bone. Cortical bone is stronger in compression than in tension [21,22]. Secondly, bone is considerably weaker when loaded transversely to primary fiber orientation compared to longitudinally. Overall, bone behaves similar to ceramics.

| Loading mode | Ultimate strength (MPa) |
|--------------|-------------------------|
| Longitudinal | |
| Tension | 133 |
| Compression | 193 |
| Shear | 68 |
| Transverse | |
| Tension | 51 |
| Compression | 133 |

^aAge span of population 19–80 years. From Hayes and Gerhart (61), with permission. Mean values from Reilly and Burstein (116b), with permission.

Figure 1.3. – Mechanical properties of cortical bone. Cortical bone exhibits higher ultimate strengths in compression than in tension [22]. Reprinted with permission from Burstein, A. H., Currey, J. D., Frankel, V. H., and Reilly, D. T., 1972, “The Ultimate Properties of Bone Tissue: The Effects of Yielding,” *J. Biomech.*, 5(1), pp. 35–44.

Water Content

Similarly, by looking at one of the basic components of bone one can see how its mechanical properties will change. Water plays a critical role in maintaining the conformation of collagen. Without sufficient hydration, collagen loses its hierarchical structure and cause a decrease in both toughness and strength [23]. In Figure 1.4 the results of 4-point bending tests performed on hydrated, dehydrated, and ashed cortical bovine bone are present. Hydrated bone is superior in strength compared to dehydrated and ashed bone [24]. Samuel et al. postulate that about 15 vol% of the original matrix water is the threshold for the shift in the mechanical behavior of bone [25].

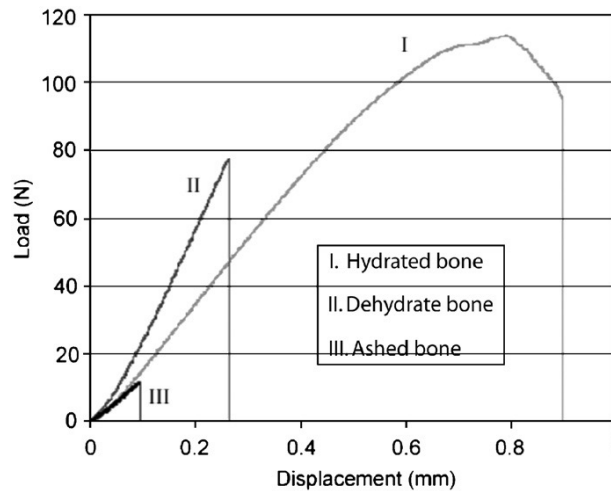


Figure 1.4. – Four-point bending curve for hydrated, dehydrated, and ashed bone. As hydration level decreases, ultimate stress and ultimate strain decrease. The modulus also changes as hydration changes [21]. Reprinted with permission from Mow, V. C., and Hayes, W. C., 1997, *Basic Orthopaedic Biomechanics*, Lippincott-Raven Publishers, Philadelphia, PA

Bone Mineral Density

Age is a factor that determines the mechanical properties bone. As an individual ages, the elastic modulus, toughness, and strength of bone decrease. After peak bone densities in an individual’s twenties there is about a 2% loss in bone density each decade. While peak volumetric bone density appears to be similar in men and women, women are thought to incur an increased incidence of fracture in old age due to smaller bones and an enhanced rate of bone loss during the first years after the menopause [26,27]. This loss in bone mass is of great concern to the elderly community due to the increased risk of fractures.

Osteoporosis is a notorious disease that directly influences the mechanical properties of bone. It can impact both men and women; however, postmenopausal women are generally more susceptible. The condition is due to an imbalance in the bone’s remodeling process. There is an increase in bone reabsorption with an overall decrease in bone deposition. This will cause for bone mass to be generally lost over time. The bone,

in turn, will become weak and more vulnerable to fractures. The condition is diagnosed by a bone mineral density (BMD) score below 2.5 standard deviations (SD) from the mean [28].

Adaptability

Not only will the mechanical loading of bone influence the bicondylar angle of the human femur, but it will also change its mechanical properties [27]. This influence was first described by Julius Wolff. His Law of Bone Remodeling stated that bone structure is not only well designed for its function but will adapt to create a new structure in response to changes in function. Bone shall remodel itself depending on the stresses it experiences. Therefore, if the bone is sufficiently underused for an extended period of time osteoclasts will reabsorb bone from the inside surface [29]. Figure 1.5 illustrates this change through the cross-section of a femur. Similarly, astronauts who spend extended periods of time in space, a microgravity environment, will experience this bone remodeling. However, an astronaut's bone loss is approximately 10 times worse than the decreased mechanical loading experienced on earth [30]. After space flight lasting

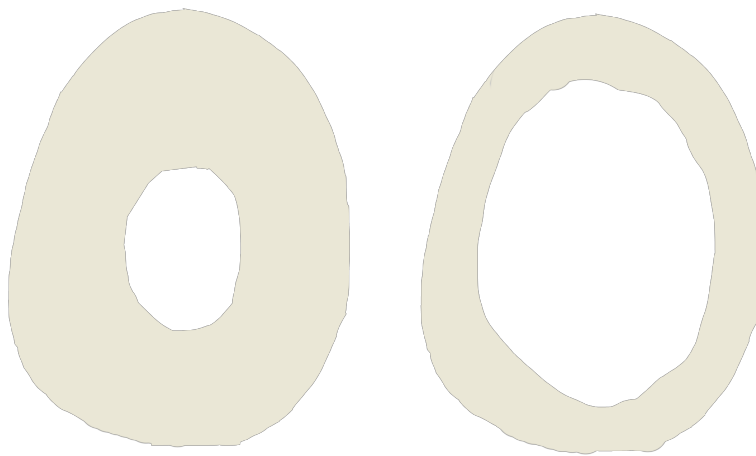


Figure 1.5. – Illustrated cross-section of femur. Left depicts healthy loaded bone. Right depicts bone immobilized for 6 months; bone remodeling took place.

between 4 and 6 months, the percentage of total bone loss is about 0-3%; moreover, the loss of weight bearing bones were scientifically higher at about 0-20% [30–33]. Similarly, the bending and compressive strength of the femur was 10% less than preflight strength as seen in Figure 1.6 [33].

| | | <i>PrFL</i> | <i>PoFL</i> | <i>R12</i> | $\Delta(\%)$ <i>Flight</i> | $\Delta(\%)$ <i>Recovery</i> | <i>Ratio (R + 12/PreFL)</i> |
|--------------------------------------|----------------|-------------|-------------|------------|----------------------------|------------------------------|-----------------------------|
| Total vBMD (g/cm ³) | Mean | 0.332 | 0.297 | 0.309 | -10.40 | 4.40 | 0.93 |
| | Median | 0.325 | 0.297 | 0.308 | -9.72 | 4.72 | 0.93 |
| | <i>p</i> value | | | | <0.001 | 0.02 | <0.001 |
| Trabecular vBMD (g/cm ³) | Mean | 0.145 | 0.124 | 0.132 | -14.40 | 6.70 | 0.91 |
| | SD | 0.026 | 0.027 | 0.026 | 6.30 | 5.90 | 0.05 |
| | <i>p</i> value | | | | <0.001 | <0.001 | <0.001 |
| Cortical vBMD (g/cm ³) | Mean | 0.539 | 0.521 | 0.523 | -3.40 | 0.60 | 0.97 |
| | SD | 0.037 | 0.035 | 0.033 | 3.60 | 3.20 | 0.03 |
| | <i>p</i> value | | | | <0.001 | 0.38 | 0.02 |
| Total mass (g) | Mean | 35.182 | 30.772 | 34.397 | -11.10 | 12.20 | 0.99 |
| | SD | 7.342 | 4.686 | 5.686 | 11.20 | 11.80 | 0.12 |
| | <i>p</i> value | | | | <0.001 | <0.001 | 0.560 |
| Cortical mass (g) | Mean | 25.502 | 22.000 | 24.547 | -12.10 | 12.40 | 0.98 |
| | SD | 5.668 | 3.675 | 4.171 | 12.20 | 14.70 | 0.13 |
| | <i>p</i> value | | | | <0.001 | 0.010 | 0.320 |
| Total volume (cm ³) | Mean | 106.322 | 104.242 | 112.008 | -0.70 | 7.20 | 1.06 |
| | SD | 19.803 | 14.678 | 19.234 | 10.10 | 7.30 | 0.11 |
| | <i>p</i> value | | | | 0.710 | <0.001 | 0.070 |
| Cortical volume (cm ³) | Mean | 47.011 | 42.091 | 46.804 | -9.2 | 11.5 | 1.01 |
| | SD | 8.447 | 5.250 | 6.957 | 10.8 | 12.2 | 0.12 |
| | <i>p</i> value | | | | 0.010 | <0.001 | 0.710 |

p values denote the statistical significance of the percentage changes and the significance of the difference between preflight and 1-year values.

Figure 1.6. – Bone loss and recovery in the femur of astronauts before and after space flight. The first row reveals that BMD was lowered overall [33]. Reprinted with permission from Lang, T. F., Leblanc, A. D., Evans, H. J., and Lu, Y., 2006, “Adaptation of the Proximal Femur to Skeletal Reloading after Long-Duration Spaceflight,” *J. Bone Miner. Res. Off. J. Am. Soc. Bone Miner. Res.*, **21**(8), pp. 1224–1230

Constitutive Fatigue Model

It is pertinent to understand how bone breaks in order to deconstruct the mechanical processes involved with bone fatigue. There is a strong consensus that bone acts like a fiber reinforced composite material, or engineered composite, when it is subjected to stresses and strains [34–43]. Cortical bone contains osteons that carry the brunt of the load and act as a reinforcing fiber within the bone tissue. Moreover, the cement lines between the individual osteons act as the weak interfaces in fiber-reinforced composites [44]. The mechanical properties shown by both bone and engineered composites mirror each other. Both are stronger when loaded in parallel to their fiber

orientation, osteon structures in bone [45]. These structures in long bones run parallel to the longitudinal axis, causing long bone to endure higher compressive and tensile stresses in the longitudinal direction.

Fatigue Process

Since bone and engineered composite compositions are analogous, bone will also experience a 3-phase fatigue process while undergoing axial cyclic loading [35,46]. When subjected to axial cyclical loading, bone will progress through three phases that ultimately end with bone fracture. In the first phase the material is within its elastic region and will experience reversible deformation. However, the bone will also experience a change in stiffness from the development of micro cracks. The micro cracks are observed in healthy bone and are believed to benefit the bone by dissipating energy from the loading process [47]. The bone will attempt to repair the crack. Osteocytic apoptosis is the trigger for this remodeling process; the apoptotic cells signal their neighbors to increase osteoclastogenesis and bone resorption [48,49]. The micro damage accumulated by the respective loading is in equilibrium with the repair and remodeling systems. However, balance is broken as the bone progresses through its yield point.

As the bone reaches its yield point it enters the second phase and into its plastic deformation region. In this phase the bone continues to have a loss in stiffness; however, it is at a significantly decreased rate compared to the first phase. Conversely to stiffness, the toughening of the bone will increase; therefore, the amount of energy required for a crack to propagate will similarly increase [44]. Within this phase, the material has accumulated permanent damage and will no longer return to its original state. Comparing bone to the idiom, “a chain is only as strong as its weakest link”, the cement lines are the weakest part of bone. Most of the damage will occur at the cement lines [35]. It is within

this phase that the bone will attempt to slow the rate of crack growth rather than prevent damage [45]. Because the body has a natural repair mechanism, it must simply have a damage accumulation rate less than or equal to its repair rate. If the rates are equal the result of this is a healthy healed bone. Yet, if the crack growth rate exceeds the body's repair rate, the bone will eventually fail in a catastrophic manner.

There are two main theories concerning the failure of bone [46]. The first theory develops a stress based method. This theory takes into account the stress intensity factor K_c . As in traditional fracture mechanics, once the threshold of K_c is reached or exceeded, a crack will initiate within the material [50]. The microstructure of the bone will control how the crack will propagate. The second theory is based upon energy. The theory accounts for the critical strain energy release rate, G_c , and the work to fracture of a specimen, W_f . These are the factors for the critical amount of energy that will lead to fracture within a specimen. Pulling again from classical fracture mechanics, a materials fracture resistance is determined by its ability to absorb energy [50]. The more energy a material is able to absorb, the less likely it is to fracture. The cement lines are the 'weakest link' within bone and are most likely to fail. Having this designated weak area increases the bone's resistance to fracture. These interlamellar surfaces absorb the energy and break, thereby redirecting the crack tip and diminishing the chances for a complete fracture [51].

The last stage of the material involves its complete failure. By this point the bone has acquired a considerable amount of damage from the two previous stages. A crack has developed and begun to propagate. The bone's mechanical properties precipitously dwindle while the crack expands. The final result is complete failure of the bone. A few cases have shown that the osteons will pull out during this final stage. Osteon pullout is

due to shear failure around the osteon cement lines, which are more viscoelastic than the surrounding bone – due to their different mineral and protein configurations [52].

Resistance Mechanisms

There are several resistance mechanisms that bone has developed to minimize crack growth. Several of these mechanisms are depicted in Figure 1.7. The first mechanism examined to combat crack propagation is microdamage as seen in Figure 1.7(b). This common mechanism has been shown to dissipate the energy of the bone thus postponing failure. This mechanism is found within healthy bone and will develop at the crack initiation site to prevent crack growth. Consequently, the microdamage will reduce the overall ability of the bone to absorb energy. Extrinsic toughening may also occur due to the formation of a “frontal process zone” ahead of the propagating crack with a consequent formation of a microcracking zone in the path of the crack [53–55]. This zone will force a reduction in modulus thus shielding the crack tip [56]. There are two distinct types of microdamage experienced by bone; each is characterized by its initiation, location, development, and restoration [47]. First, linear microcracks are common forms of microdamage and are found in the mineralized interstitial bone. They are formed from compressive stresses and indicate the location of where the material has deformed. The second type is diffuse microdamage. These are groupings of small cracks that are caused by tensile loading. When these cracks are in close proximity to one another, they tend to nucleate, coalesce, and grow. The dynamic nature of the cracks divert energy away from the main crack tip [44].

The second mechanism to promote resistance to fracture within bone is crack bridging. Crack bridging is the dominant toughening mechanism in cortical bone [57–59]. It involves the formation of unbroken regions that span the crack ahead of the crack

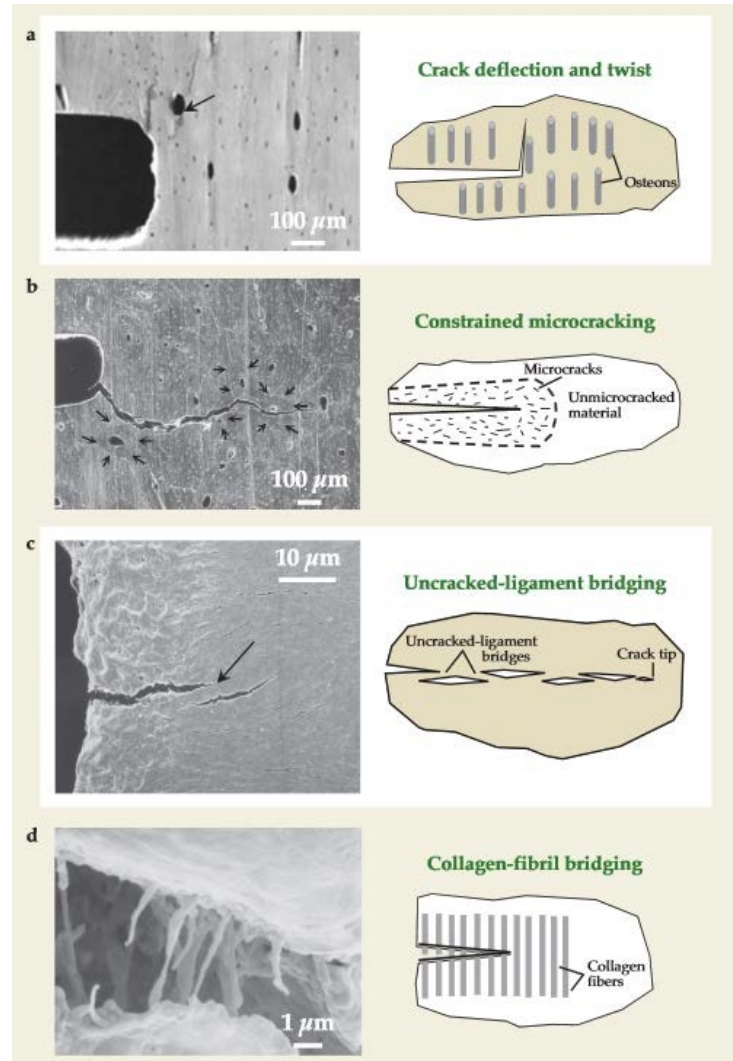


Figure 1.7. – Various fracture prevention mechanisms within bone. The mechanisms allow for damage to be mitigated in hopes that the bone’s remodeling process will repair the damage [51]. Reproduced with permission from R.O. Ritchie, M.J. Buehler, and P. Hansma, *Physics Today*, 62(6),41 (2009), with the permission of the American Institute of Physics.

tip to resist the crack. Within bone, collagen fibrils and mainly uncracked ligaments act as these unbroken regions by sustaining part of the applied load that would otherwise add to the crack advancement [56]. Collagen fibril bridging and uncracked ligament bridging can be visualized in Figure 1.7(d) and Figure 1.7(c) respectively.

The theory of the ‘sacrificial bond’ is the final strengthening mechanism that will be examined. The theory articulates that reforming, yielding, and breaking bonds within the organic molecule in bone toughen the material by absorbing large quantities of energy [60–64]. However, not all bonds contribute to the toughening mechanism. The breaking of specific bonds will ultimately fracture the bone. A principal example is that breaking ionic bonds within bone causes irreversible damage.

Break Classifications

The subject matter presented in this section refer to the work of this study, that is a continuation of Cler’s and Campbell’s previous studies. There are three main break classifications that have been noted [44,45]. The first is a brittle break. To the naked eye, a brittle break appears as a relatively smooth fracture surface with straight edges. This is evidence of a fast fracture. Under higher magnification in an SEM, the specimen was observed to have broken across the thickness of the specimen. Also, a separation of the bone layers is observed (Figure 1.8a). This delamination of the layers is a result of high forces separating individual layers of bone along the specimen’s thickness. The crack grows through the interstitial matrix due to high stress while additionally weakening the interfaces between the bone as well. Toughening mechanisms that attempt to combat a brittle break are void coalescence and ligament crack bridging. These toughening mechanisms are extrinsic, occurring behind the crack tip. The second break classification is a ductile break. A characteristic of a ductile break are beach markings. Clamshell or beach markings (Figure 1.8(b)) are curved lines that often appear on a fatigue fracture surface. They indicate changes in load or environment conditions that occurred during the lifetime of the specimen [50]. Beach markings elucidate the travel route of the crack propagation. Crack propagation occurs along the width of the bone for a ductile break.

Also, osteon pullout may be observed within this mode of breaking. Lastly, a mixed mode classification has been noted (Figure 1.8(c)). It exhibits a combined brittle and ductile break mode and has characteristics of both. Beach markings are observed; however, they do not populate the entire surface. Part of the surface displays smooth and straight edges coupled with delamination. Scanning electron microscope (SEM) images of these failure modes are represented in Figure 1.8.

Fatigue Limit - Prediction Methods

The fatigue limit of a material is defined as the maximum stress amplitude it can endure, indefinitely, without failing [65]. There are several mathematical methods used to estimate this limit for common materials. The methods that are tested rely on the examination of motion of the specimen. One method counts the loading cycles while the other utilize novel nonlinear dynamics to determine fatigue. If such a method could accurately describe the fatigue limit in vitro it has the potential to revolutionize stress fracture prevention.

Palmgren-Miner Rule

The first method that will be examined is the Palmgren-Miner rule (PMR). The rule is a linear cumulative damage standard that is used to estimate the fatigue limit of a material. PMR states that the total sum of the ratio of the number of cycles of a given amplitude and the number of cycles to failure equal the damage accumulated. This is expressed mathematically in Equation 1.1.

$$D_p = \sum_{i=1}^k \frac{n_i}{N_i} \quad (1.1)$$

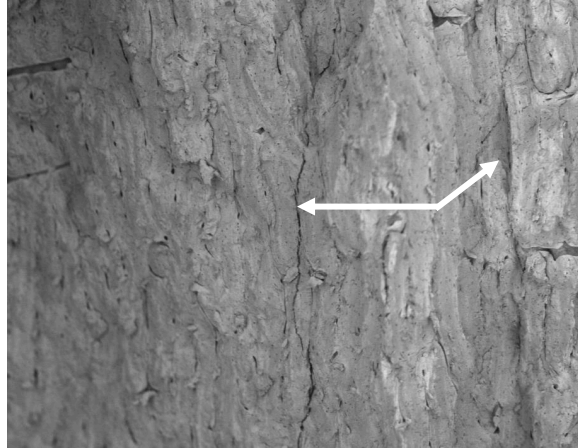


Figure 1.8.a – SEM image of cortical bone of a brittle break. The arrows reveal delamination [45]. Printed with permission from M. Cler et al.

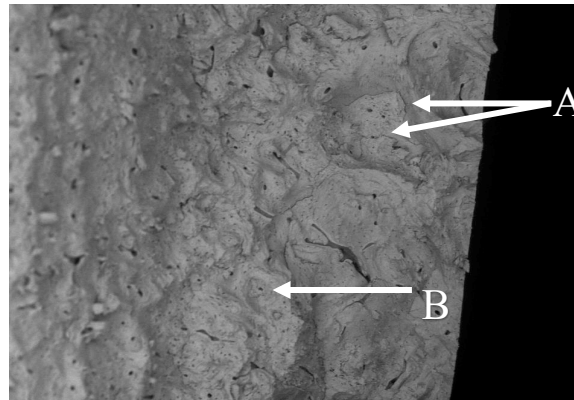


Figure 1.8.b – SEM image of cortical bone of a ductile break. The arrows (A) point to beach marking while the arrows (B) show osteon pullout [45]. Printed with permission from M. Cler et al.

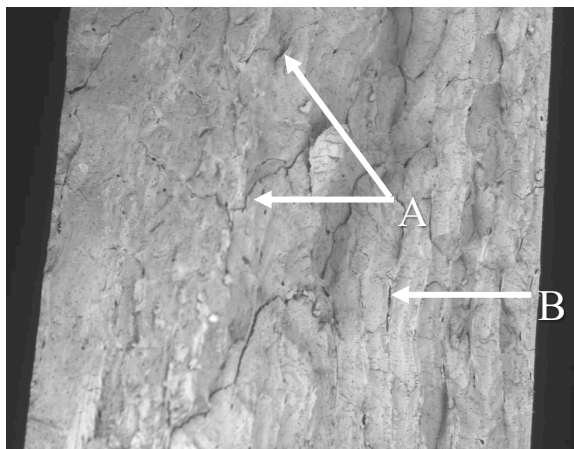


Figure 1.8.c – SEM image of cortical bone of a mixed mode break. The arrows (A) point to beach marking while the arrows (B) show delamination [45]. Printed with permission from M. Cler et al.

where D_p denotes the damage parameter, n_i is the number of cycles at a specific amplitude, and N_i is the total number of cycles the material can withstand till failure at that amplitude. The material will fracture when the accumulated damage is equal to one. For PMR, it is assumed that the order of the differing loads and cycles is irrelevant. Secondly, it is assumed that the material's history and loading pattern do not influence how the material will fail. PMR is not without its flaws. Behavior of materials commonly diverge from the PMR prediction [66–69]. Several of the main causes for differences between observed and PMR predicted fatigue life are independent of the load level, load sequence, and the load interaction. Furthermore, the fatigue limit stress and the critical stress appear to impact fatigue life. Lastly, PMR must account for the fact that applied stress is dynamic. It shifts moment to moment with the change in crack length.

Rainflow Counting

It is easy to calculate the number of cycles when a specimen is subjected to cyclical loading at a constant amplitude. However, within the natural world and this study, the number of cycles at a specific amplitude is difficult to count because they may be intermixed with other amplitudes. In order to combat this, the rainflow counting method (RCM) was utilized. This method is commonly accepted as a standard for cycle counting and is used in conjunction with PMR for fatigue tests [70–72]. It is easiest to visualize RCM as water flowing down a structure, such as a pagoda. As the flow runs off an edge of the building, it is considered a cycle count. Apply the principle to a 90 degrees clockwise rotated plot of strain versus time. An example of RCM is seen in Figure 1.9. Each trough is considered a water source. The water flows down the peaks until it comes to a larger trough, encounters the flow from above, or reaches the end of the recorded time for the plot [73]. Each of the flows are counted as a half cycle whose magnitude is

the difference of the values of the strain at the start and end of the flow. Lastly, the total cycle count is the sum of the half-cycle pairs. Applying these rules to Figure 1.9 a total of 15 half cycles can be counted, therefore, the total cycle count is 7.5.

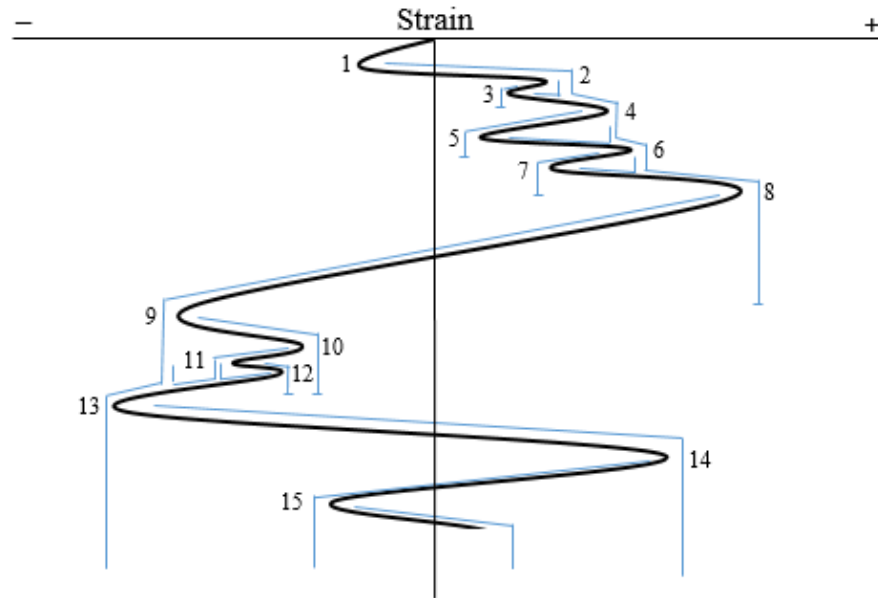


Figure 1.9. – Rainflow counting plot. Location 1 reveals a water source while location 2 shows an encounter with a flow from above. Location 7 is an encounter with a large trough. Lastly, location 15 is the end of the recorded time [44]. Printed with permission from A. Campbell et al.

Phase Space Warping

The second method for fatigue prediction is phase space warping (PSW) that utilizes fast time measures to reconstruct slow time dynamics. The reconstructed phase-space can then be used to track damage evolution through small drifts in the phase space [74–76]. A useful method and mathematical model has been developed by Dr. Chelidze at the University of Rhode Island that analyzes the slow time processes using fast-time, vibration measurements [74,77–82]. The method employs an updated version of the two-well magneto-elastic oscillator, termed Moon’s beam set-up, while the mathematical

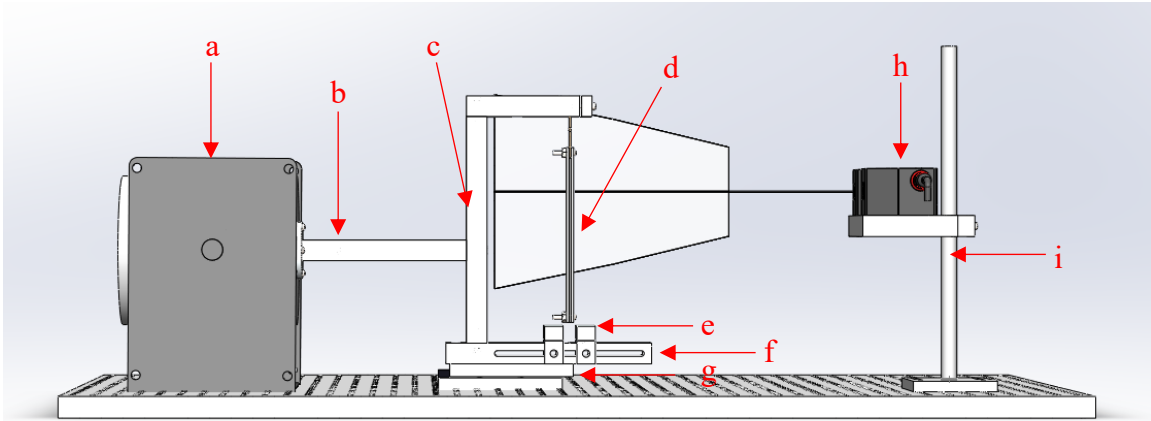


Figure 1.10. – Moon’s beam apparatus set up with components labeled. (a) shaker (b) 9-in aluminum bar (c) C-Frame (d) specimen pendulum (e) magnets (f) linear guide conversion piece (g) linear guide (h) laser vibrometer (i) aluminum laser stand (j) vibration isolation table [45]. Printed with permission from M. Cler et al.

model is the Duffing equation. PSW has appeared to successfully identify the various modes of damage experienced from chaotic loading of bovine bone [45].

A similar set-up to Dr. Chelidze’s apparatus was used in this study. A CAD model of the experimental set up is provided in Figure 1.10. A C-Frame holding the specimen that is clamped between two steel plates is attached to a shaker. The pendulum is held over two rare earth magnets, thus creating two potential wells for the specimen to fall into. The situation the pendulum is put in is best understood through a ball and two valley analogy. The pendulum will represent the ball while the two valleys are the two magnets wells. The ball sits atop of a hill that separates two valleys. This hilltop is an unstable point, so the ball will roll into either the right or left valley. Once the ball rolls into a valley it will stay there. It will only be able to move out of that valley if enough energy is added to the system such that the ball can roll back up the hill to its top. Once the ball is back to the hill top it is again put into an unstable point. It will either roll back into the previous valley or fall into the other one. This motion can be described by the equations developed by Dr. Chelidze [74,83]. The Duffing equation can be utilized to model this

vibrating beam system over a double potential well. The forced Duffing equation form is revealed in equation 1.2.

$$\ddot{x} + \gamma\dot{x} - \alpha x + \beta x^3 = f \sin(\omega t) \quad (1.2)$$

where:

x = fast time dynamics

f = amplitude

ω = frequency

t = time

Also, γ , α , and β are positive real constants. From the equation, the displacement of the pendulum, or the directly observable fast-time dynamics, can be related to the forcing of the specimen. To better visualize this outcome, Figure 1.11 displays the phase space of the unforced Duffing equation. This is simpler than the forced Duffing equation but is used to illustrate the more complex yet similar concepts. Figure 1.11 displays several points of interests. At point (-3,0) and point (3,0) there are stable fixed points, the bottom of potential wells, or valleys from the analogy. These are the wells that will hold the pendulum until a sufficient amount of energy is brought into the system to force it out from the well. When the pendulum swings from one well to another it is termed to have a large amplitude of vibration. If the pendulum swings and falls back into the well it is termed to have a small amplitude of vibration. These wells represent the magnets within this study. At point (0,0) is the unstable point, or the hill separating the two valleys. This is the initial position of the pendulum, or ball, and the position from which it will fall into either well.

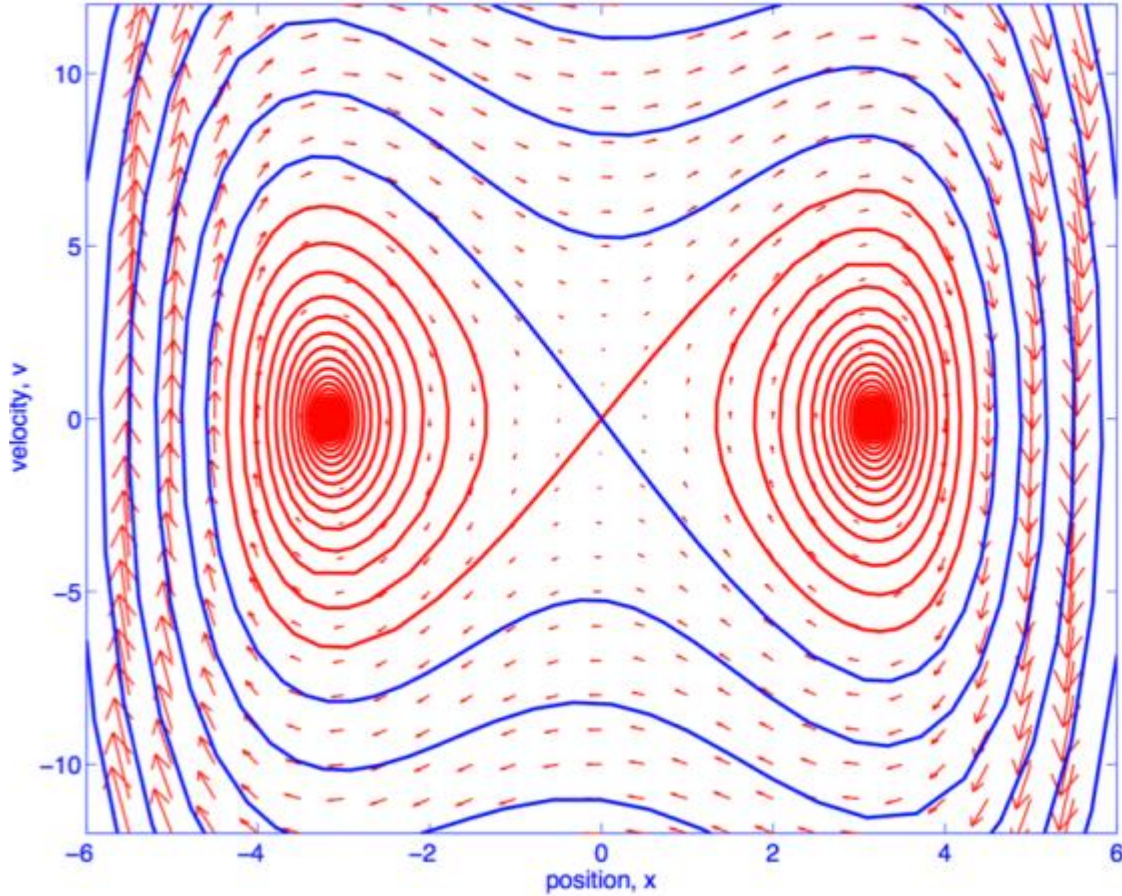


Figure 1.11. – Unforced Duffing equation phase space. The dense red areas are the location of the wells. The intersection of the red and blue lines at (0,0) is the starting position of the pendulum [45]. Printed with permission from Dr. David Chelidze, University of Rhode Island.

Upon investigation, it is found that the system can be modeled using hierarchical dynamical systems. The model is derived from the relationship between fast-time dynamics and slow-time dynamics along with equation 1.2. The system of equations is expressed in equation 1.3 through equation 1.5

$$\dot{x} = f(x, \mu(\phi), t) \tag{1.3}$$

$$\dot{\phi} = \epsilon g(x, \phi) \tag{1.4}$$

$$y = h(x) \tag{1.5}$$

where:

x = directly observable fast-time variable

ϕ = slow time variable

μ = vector of parameters

t = time

ϵ = small rate constant

y = scalar measurement

The vector of parameters is a function of the slow-time variable. The small rate constant is also known to be the time-scale separation between the fast and slow dynamics. It is a value that is greater than zero but much less than one. Lastly, the scalar measurement is determined by the smooth function h of the fast time variable. From these equations it is revealed that the slow time variable, ϕ , can change and develop on a time scale that is slower than the fast time scale that is directly observed.

For this slow time scale to be understood and analyzed, the experiment needs to run for a sufficient amount of time to induce change. A long capture time coupled with a high data sample rate inevitably leads to these experiments having sizable data sets that sometime exceed a gigabyte of memory. To reduce the data down to a manageable size, it is broken up into intermediate time scales. By doing so one can treat the fast-time dynamics as quasi-stationary and are molded as feature vectors. Therefore, the fast-time dynamics can be characterized with a local linear model. This allows for a non-linear function to be approximated with piece-wise linear functions. With these local linear models, the fast time dynamics can be reconstructed with the help of delay coordinate embedding.

Delay coordinate embedding requires that a proper time delay be established. If the time delay is too small the resulting delay vectors are too close to the hyper-diagonal of the reconstructed phase space. Thus, information on variations in motion is poorly defined and lost. Yet the time delay should be small enough such that the coordinates are not statically independent from one another. The coordinates should maintain important characteristics. A useful method to determine the delay time is the average mutual information (AMI) method, which measures the dependence between variables [78–80,83–85]. It aims to reduce the uncertainty of one random variable due to knowing another variable. AMI traditionally relates to a variable's entropy for entropy is 'self-information'. By this the AMI between two variables is the negative of the entropy of the variables' joint density function with respect to their marginal product [86]. The AMI between two random variables is expressed in equation 1.6.

$$I(X; Y) = \sum_{x \in X} \sum_{y \in Y} p(x, y) \log \frac{p(x, y)}{p(x)p(y)} = D(p(x, y) || p(x)P(y)) \quad (1.6)$$

where:

$p(x, y)$ = joint density function

$p(x)$ = marginal of X

$p(y)$ = marginal of Y

Once this function is plotted, the independent variable value of the first minimum can be ascertained visually, this minimum will then become the time delay, τ . Along with the time delay, an embedding dimension needs to be determined.

The minimal necessary condition for this embedding dimension is provided by the false nearest neighbor (FNN) method [87,88]. The FNN method is visualized in Figure 1.12. Two points in d dimension are true nearest neighbors (TNN), C' and D' , then simply adding the $(d + 1)$ -th coordinate will not separate them from each other. These projected coordinates remain close to the original coordinates, C and D . If points are TNNs in the projection, then observing the points in the original dimension will show they are neighbors. If two points are FNN, A' and B' , then adding the $(d + 1)$ -th coordinate will separate them. The two points were only neighbors on the projection of a higher dimensional structure. Viewing the original two points, A and B , will reveal that they are not neighbors. A and B do not reside next to each other in the 3-dimensional space. Thus the embedding dimension is found by finding the smallest dimension with zero numbers of FNNs.

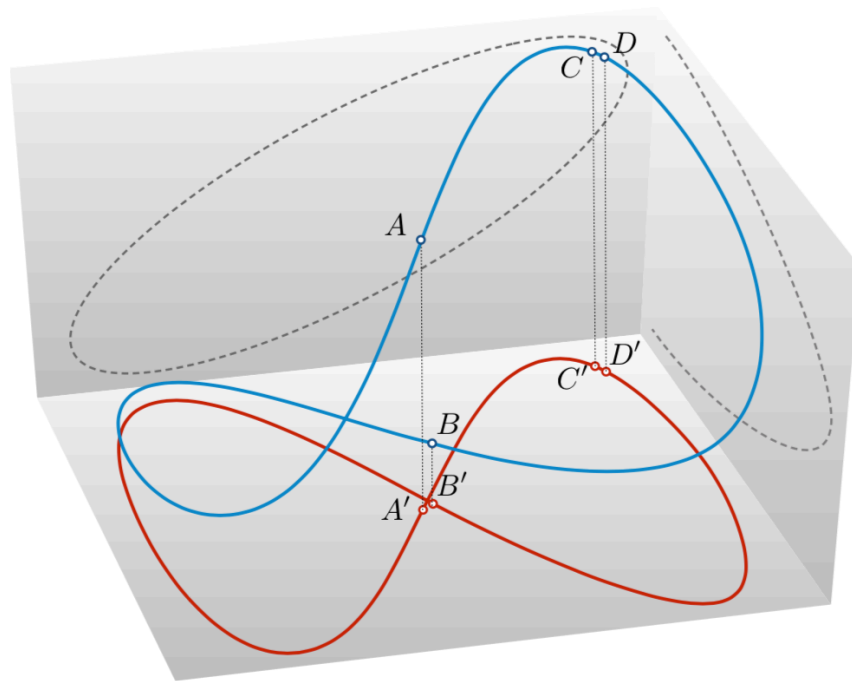


Figure 1.12. – An illustration of false nearest neighbors. Original three-dimension closed curve in blue. Two-dimensional projection in red. Dotted lines are projections onto other planes. C' and D' are TNN while A' and B' are FNN [87]. Printed with permission from Dr. David Chelidze, University of Rhode Island.

This process of finding a delay time and embedding space is calculated for each intermediate time scales. Once the intermediate time scales are compiled, the shifting of the feature vector is analyzed to see if there are changes; these changes are potentially caused by damage [77–79,83]. The phase space warping function is the difference between the feature function of the original system to the fatigued system. The phase space warping function will also elucidate where the warping is taking place. An example of the differences between phase spaces of original and fatigued bodies is shown in Figure 1.13. Lastly, all of the phase space warping functions are compiled to create the tracking matrix [79].

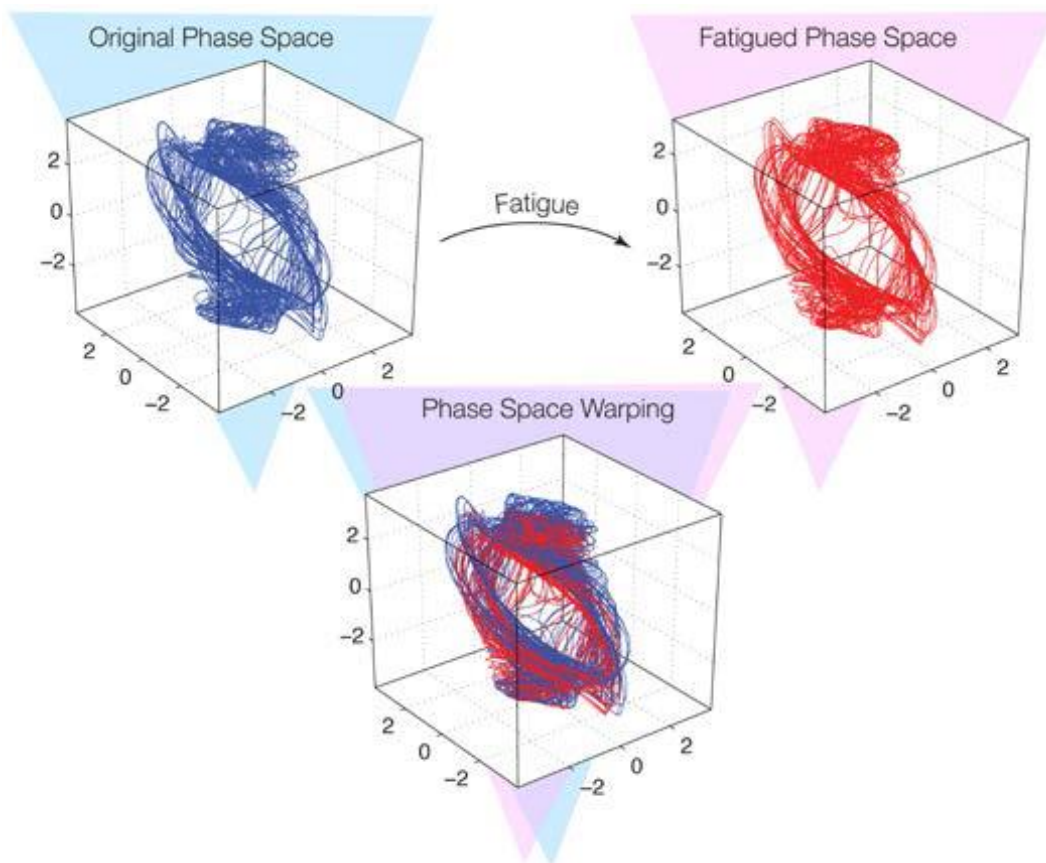


Figure 1.13. – Phase space warping diagram. A comparison between the original phase space and its fatigued phase space. The difference is possible damage [45]. Printed with permission from Dr. David Chelidze, University of Rhode Island.

Smooth orthogonal decomposition (SOD) is performed on the tracking matrix to find the fatigue modes. SOD is related to but distinct from proper orthogonal decomposition (POD). Both SOD and POD employ the same method in which a singular value decomposition is performed on the data matrix. Either method then decomposes the data into statistical normal modes. These normal modes are used to show the statistical models that best account for the variance in amplitudes. SOD is preferred in this case because it handles the bifurcations that are present in fast-time dynamics better than POD [89,90]. SOD utilizes the maximization problem presented in equation 1.7. POD uses a similar maximization problem that is constrained differently.

$$\max_{\phi} \|X\phi\| \text{ subject to } \min_{\phi} \|V\phi\| \quad (1.7)$$

where:

X = tracking matrix

V = temporal derivative of X

The tracking matrix is then projected onto the SOD modes to find the slow time damage phase space. This phase space will then be reconstructed via the SOD coordinates [91]. Lastly, the slow-time dynamics can be used to identify the dynamics of fatigue [77–80,83]. The method developed by Chelidze and his team has been shown to predict failures in stationary operating environments [92].

CHAPTER TWO

Methods and Materials

Introduction

For the experiments in this study bovine bones were used. The bones were then processed. Each bone yielded six specimens of similar shape and size. Specimens taken from the same location of the bone were utilized for one of three tests. Three specimens were used for the chaotic loading test, two specimens for the variable amplitude test, and one specimen for the four point bend test. This was done to allow the use of repeated measures statistical analysis that takes into account the variability between bones. The chaotic loading test forced specimens under chaotic loading conditions. The variable amplitude test had two distinct failure mechanics act upon the specimen. A four-point bend test was carried out on specimens to determine the mechanical properties of each bone.

Specimen Preparation

Ten bovine femurs were purchased from Animal Technologies, Inc. (Tyler, TX). Femurs were chosen because their large size allowed for multiple cortical bone specimens to be cut from the same bone. The gender, age, and health of the cattle that the bones are taken from are unknown. Animal Technologies, Inc. indicated that the cows were between the ages of 8 and 30 months. The femurs were shipped frozen on dry ice. Upon arrival the bones were stored in a commercial freezer at 20°C (Artic Air, WCI/Frigidaire Co., Eden Prairie, MN). Prior to specimen preparation, the bones were

allowed to thaw for 24 hours in a compact refrigerator (Kenmore, Sears Roebuck and Co., Chicago, IL).

Any remaining soft tissues attached to the shaft of the femur were removed. A Craftsman band saw (Stanley Black & Decker, New Britain, CT) was used to cut off the femur's epiphyses and to cut the shaft longitudinally into medial and lateral halves. The marrow was removed. The halves were each cut longitudinally into thirds. Each of the six sections was further trimmed with a Buehler IsoMet™ 1000 precision saw (Buehler, Lake Bluff, IL) with an IsoMet™ 15 LC diamond blade. The cooling fluid used was 1 part Buehler Cool 2 cutting fluid to 33 parts water. Each specimen was trimmed to approximately 2-3 inches long, 0.1 inches thick, and 0.5 inches wide. Next, a black Sharpie® marker (Newell Brands, Atlanta, GA) was used to label the specimens. The specimen was labelled with the number assigned to the femur plus A-F, depending on the

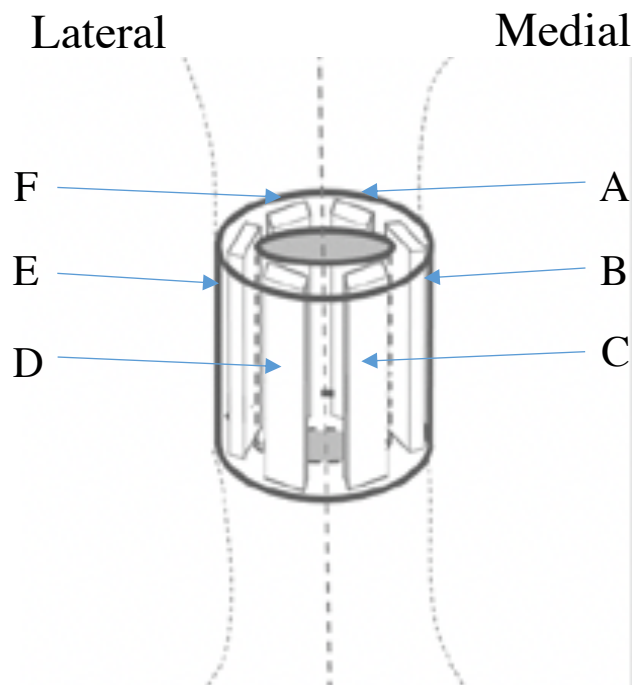


Figure 2.1. – Schematic of specimens extracted from a left femur. Blue arrows lead from label name to location extracted from femur. Specimens A and F are from the cranial part of the shaft and C and D are from the caudal part.

location from which they were cut (Figure 2.1). For example, a specimen created from bone 6 location D would be labeled 'SP6D'. Each specimen was then wrapped in gauze and misted with 0.9% saline solution in a Ziplock™ bag. Lastly, all specimens from a bone were grouped together in a larger Ziplock™ bag based on bone number.

Further specimen preparation was performed on specimens destined for variable and chaotic amplitude loading. To reduce the width of the specimen, notches approximately 0.32 – 0.35 inches deep were made on both sides with a triangular file. A custom aluminum jig was used for appropriate placement of the notches. The notches were at least 1.25 inches down from the top of the specimen. The notches served to concentrate the stresses in the center of the test section and cause bone to fail at this location. A Central Machinery 13" drill press (Harbor Freight Tools, Calabasas, CA) was then used to drill an 11/64" hole approximately 0.625 inches down from the notches on the specimen. The hole was used to attach steel plates to the bone specimen with a nut and bolt.

If testing occurred within one week of preparation the specimen was stored in the compact refrigerator. However, if the specimen's test date was more than one week after preparation, it was stored in the commercial freezer. The frozen specimens were thawed in the refrigerator for 24 hours prior to testing. After, the specimen was removed from the Ziplock™ bag and moist gauze, it was air dried for seven hours. This drying process was determined from prior work [44,45]; after seven hours of air drying the specimen's resonant frequency becomes stabilized.

Chaotic Loading Test

Hardware

The main testing setup is the same used in Cler et al [45] because this study is a continuation of previous work. To summarize, the system used for testing was modeled after Dr. Chelidze and his team at the University of Rhode Island. The set-up is called Moon's Beam apparatus; it is mathematically modelled using the Duffing Equations.

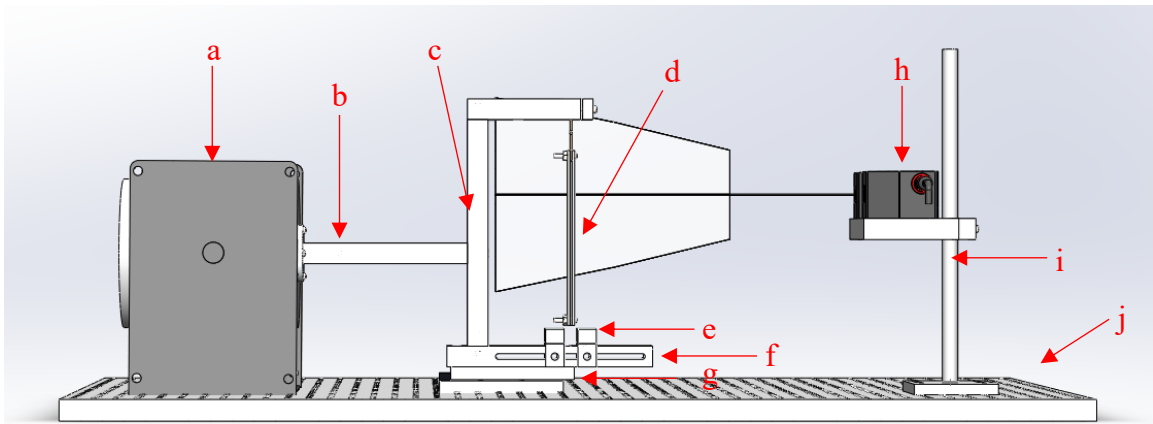


Figure 2.2. – Moon's beam apparatus. (a) shaker (b) 9-in aluminum bar (c) C-Frame (d) specimen pendulum (e) magnets (f) linear guide conversion piece (g) linear guide (h) laser vibrometer (i) aluminum laser stand (j) vibration isolation table [45]. Printed with permission from M. Cler et al.

Figure 2.2 illustrates the components of the Moon's Beam apparatus. This set up fatigues bone specimens in a chaotic manner in an attempt to more accurately simulate the natural variable loading which bone is subjected to *in vivo*.

The Moon's Beam apparatus was mounted on a vibration isolation table (Figure 2.2 (j)) (Nexus Breadboard, Thorlabs, Newton, NJ) to isolate the system from external vibration. A VTS-100 electromagnetic shaker (Figure 2.2 (a)) (Vibration Test Systems, Aurora, Ohio) provided the forcing function to the apparatus. An 8 in long aluminum bar (Figure 2.2(b)) connected the shaker to a custom aluminum C-frame (Figure 2.2(c)). The C-frame was mounted to an AC-NMS-4 linear guide (Figure 2.2 (g)) (Del-Tron

Precision, Inc., Bethel, CT) which was mounted to the vibration isolation table. A conversion piece (Figure 2.2 (f)) was used to connect the C-frame to the linear guide. The linear guide was used to minimize friction as the C-frame translated, restrict motion to translation, and minimize wear and tear on the shaker. A laser vibrometer (Figure 2.2 (h)) (LJ-V7300, Keyence, Elmwood Park, NJ) was mounted on a custom stand (Figure 2.2 (i)) that was attached to the vibration isolation table. The laser vibrometer was used to record the displacement of the pendulum relative to the C-frame throughout testing. Two rare-earth permanent magnets (Figure 2.2 (e)) (5/8" x 5/8" Cylinders – Neodymium Rare Earth Magnets, Apex Magnets, Petersburg, WV) were mounted to the bottom of the C-frame via the conversion piece.

Several components of the experimental setup resided on a table next to the vibration isolation table. The components consist of a computer, amplifier (2002 XTi Series, Crown by Harman), low-pass filter (SR640, Stanford Research Systems, Sunnyvale, CA), DAQ chassis (NI cDAQ-9174, National Instruments, Austin, TX), VTS blower (Vibration Test Systems, Aurora, Ohio), Keyence 24 V DC power supply and

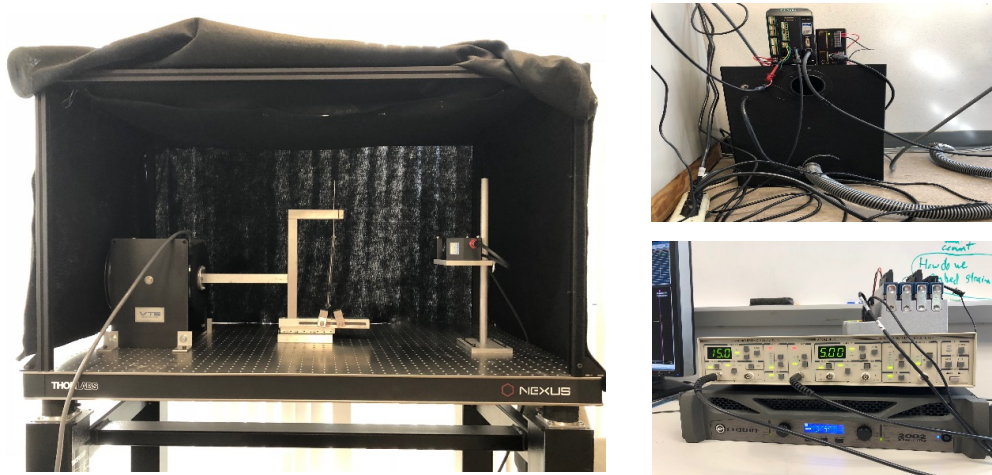


Figure 2.3. – Picture of testing hardware. Left image shows Moon's beam apparatus. The pendulum, shaker, and laser vibrometer are visible. Upper right image is of the blower unit on bottom with Keyence controllers atop it. Lower right reveals amplifier (bottom), low-pass filter (middle), and DAQ chassis (top).

controller (Keyence, Elmwood Park, NJ). The computer connected to both the Keyence controller and the amplifier. The computer required the analog output of the NI-9263 DAQ card to connect to the amplifier. The amplifier was also connected to the shaker. The shaker was cooled using the blower which was connected via hose. The NI-9205 DAQ card was used to continuously collect data from the low-pass filter that was connected to the Keyence controller. Photos of the testing rig are provided in Figure 2.3.

The specimen pendulum was mounted to the top of the C-frame. A detailed illustration of the pendulum is provided in Figure 2.4. The bottom end of the test specimen was mounted between two steel plates while the top was clamped into the C-frame. The pendulum was suspended over the two rare earth magnets. The magnets were used to induce a double potential well for the pendulum. The oscillating motion of the pendulum delivered the bending load to the specimen. With this double potential well, harmonic, variable, or chaotic forces could be applied to the specimen. The double

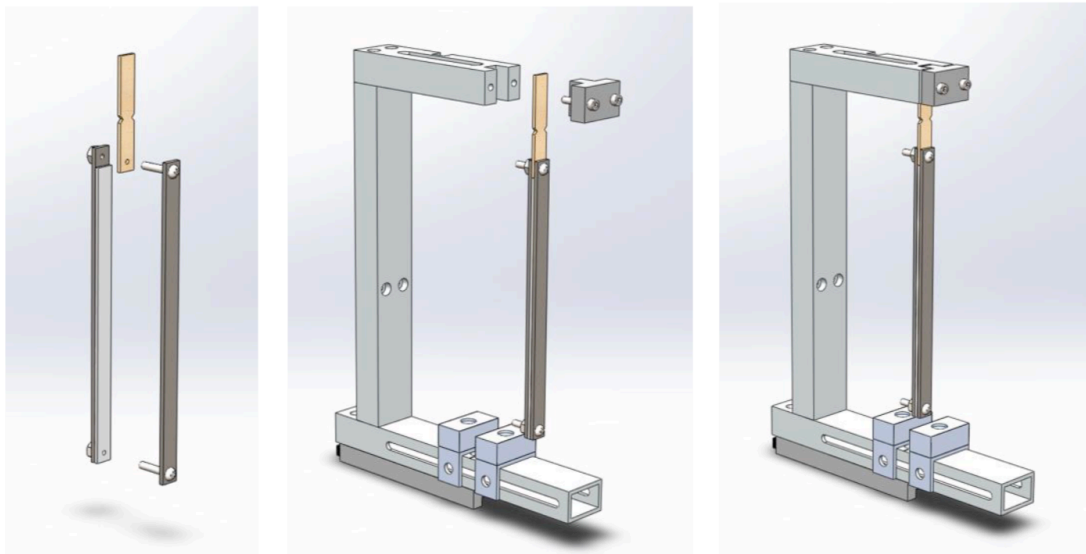


Figure 2.4. – Specimen Pendulum. The bovine bone specimen is sandwiched between two steel plates that will react to the magnetic field (left). The specimen was clamped to the C-frame to induce bending at the notch site (middle). The pendulum is suspended over the magnets to produce a double potential well (right) [44]. Printed with permission from A. Campbell et al.

potential well was used because a single potential well can only provide harmonic forcing.

The motion of the pendulum could be related to the study conducted by Campbell [45]. If the pendulum moved from one potential well to the other, it was considered to have a large amplitude motion and typically resulted in a brittle break. If the pendulum stayed over only one potential well it was considered to have a small amplitude motion and likely resulted in a ductile break.

Software

LabVIEW programs were developed to be used in tandem with the factory provided Keyence software to control the shaker and record collected data from the laser. The graphical user interface (GUI) and block code of the programs are located in Appendix E. A LabVIEW program controlled the waveform of the shaker (WaveGeneration.vi). This virtual instrument (VI) is able to control the amplitude, waveform, and frequency of the shaker's motion. The amplitude of the shaker could be controlled with other instruments; however, it was decided to only use the WaveGeneration.vi to control it.

Another LabVIEW program collected the step data of the Keyence laser and wrote the data to a .lvm file (LASER-Voltage-ContinuousInput.vi). This program was created to cover for the short falls of the Keyence software and its limited memory. The LASER-Voltage-ContinuousInput.vi allowed for all the data to be collected from the Keyence software, preventing any loss of data. The Keyence software calibrated the laser such that 1 V corresponded to 1 mm of deflection. The Keyence software was also used to collect profile data to set measurement points to determine the swing distance of the pendulum.

Variable Amplitude Test

Hardware

Only minor modifications to the testing apparatus were needed for performance of the variable amplitude experiment. The variable amplitude set up is the same as described in a previous study by Campbell et al [44]. The 8-inch aluminum bar that connected the shaker to the C-frame was replaced with a 1.5-inch aluminum rectangle that held two $\frac{3}{4}$ inch cams (MSC, Melville, NY). The 1.5-inch arm did not connect to the C-frame. The different set up applied a load to the pendulum that acted as a reversible single cantilever beam. The C-frame was dismantled from the linear guide and secured directly to the vibration isolation table. The cams applied the load to the pendulum. The specimen pendulum remained the same but moved from the front of the C-frame to its side. Figure 2.5 reveals the changes described above to the setup. The other hardware pieces remained the same.

Software

A LabVIEW program, VariableAmplitudeWaveGeneration-VoltageOutput.vi, was developed to control the waveform of the shaker. The program differed from the

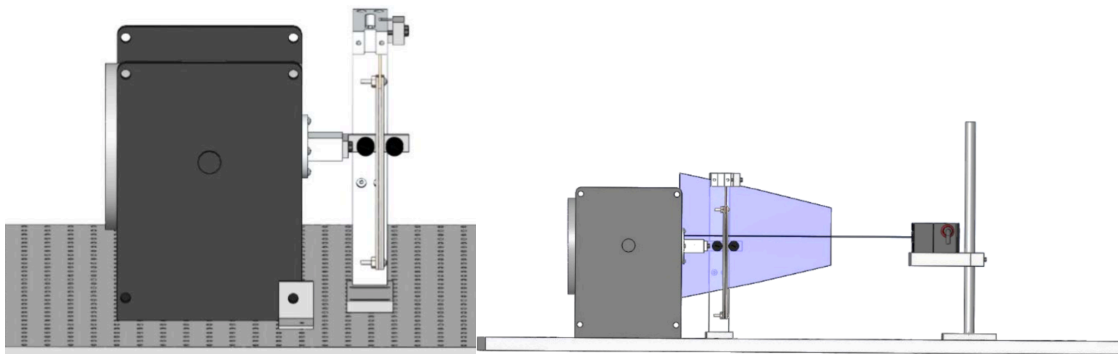


Figure 2.5. – Variable Amplitude hardware changes. The left image reveals the short arm with attached cams. Right image depicts side view of overall setup [44]. Printed with permission from A. Campbell et al.

WaveGeneration.vi for it allowed the user to select up to three different wave amplitudes and frequencies. The program also allowed the user to select the number of cycles for each waveform. The LASER-Voltage-ContinuousInput.vi was used in the same fashion as in the chaotic loading test.

Four-Point Bend Test

Hardware

The four-point bend test utilized TESTRESOURCES 100 series system coupled with a custom jig to carry out the test. Figure 2.6 details the components of this setup. The actuator (Figure 2.6 (a)) (DG.1000 ACTUATOR, TESTRESOURCES, Shakopee, MN) is attached to a 1000 lbf load cell (Figure 2.6 (b)) (SM-1000-294, TESTRESOURCES, Shakopee, MN) that in turn is connected to the top half of the four-point bend jig (Figure 2.6 (c)). The bottom half is attached to the bottom of the TESTRESOURCES 100 series frame (Figure 2.6 (e)) (Shakopee, MN). A detailed diagram of the jig is located in Appendix F. The system is controlled by an external controller (Figure 2.6 (d)) (P-Q Series, TESTRESOURCES, Shakopee, MN) that is connected to a computer.

Software

The TESTRESOURCE Xy Plot was utilized to control the four-point bend test apparatus through the controller. The software was used to collect data of the position of the pneumatic head, test time, and stress. The software was also employed to identify the maximum stress from the four-point bend test via a built in function.



Figure 2.6. – TESTRESOURCES apparatus. (a) actuator (b) load cell (c) four-point bend jig (d) controller (e) frame.

Specimen and System Preparation

Chaotic Loading Test

Approximately 30 minutes before the testing began, the laser was turned on to warm up. Specimens from cut location D through F were used in chaotic loading test. The specimen was measured with a digital micrometer; the notch width, thickness, and gage length were recorded. The specimen was then secured between the steel plates and mounted to the C-frame.

The pendulum and the magnets were adjusted such that the magnets had the same inward tilt and the pendulum was centered between the magnets. The precise frequency for the pendulum was determined by gently tapping the pendulum while it was over only one of the potential wells. The laser vibrometer collected data at 200 samples per second to capture the gentle tap motion. The data was then put through the ResonantFrequencyLVM.m MATLAB program to determine the precise frequency. In order to achieve the desired frequency of 9 – 10 Hz, the pendulum was adjusted along the vertical axis: up to decrease the frequency or down to increase it. This procedure was repeated for the other potential well. The objective was to have the frequency for both potential wells to be within 0.2 Hz of each other. If the frequencies were outside of this range then the second potential well would be slightly adjusted inward to increase the frequency or outward to decrease it. Once the frequency was calibrated the test procedure could begin.

Variable Amplitude Test

The laser was turned on approximately 30 minutes before experimentation to allow it to warm up. Specimens from cut location B and C were used for the variable amplitude test. Each specimen was measured with a digital micrometer; the notch width, thickness, and gauge length were recorded. The specimen was then secured between the steel plates to form the pendulum. The pendulum was mounted to the C-frame between the two cams.

Four –Point Bend Test

Specimens taken from cutting location A were used for the four-point bend procedure. A digital micrometer was used to measure the width, length, and thickness of

the specimen. The specimen was placed onto the lower half of the custom four-point bend jig. The specimen was centered over the gap of the jig.

Test Procedure

Chaotic Loading Test

Chaotic loading testing was performed on 30 bovine bone specimens. The frequency of the waveform generator was set using the WaveGeneration.vi. The frequency selected was the frequency of the potential wells. However, if the frequencies of the potential wells differed, then the average of the frequencies was used. The frequency of the waveform generator was set close, if not exactly, to the resonant frequency of each well in order to maximize results. By doing this, the work done on the system increased both the mechanical energy and the amplitude of the system's response.

The amplitude of the waveform generator was set to zero before the test began. The blower was turned on. The Keyence program and the LabVIEW VI programs were initiated to collect data, save the collected data, and control the waveform generator. Before chaotic motion was reached, the amplitude of the waveform generator had to

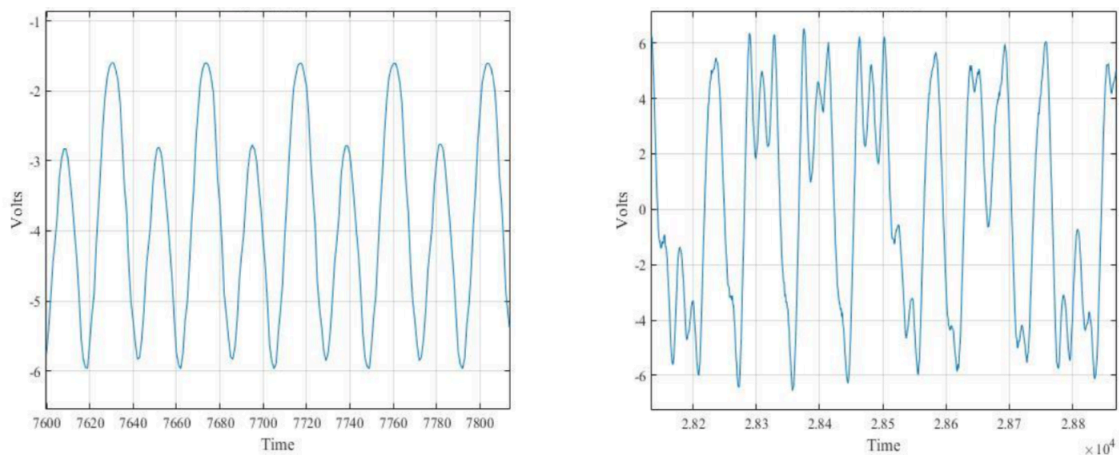


Figure 2.7 – Types of motion. The left image shows reaching motion. The motion is characterized by alternating different peak amplitudes. The right image depicts chaotic motion. This motions displays various amplitude peaks that change chaotically [45]. Printed with permission from M. Cler et al.

induce a reaching pattern on the specimen. The difference between reaching and chaotic motion are illustrated in Figure 2.7. Reaching motion was accomplished by increasing the amplitude of the waveform generator by 0.25 units until the reaching pattern was observed. Afterwards, chaotic motion would be accomplished by increasing the amplitude by 0.10 units until chaotic motion was seen. The final amplitude of the waveform generator was set 0.05 units above the chaotic motion threshold.

The test continued until the specimen broke into two or more pieces. Once failure was achieved, the specimen was carefully removed from the testing apparatus to preserve the fracture surface. The rainflow counting method was utilized to count the cycles for the chaotic loading test. There were two different binned methods used for counting. The first was a bin size of 0.25 mm. The other consisted of 3 bins of small, medium, and large amplitudes. From prior studies, low amplitudes correspond to a ductile break, medium amplitudes correspond to a mixed break - exhibiting both ductile and brittle break characteristics, and large amplitudes correspond to a brittle break. Then the slow time dynamics of the system were analyzed for the specimen.

Variable Amplitude Test

Similarly, the variable amplitude test ran the VariableAmplitudeWaveGeneration-VoltageOutput.vi. Pattern three from Campbell's work was used for setting the motion. This entailed 1000 cycles at an amplitude of 3 volts followed by 100 cycles at an amplitude of 6 volts. One volt corresponds to one millimeter of deflection of the tip of the pendulum. This pattern was carried out on 16 bone specimens at a frequency of 5 Hz and operated at this way until the specimen failed. The Keyence and its companion LabVIEW VI programs were utilized to collect and save data. After the specimen failed, it was removed from the testing jig and was placed carefully on a nearby table for further

examination. The rainflow counting method was utilized to count the cycles for the variable amplitude test. The binning method presented in the chaotic loading test section was utilized to count the cycles for the variable amplitude test.

Four-Point Bend Test

A four-point bend test was performed on specimens from every bone. The stress vs. strain curve of every specimen was created to elicit the modulus, maximum stress, and strain at maximum stress. The actuator and top part of the four-point bend jig was lowered as close as possible to the specimen without touching it. The system was zeroed to this position. The test parameters for the experiment was set through the Xy Plot software. The default settings of “Beam” were used for the test procedure. The experiment was self-terminated once the “Sample Break” value of 50% was reached. The Xy plot software sent the test profile to the controller. The start button was pressed on the controller to start the experiment. The Xy plot software then collected, stored, and analyzed the data.

Analysis

Custom MATLAB programs were coded in house for data reduction and analysis. The programs are provided in Appendix E.

ResonantFrequencyLVM.m

The resonant frequency of each well was determined by using this program. The program is only used for the chaotic loading analysis. During the tuning process the conde employed the built in MATLAB pwelch function to visually display a graph of the frequencies. From there, the maximum ideal frequency could be visually located.

LaserLabViewCUTv2.m

The program allows for the user to manually select cut-off times for the start and stop of the experiment from the LabVIEW.lmv file. The selected data was then saved to a new text file. This was done because each experiment took multiple hours to run, some of which was unsupervised overnight. This enormous set of data needed to be reduced so that only the desired bone fatigue section was seen. The program was utilized in both the chaotic and variable amplitude loading analysis.

rainflow_bins_mod3.m

The first of the rainflow counting codes. The trimmed data was run filtered through this code to separate the cycles counts into 0.25 mm bins. A histogram was also generated so the user could visually see the distribution. After all specimen data was processed to this step, three categories of small, medium, and high amplitude bins were chosen. The categories were then cross referenced with the previous studies' findings to check for correlation between the small, medium, and large amplitude cycles. The program was used in both the chaotic and variable amplitude loading analysis.

rainflow_bins_mod4.m

After the small, medium, and high amplitude bins were set, the trimmed data was sent through this code. The difference between this code and its previous version is the bin size. This code is used to determine the number of cycles of small, medium, and high amplitudes. The program was employed in both the chaotic and variable amplitude loading analysis.

SpeedPMR.m

This code employs the Palmgren-Miner rule as exhibited in Equation 1, for both the chaotic and variable amplitude loading analysis. The small, medium, and high amplitudes used for the code are based off of the values determined by Campbell [44]. From Campbell's study, the uncertainty within the calculated damage accumulation and parameter can be determined using the standard deviation from each of the cyclic amplitude loading cycles to failure and tracking the uncertainty through the damage parameter calculation [45]. After the damage parameter and the uncertainty were found, the success of the PMR was evaluated. If the PMR result's range encompassed a value of one, the PMR was deemed a successful prediction of the fatigue life for the specimen. This claim is rationalized by the PMR for it predicts that the material will fail when the damage accumulation parameter equals one. The converse holds true as well. If the bounds of the damage accumulation parameter did not encompass a value of one, then the PMR was deemed unsuccessful for predicting the fatigue life for the specimen.

PSW_protocol2v2.m

This is the master program that runs the PSW analysis for the chaotic loading analysis. The code and its subsequent programs were developed by Dr. Chelidze from the University of Rhode Island. His code may be accessed from <http://egr.uri.edu/nld/software/>. Parameters for the PSW analysis were decided based on Cler's previous findings [45]. The basic parameters are as follows: 8000 points for the reference model size, 32 boxes in the phase space, 20 pints for the local linear model, 1 for the model prediction time, 0 for the scalar tracking metric, and 2000 points in each record. The time delay was determined from the average mutual information. Its parameters were 8000-point limit, 60 for the maximum delay, and 32 bins used for the

calculation. False nearest neighbor analysis was then performed to determine the embedded dimension. This analysis used the same time delay parameter as the previous action, 6 for the maximum embedded dimension, and was set to the same 8000-point limit. The output of the program was a set of two graphs that are visually analyzed. The first type of graph shows the smooth orthogonal values (SOV), or eigenvalues, plotted with the individual or groups of SOV's that are separated from the continuum. The eigenvalues that are separate from the continuum identified the active fatigue damage models. The second type of graph displays the smooth orthogonal coordinates (SOC), the projection of the data onto the smooth orthogonal modes, and the corresponding SOV's that are of interest. The SOCs are then compared to other specimens to identify patterns in the fatigue process.

Four_Point_Bend_Analysis.m

The program was utilized to analyze the results of the four-point bend test. First, the maximum stress value was calculated. The corresponding strain value is then found and recorded. A user manually selects the linear range from a generated stress vs. strain plot. A linear regression is fitted to the data and the slope is recorded as the Young's modulus.

Fracture Surface Classification

After each test was completed the fracture surface of the specimen was visually inspected. A photograph of the fracture was taken with an 18-megapixel camera (EOS Rebel T5i, Canon U.S.A. Inc., Melville, NY) as seen in Figure 2.8. A complete catalog of images appears in Appendix B.

The fractures were classified based features found by SEM images taken with a tabletop microscope (TM3030Plus, Hitachi, Tokyo, Japan). The magnification of the SEM was set to 50x and was tuned to 15 kV SE settings. A catalog SEM images are found in Appendix C. Figure 2.8 reveals the fracture types and Figure 2.9 shows features associated with a BD break.

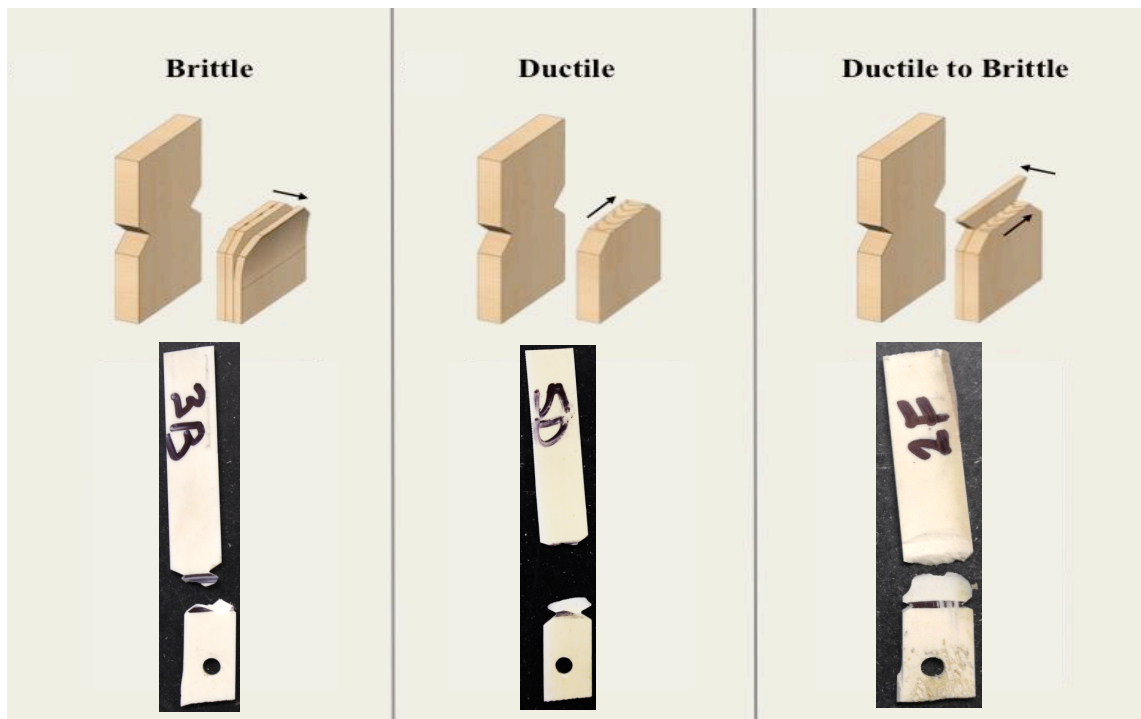


Figure 2.8. – Fracture classifications. Specimen 3B, 5D, 2F, are utilized to show brittle, ductile, and ductile to brittle breaks respectively [44]. Printed with permission from A. Cler et al.

Statistical Analysis

Multiple programs for statistical analysis of the chaotic loading test were utilized. First, Microsoft Excel (Microsoft Corporation, Redmond, WA) was utilized to run linear regression between cycles to failure and various mechanical properties: EI, Young's modulus, maximum stress, and strain at maximum stress. Next SAS 9.4 for Windows

(SAS Institute, Cary, NC) was used to perform logistic regression with stepwise variable selection. Break type was utilized as the category.

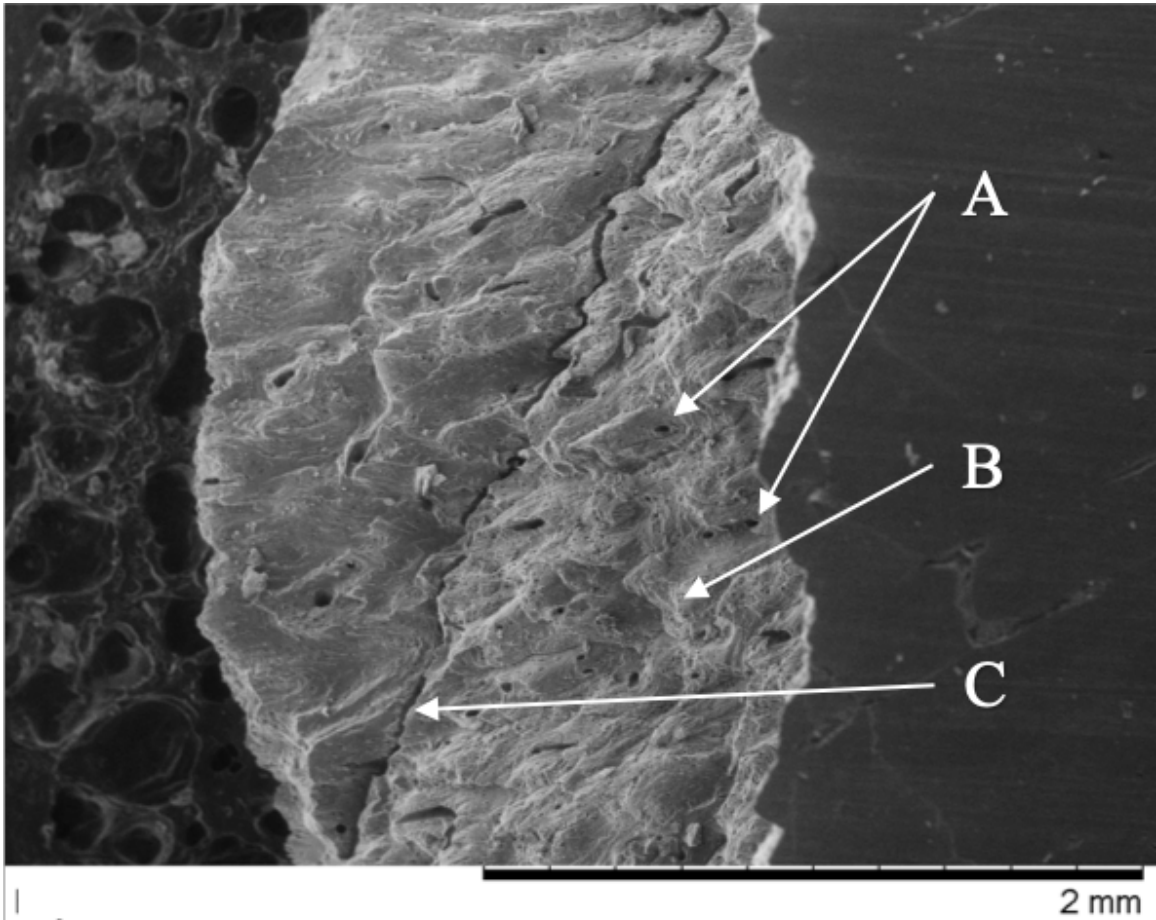


Figure 2.9. – Fracture features. Arrows 'A' and 'B' denote osteon pullout and beach markings respectively; both are features of ductile breaks. Arrow 'C' points to delamination, which is a hallmark of a brittle break.

CHAPTER THREE

Results

The order of this chapter will mirror the order presented in chapter 2. The results of the chaotic loading test will be presented first. Then the variable amplitude test results, and finally the results of the four-point bend test.

Chaotic Loading

Voltage vs. Time Series

A time series for a specimen is presented in Figure 3.1. The time series for each chaotic loading specimen is located in Appendix D. Within Figure 3.1, the vertical axis

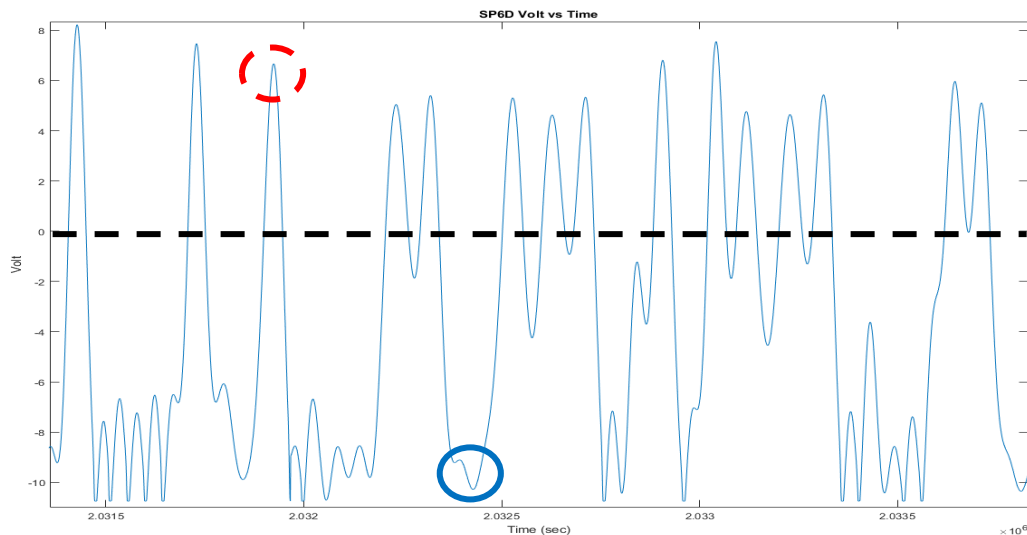


Figure 3.1. – Time series for SP6D. The image shows a zoomed in version of the time series revealing chaotic motion. The red dashed circle is an example of a positive voltage that signifies the pendulum being in the right potential well. Similarly, the blue circle is an example of a negative value representing the pendulum's location within the left potential well. The dashed black line is the zero value between the potential wells.

corresponds to the trajectory of the tip of the pendulum with 1 Volt equivalent to 1 millimeter. Positive values represent the right potential well, circled red dash, while negative values correspond to the left potential well, circled blue. A value of zero is the position between both of the potential wells, denoted by the black dashed line.

Fracture Surface Classification

Figure 3.2 reports on all of the specimen's break classifications.

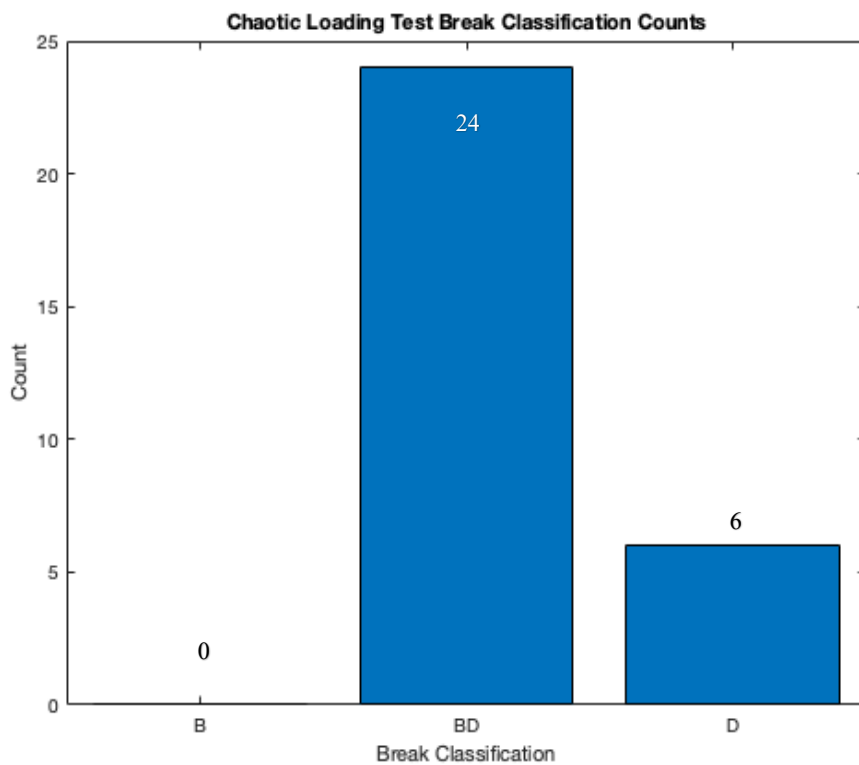


Figure 3.2 – Chaotic Loading Test Break Classification Counts. B, BD, and D stand for brittle, brittle to ductile, and ductile, respectively.

Cycles Counts

Figure 3.3 shows a sample result of the two graphs generated per specimen. A complete collection of graphs per specimen is located in Appendix D. Table 3.1 reveals the number of cycles for the different amplitude ranges and the number of total cycles.

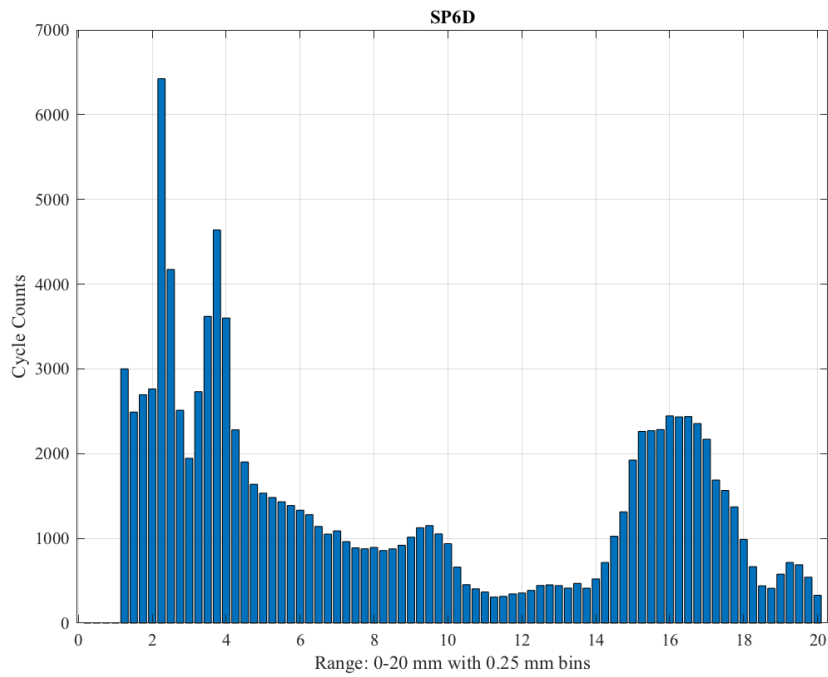
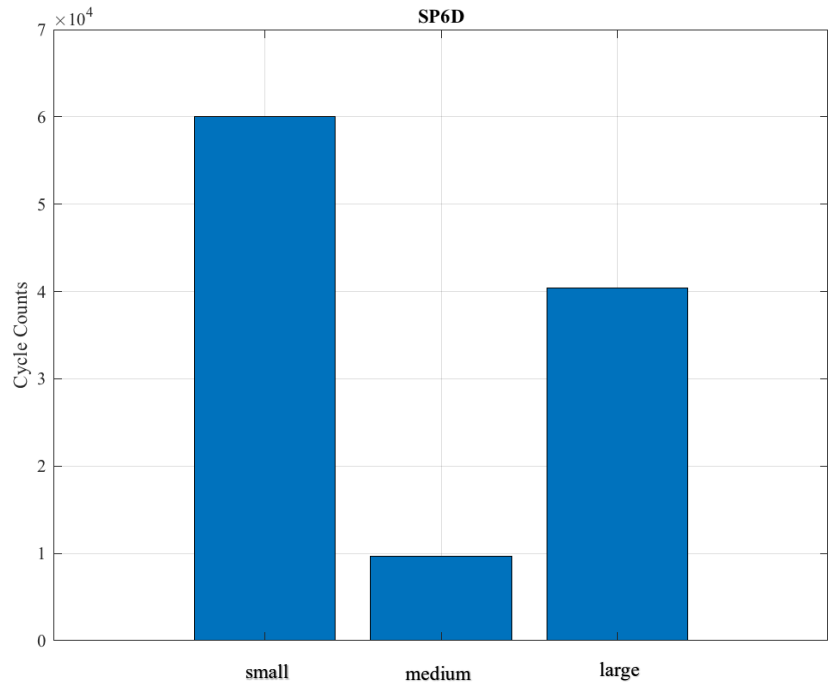


Figure 3.3 – Histograms of cycles. The histograms were created from SP6D data. The top graph depicts a histogram of three bins. The bottom graph shows a histogram of bin size 0.25 mm

Table 3.1 – Cycle count and break classification for chaotic loading test specimens.
B,BD, and D stand for brittle, brittle to ductile, and ductile, respectively.

| Chaotic Loading Test Cycle Count | | | | | |
|----------------------------------|------------|------------------------|-------------------------|------------------------|-------------------------|
| Specimen | Break Type | Small Amplitude Cycles | Medium Amplitude Cycles | Large Amplitude Cycles | Total Cycles to Failure |
| 1D | BD | 11,356.0 | 12,502.5 | 0.0 | 23,858.5 |
| 1E | BD | 21,751.5 | 14,952.5 | 0.0 | 36,704.0 |
| 1F | BD | 9,035.5 | 21,102.0 | 9,103.5 | 39,241.0 |
| 2D | BD | 11,418.5 | 12,641.0 | 2,784.0 | 26,843.5 |
| 2E | D | 13,406.0 | 4,583.5 | 25,314.0 | 43,303.5 |
| 2F | BD | 42,723.5 | 1,167.5 | 65,212.0 | 109,103.0 |
| 3D | D | 28,783.5 | 4,240.0 | 23,523.5 | 56,547.0 |
| 3E | BD | 20,431.0 | 614.0 | 10,285.0 | 31,330.0 |
| 3F | BD | 15,429.0 | 498.5 | 11,597.0 | 27,524.5 |
| 4D | BD | 34,454.5 | 6,000.0 | 14,700.0 | 55,154.5 |
| 4E | BD | 1,588.0 | 1,178.5 | 1,044.0 | 3,810.5 |
| 4F | BD | 32,693.0 | 14,132.0 | 825.5 | 47,650.0 |
| 5D | D | 9,592.5 | 4,037.5 | 556.0 | 14,186.0 |
| 5E | BD | 29,490.0 | 5,940.0 | 24,989.5 | 60,419.5 |
| 5F | BD | 4,835.0 | 652.5 | 3,214.0 | 8701.5 |
| 6D | BD | 60,002.5 | 9,705.5 | 40,379.0 | 110,087.0 |
| 6E | D | 37,653.0 | 6,930.0 | 27,901.0 | 72,484.0 |
| 6F | D | 9,317.5 | 386.5 | 5,645.0 | 15,349.0 |
| 7D | D | 22,828.5 | 2,949.0 | 10,058.5 | 35,836.0 |
| 7E | BD | 19,840.0 | 1,214.5 | 7,648.0 | 24,359.5 |
| 7F | BD | 10,971.5 | 3.5 | 5,467.5 | 16,442.5 |
| 8D | BD | 2,808.0 | 642.0 | 2,644.0 | 6,094.0 |
| 8E | BD | 8,359.0 | 909.5 | 5,840.5 | 15,109.0 |
| 8F | BD | 17,093.0 | 2,706.0 | 7,128.0 | 26,927.0 |
| 9D | BD | 10,556.5 | 1,430.0 | 7,648.0 | 19,634.5 |
| 9E | BD | 18,279.5 | 6.0 | 9,143.0 | 27,428.0 |
| 9F | BD | 19,308.5 | 1,488.0 | 12,359.5 | 33,156.0 |
| 10D | BD | 6,051.0 | 1,590.5 | 748.0 | 8,389.5 |
| 10E | BD | 10,896.5 | 32,687.0 | 0.0 | 42,958.5 |
| 10F | BD | 37,969.0 | 16,600.0 | 877.5 | 55,446.5 |

Palmgren-Miner Rule

Table 3.2 shows the damage accumulation parameters, uncertainty parameters, and PMR prediction success.

Table 3.2 – Palmgren-Miner Rule analysis for chaotic loading test specimens. B,BD, and D stand for brittle, brittle to ductile, and ductile, respectively.

| Chaotic Loading Test PMR | | | | | |
|--------------------------|------------|-------------------------|-----------------------------|---------------------|--------------------|
| Specimen | Break Type | Total Cycles to Failure | Predicted Cycles to Failure | Damage Accumulation | Prediction Success |
| 1D | BD | 23,858.5 | 59,984.8 | 0.40 ± 0.12 | No |
| 1E | BD | 36,704.0 | 68,621.1 | 0.53 ± 0.14 | No |
| 1F | BD | 39,241.0 | 25,970.2 | 1.51 ± 0.46 | No |
| 2D | BD | 26,843.5 | 39,422.0 | 0.68 ± 0.17 | No |
| 2E | D | 43,303.5 | 15,736.4 | 2.75 ± 1.15 | No |
| 2F | BD | 109,103.0 | 15,858.4 | 6.88 ± 2.97 | No |
| 3D | D | 56,547.0 | 21,139.4 | 2.67 ± 1.07 | No |
| 3E | BD | 31,330.0 | 26,215.0 | 1.20 ± 0.47 | Yes |
| 3F | BD | 27,524.5 | 21,377.3 | 1.29 ± 0.53 | Yes |
| 4D | BD | 55,154.5 | 26,622.9 | 1.45 ± 0.54 | Yes |
| 4E | BD | 3,810.5 | 19,384.2 | 0.20 ± 0.05 | No |
| 4F | BD | 47,650.0 | 70,463.0 | 0.68 ± 0.14 | No |
| 5D | D | 14,186.0 | 13,282.3 | 1.07 ± 0.44 | Yes |
| 5E | BD | 60,419.5 | 18,371.2 | 3.29 ± 1.34 | No |
| 5F | BD | 8,701.5 | 16,583.6 | 0.52 ± 0.22 | No |
| 6D | BD | 110,087.0 | 23,275.8 | 4.73 ± 1.84 | No |
| 6E | D | 72,484.0 | 17,450.7 | 4.15 ± 1.72 | No |
| 6F | D | 15,349.0 | 23,853.9 | 0.64 ± 0.26 | No |
| 7D | D | 35,836.0 | 28,699.0 | 1.25 ± 0.46 | Yes |
| 7E | BD | 24,359.5 | 30,486.2 | 0.94 ± 0.35 | Yes |
| 7F | BD | 16,442.5 | 14,421.3 | 1.14 ± 0.50 | Yes |
| 8D | BD | 6,094.0 | 20,196.2 | 0.30 ± 0.12 | No |
| 8E | BD | 15,109.0 | 22,573.7 | 0.67 ± 0.27 | No |
| 8F | BD | 26,927.0 | 14,679.2 | 1.83 ± 0.78 | No |
| 9D | BD | 19,634.5 | 22,320.4 | 0.88 ± 0.35 | Yes |
| 9E | BD | 27,428.0 | 26,131.3 | 1.05 ± 0.42 | Yes |
| 9F | BD | 33,156.0 | 16,065.9 | 2.06 ± 0.88 | No |
| 10D | BD | 8,389.5 | 12,858.0 | 0.65 ± 0.28 | No |
| 10E | BD | 42,958.5 | 48,227.3 | 0.90 ± 0.30 | Yes |
| 10F | BD | 55,446.5 | 13,097.0 | 4.23 ± 1.74 | No |

Phase Space Warping Analysis

PSW analysis was performed on 19 out of 30 chaotic loading test specimens. Several of the other specimens exhibited signs of high frequency contamination and therefore were not able to undergo PSW analysis. An example result of PSW analysis is seen in Figure 3.4 and 3.5a-b. Figure 3.4 denotes a graph of the SOV. Breaks in the continuum signify points of interest of the SOC. Figure 3.5a depicts SOC that correspond to brittle and ductile mechanisms. Figure 3.5b shows the first few smooth orthogonal modes (SOM) of the high frequency continuum. The SOC selected are specimen specific. A complete catalog of specimens with their respective PSW outputs are contained in Appendix D. Table 3.3 reveals the time scale of the fatigue damage versus the specimen's break classification.

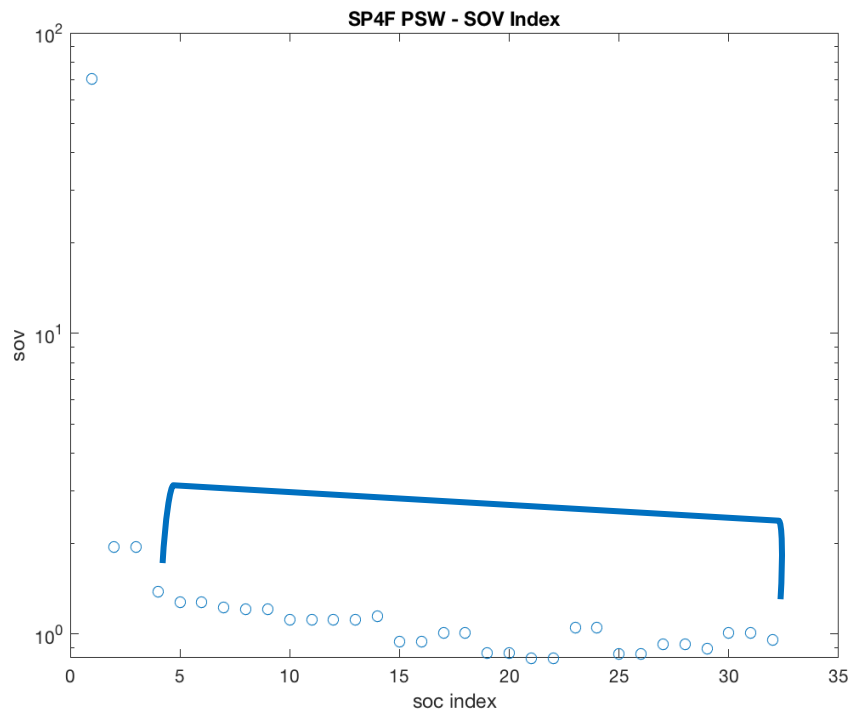


Figure 3.4 – Index of SOC for SP4F. The first three points differ from the continuum and are utilized to generate Figure 3.6. The bracketed area indicates the SOM continuum.

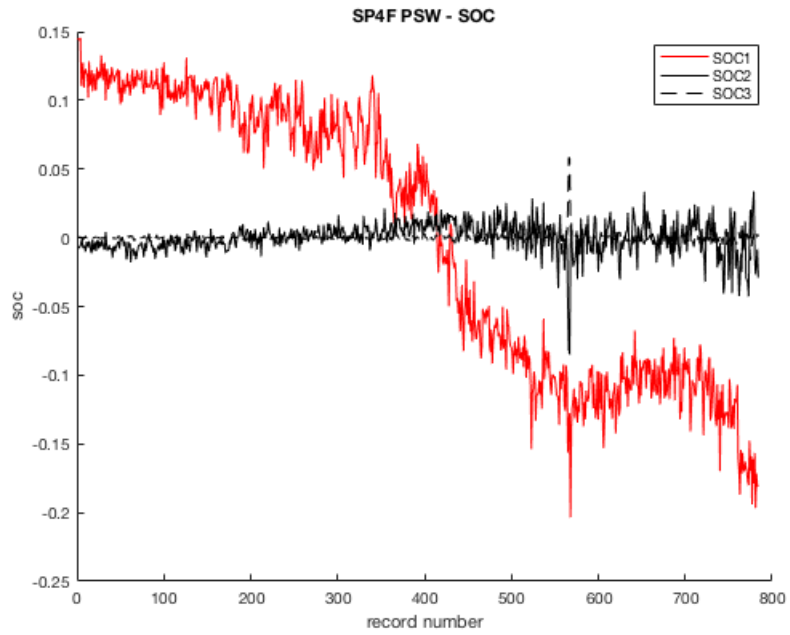


Figure 3.5.a – SOC graphs of SP4F. The black lines signify brittle mechanisms while the red lines indicate ductile mechanisms.

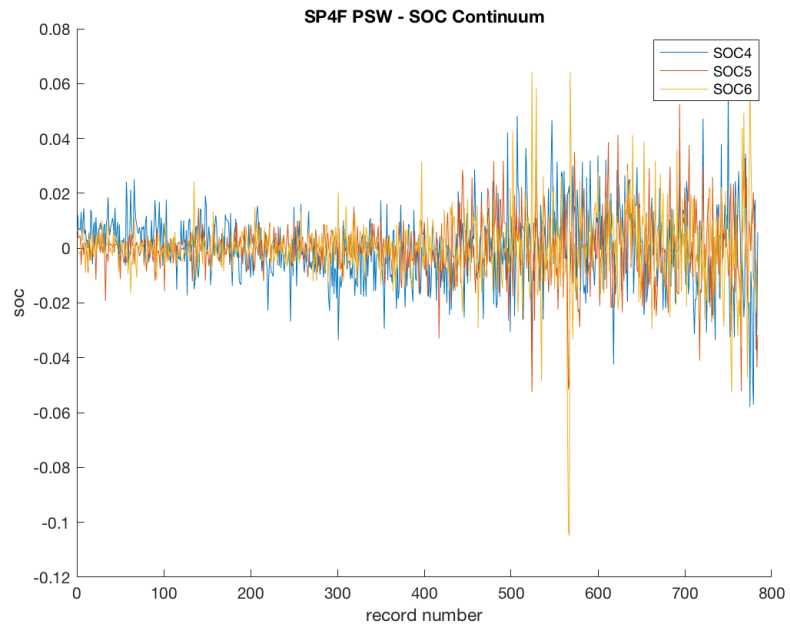


Figure 3.5.b – SOC continuum graphs of SP4F. The first several smooth orthogonal modes of the continuum are distinguished by color.

Table 3.3. – SOV values from PSW analysis. B,BD, and D stand for brittle, brittle to ductile, and ductile, respectively. SOV with dashes indicate that PSW analysis was not conducted on the specimen.

| Chaotic Loading Test PSW | | |
|--------------------------|------------|-------------------------------|
| Specimen | Break Type | Eigenvalues (SOV) |
| 1D | BD | 0.58; 0.56 |
| 1E | BD | -- |
| 1F | BD | 0.61; 0.58 |
| 2D | BD | 0.91; 0.73 |
| 2E | D | -- |
| 2F | BD | 0.56; 0.54 |
| 3D | D | -- |
| 3E | BD | 0.60; 0.58; 0.56 |
| 3F | BD | -- |
| 4D | BD | 10.18; 3.25 |
| 4E | BD | 8.80; 2.81; 2.36 |
| 4F | BD | 70.31; 1.94 |
| 5D | D | 46.63 |
| 5E | BD | 1.45; 1.37 |
| 5F | BD | 0.83; 0.80; 0.76 |
| 6D | BD | -- |
| 6E | D | 4.18 |
| 6F | D | -- |
| 7D | D | -- |
| 7E | BD | 55.03; 3.05 |
| 7F | BD | 608; 9.67; 6.34 |
| 8D | BD | -- |
| 8E | BD | -- |
| 8F | BD | 4.28; 3.50 ; 2.98; 1.67; 1.31 |
| 9D | BD | -- |
| 9E | BD | 755.4; 22.54 |
| 9F | BD | -- |
| 10D | BD | 4.83; 1.82; 1.81 |
| 10E | BD | 1.56; 1.45; 1.30 |
| 10F | BD | 78.15; 2.35; 2.30 |

Variable Amplitude Test

Voltage vs. Time Series

An example time series is seen in Figure 3.6. The area bracketed in red dash denotes a small amplitude region while the blue bracketed area shows a large amplitude region. The transition from small to large amplitude is revealed by the green circle.

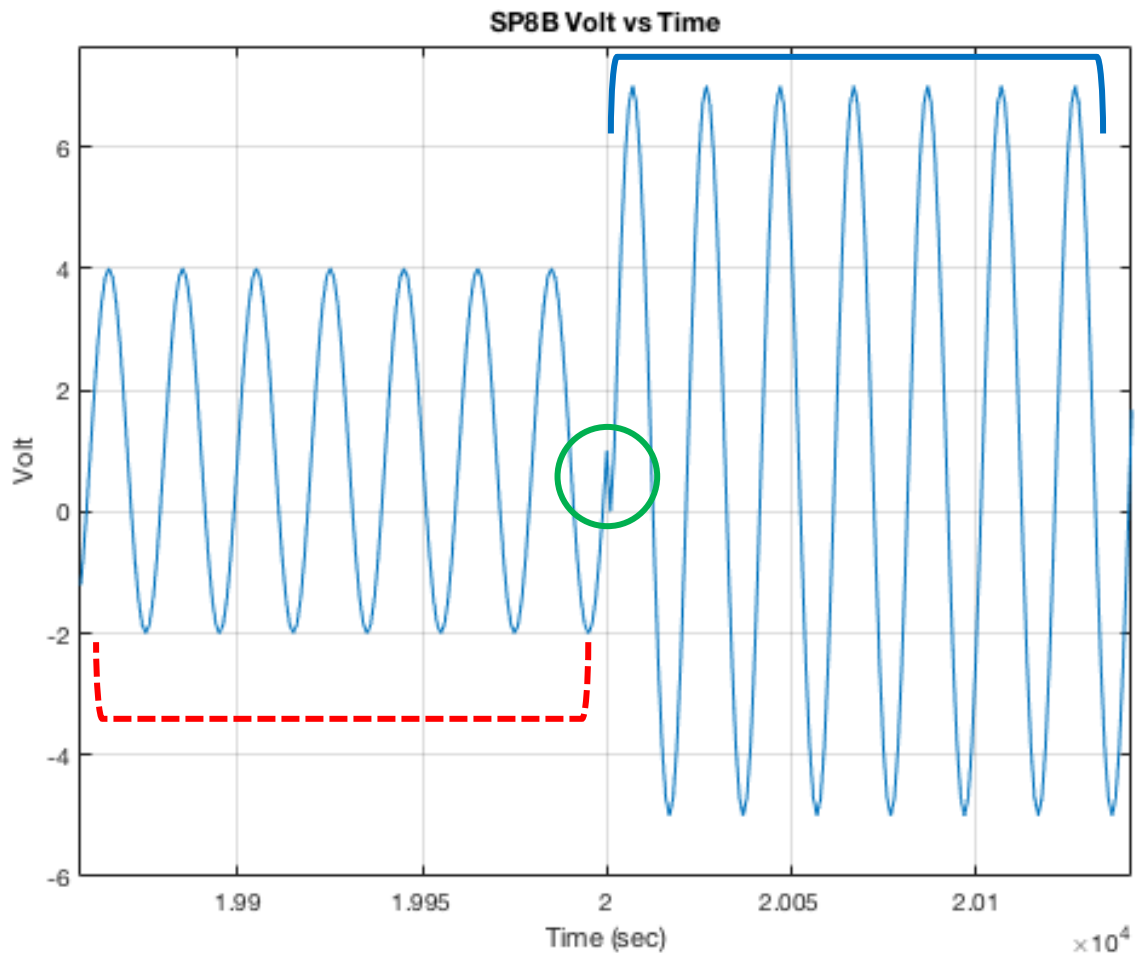


Figure 3.6 – Time series of SP8B. The image shows a zoomed in portion of the time series for clarification. The small amplitude region is highlighted by the red dash bracket. The large amplitude region is shown by the blue bracket. The transition zone from small to large amplitude is circled in green.

Fracture Surface Classification

Figure 3.7 reports on all of the specimen's break classifications.

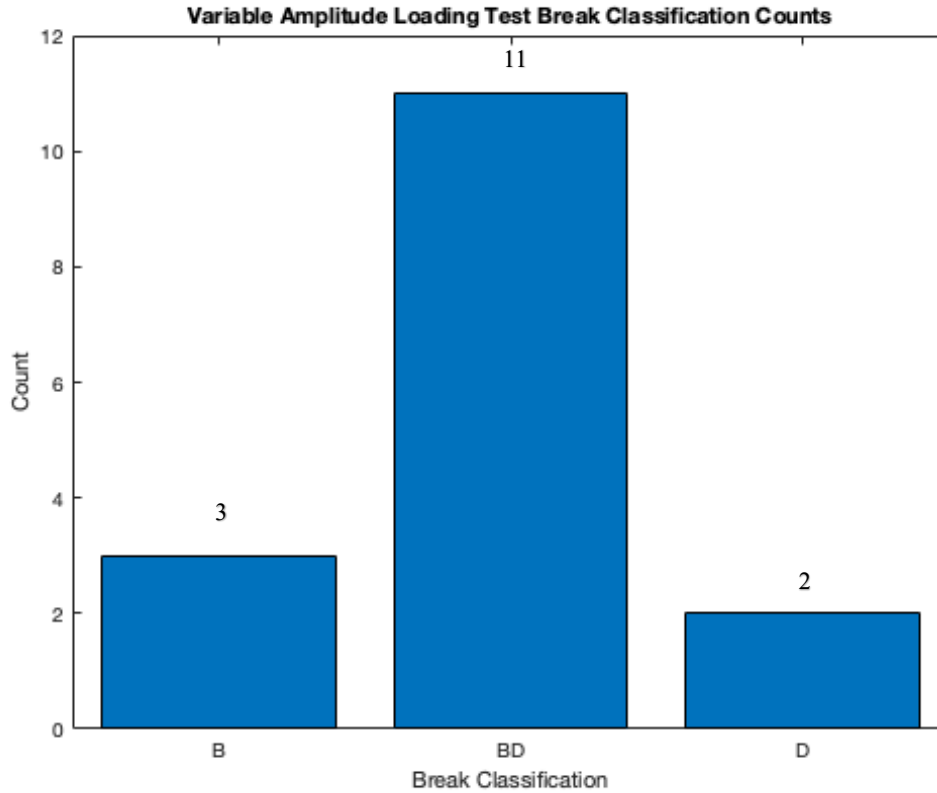


Figure 3.7 – Variable Amplitude Test Break Classification Counts. B, BD, and D stand for brittle, brittle to ductile, and ductile, respectively.

Cycle Counts

Figure 3.8 shows the large bin graph. Table 3.4 reveals the number of cycles for the different amplitude ranges and the number of total cycles.

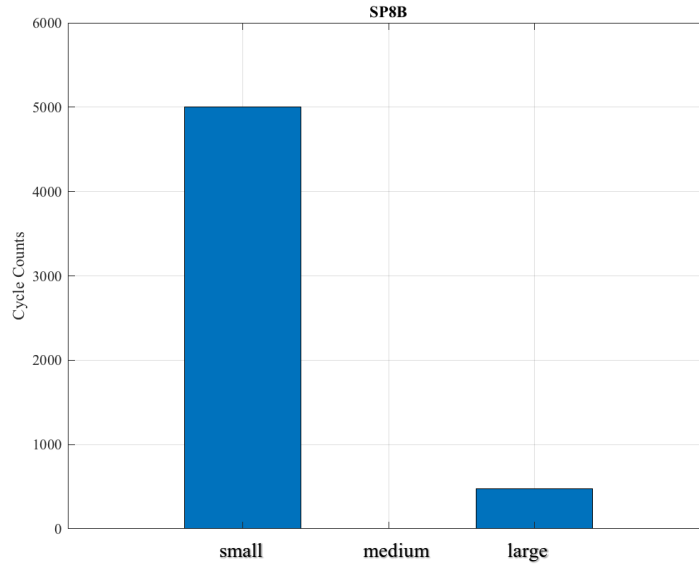


Figure 3.8 – Histogram of SP8B cycles. The three bin method was used to generate the graph. Medium cycles are present but are not seen due to scale.

Table 3.4 – Cycle count and break classification for variable amplitude test specimens. B,BD, and D stand for brittle, brittle to ductile, and ductile, respectively.

| Variable Amplitude Test Cycle Count | | | | | |
|-------------------------------------|------------|------------------------|-------------------------|------------------------|-------------------------|
| Specimen | Break Type | Small Amplitude Cycles | Medium Amplitude Cycles | Large Amplitude Cycles | Total Cycles to Failure |
| 3B | B | 27,008.5 | 19.5 | 2,662.0 | 29,690 |
| 3C | BD | 11,004.5 | 7.5 | 999.0 | 12,011 |
| 4B | BD | 12,005.5 | 8.0 | 1,135.5 | 13,149 |
| 4C | D | 11,004.5 | 7.5 | 1,040.0 | 12,052 |
| 5B | BD | 15,008.5 | 9.5 | 1,461.0 | 16,479 |
| 5C | B | 8,006.0 | 4.5 | 702.5 | 8,713 |
| 6B | BD | 14,007.5 | 9.0 | 1,385.5 | 15,402 |
| 6C | BD | 16,008.0 | 10.5 | 1,546.5 | 17,565 |
| 7B | BD | 25,008.0 | 18.0 | 2,422.0 | 27,448 |
| 7C | BD | 20,006.0 | 14.5 | 1,904.5 | 21,925 |
| 8B | BD | 5,003.0 | 3.0 | 477.0 | 5,483 |
| 8C | BD | 14,007.5 | 9.0 | 1,324.5 | 15,341 |
| 9B | B | 8,006.0 | 4.5 | 758.5 | 8,769 |
| 9C | BD | 19,006.5 | 13.5 | 1,869.0 | 20,889 |
| 10B | D | 33,010.0 | 24.0 | 3,237.0 | 36,271 |
| 10C | BD | 21,007.0 | 15.0 | 2,055.0 | 23,077 |

Palmgren-Miner Rule

PMR analysis was carried out on the variable amplitude test specimens. The damage accumulation parameters, uncertainty parameters, along with PMR prediction success is reported in Table 3.5.

Table 3.5. – Palmgren-Miner Rule analysis for variable amplitude test specimens. B,BD, and D stand for brittle, brittle to ductile, and ductile, respectively.

| Variable Amplitude Test PMR | | | | | |
|-----------------------------|------------|-------------------------|-----------------------------|---------------------|--------------------|
| Specimen | Break Type | Total Cycles to Failure | Predicted Cycles to Failure | Damage Accumulation | Prediction Success |
| 3B | B | 29,690 | 64,101 | 0.46 ± 0.12 | No |
| 3C | BD | 12,011 | 66,683 | 0.18 ± 0.05 | No |
| 4B | BD | 13,149 | 65,393 | 0.20 ± 0.05 | No |
| 4C | D | 12,052 | 65,417 | 0.18 ± 0.05 | No |
| 5B | BD | 16,479 | 64,492 | 0.26 ± 0.07 | No |
| 5C | B | 8,713 | 67,763 | 0.13 ± 0.03 | No |
| 6B | BD | 15,402 | 63,993 | 0.24 ± 0.06 | No |
| 6C | BD | 17,565 | 64,729 | 0.27 ± 0.07 | No |
| 7B | BD | 27,448 | 64,649 | 0.42 ± 0.11 | No |
| 7C | BD | 21,925 | 65,187 | 0.34 ± 0.09 | No |
| 8B | BD | 5,483 | 65,144 | 0.08 ± 0.02 | No |
| 8C | BD | 15,341 | 65,402 | 0.23 ± 0.06 | No |
| 9B | B | 8,769 | 65,344 | 0.13 ± 0.03 | No |
| 9C | BD | 20,889 | 64,173 | 0.33 ± 0.09 | No |
| 10B | D | 36,271 | 64,259 | 0.56 ± 0.15 | No |
| 10C | BD | 23,077 | 64,335 | 0.36 ± 0.09 | No |

Four-Point Bend Test

A sample graph of the stress vs. strain curve is shown in Figure 3.9. A complete catalog of stress vs. strain graphs are located in Appendix D. The modulus, maximum stress, and strain at maximum stress are detailed in Table 3.6.

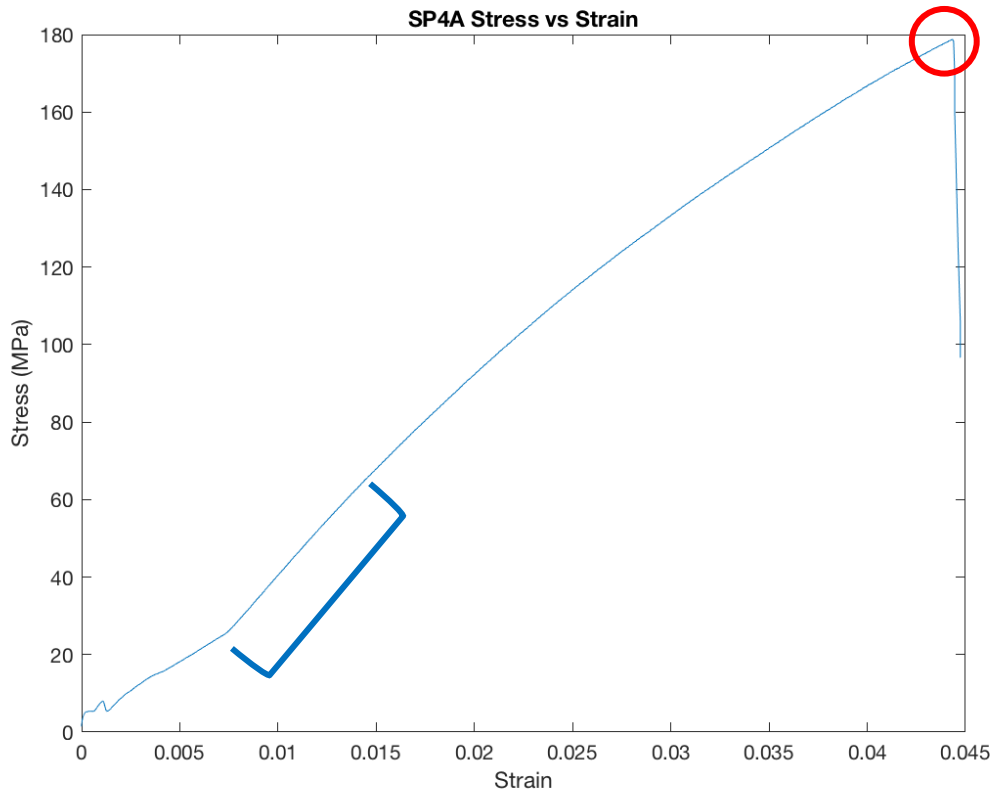


Figure 3.9 – Stress vs. strain plot. The plotted specimen is SP4A. The maximum stress is circled in red. The Young’s modulus is the slope of the linear region bracketed in blue.

Table 3.6. – Results from four-point bend test.

| Four-Point Bend Results | | | |
|-------------------------|---------------|-----------------------|----------------------------------|
| Specimen | Modulus (GPa) | σ_{\max} (MPa) | $\epsilon_{@ \sigma_{\max}}$ (%) |
| 1A | 5.30 | 133.61 | 3.10 |
| 2A | 6.60 | 167.24 | 3.93 |
| 3A | 5.51 | 198.77 | 5.46 |
| 4A | 5.74 | 178.75 | 4.43 |
| 5A | 4.34 | 98.66 | 2.83 |
| 6A | 4.68 | 96.26 | 2.54 |
| 7A | 6.43 | 168.17 | 3.60 |
| 8A | 5.74 | 164.22 | 4.58 |
| 9A | 6.75 | 273.97 | 6.88 |
| 10A | 5.01 | 113.57 | 2.92 |

Statistical Analysis

From both tests of linear regression and logistic regression with stepwise variable selection, no statistically significant correlations were determined. This is exemplified by Figure 3.10 that shows a linear regression applied to the data with a low R^2 value. A full report of the statistical analysis results are contained in Appendix D.

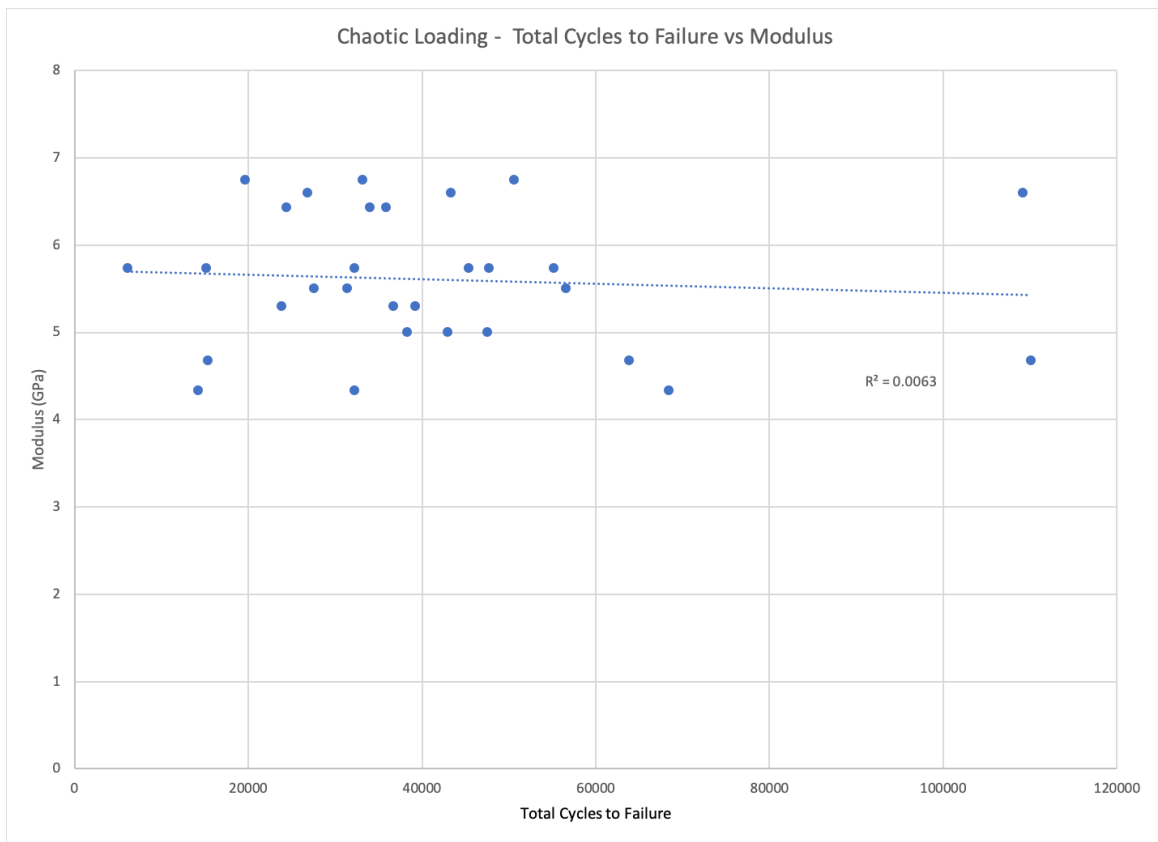


Figure 3.10 – Scatter plot of total cycles to failure vs. modulus for chaotic loading specimens. A linear regression was conducted on the data and has a reported R^2 value of 0.0063.

CHAPTER FOUR

Discussion

This study acted as a continuation of Cler's research to elicit the difference in the prediction capabilities of both PMR and PSW [45]. By using chaotic loading, the bone was forced under conditions that more accurately describe natural loading conditions. Therefore, the prediction method that could determine the fatigue point of the chaotically loaded bone was a superior prediction mode. By utilizing a larger sample size and examining the mechanical properties of the bone, the natural variance of the specimens was intended to be accounted for.

The order of discussion will be the reverse of the order in which the results were presented. The logic is to take what is learned from the simpler case and apply it the next, more complex, case. First, the four-point bend test results are analyzed. Then, the variable amplitude test results are examined. Lastly, the results of the chaotic loading test will be analyzed and compared to the pilot study.

Four-point Bend

The results of the four-point bend were used to determine the baseline characteristics of each individual bone. By identifying specimens that were outside of normal property ranges, the further results within variable amplitude and chaotic loading tests could be held to a certain level of scrutiny. It was found that the average of the ten specimens' maximum stress was 159.32 MPa which was within the range of values found in literature. The literature value used for maximum stress was 142 ± 13 MPa [94]. The strain and Young's modulus are dependant on multiple factors, such as strain rate, bone

density, and anatomic localization of the specimen, which make it difficult to compare values between results and published sets of data [95]. Although the average value fell within a suitable range, there is great variance present among the maximum stress. The variance is attributed to natural variance between bones. However, more specific factors such as age, gender, and health of the animals from which the bones were collected cannot be examined due to limiting information from the procurement source.

Variable Amplitude Test

From Campbell's study, the foundation work of this investigation, a relationship was established that correlated amplitude to fracture mechanic [45]. Cyclic low amplitude fatigue corresponded to the specimen breaking in a ductile fashion, cyclic high amplitude fatigue corresponded to the specimen experiencing a brittle break, and cyclic medium amplitude fatigue had specimens exhibit a mixed ductile and brittle fracture. Within the study, the majority of specimens that underwent this loading experienced a mixed mode break (BD). The results paralleled Campbell's findings and are expected, due to the mixed loading nature of the method [44]. Although five samples did not adhere to the mixed mode break, the ratio of single mode to mixed mode breaks resemble those found in Campbell's study. These five samples could have had specimen specific conditions; their pre-test state may have contained malformations or significantly accumulated damage that skewed the results. By examining the results of the four point bend, three of the five specimens that exhibited a single mode fracture are from bones that exhibit maximum stress more than two deviations away from the average. The natural variance within the specimens can explain the discrepancies these specimens experienced when compared to the other specimens.

By using the PMR, the predicted cycles to failure for this loading pattern was determined to be 63,780. However, when factoring in the uncertainty for each specimen, the true endurance limits fluctuated slightly around this number and varied from specimen to specimen. Yet, all of the specimens broke much sooner than the predicted endurance limit. All of the specimens broke during the large amplitude phase. This result reinforces the findings of Campbell. Therefore, the specimen accumulated too much damage to withstand the higher amplitude forcing and not enough to fracture during the small amplitude phase. This result is supported by the BD fracture surface of the majority of the specimens. The specimens exhibited behavior of a transition from slow ductile to fast brittle breaks.

The fracture surfaces and cycles to failure of specimens clearly demonstrate that the PMR was inadequate in predicting the endurance limit for this variable amplitude forcing. The poor prediction success of the PMR was also reported by Campbell and Zioupos et al [44,93]. The linear accumulation rule was not accurate enough to handle a true mixing of failure mechanics. Therefore, it is evident there is a need for a more sophisticated prediction method.

Chaotic Amplitude Loading

The success of the PMR will be analyzed first. For 20 of the 30 specimens the PMR did not accurately predict the endurance limit of the sample. Seven of the twenty specimens broke much later than the PMR predicted. This phenomenon is noted in Cler's work and is contrary to the variable amplitude results [45]. It is important to note that there are several key differences in the experimental setups that can be factors for this contradiction.

The first is that within the variable amplitude hardware, two rollers are utilized to control the specimen's movement. The rollers limit the bending amount of each cycle and did not actively apply a load to the specimen. The chaotic loading test had the specimen be a pendulum that hung over two magnetic wells. The specimen had the ability to swing freely over the wells. The magnetic wells also applied a tensile load to the specimen. The presence of a tensile load is supported by scanning electron microscope images detailing osteon pullout within the specimens. Osteon pullout is dependent upon the location and the manner in which the bone was fractured [52]. The tensile load may have changed how the specimen reacted to the fatiguing process. Lastly, the amplitude of each cycle was not dictated. This allowed for three categories of amplitude to exist within the chaotic loading test compared to two major amplitudes found in the variable amplitude test. The medium amplitude was seen only a handful of times within the variable amplitude test. Therefore, the medium amplitude played only a minute role in the variable amplitude test. A more prevalent medium amplitude could have triggered different strengthening mechanisms of the material that would have lowered the stresses experienced by the specimen. The change in experimental setup overall could have allowed for the specimen to adjust its motion to experience less overall stress during the fatiguing process.

For the remaining ten specimens, the fatigue limit was successfully predicted by the PMR. Within Cler's pilot study, it was determined that if a singular fracture mechanism was present then the PMR would most likely be successful for predicting the fatigue life [45]. Of the ten specimens that the PMR successfully predicted, three were expected because the specimens exhibited only one predominate fracture type. Based on the results and previous section results of PMR, it is evident that it becomes less reliable with a more complex loading system.

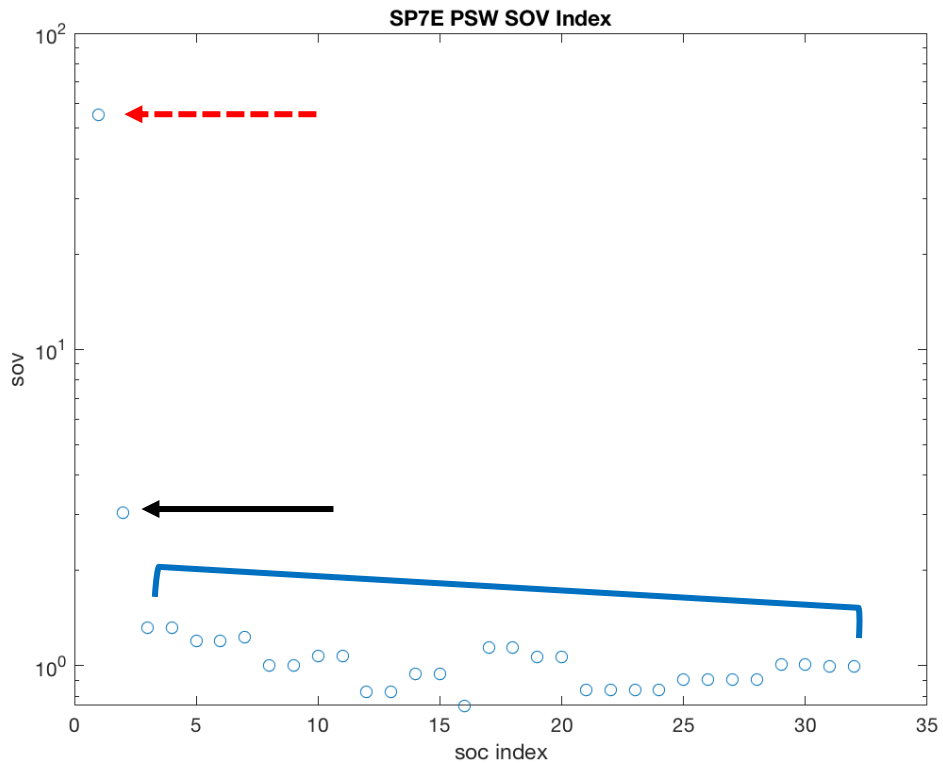


Figure 4.1 – SOV index for SP7E. The red dash and black arrows reveal ductile and brittle damage modes respectively. The blue bracket reveals the high frequency noise floor.

Next, the results of PSW will be examined. This study reinforced several of the findings presented in the previous study [45]. PSW is capable of distinguishing between different fatigue modes within the specimens. The graphs of the SOV indexes reveal the various damage modes along with their time scale. Figure 4.1 demonstrates this capability. The red dash and black arrows point to the SOV that corresponds to the ductile and brittle damage modes, respectively. The damage modes are distinctly isolated from the continuum that is bracketed in blue. The continuum is defined as the high frequency noise floor.

PSW analysis presents a mean for identifying damage modes based off of the SOV. Cler was able to link SOV to damage types identified from SEM images [45]. The

larger SOV correspond the lower frequencies of damage accumulation. The lower frequencies, slow time scale, of damage accumulation denote a ductile break. The smaller SOV correspond to the higher frequencies of damage. These higher frequencies, fast time scale, of damage accumulation are linked to a brittle break. The distinction between the different damage accumulation modes is, for the most part, easy to observe. As in Figure 4.1, there is a large distance between the red and black arrowed values. However, when comparing inter-experimental SOV, difficulties arise. For example, the SOV for 5D and 6E are 46.63 and 4.18, respectively. Both SOVs are describing ductile fractures and yet their values differ by an order of magnitude. The unique nature of each specimen's stiffness damage evolution may be the source of discrepancies.

Graphs of SOCs were generated based off of the distinct SOVs for each specimen. Each separate group of SOVs corresponds to distinct damage modes. Figure 3.6.a shows the SOC for the specific SOVs while Figure 3.6.b graphs the SOCs that are linked to the first 3 SOVs of the continuum. The graphs of the continuum's SOC contain a great amount of high frequency noise; therefore, they were not used within the analysis. Those graphs are only used for reference. The graphs of the significant SOVs appear to hold no trend for the SOCs. Like the distinct SOVs themselves, the specific damage evolution of each specimen may be the rationale for this observation.

It is important to reiterate that PSW is capable of isolating ductile and brittle fracture mechanics for each specimen. This is the first step in developing new damage/fatigue laws for bone. Although trends of SOVs and their corresponding SOCs have yet to be developed, the success of PSW conducted on metal demonstrates its possibility [76]. More testing that limits specimen variability should be conducted.

Statistical Analysis

From the results of the statistical analysis it is seen that there is a substantial amount of variability between specimens. All linear regressions reported low R^2 values that indicate a lack of statistically significant correlation between the variables. The variability has possibly prevented more trends to be established between SOVs and damage modes.

Conclusion

From the evidence put forth, in conjunction with data from both the pilot studies of Campbell and Cler, the PMR does not appear to provide a reliable and accurate prediction for fatigue life of bovine bone when there is more than one active damage mechanism [44,45]. There are differences between the reliability of the PMR for the variable amplitude and chaotic loading tests. The differences can be attributed to the change in experimental hardware, such as changing between cam rollers and magnetic wells, that allowed the specimens to experience the fatigue process differently.

This study acted as a continuation of Cler's novel pilot study that applied PSW to bone tissue [45]. Similarly, the findings indicate that PSW may be a novel method to monitor bone health and more reliably predict the fatigue life of bone. PSW has the ability to differentiate between ductile and brittle damage modes for individual specimens. Although no trends have been established for SOVs, the fact SOVs are correlated with damage modes within bone specimens is a promising first step to developing a more comprehensive bone damage law. It is evident from the variance of mechanical properties and lack of statistical correlations that variance should be controlled.

Being a continuation, this study has produced results of a similar nature to both pilot studies but on a larger scale [44,45]. With more evidence supporting the promise of PSW, the prediction method should be pursued to gain more knowledge of the fatigue and fracture mechanics of bone.

CHAPTER FIVE

Future Work

This final chapter will discuss the changes that were enacted from the previous study alongside proposed changes for future work. It is thought by examining changes in the experimental design that a more consistent procedure may be produced.

Improvements – Previous Study

Several recommendations from Cler's study were enacted [45]. The first was the addition of the low-pass filter to prevent high frequency noise from infiltrating the data. The success of the low pass filter is questionable. It is evident that several of the specimens were not able to undergo PSW due to high frequency contamination. The filter may have helped in refining the successful PSW analyses results but it is not a perfect solution to contamination. The modifications to specimen production has yielded six specimens, compared to three, from a single bovine femur. This has allowed for statistical significance to be more easily achieved.

Improvements – Future Study

Even with implementing the changes there are several areas that may be addressed to help control variance. The first is attempting to reduce the high frequency noise present in the chaotic loading test. The arm that connects the shaker to the C-Frame has been identified as the possible source of the high frequency noise contamination. The connector piece was extended from 1.5 in, from the variable amplitude test, to 8 in. The elongation was conducted to reduce the magnetic interference of the shaker with the rare earth magnets. In order to reduce the high frequency noise, the connector arm must

change. It is proposed that the strength of the magnetic field generated by the shaker be determined. Once the source of the strength is determined then the force it exerts on the rare earth magnets may be determined. Knowing this force value, the connector arm will be reduced until a significant difference of one percent increase is determined. Then effects of electromagnetic shielding should be examined to further reduce the connector arm length. The goal is to utilize distance and shielding to reduce the overall arm length in hopes of reducing high frequency noise contamination.

Second, the variance in the age of the bovine should be reduced. The current information of the cattle is highly limited. The cows range from 8 to 30 months old. This can be seen as highly problematic. In general, cows begin puberty around 12.5 months old and are typically bred at 24 months [96]. Puberty is seen as a time of great change within the body that indeed affect bone in structure and BMD [97,98]. Thus, the structure and properties of bone will be drastically different between cows before, during, and after puberty. Even during the stages of puberty the bone will be vastly different. Even at the 24 month mark, first-time breeding heifers are typically only at 60 percent of their mature weight [99,100]. Weight also impacts the properties of bone. Therefore, to reduce variability between specimens and to establish SOV patterns, animals who have undergone puberty and are skeletally mature should be selected. This may involve selecting an animal model in which the age, gender, and health of the individual are readily available. An example would be sheep. There is already natural variance between individuals, this variance is being amplified by the lack of control of the experimental subject selection. Once patterns have been established, less consistent subject groups may be selected to eliciting more complex system laws.

Lastly, a method to maintain a consistent bone moisture level should be developed. Within the study, dry bone specimens were tested. The specimens were set out to dry 7 hours before testing began. This was done in order to have a uniform moisture level between specimens and to stabilize the resonance frequency of the specimen. It is known that wet bone has different mechanical properties than dry bone. In order to better capture the true fatigue process of bone, wet bone should be used. A proposed solution is to have a saline drip for the specimen while in the testing rig. This will keep the bone properly moisten over the entirety of the test. It should be validate that the resonant frequency does not change over an twelve hour time span, or the length of time for the longest test with a factor of safety of 1.5. The goal is to maintain wet bone properties while stabilizing resonant frequency. With the described changes a more holistic view of the fatigue process of bone can be determined.

APPENDICES

APPENDIX A

Data Logbook

Table A.1 – Chaotic loading test data logbook. This contains specifications of specimen and parameters the chaotic loading test were run at.

| Chaotic Loading Data Logbook | | | | | | | |
|------------------------------|----------------|------------------|-------------------|---------------------------|--------------------------|------------------------|-----------|
| Specimen Name | Thickness (in) | Notch Width (in) | Gauge Length (in) | Right well frequency (Hz) | Left well frequency (Hz) | Average Frequency (Hz) | Amplitude |
| 1D | 0.0840 | 0.3472 | 0.9190 | 9.7690 | 9.4923 | 9.63 | 1.60 |
| 1E | 0.1180 | 0.3464 | 0.9495 | 9.5814 | 9.6947 | 9.64 | 1.65 |
| 1F | 0.0960 | 0.3445 | 0.9148 | 9.9283 | 9.9727 | 9.95 | 2.00 |
| 2D | 0.0950 | 0.3278 | 0.9055 | 9.5801 | 9.3278 | 9.45 | 3.60 |
| 2E | 0.1000 | 0.3378 | 0.9851 | 9.0170 | 9.8378 | 9.43 | 2.40 |
| 2F | 0.1010 | 0.3207 | 0.9561 | 9.1209 | 9.7391 | 9.43 | 2.20 |
| 3D | 0.0940 | 0.3328 | 0.9930 | 9.8627 | 9.9542 | 9.91 | 1.50 |
| 3E | 0.0960 | 0.3294 | 0.9697 | 9.4843 | 9.0319 | 9.26 | 3.90 |
| 3F | 0.0830 | 0.3248 | 0.9583 | 9.8449 | 9.3569 | 9.60 | 2.25 |
| 4D | 0.0964 | 0.3254 | 0.9815 | 9.2094 | 9.6627 | 9.44 | 3.50 |
| 4E | 0.0980 | 0.3327 | 0.9879 | 9.5523 | 9.2815 | 9.42 | 2.80 |
| 4F | 0.0900 | 0.3228 | 0.9989 | 9.6299 | 9.2304 | 9.43 | 2.10 |
| 5D | 0.0928 | 0.3380 | 0.9001 | 9.0320 | 9.7111 | 9.37 | 3.60 |
| 5E | 0.1050 | 0.3341 | 0.9865 | 9.6147 | 9.6246 | 9.62 | 3.40 |
| 5F | 0.0939 | 0.3409 | 0.9613 | 9.3624 | 9.5906 | 9.48 | 2.35 |
| 6D | 0.0980 | 0.3410 | 0.9990 | 9.0495 | 9.6604 | 9.35 | 2.40 |
| 6E | 0.0917 | 0.3392 | 0.9528 | 9.4896 | 9.0476 | 9.27 | 3.70 |
| 6F | 0.1030 | 0.3210 | 0.9480 | 9.1925 | 9.3488 | 9.27 | 2.25 |
| 7D | 0.0979 | 0.3221 | 0.9801 | 9.1231 | 9.4513 | 9.29 | 2.05 |
| 7E | 0.1080 | 0.3296 | 0.9228 | 9.2055 | 9.2409 | 9.22 | 2.80 |
| 7F | 0.0980 | 0.3359 | 0.9498 | 9.1465 | 9.7150 | 9.43 | 3.70 |
| 8D | 0.1100 | 0.3396 | 0.9901 | 9.1891 | 9.8562 | 9.52 | 3.10 |
| 8E | 0.0970 | 0.3322 | 0.9575 | 9.0427 | 9.2815 | 9.16 | 2.10 |
| 8F | 0.1110 | 0.3446 | 0.9845 | 9.6352 | 9.7311 | 9.68 | 3.20 |
| 9D | 0.0990 | 0.3416 | 0.9739 | 9.2819 | 9.1378 | 9.21 | 3.80 |
| 9E | 0.1051 | 0.3491 | 0.9586 | 9.5386 | 9.8367 | 9.69 | 2.60 |
| 9F | 0.0975 | 0.3359 | 0.9247 | 9.6952 | 9.1386 | 9.42 | 2.60 |
| 10D | 0.1080 | 0.3298 | 0.9666 | 9.4991 | 9.5882 | 9.54 | 1.90 |
| 10E | 0.0900 | 0.3232 | 0.9083 | 9.5358 | 9.3662 | 9.45 | 1.20 |
| 10F | 0.1110 | 0.3383 | 0.9626 | 9.4452 | 9.8068 | 9.63 | 1.55 |

Table A.2 – Variable amplitude test data logbook. This contains specifications of specimen used in the variable amplitude test.

| Variable Amplitude Data Logbook | | | |
|---------------------------------|----------------|------------------|-------------------|
| Specimen Name | Thickness (in) | Notch Width (in) | Gauge Length (in) |
| 3B | 0.0950 | 0.3354 | 0.9661 |
| 3C | 0.1110 | 0.3465 | 0.9730 |
| 4B | 0.0955 | 0.3376 | 0.9891 |
| 4C | 0.0972 | 0.3246 | 0.9982 |
| 5B | 0.0970 | 0.3260 | 0.9769 |
| 5C | 0.1200 | 0.3322 | 0.9581 |
| 6B | 0.0980 | 0.3425 | 0.9928 |
| 6C | 0.0922 | 0.3448 | 0.9580 |
| 7B | 0.0980 | 0.3437 | 0.9017 |
| 7C | 0.0960 | 0.3296 | 0.9121 |
| 8B | 0.0930 | 0.3360 | 0.9863 |
| 8C | 0.1090 | 0.3227 | 0.9484 |
| 9B | 0.1050 | 0.3234 | 0.9845 |
| 9C | 0.0985 | 0.3241 | 0.9209 |
| 10B | 0.0938 | 0.3404 | 0.9552 |
| 10C | 0.1000 | 0.3349 | 0.9630 |

Table A.3 – Four-point bend test data logbook. This contains specifications of specimen used in the four-point bend test.

| Four-Point Bend Data Log Book | | | |
|-------------------------------|-------------|------------|----------------|
| Specimen Name | Length (in) | Width (in) | Thickness (in) |
| 1A | 3.067 | 0.520 | 0.1100 |
| 2A | 2.527 | 0.500 | 0.0950 |
| 3A | 2.764 | 0.470 | 0.1030 |
| 4A | 2.530 | 0.495 | 0.0980 |
| 5A | 2.935 | 0.496 | 0.0970 |
| 6A | 2.874 | 0.476 | 0.0930 |
| 7A | 2.511 | 0.498 | 0.1135 |
| 8A | 2.575 | 0.495 | 0.1060 |
| 9A | 2.994 | 0.497 | 0.1160 |
| 10A | 3.235 | 0.500 | 0.0920 |

APPENDIX B

Specimen photos with 18-megapixel camera

Group 1



Figure B.1.a – Specimen 1D: chaotic loading



Figure B.1.b – Specimen 1E: chaotic loading



Figure B.1.c – Specimen 1F: chaotic loading

Group 2



Figure B.2.a – Specimen 2D: chaotic loading



Figure B.2.b – Specimen 2E: chaotic loading



Figure B.2.c – Specimen 2F: chaotic loading

Group 3



Figure B.3.a – Specimen 3B: variable amplitude loading

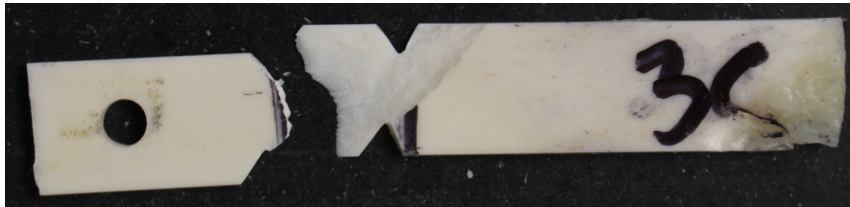


Figure B.3.b – Specimen 3C: variable amplitude loading



Figure B.3.c – Specimen 3D: chaotic loading



Figure B.3.d – Specimen 3E: chaotic loading

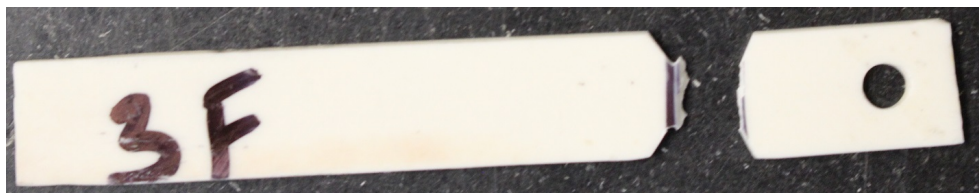


Figure B.3.e – Specimen 3F: chaotic loading

Group 4



Figure B.4.a – Specimen 4B: variable amplitude loading

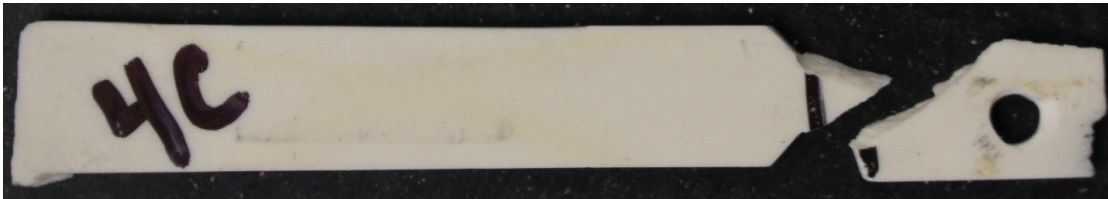


Figure B.4.b – Specimen 4C: variable amplitude loading



Figure B.4.c – Specimen 4D: chaotic loading

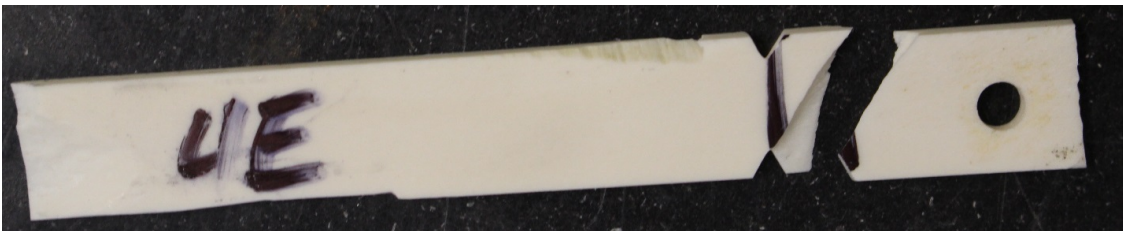


Figure B.4.d – Specimen 4E: chaotic loading



Figure B.4.e – Specimen 4F: chaotic loading

Group 5



Figure B.5.a – Specimen 5B: variable amplitude loading



Figure B.5.b – Specimen 5C: variable amplitude loading



Figure B.5.c – Specimen 5D: chaotic loading



Figure B.5.d – Specimen 5E: chaotic loading



Figure B.5.e – Specimen 5F: chaotic loading

Group 6



Figure B.6.a – Specimen 6B: variable amplitude loading



Figure B.6.b – Specimen 6C: variable amplitude loading



Figure B.6.c – Specimen 6D: chaotic loading



Figure B.6.d – Specimen 6E: chaotic loading



Figure B.4.e – Specimen 6F: chaotic loading

Group 7

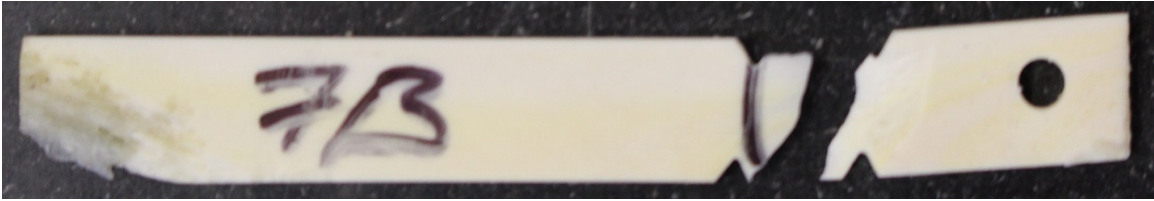


Figure B.7.a – Specimen 7B: variable amplitude loading

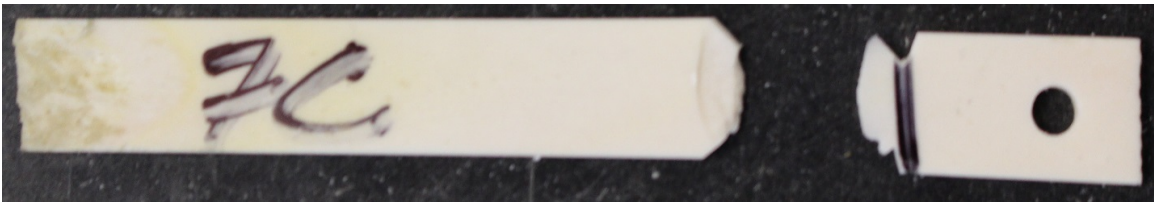


Figure B.7.b – Specimen 7C: variable amplitude loading



Figure B.7.c – Specimen 7D: chaotic loading



Figure B.7.d – Specimen 7E: chaotic loading



Figure B.7.e – Specimen 7F: chaotic loading

Group 8



Figure B.8.a – Specimen 8B: variable amplitude loading



Figure B.8.b – Specimen 8C: variable amplitude loading



Figure B.8.c – Specimen 8D: chaotic loading



Figure B.8.d – Specimen 8E: chaotic loading



Figure B.8.e – Specimen 8F: chaotic loading

Group 9



Figure B.9.a – Specimen 9B: variable amplitude loading



Figure B.9.b – Specimen 9C: variable amplitude loading



Figure B.9.c – Specimen 9D: chaotic loading



Figure B.9.d – Specimen 9E: chaotic loading



Figure B.9.e – Specimen 9F: chaotic loading

Group 10



Figure B.10.a – Specimen 10B: variable amplitude loading



Figure B.10.b – Specimen 10C: variable amplitude loading



Figure B.10.c – Specimen 10D: chaotic loading



Figure B.10.d – Specimen 10E: chaotic loading



Figure B.10.e – Specimen 10F: chaotic loading

APPENDIX C

Fracture Surface SEM Images

Chaotic Loading Test

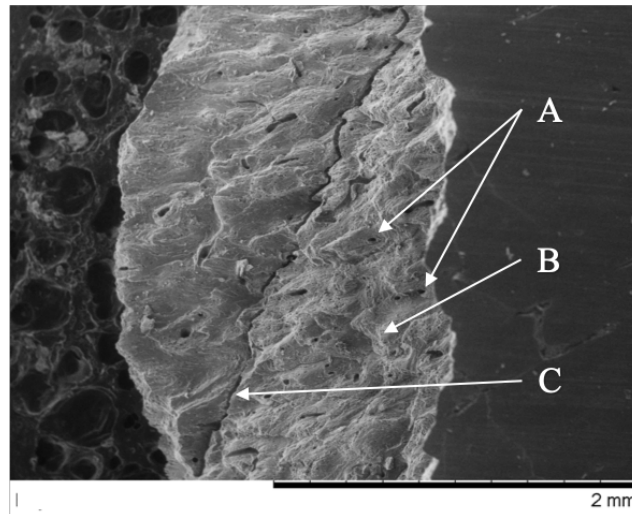


Figure C.1 – Specimen 1D: BD break. Taken with the 15kV SE settings at 50x magnification. Arrows 'A', 'B', and 'C' denote osteon pullout, beach markings and delamination, respectively.

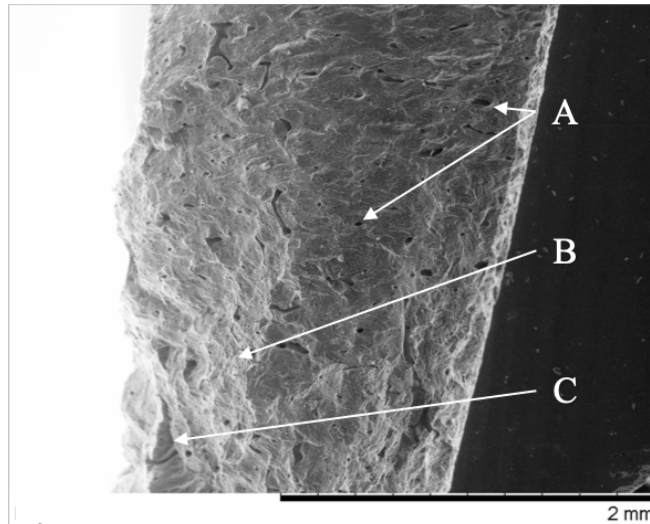


Figure C.2 – Specimen 1E: BD break. Taken with the 15kV SE settings at 50x magnification. Arrows 'A', 'B', and 'C' denote osteon pullout, beach markings and delamination, respectively.

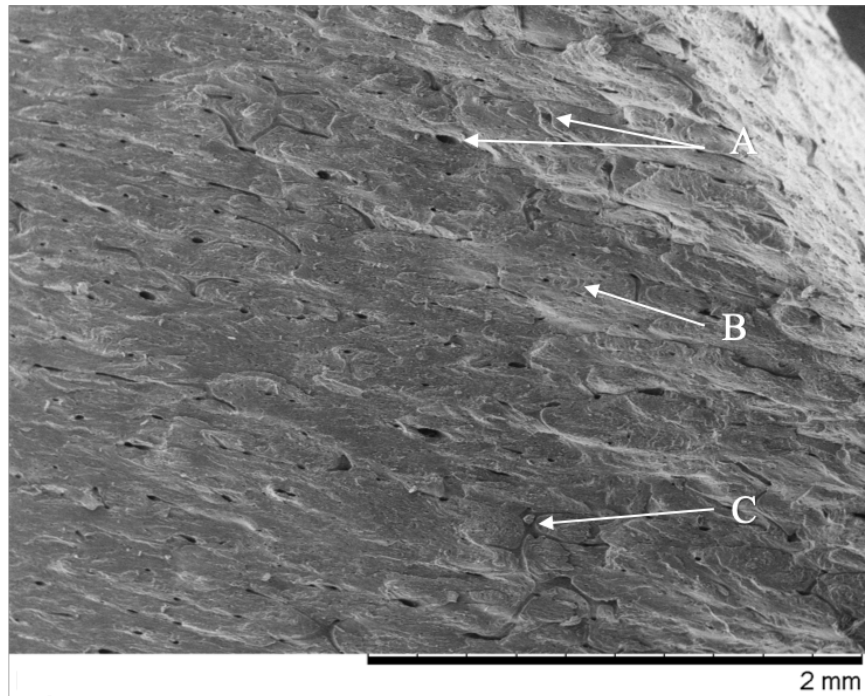


Figure C.3 – Specimen 1F: BD break. Taken with the 15kV SE settings at 50x magnification. Arrows ‘A’, ‘B’, and ‘C’ denote osteon pullout, beach markings and delamination, respectively.

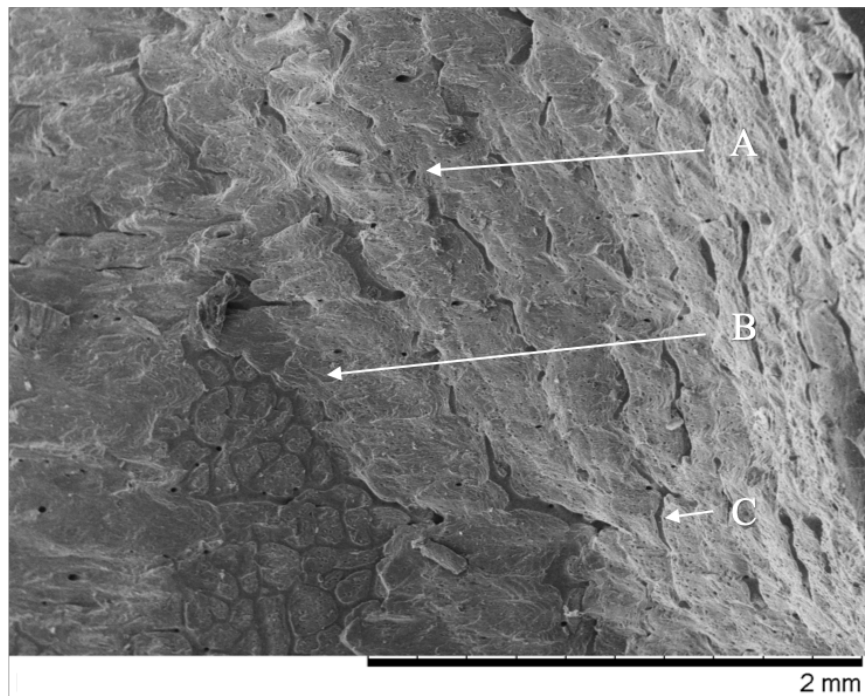


Figure C.4 – Specimen 2D: BD break. Taken with the 15kV SE settings at 50x magnification. Arrows ‘A’, ‘B’, and ‘C’ denote osteon pullout, beach markings and delamination, respectively.

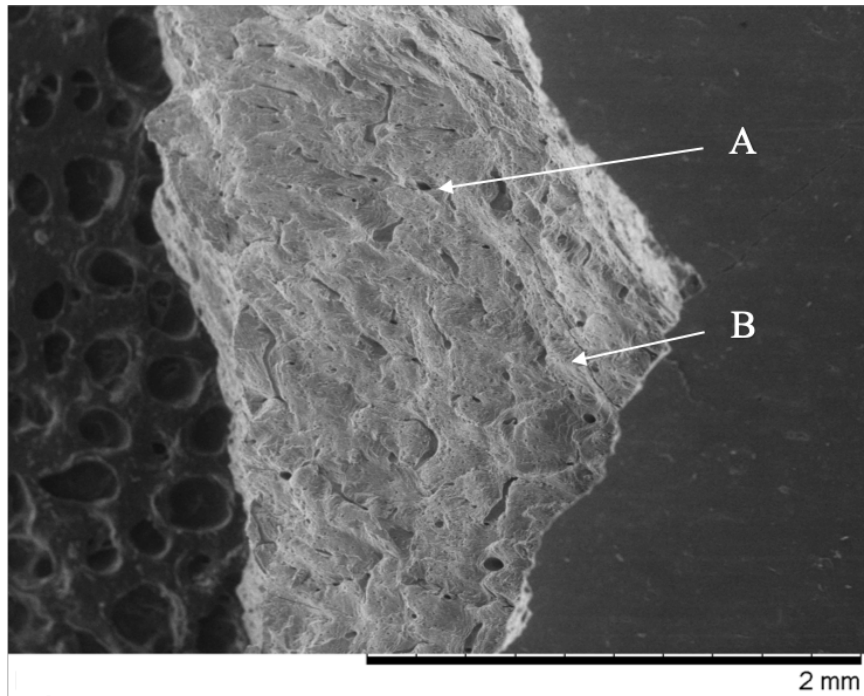


Figure C.5 – Specimen 2E: D break. Taken with the 15kV SE settings at 50x magnification. Arrows 'A' and 'B' denote osteon pullout and beach markings, respectively.

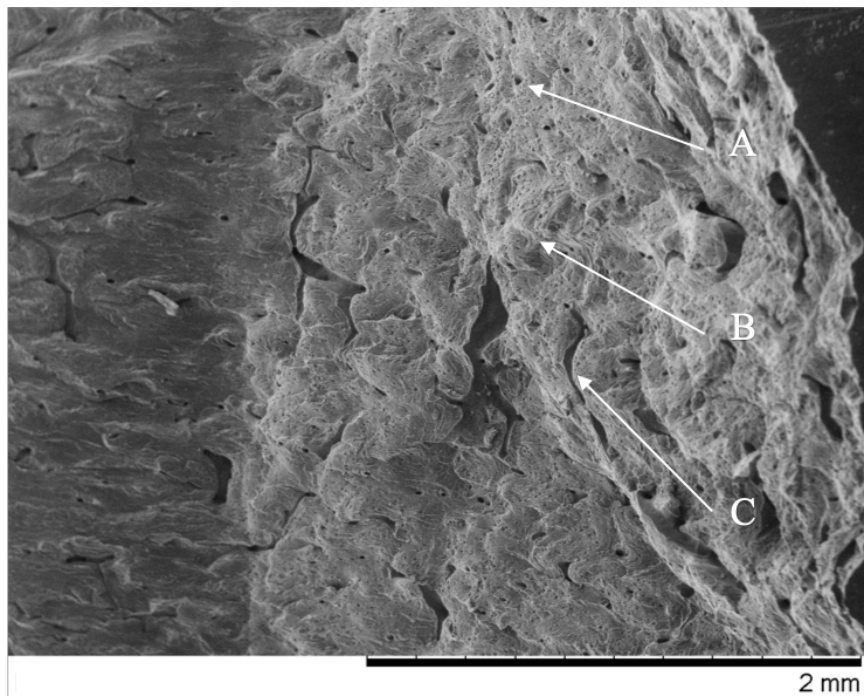


Figure C.6 – Specimen 2F: BD break. Taken with the 15kV SE settings at 50x magnification. Arrows 'A', 'B', and 'C' denote osteon pullout, beach markings and delamination, respectively.

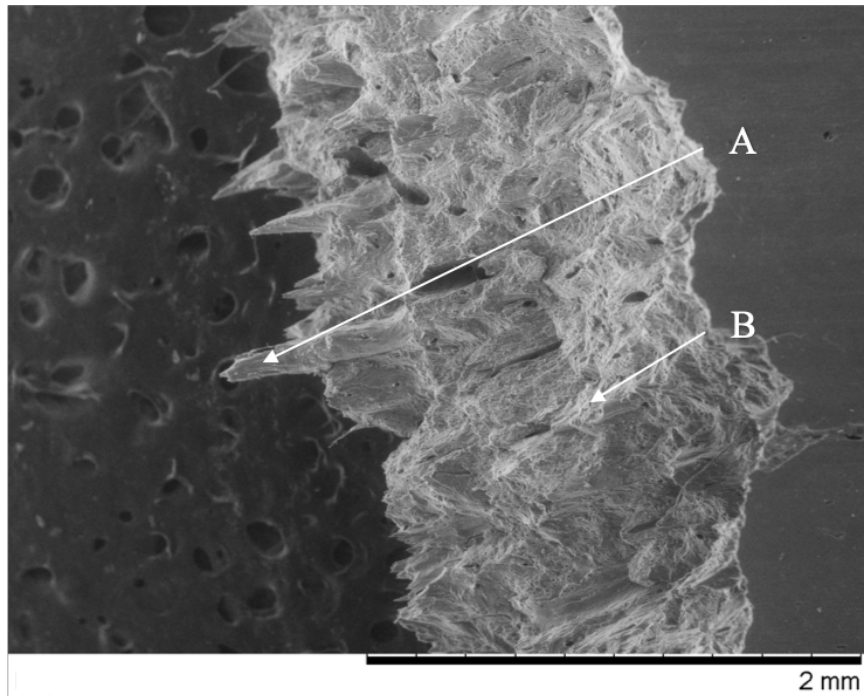


Figure C.7 – Specimen 3D: D break. Taken with the 15kV SE settings at 50x magnification. Arrows 'A' and 'B' denote osteon pullout and beach markings, respectively.

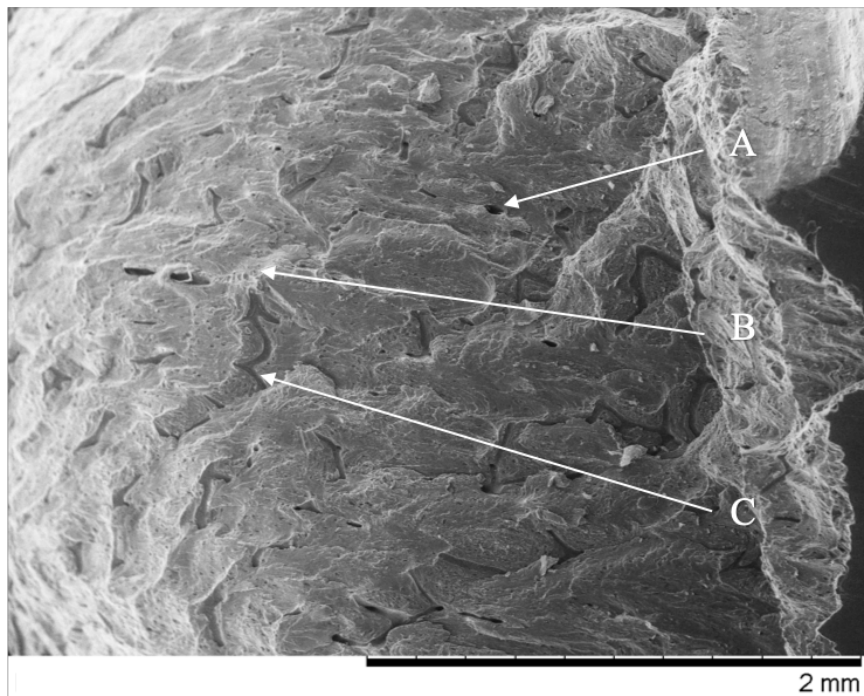


Figure C.8 – Specimen 3E: BD break. Taken with the 15kV SE settings at 50x magnification. Arrows 'A', 'B', and 'C' denote osteon pullout, beach markings and delamination, respectively.

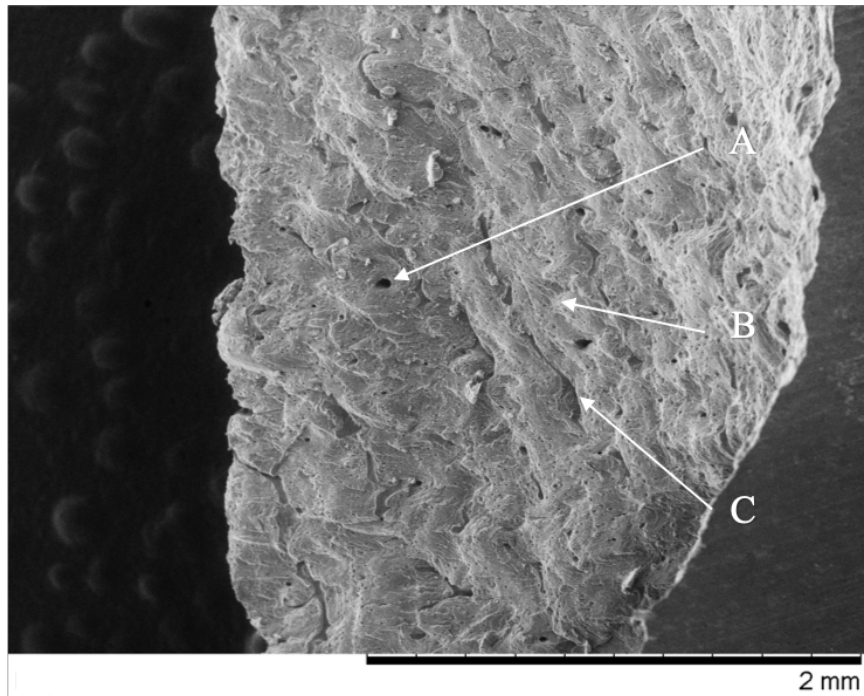


Figure C.9 – Specimen 3F: BD break. Taken with the 15kV SE settings at 50x magnification. Arrows ‘A’, ‘B’, and ‘C’ denote osteon pullout, beach markings and delamination, respectively.

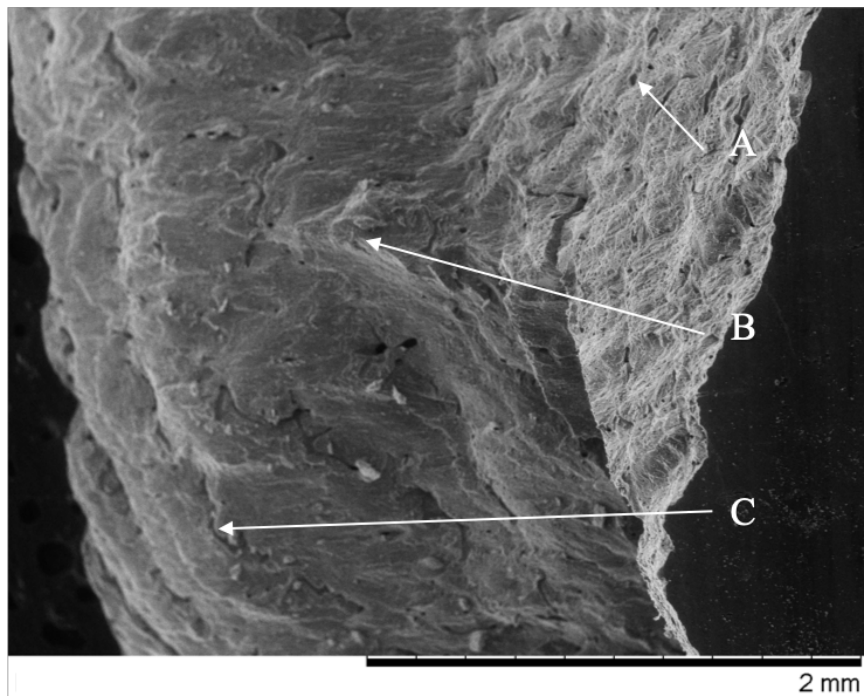


Figure C.10 – Specimen 4D: BD break. Taken with the 15kV SE settings at 50x magnification. Arrows ‘A’, ‘B’, and ‘C’ denote osteon pullout, beach markings and delamination, respectively.

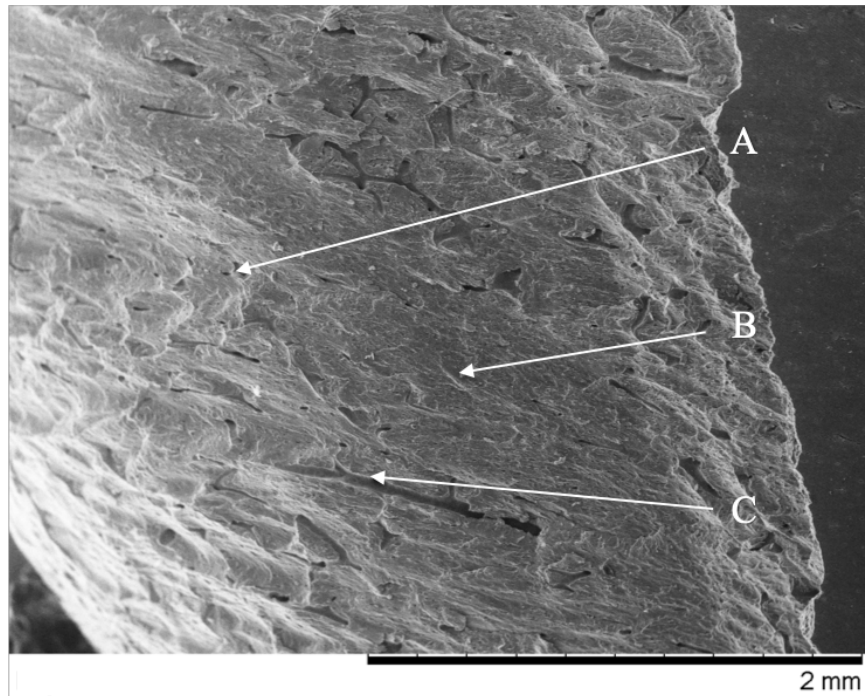


Figure C.11 – Specimen 4E: BD break. Taken with the 15kV SE settings at 50x magnification. Arrows ‘A’, ‘B’, and ‘C’ denote osteon pullout, beach markings and delamination, respectively.

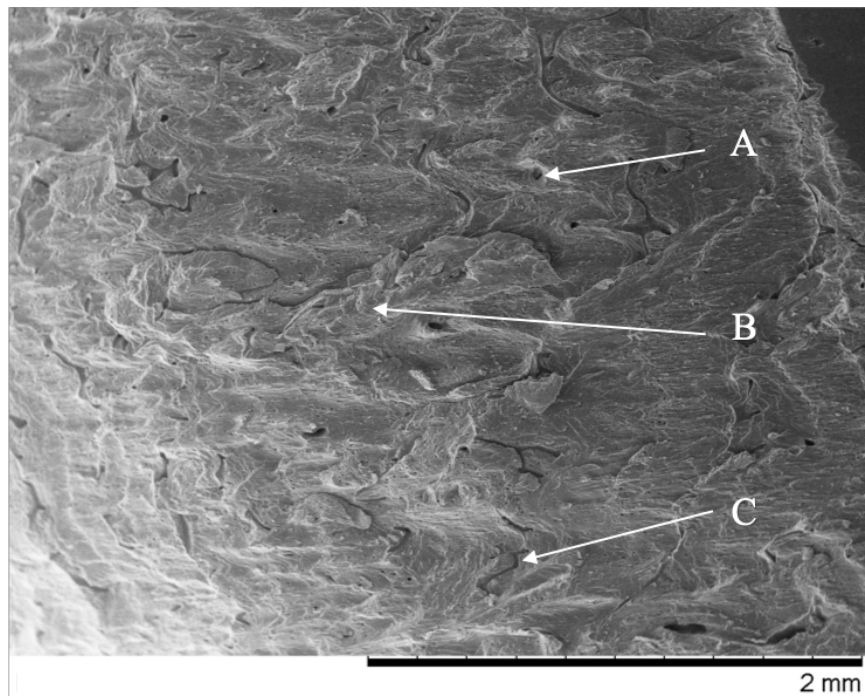


Figure C.12 – Specimen 4F: BD break. Taken with the 15kV SE settings at 50x magnification. Arrows ‘A’, ‘B’, and ‘C’ denote osteon pullout, beach markings and delamination, respectively.

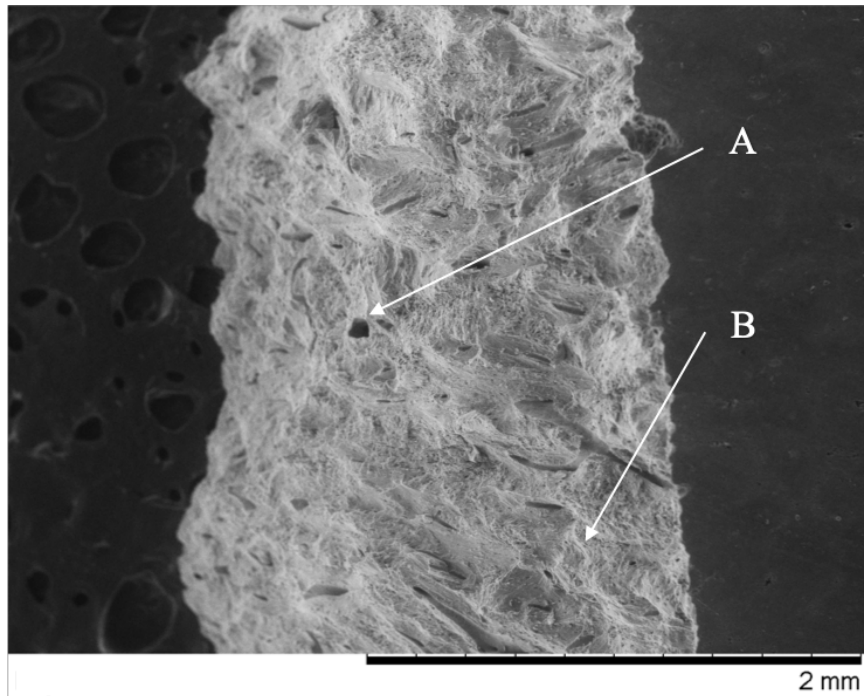


Figure C.13 – Specimen 5D: D break. Taken with the 15kV SE settings at 50x magnification. Arrows 'A' and 'B' denote osteon pullout and beach markings, respectively.

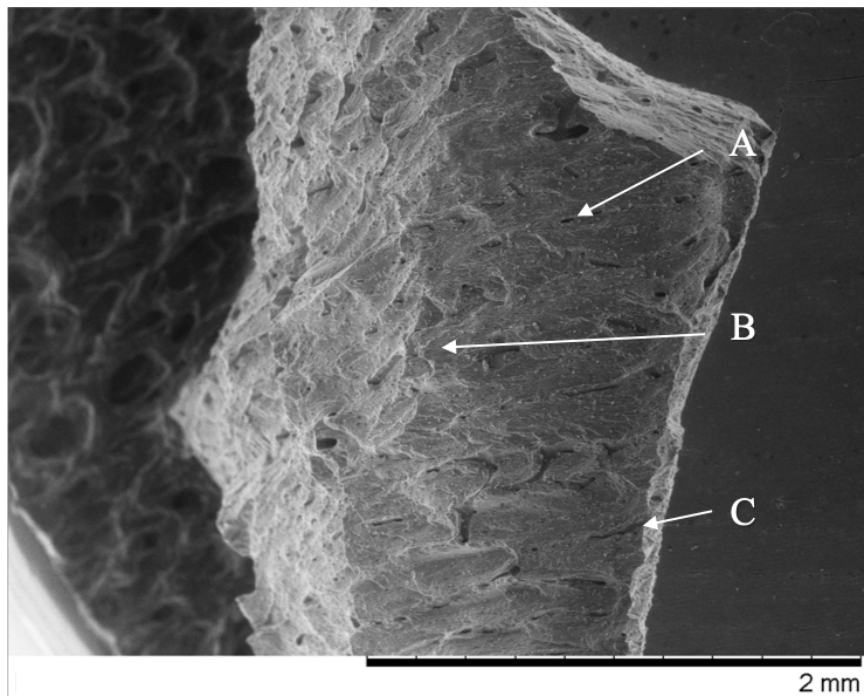


Figure C.14 – Specimen 5E: BD break. Taken with the 15kV SE settings at 50x magnification. Arrows 'A', 'B', and 'C' denote osteon pullout, beach markings and delamination, respectively.

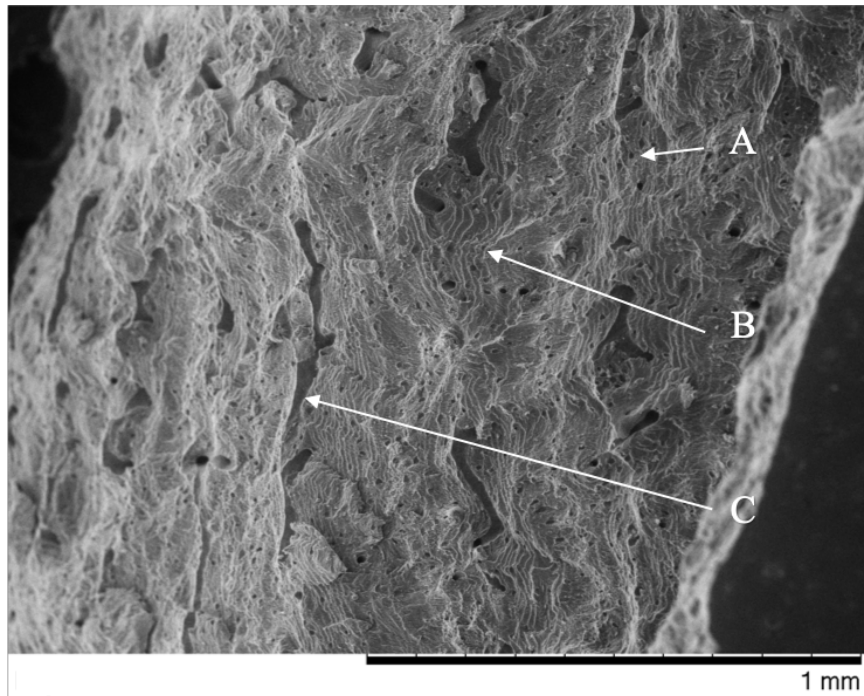


Figure C.15 – Specimen 5F: BD break. Taken with the 15kV SE settings at 50x magnification. Arrows ‘A’, ‘B’, and ‘C’ denote osteon pullout, beach markings and delamination, respectively.

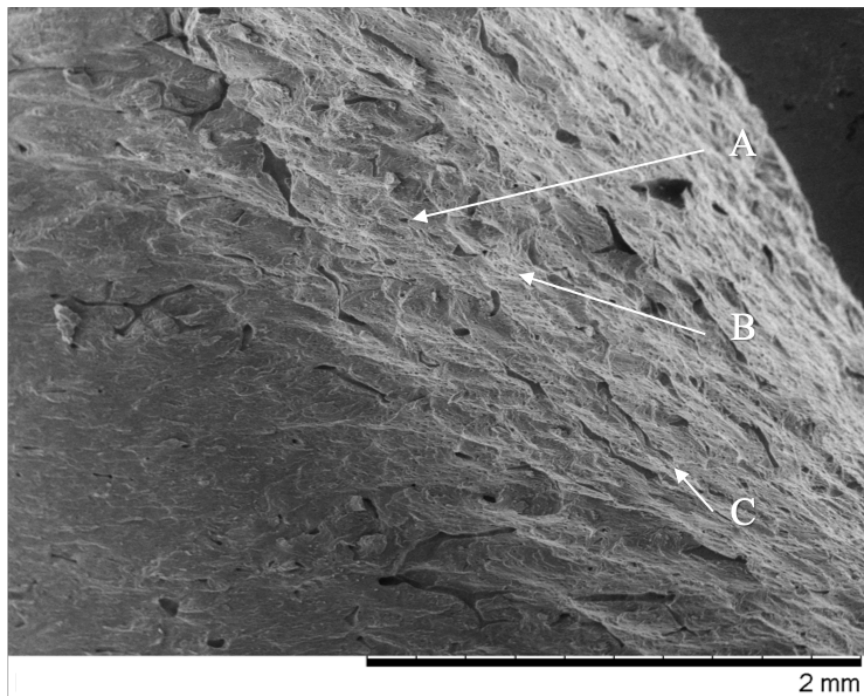


Figure C.16 – Specimen 6D: BD break. Taken with the 15kV SE settings at 50x magnification. Arrows ‘A’, ‘B’, and ‘C’ denote osteon pullout, beach markings and delamination, respectively.

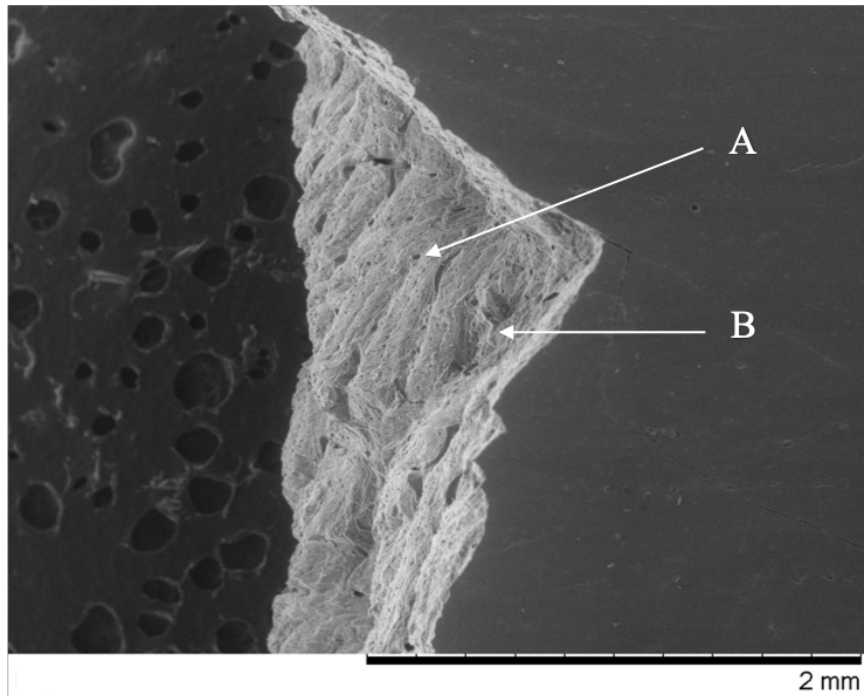


Figure C.17 – Specimen 6E: D break. Taken with the 15kV SE settings at 50x magnification. Arrows 'A' and 'B' denote osteon pullout and beach markings, respectively.

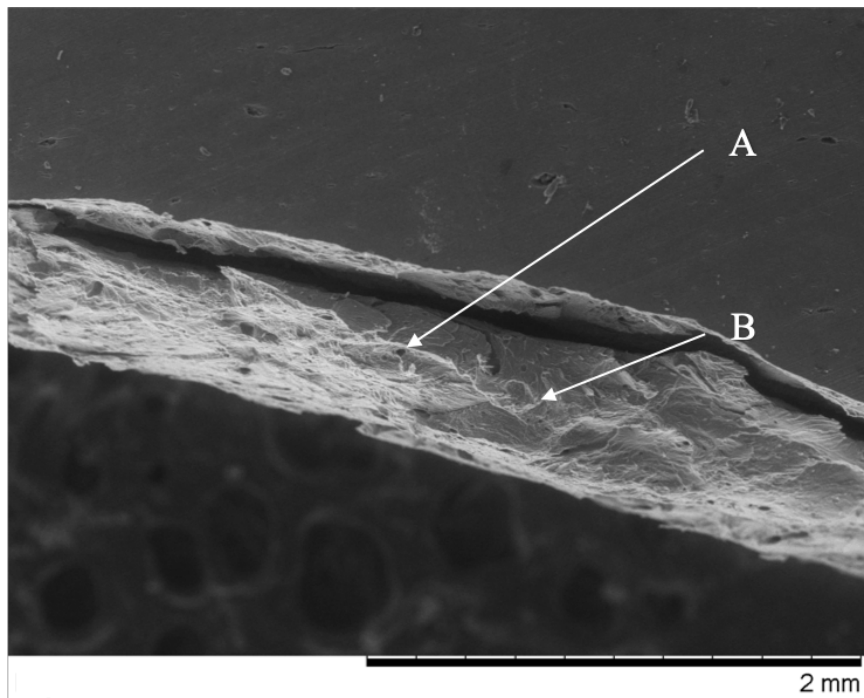


Figure C.18 – Specimen 6F: D break. Taken with the 15kV SE settings at 50x magnification. Arrows 'A' and 'B' denote osteon pullout and beach markings, respectively.

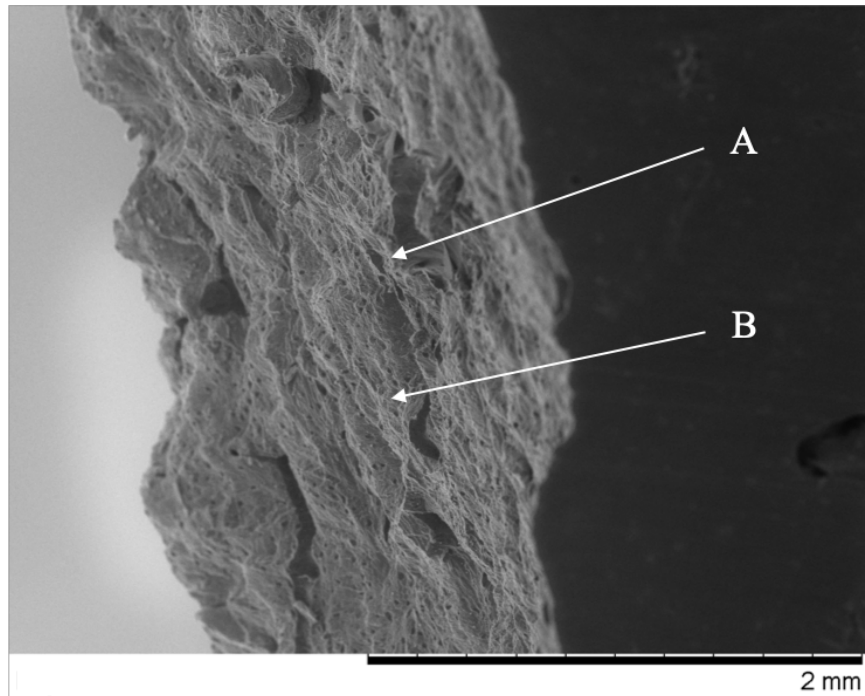


Figure C.19 – Specimen 7D: D break. Taken with the 15kV SE settings at 50x magnification. Arrows 'A' and 'B' denote osteon pullout and beach markings, respectively.

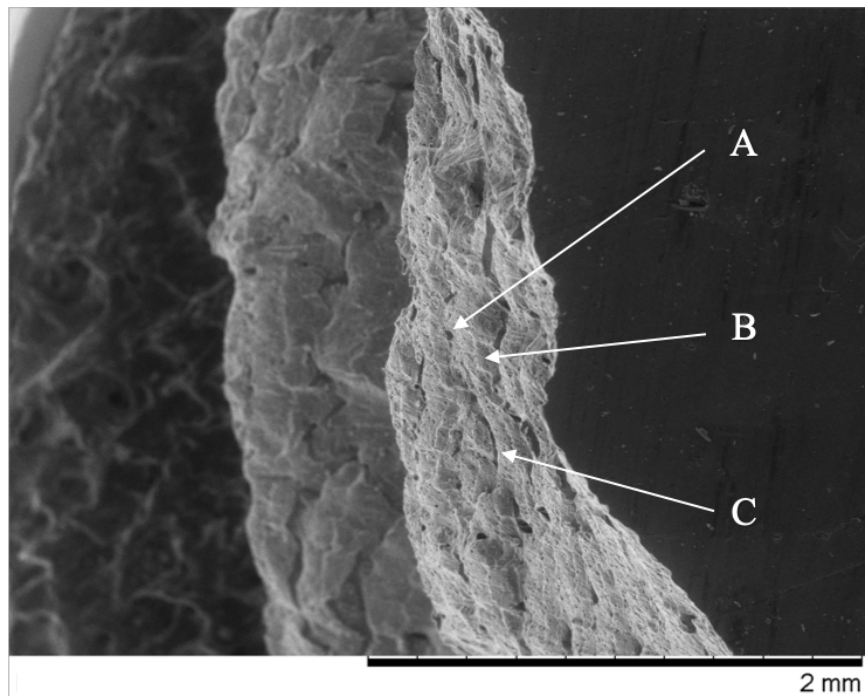


Figure C.20 – Specimen 7E: BD break. Taken with the 15kV SE settings at 50x magnification. Arrows 'A', 'B', and 'C' denote osteon pullout, beach markings and delamination, respectively.

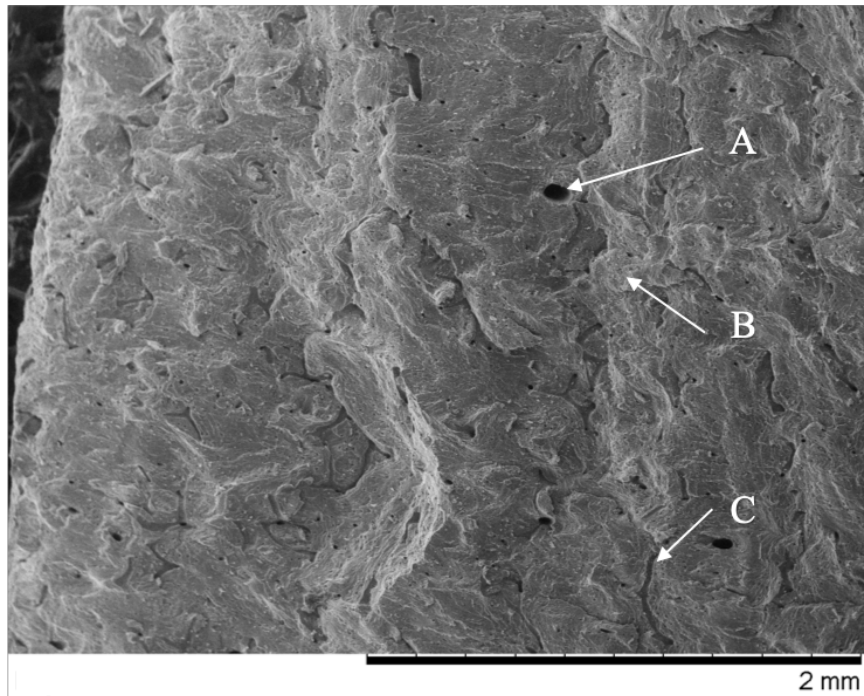


Figure C.21 – Specimen 7F: BD break. Taken with the 15kV SE settings at 50x magnification. Arrows ‘A’, ‘B’, and ‘C’ denote osteon pullout, beach markings and delamination, respectively.

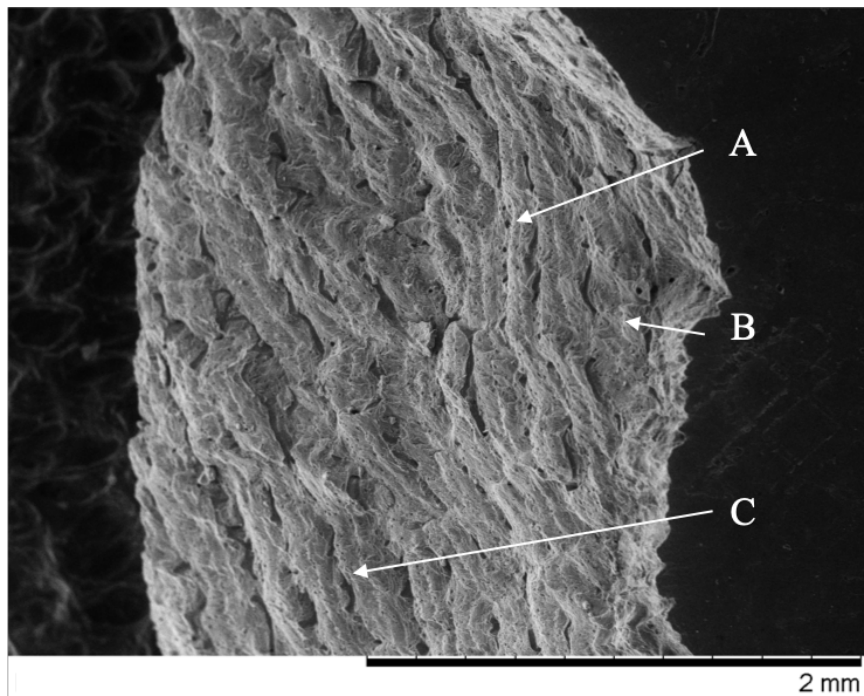


Figure C.22 – Specimen 8D: BD break. Taken with the 15kV SE settings at 50x magnification. Arrows ‘A’, ‘B’, and ‘C’ denote osteon pullout, beach markings and delamination, respectively.

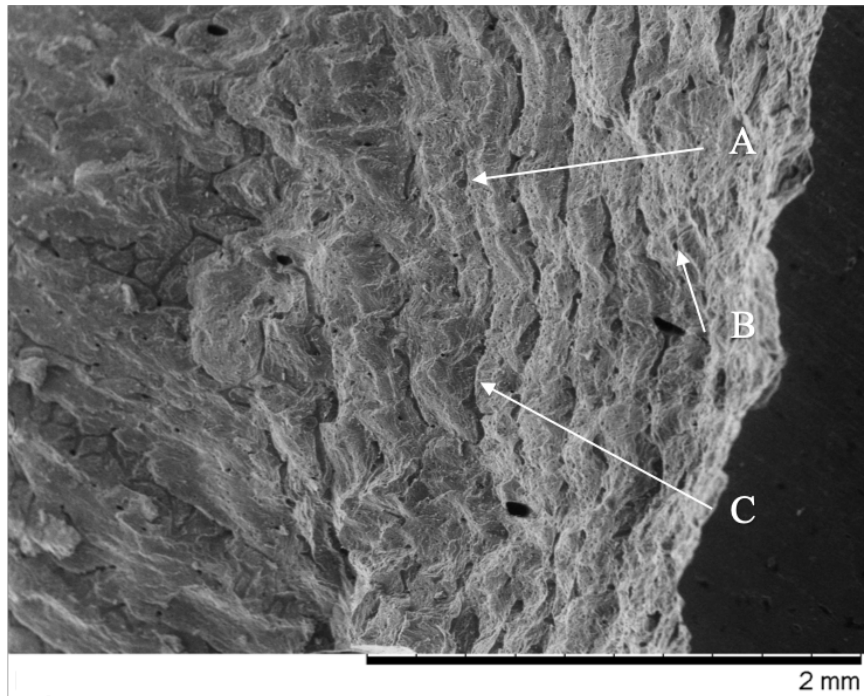


Figure C.23 – Specimen 8E: BD break. Taken with the 15kV SE settings at 50x magnification. Arrows ‘A’, ‘B’, and ‘C’ denote osteon pullout, beach markings and delamination, respectively.

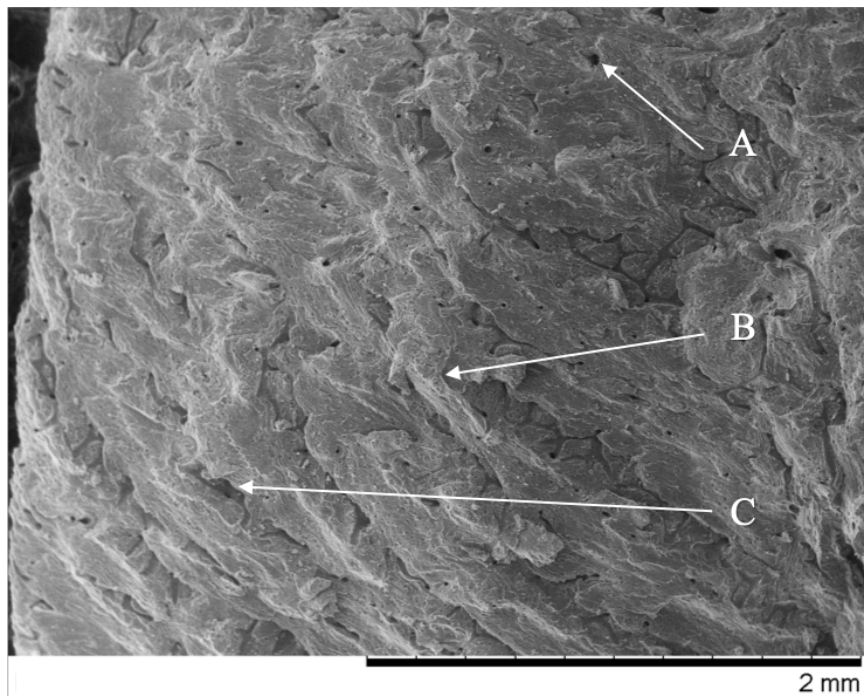


Figure C.24 – Specimen 8F: BD break. Taken with the 15kV SE settings at 50x magnification. Arrows ‘A’, ‘B’, and ‘C’ denote osteon pullout, beach markings and delamination, respectively.

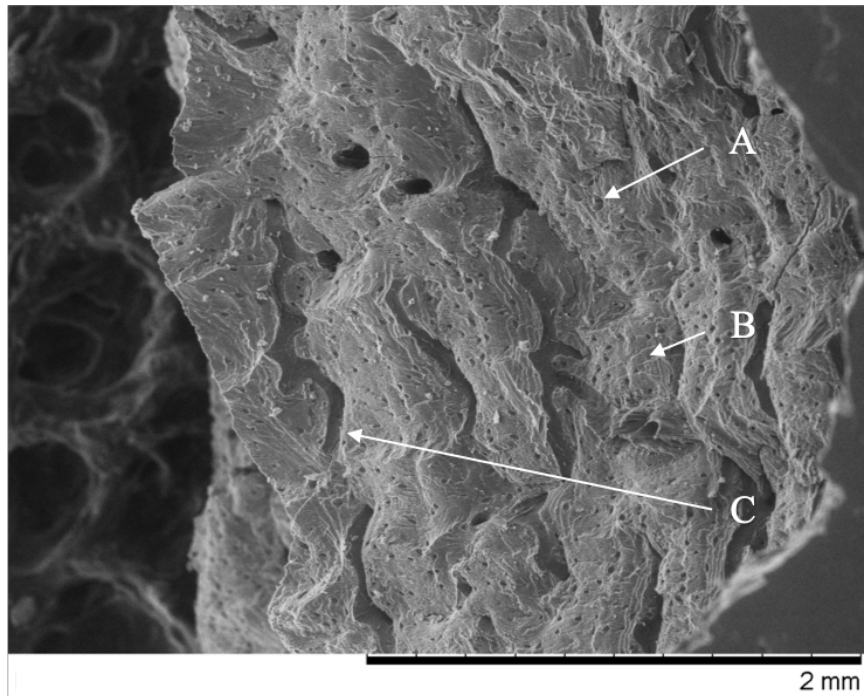


Figure C.25 – Specimen 9D: BD break. Taken with the 15kV SE settings at 50x magnification. Arrows ‘A’, ‘B’, and ‘C’ denote osteon pullout, beach markings and delamination, respectively.

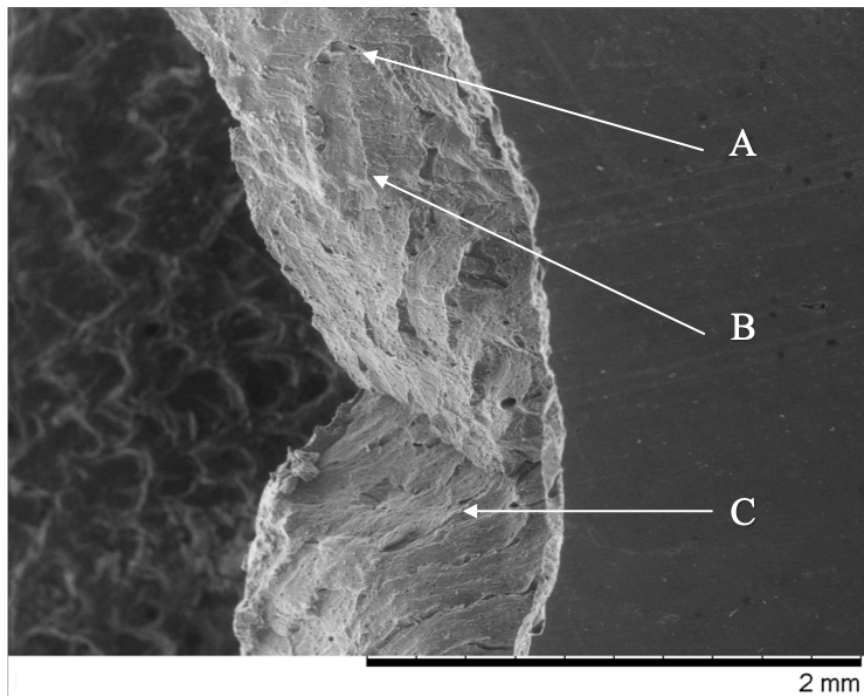


Figure C.26 – Specimen 9E: BD break. Taken with the 15kV SE settings at 50x magnification. Arrows ‘A’, ‘B’, and ‘C’ denote osteon pullout, beach markings and delamination, respectively.

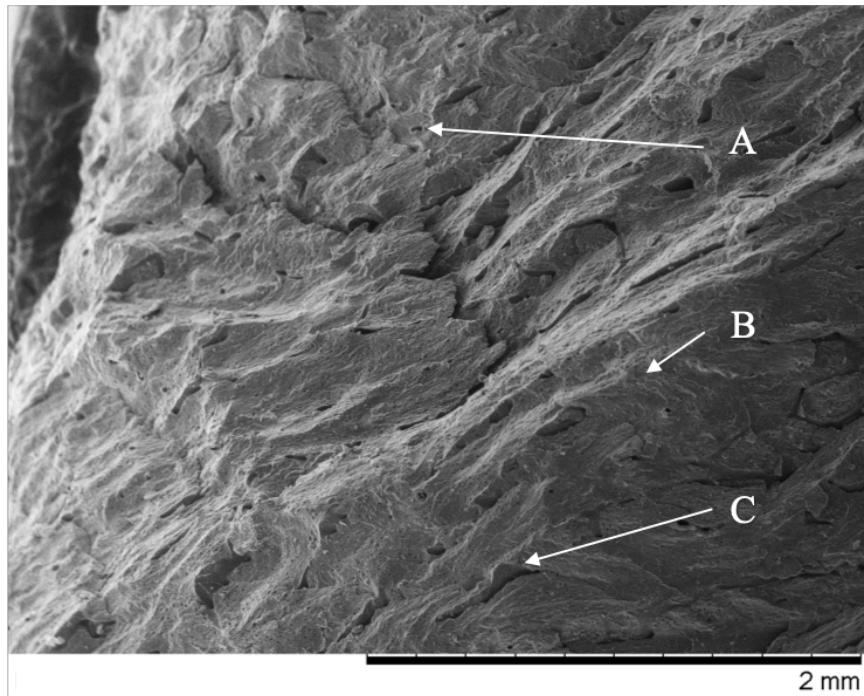


Figure C.27 – Specimen 9F: BD break. Taken with the 15kV SE settings at 50x magnification. Arrows ‘A’, ‘B’, and ‘C’ denote osteon pullout, beach markings and delamination, respectively.

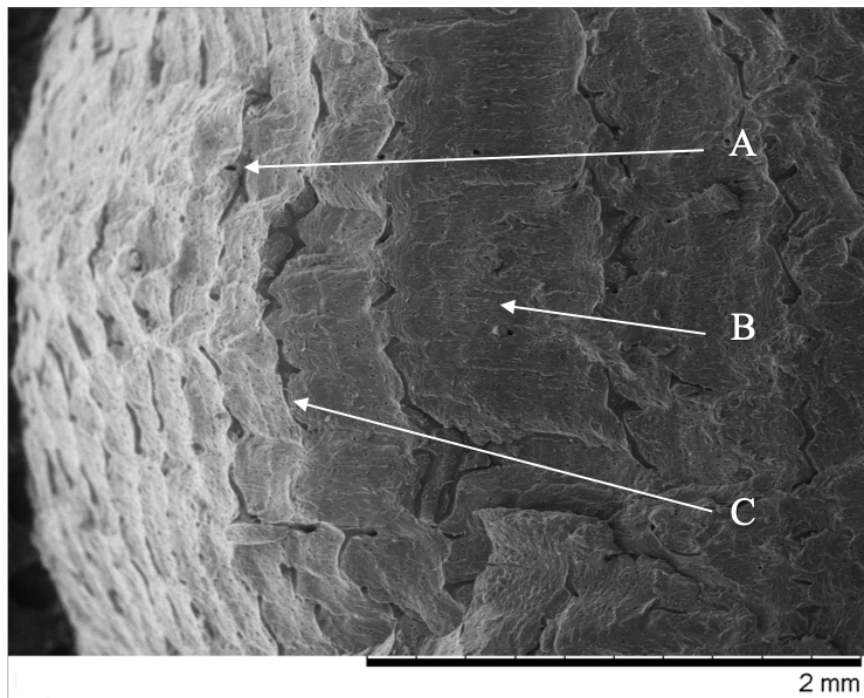


Figure C.28 – Specimen 10D: BD break. Taken with the 15kV SE settings at 50x magnification. Arrows ‘A’, ‘B’, and ‘C’ denote osteon pullout, beach markings and delamination, respectively.

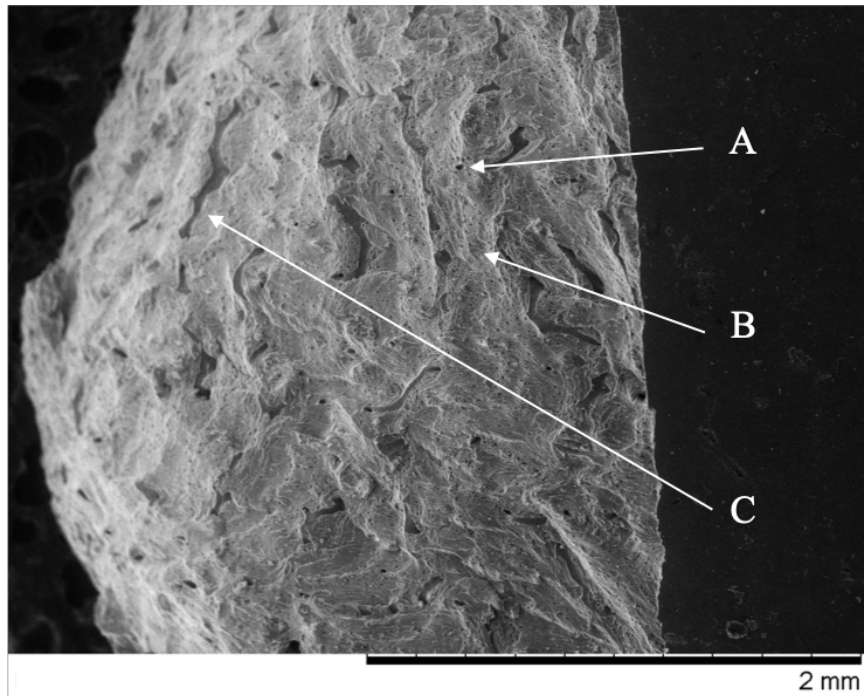


Figure C.29 – Specimen 10E: BD break. Taken with the 15kV SE settings at 50x magnification. Arrows ‘A’, ‘B’, and ‘C’ denote osteon pullout, beach markings and delamination, respectively.

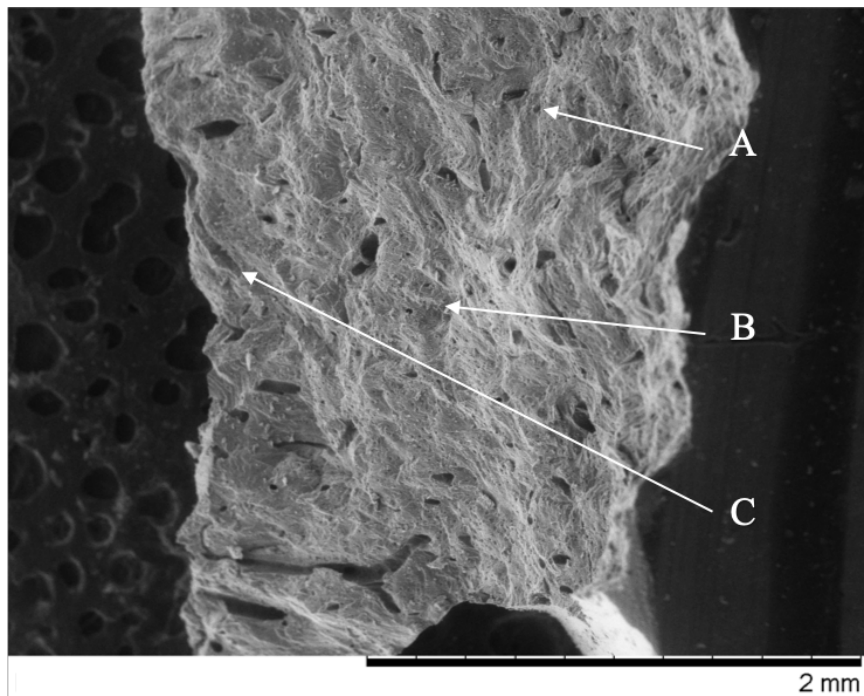


Figure C.30 – Specimen 10F: BD break. Taken with the 15kV SE settings at 50x magnification. Arrows ‘A’, ‘B’, and ‘C’ denote osteon pullout, beach markings and delamination, respectively.

Variable Amplitude Test

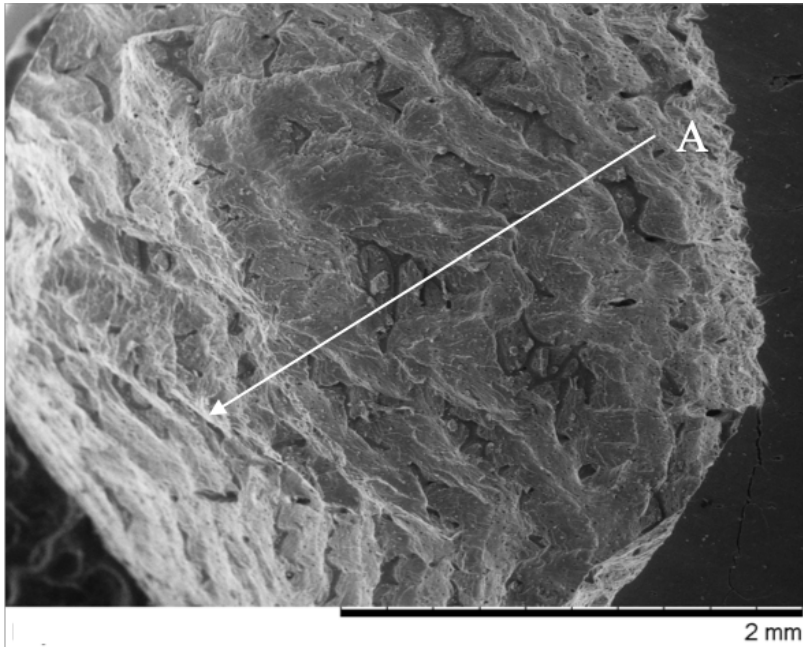


Figure C.31 – Specimen 3B: B break. Taken with the 15kV SE settings at 50x magnification. Arrows 'A' denotes delamination.

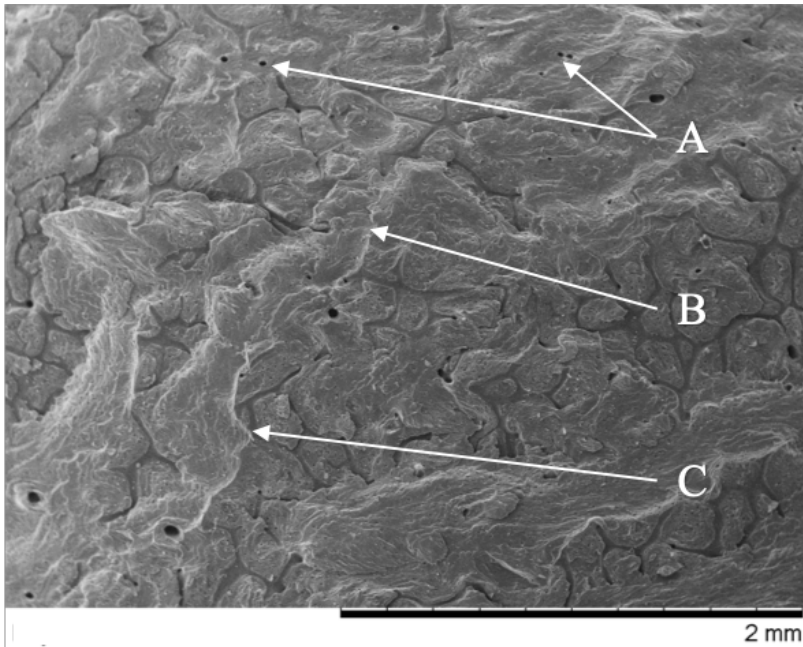


Figure C.32 – Specimen 3C: BD break. Taken with the 15kV SE settings at 50x magnification. Arrows 'A', 'B', and 'C' denote osteon pullout, beach markings and delamination, respectively.

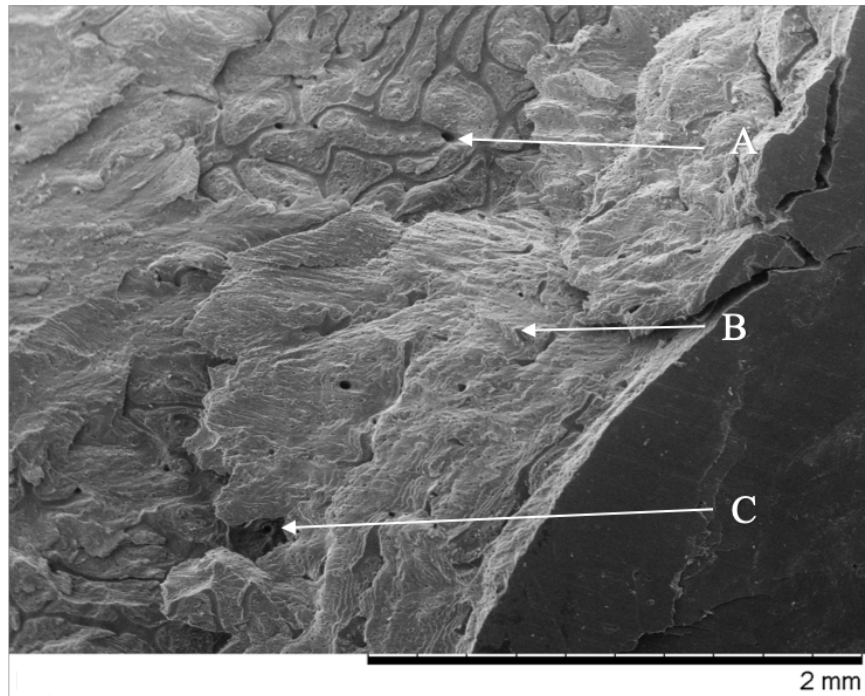


Figure C.33 – Specimen 4B: BD break. Taken with the 15kV SE settings at 50x magnification. Arrows ‘A’, ‘B’, and ‘C’ denote osteon pullout, beach markings and delamination, respectively.

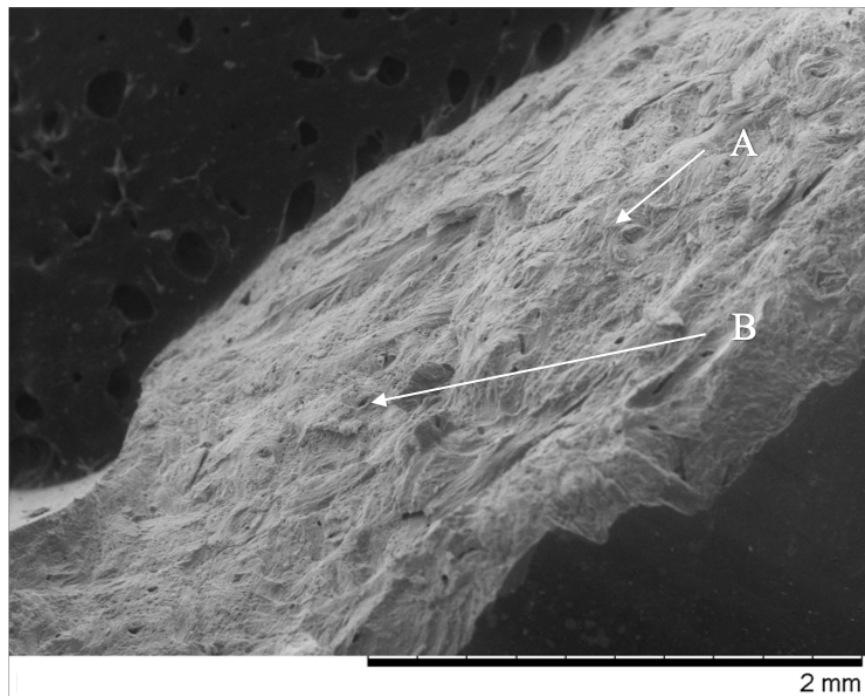


Figure C.34 – Specimen 4C: D break. Taken with the 15kV SE settings at 50x magnification. Arrows ‘A’ and ‘B’ denote osteon pullout and beach markings, respectively.

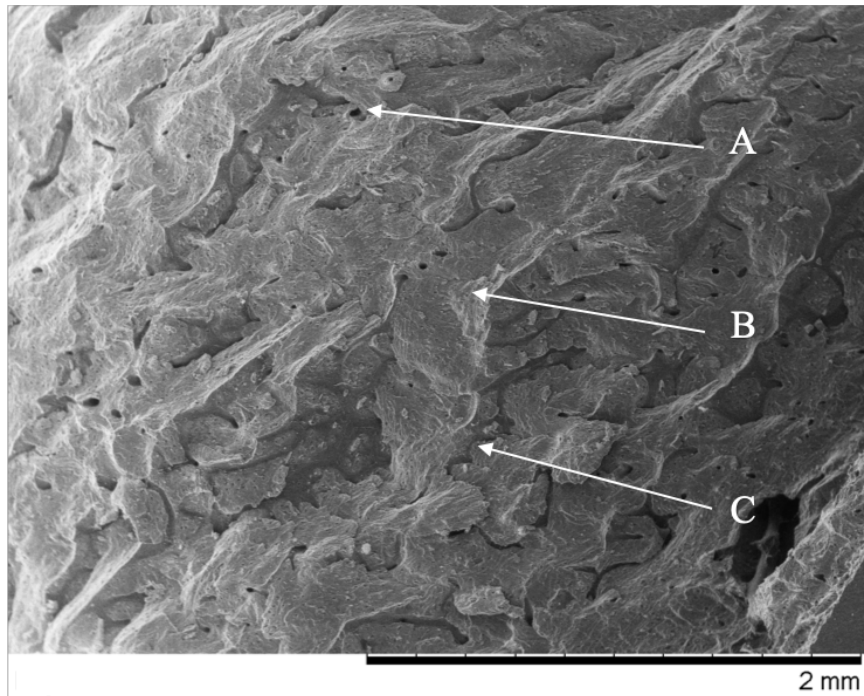


Figure C.35 – Specimen 5B: BD break. Taken with the 15kV SE settings at 50x magnification. Arrows ‘A’, ‘B’, and ‘C’ denote osteon pullout, beach markings and delamination, respectively.

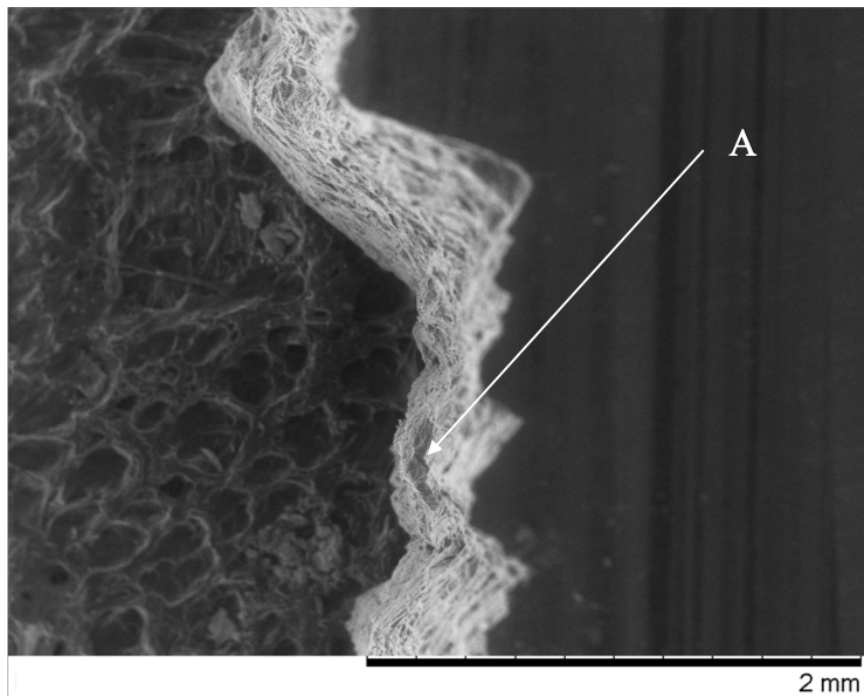


Figure C.36 – Specimen 5C: B break. Taken with the 15kV SE settings at 50x magnification. Arrows ‘A’ denotes delamination.

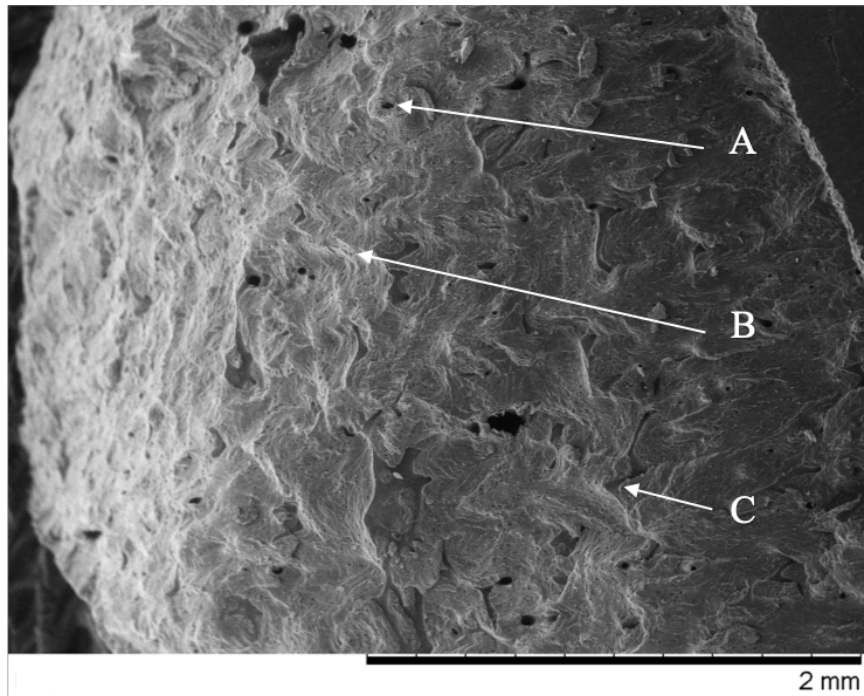


Figure C.37 – Specimen 6B: BD break. Taken with the 15kV SE settings at 50x magnification. Arrows ‘A’, ‘B’, and ‘C’ denote osteon pullout, beach markings and delamination, respectively.

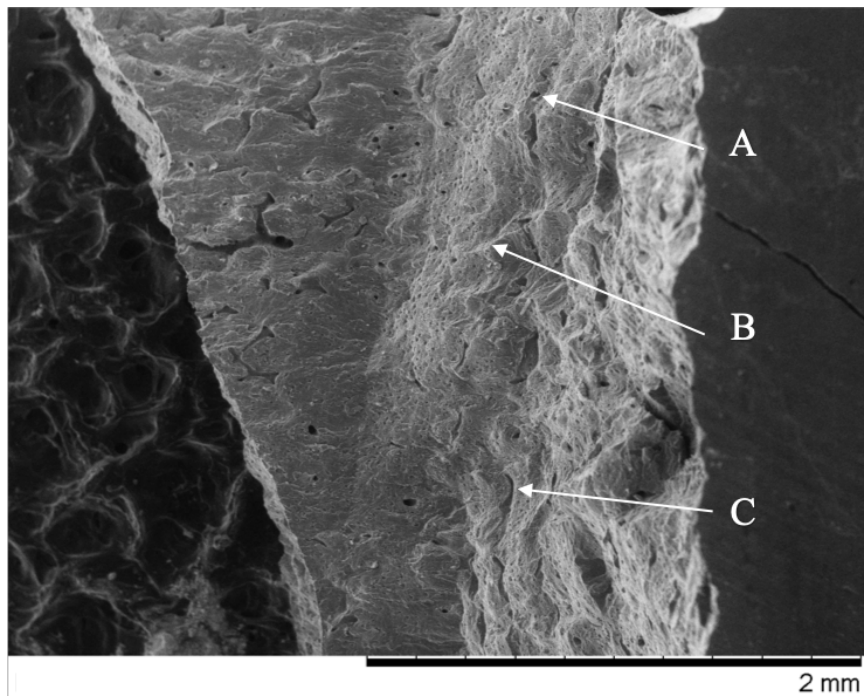


Figure C.38 – Specimen 6C: BD break. Taken with the 15kV SE settings at 50x magnification. Arrows ‘A’, ‘B’, and ‘C’ denote osteon pullout, beach markings and delamination, respectively.

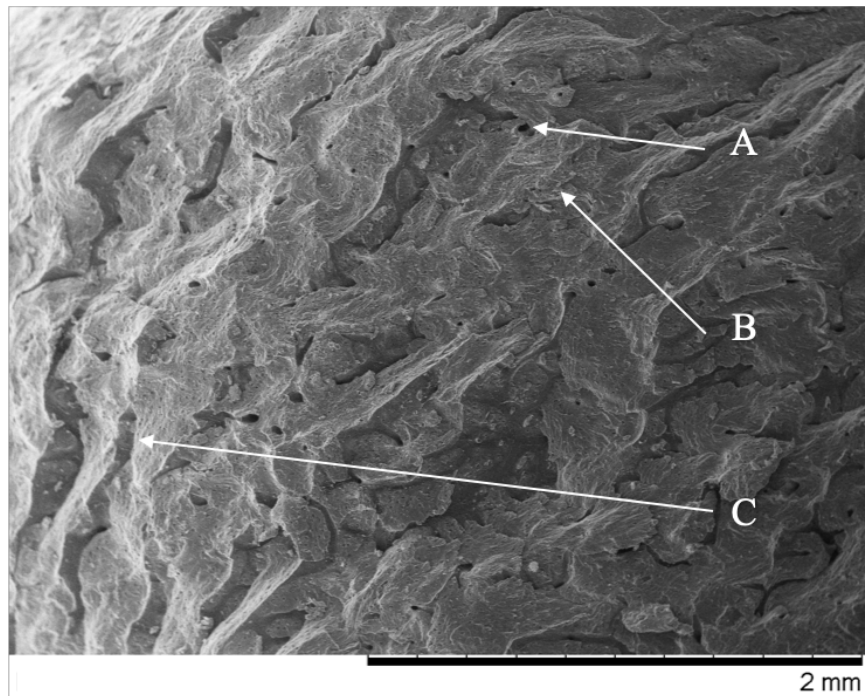


Figure C.39 – Specimen 7B: BD break. Taken with the 15kV SE settings at 50x magnification. Arrows ‘A’, ‘B’, and ‘C’ denote osteon pullout, beach markings and delamination, respectively.

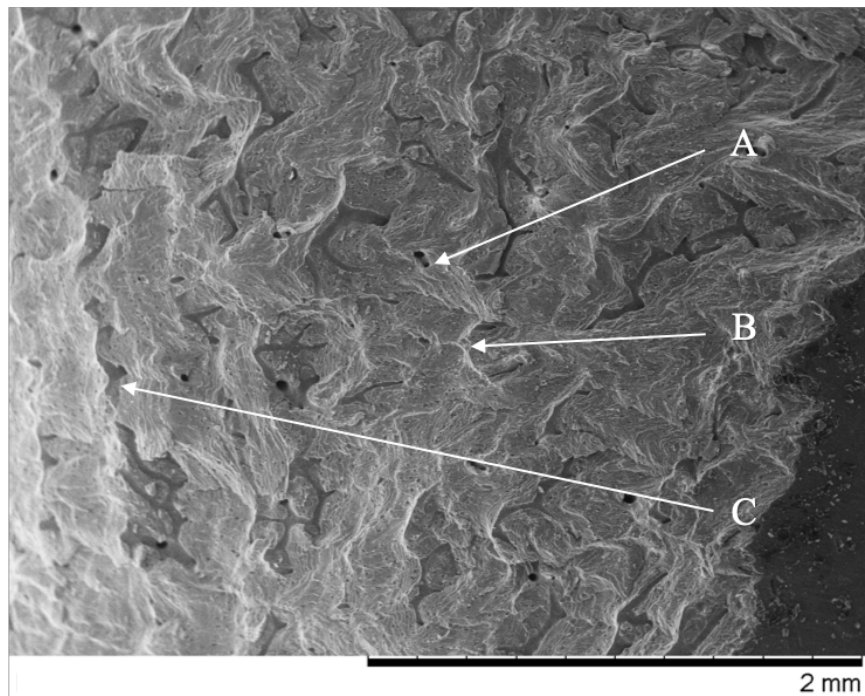


Figure C.40 – Specimen 7C: BD break. Taken with the 15kV SE settings at 50x magnification. Arrows ‘A’, ‘B’, and ‘C’ denote osteon pullout, beach markings and delamination, respectively.

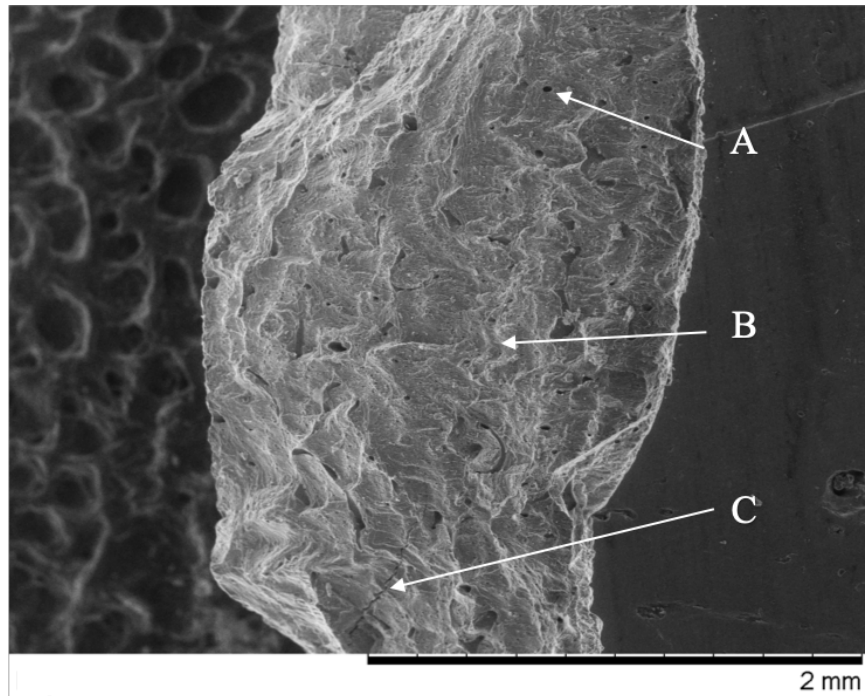


Figure C.41 – Specimen 8B: BD break. Taken with the 15kV SE settings at 50x magnification. Arrows ‘A’, ‘B’, and ‘C’ denote osteon pullout, beach markings and delamination, respectively.

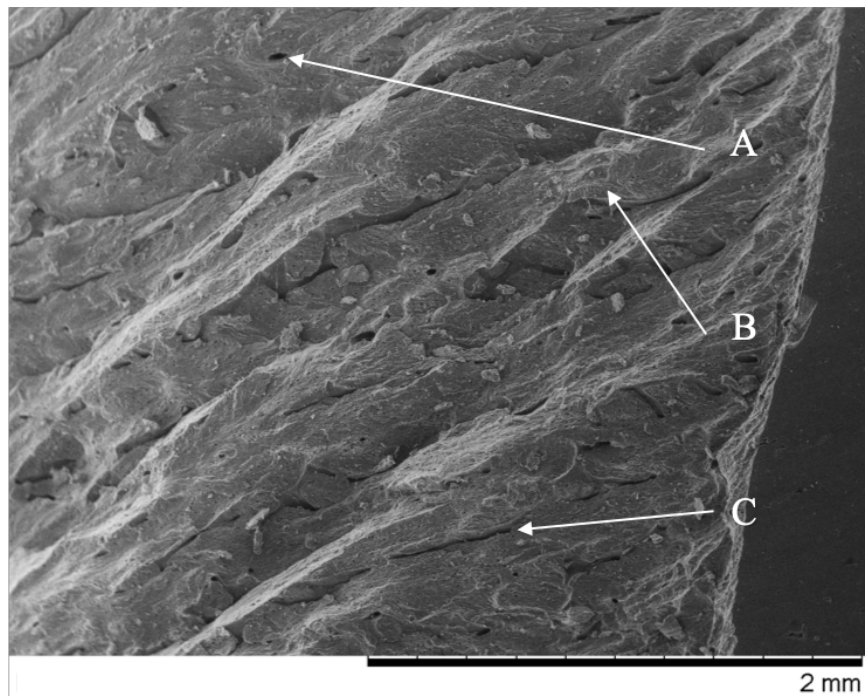


Figure C.42 – Specimen 8C: BD break. Taken with the 15kV SE settings at 50x magnification. Arrows ‘A’, ‘B’, and ‘C’ denote osteon pullout, beach markings and delamination, respectively.

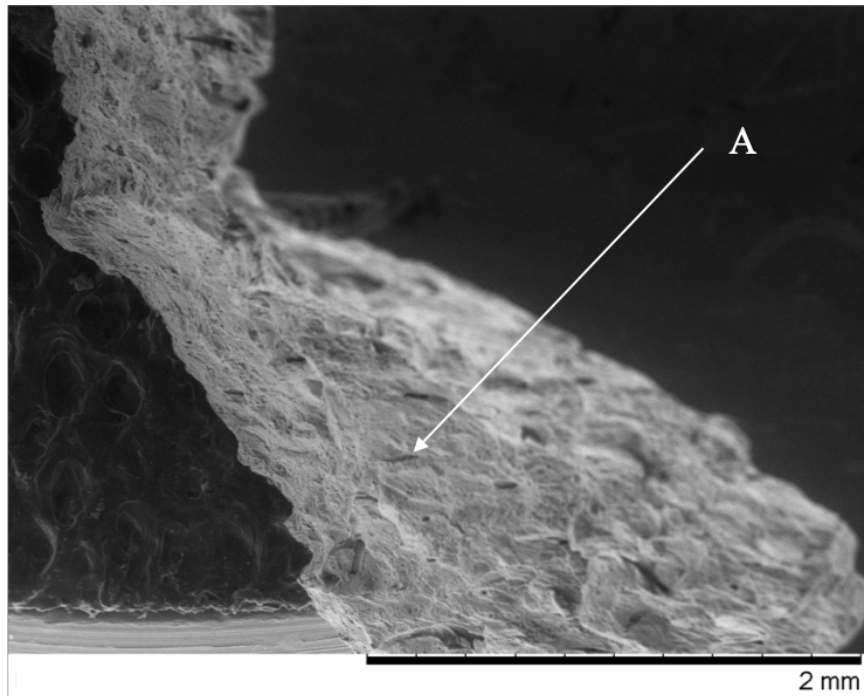


Figure C.43 – Specimen 9B: B break. Taken with the 15kV SE settings at 50x magnification. Arrows ‘A’ denotes delamination.

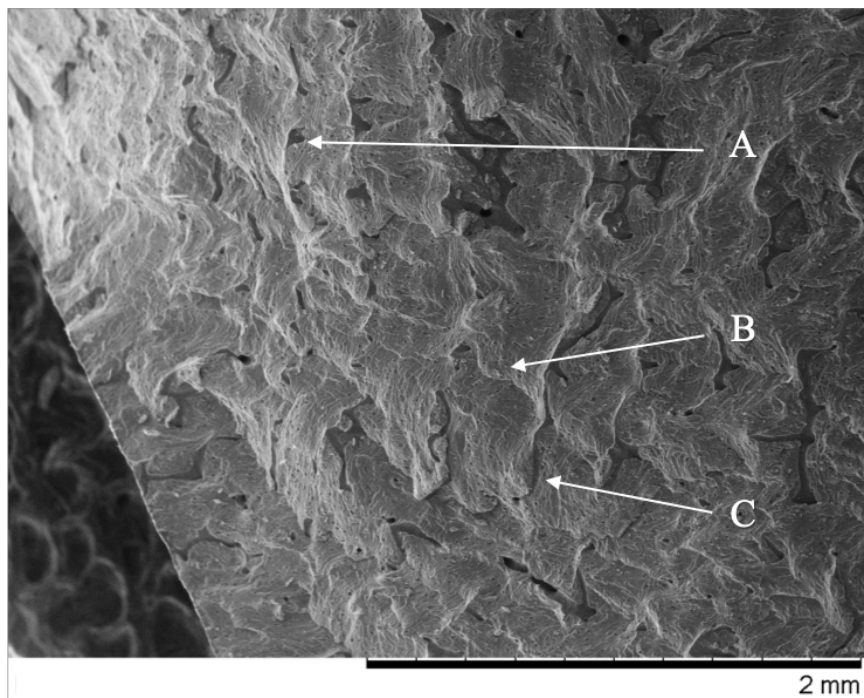


Figure C.44 – Specimen 9C: BD break. Taken with the 15kV SE settings at 50x magnification. Arrows ‘A’, ‘B’, and ‘C’ denote osteon pullout, beach markings and delamination, respectively.

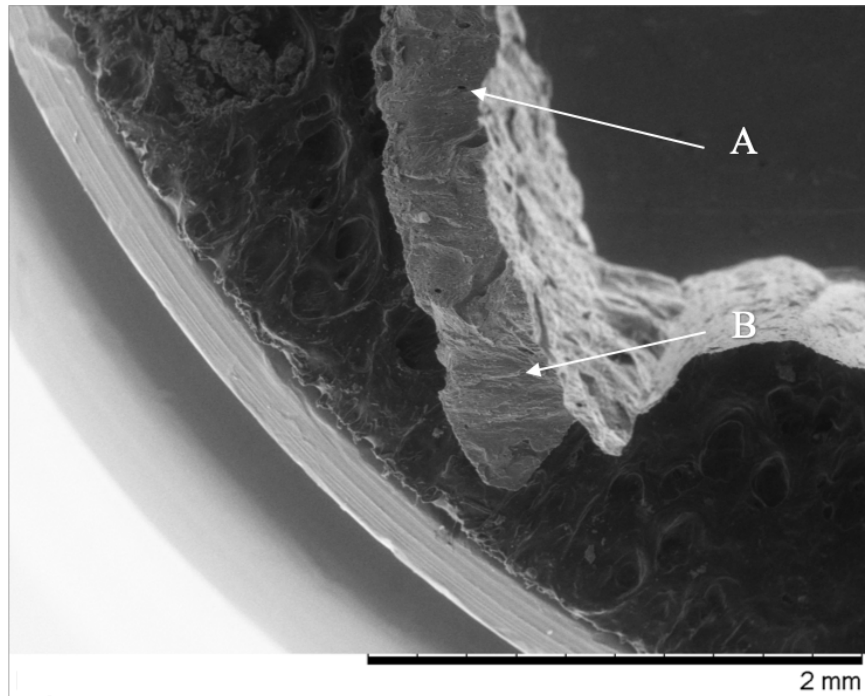


Figure C.45 – Specimen 10B: D break. Taken with the 15kV SE settings at 50x magnification. Arrows ‘A’ and ‘B’ denote osteon pullout and beach markings, respectively.

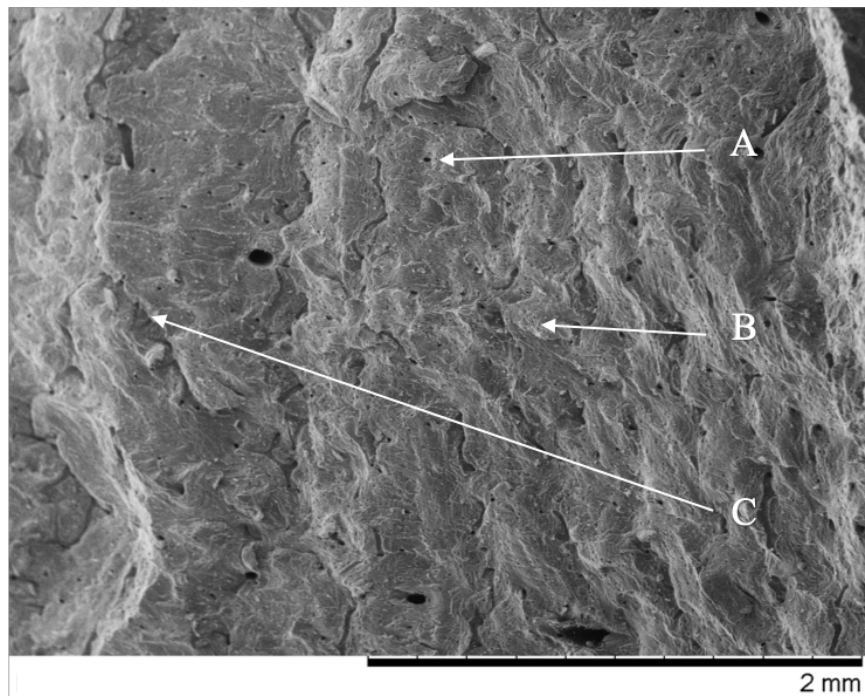


Figure C.46 – Specimen 10C: BD break. Taken with the 15kV SE settings at 50x magnification. Arrows ‘A,’ ‘B,’ and ‘C’ denote osteon pullout, beach markings and delamination, respectively.

APPENDIX D

Data Summaries

Chaotic Loading Test

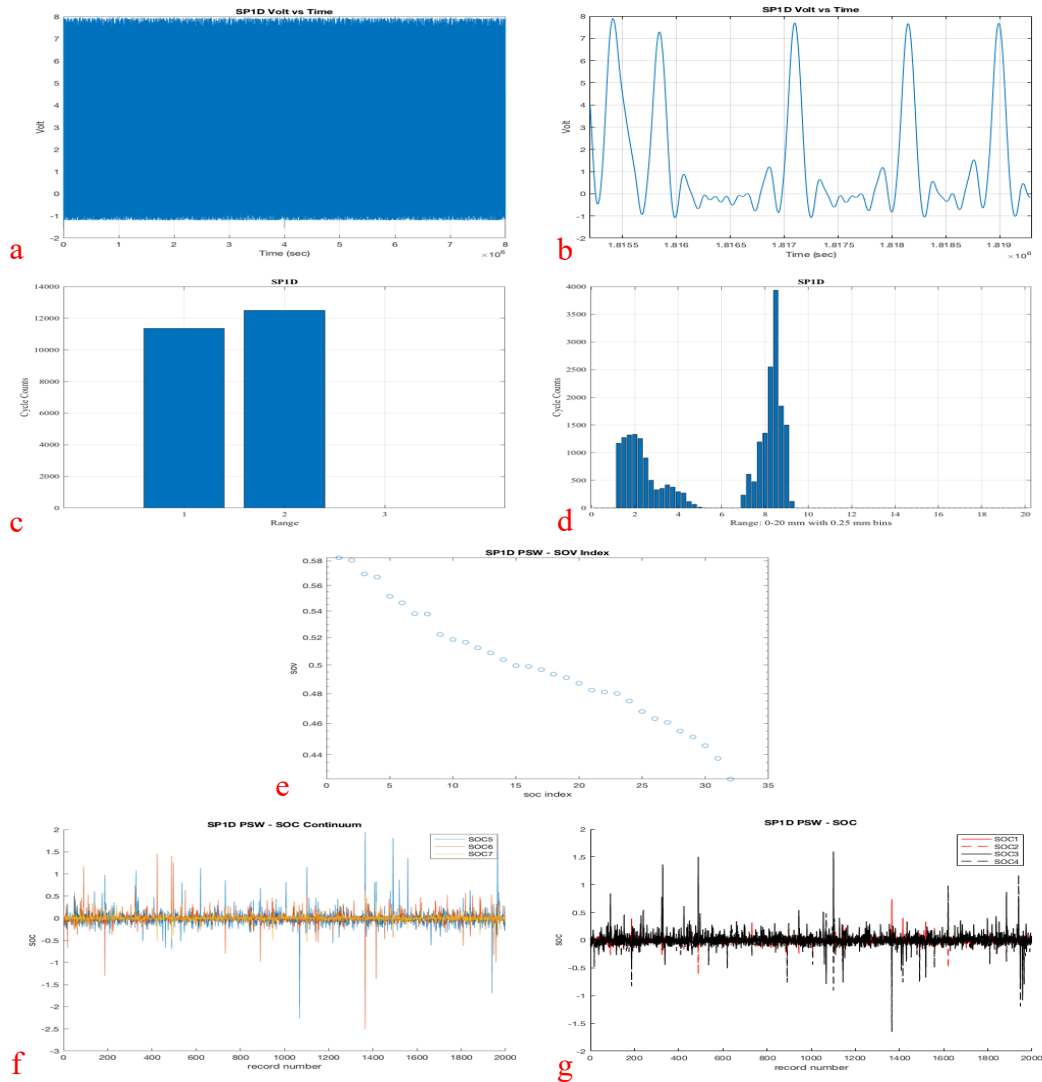


Figure D.1 – Specimen 1D plots. a) voltage vs. time b) zoomed time series c) three bin histogram of cycle count d) 0.25mm bin cycle count histogram e) SOC index f) SOM of eigenvalue g) SOC continuum

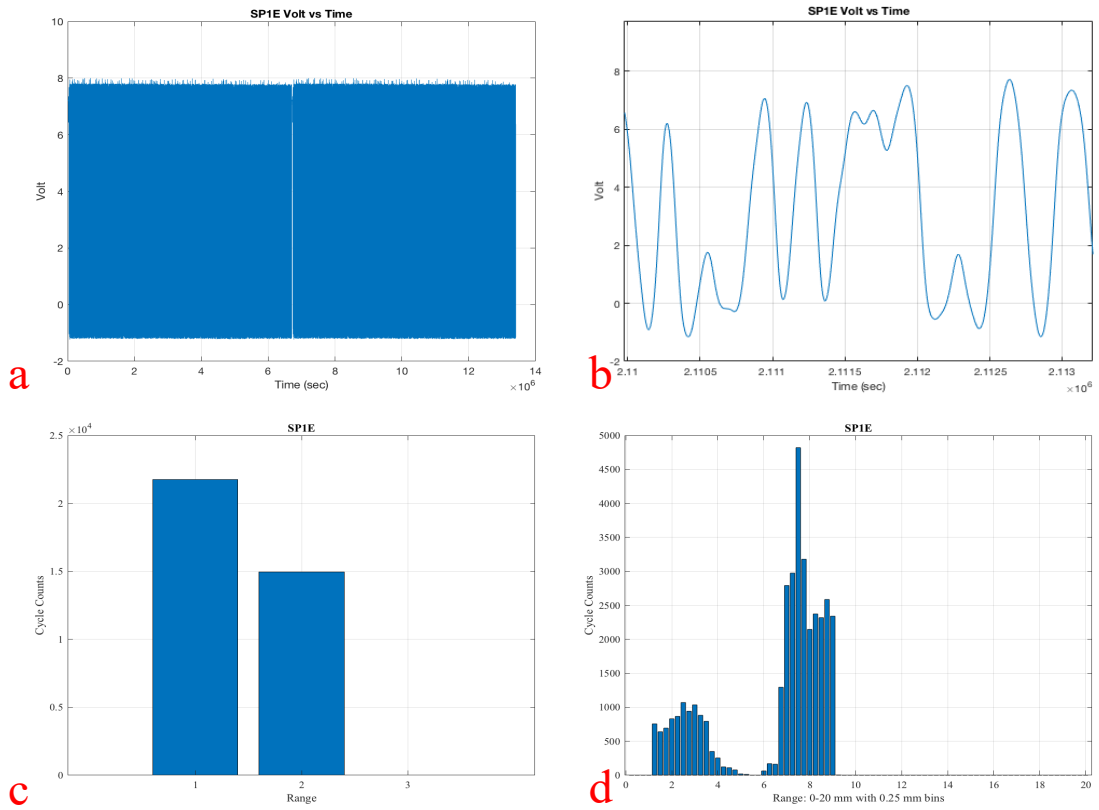


Figure D.2 – Specimen 1E plots. a) voltage vs. time b) zoomed time series c) three bin histogram of cycle count d) 0.25mm bin cycle count histogram. There was no PSW data.

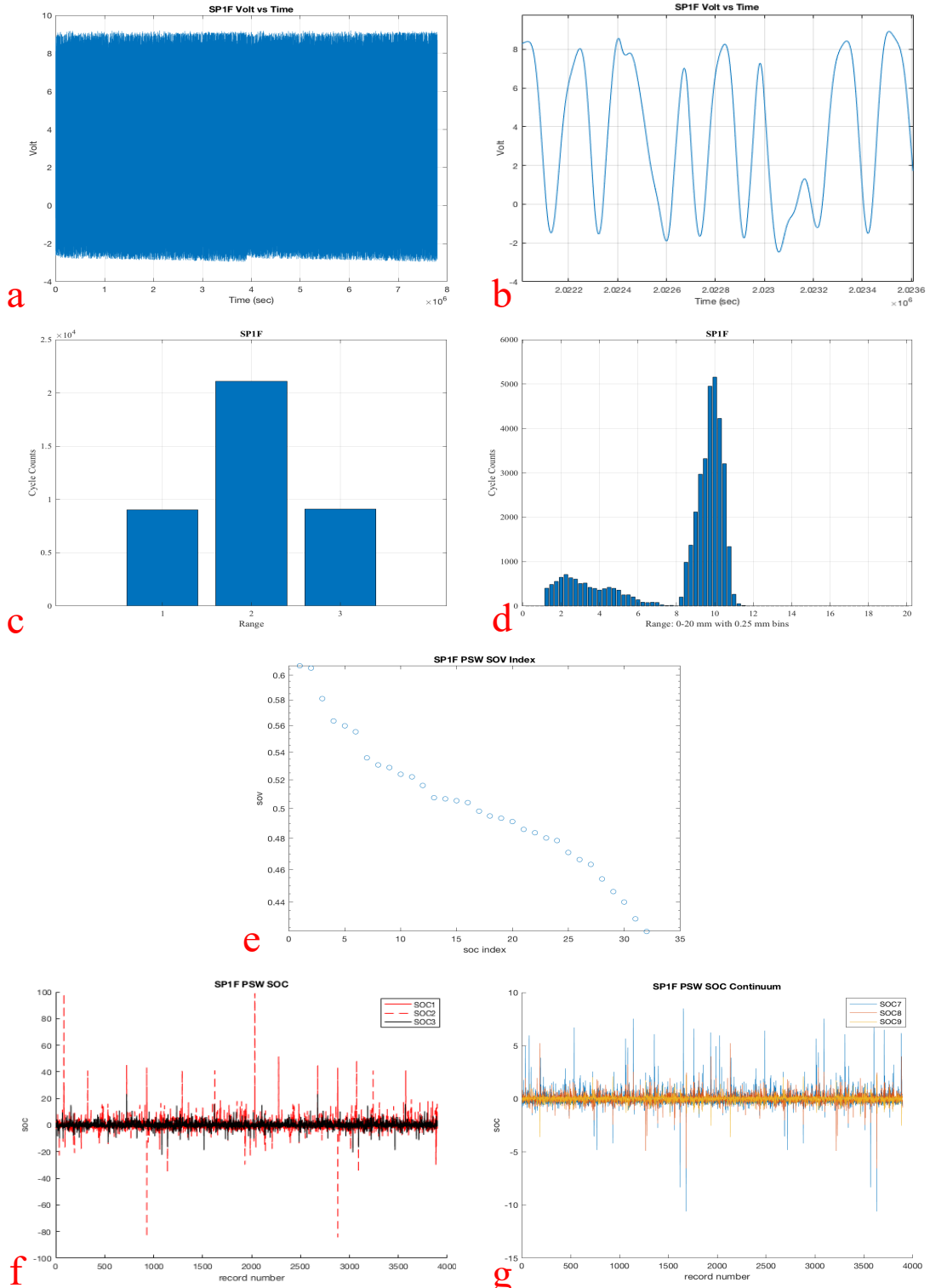


Figure D.3 – Specimen 1F plots. a) voltage vs. time b) zoomed time series c) three bin histogram of cycle count d) 0.25mm bin cycle count histogram e) SOC index f) SOM of eigenvalue g) SOC continuum

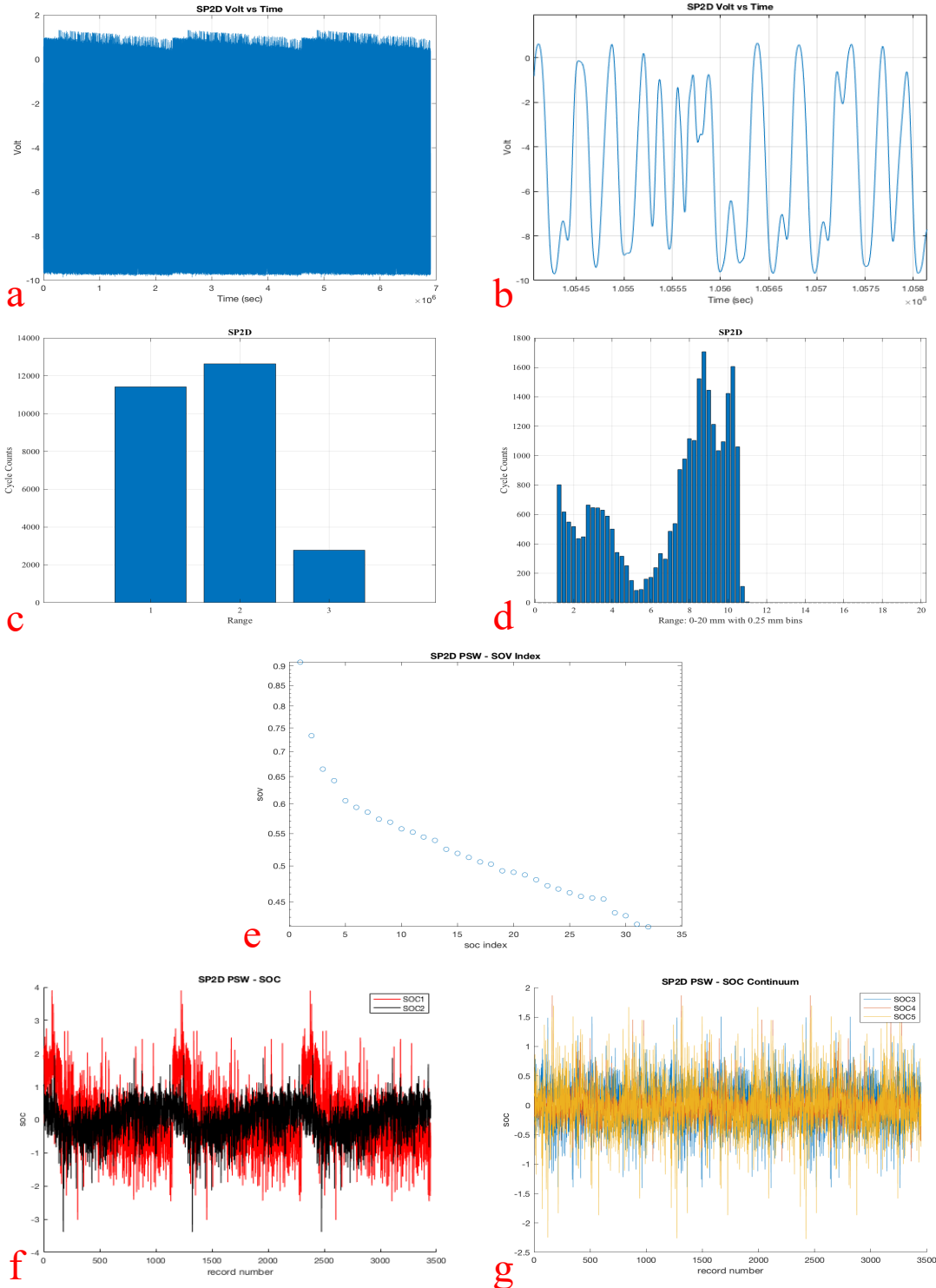


Figure D.4 – Specimen 2D plots. a) voltage vs. time b) zoomed time series c) three bin histogram of cycle count d) 0.25mm bin cycle count histogram e) SOC index f) SOM of eigenvalue g) SOC continuum

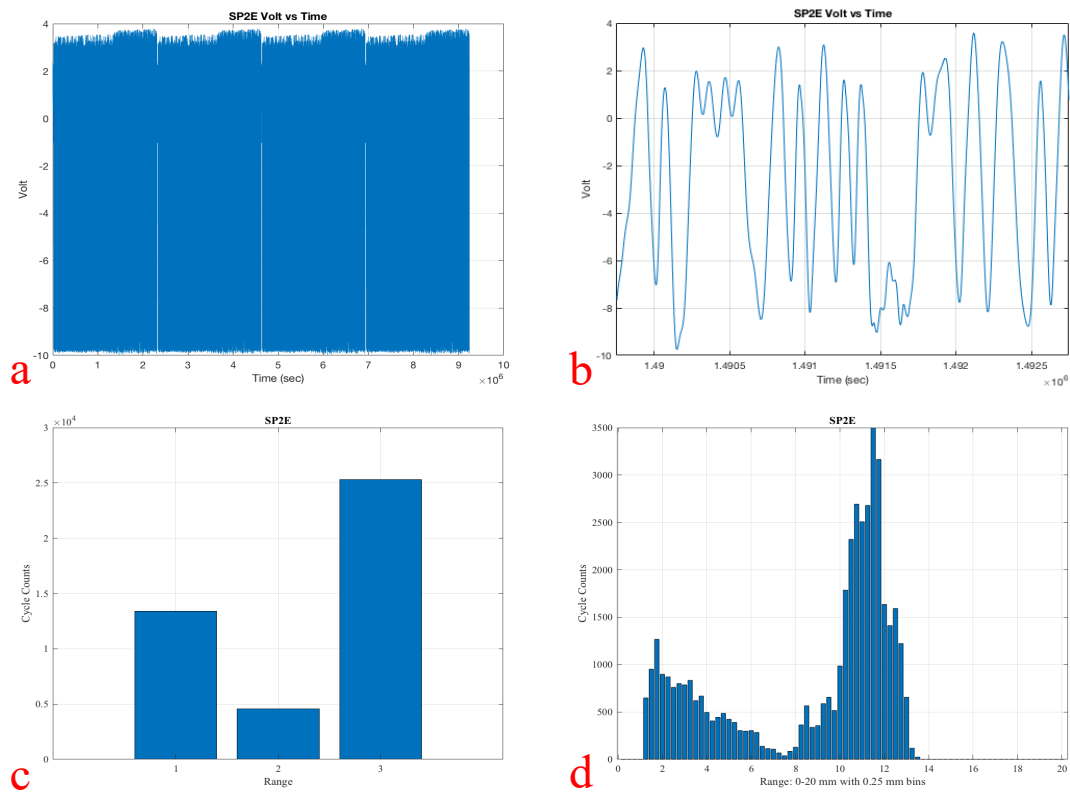


Figure D.5 – Specimen 2E plots. a) voltage vs. time b) zoomed time series c) three bin histogram of cycle count d) 0.25mm bin cycle count histogram. There was no PSW Data.

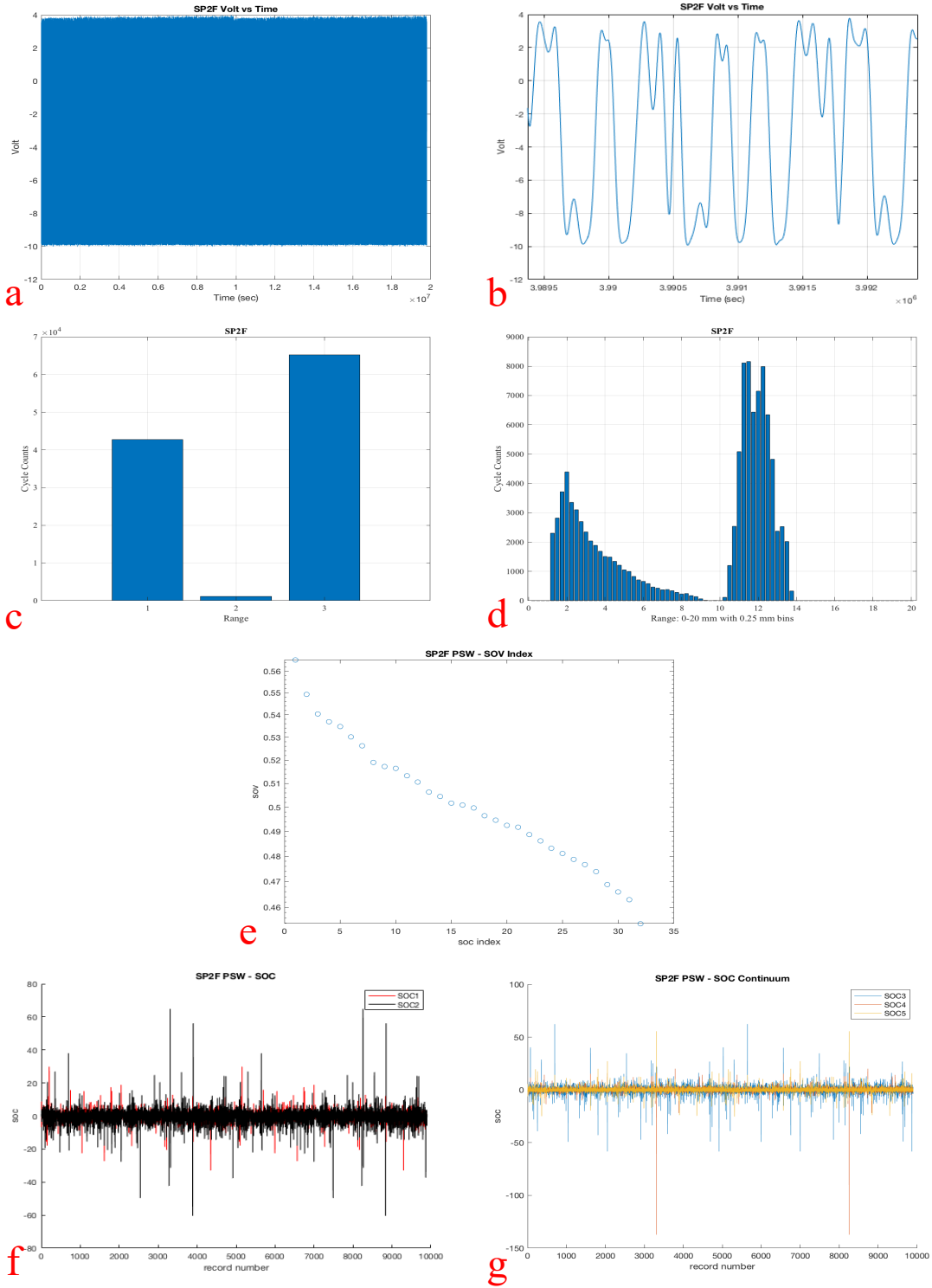


Figure D.6 – Specimen 2F plots. a) voltage vs. time b) zoomed time series c) three bin histogram of cycle count d) 0.25mm bin cycle count histogram e) SOC index f) SOM of eigenvalue g) SOC continuum

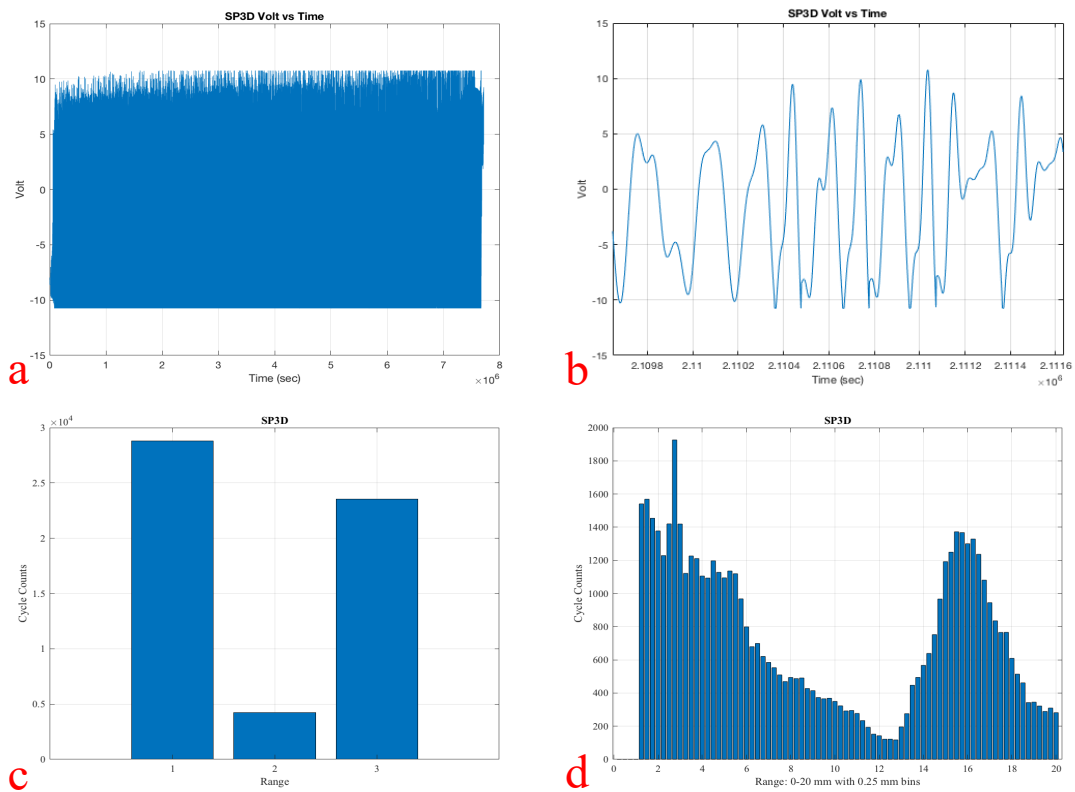


Figure D.7 – Specimen 3D plots. a) voltage vs. time b) zoomed time series c) three bin histogram of cycle count d) 0.25mm bin cycle count histogram. There was no PSW data.

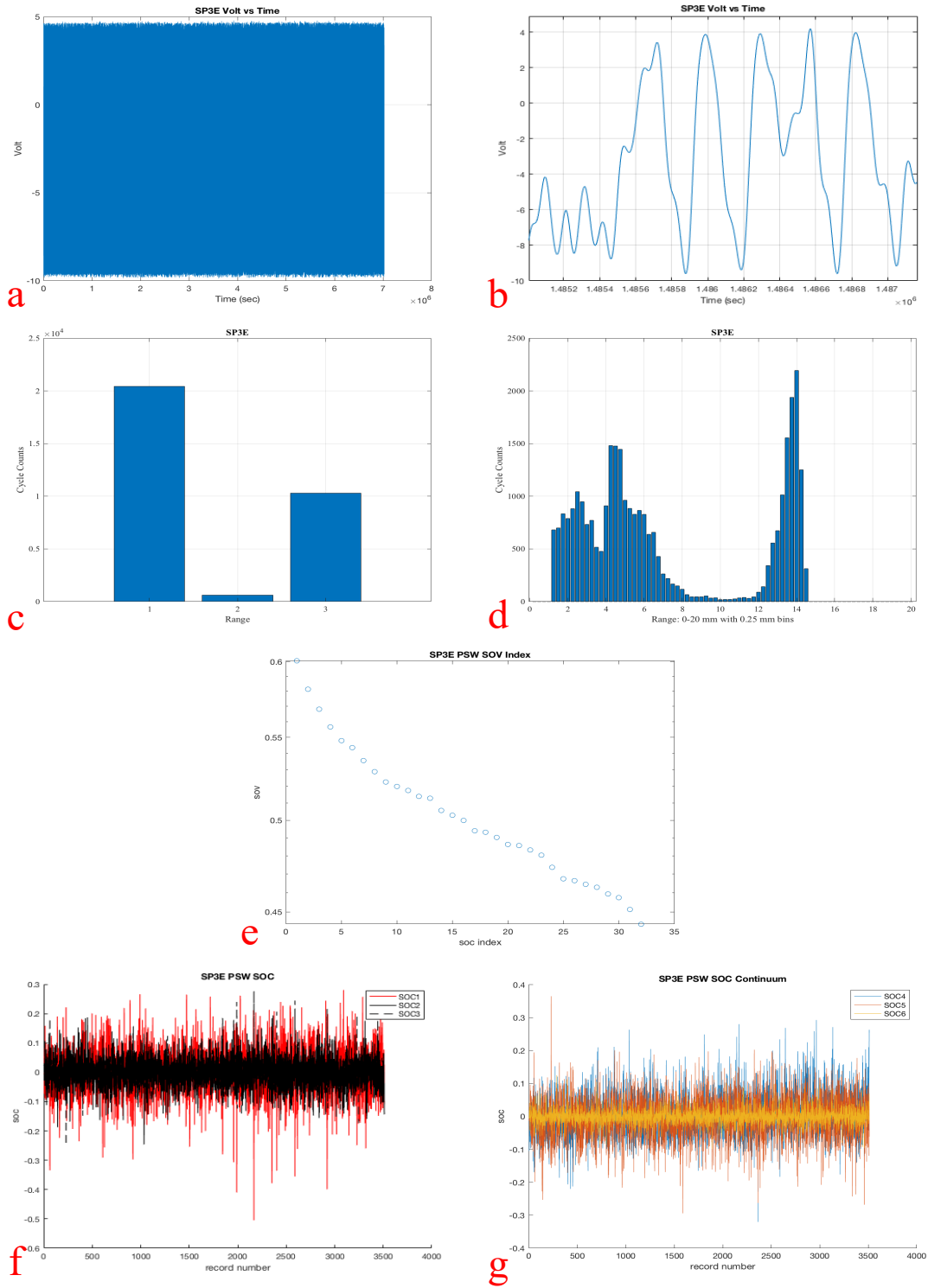
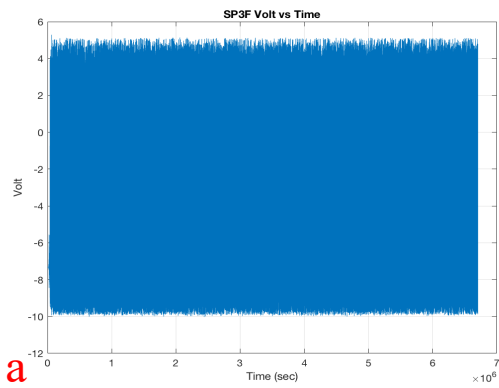
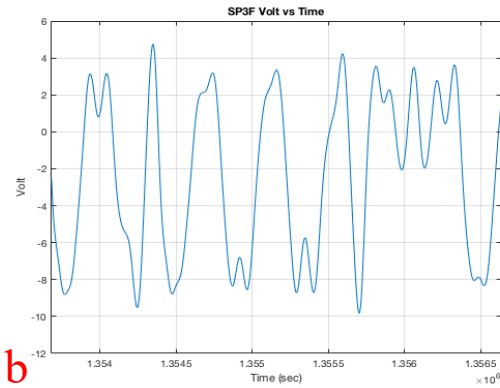


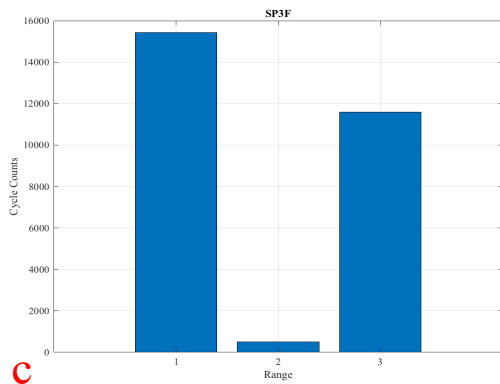
Figure D.8 – Specimen 3E plots. a) voltage vs. time b) zoomed time series c) three bin histogram of cycle count d) 0.25mm bin cycle count histogram e) SOC index f) SOM of eigenvalue g) SOC continuum



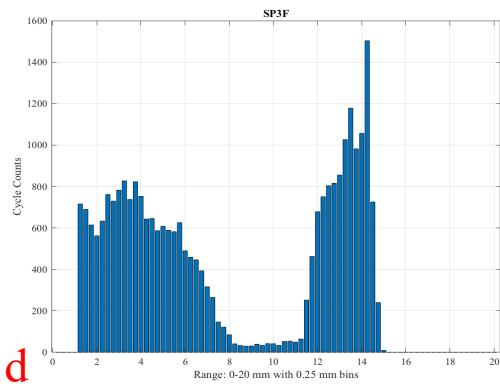
a



b



c



d

Figure D.9 – Specimen 3F plots. a) voltage vs. time b) zoomed time series c) three bin histogram of cycle count d) 0.25mm bin cycle count histogram. There was no PSW data.

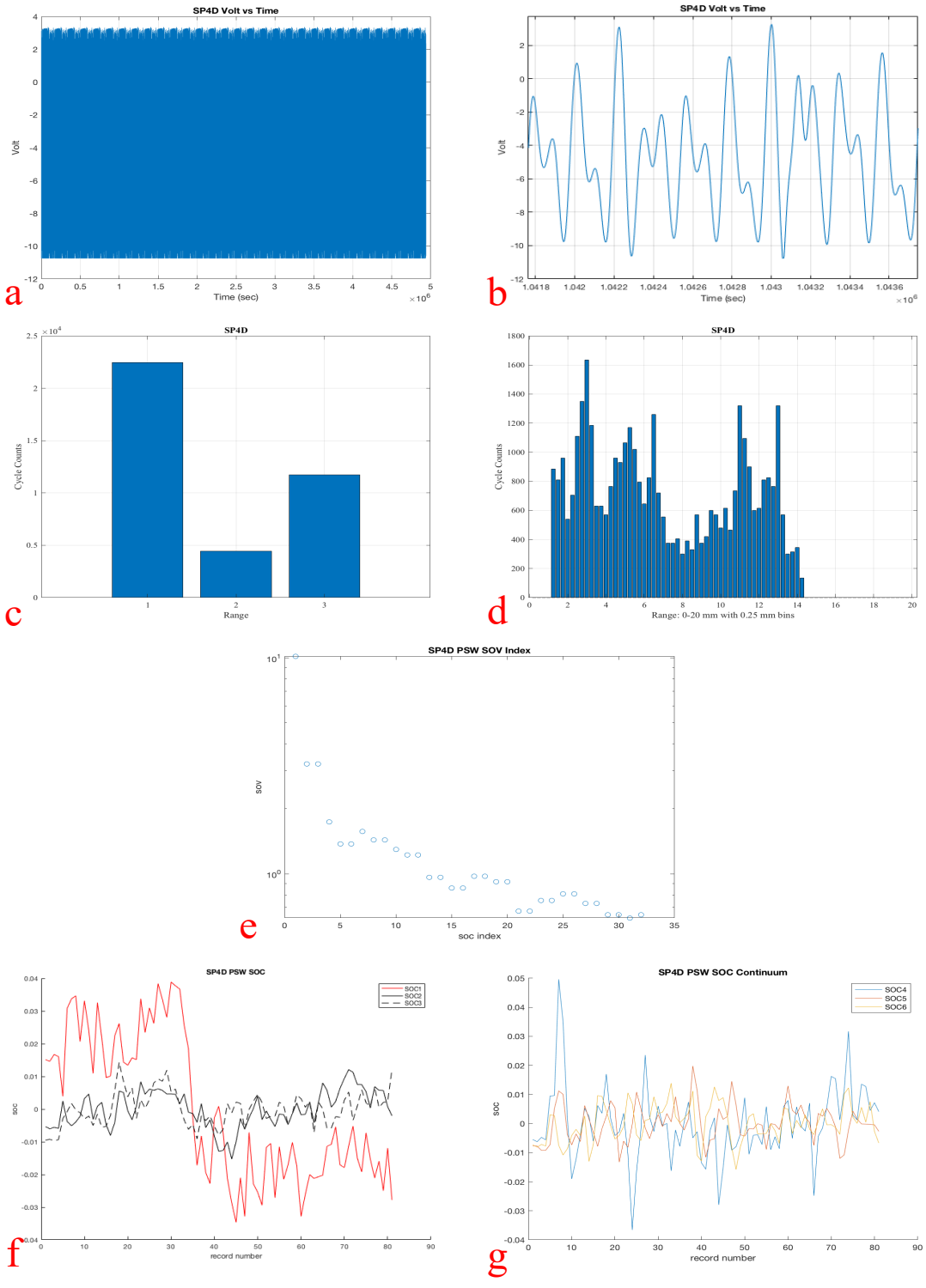


Figure D.10 – Specimen 4D plots. a) voltage vs. time b) zoomed time series c) three bin histogram of cycle count d) 0.25mm bin cycle count histogram e) SOC index f) SOM of eigenvalue g) SOC continuum

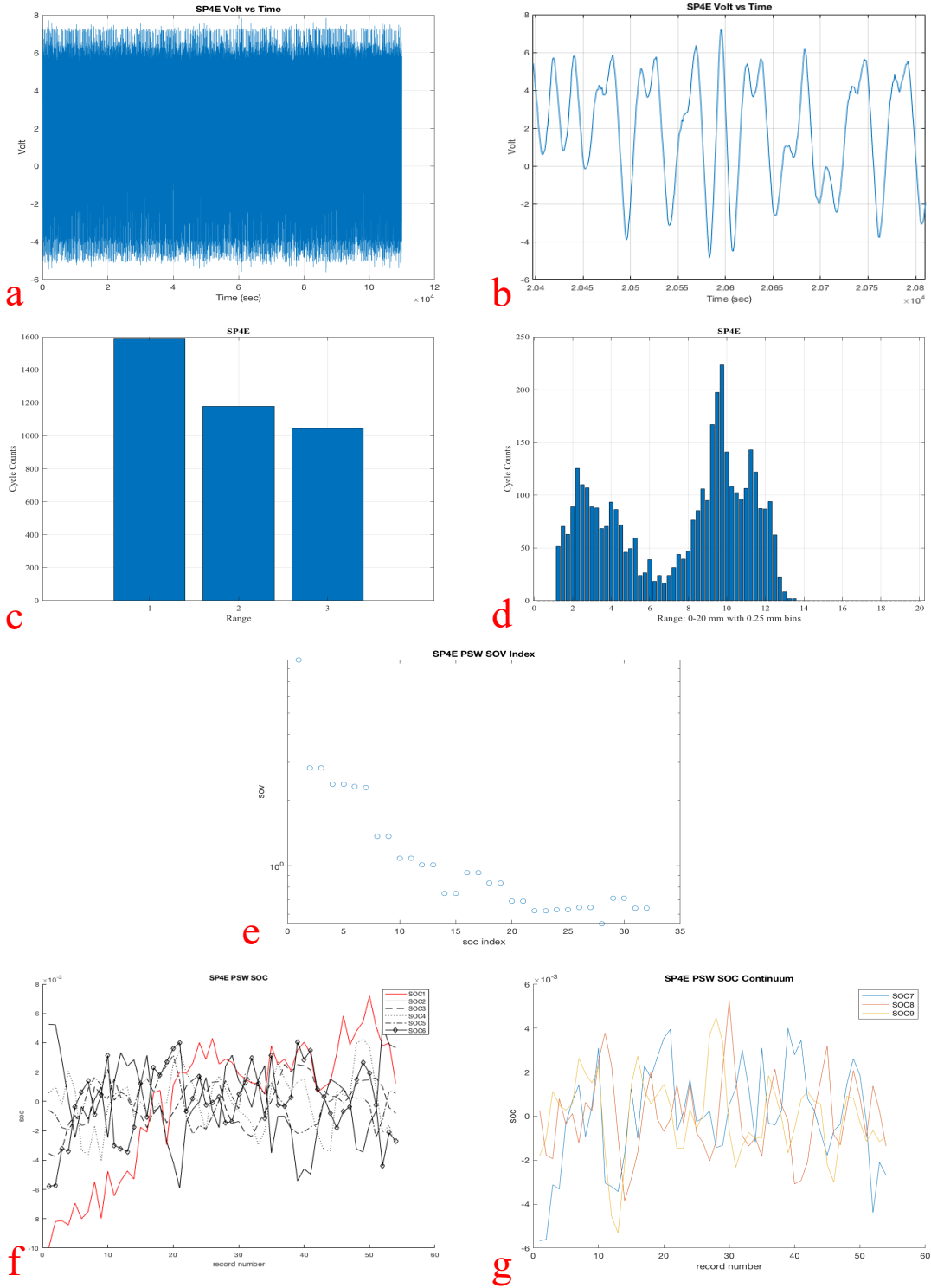


Figure D.11 – Specimen 4E plots. a) voltage vs. time b) zoomed time series c) three bin histogram of cycle count d) 0.25mm bin cycle count histogram e) SOC index f) SOM of eigenvalue g) SOC continuum

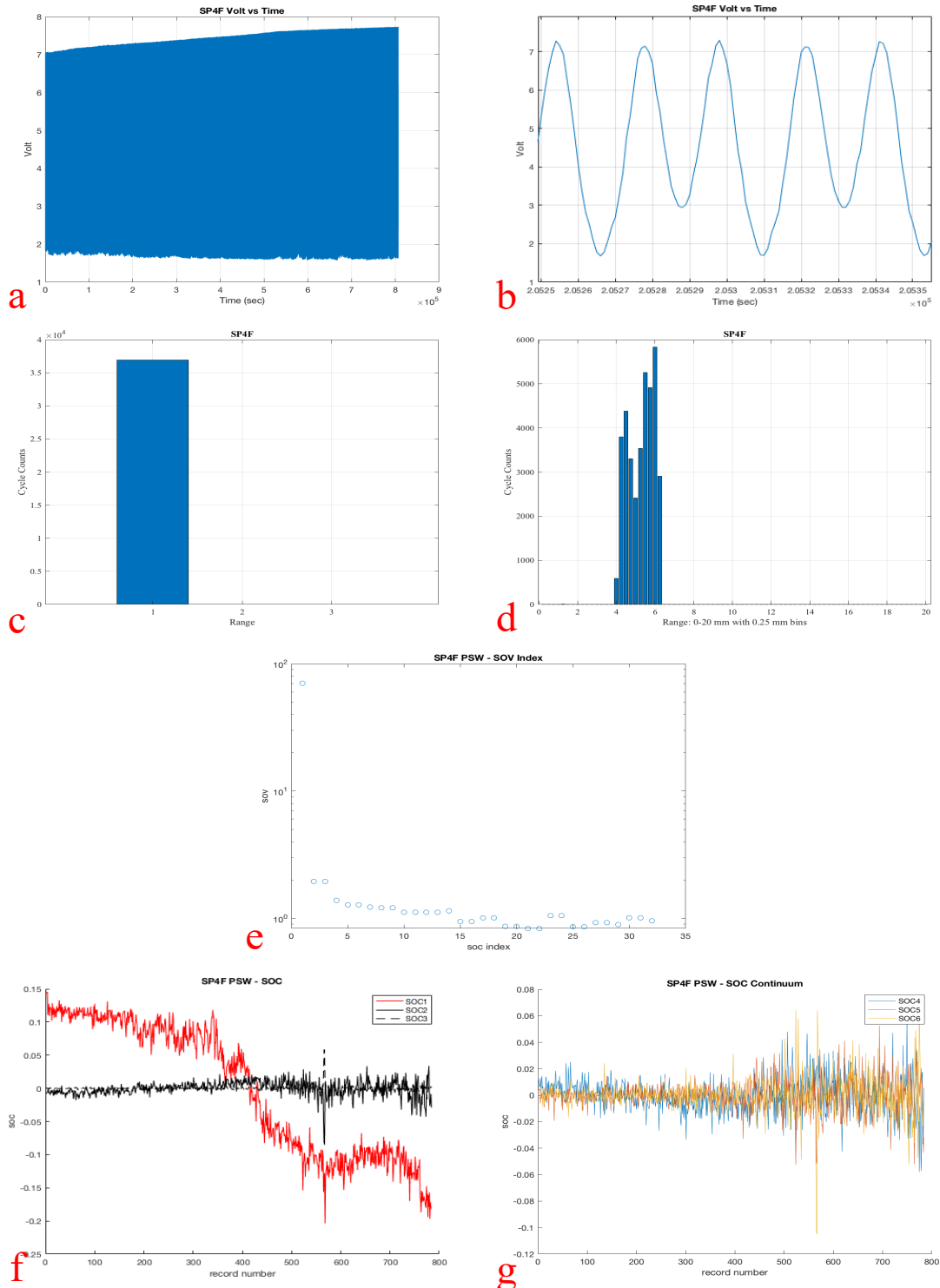


Figure D.12 – Specimen 4F plots. a) voltage vs. time b) zoomed time series c) three bin histogram of cycle count d) 0.25mm bin cycle count histogram e) SOC index f) SOM of eigenvalue g) SOC continuum

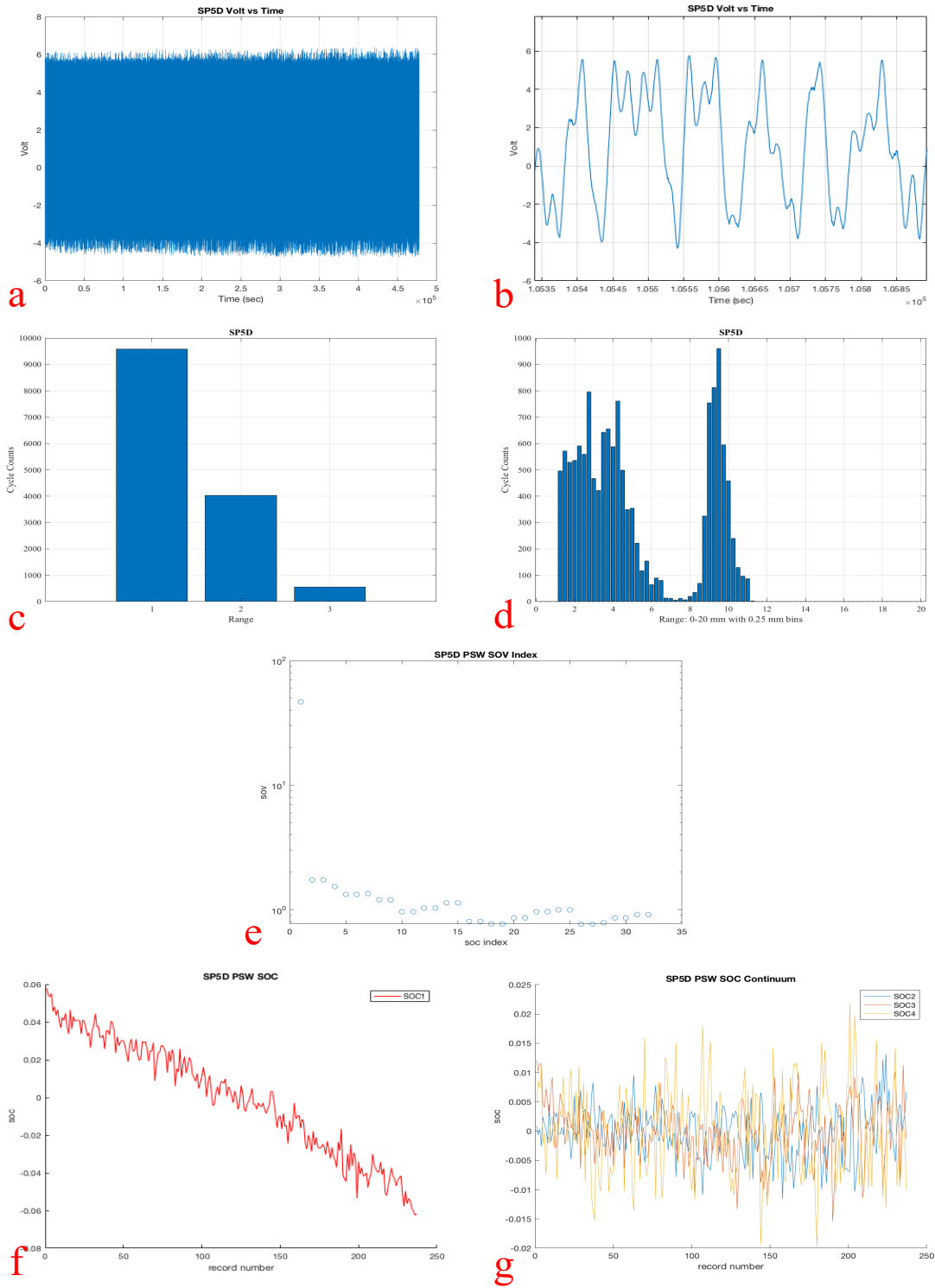


Figure D.13 – Specimen 5D plots. a) voltage vs. time b) zoomed time series c) three bin histogram of cycle count d) 0.25mm bin cycle count histogram e) SOC index f) SOM of eigenvalue g) SOC continuum

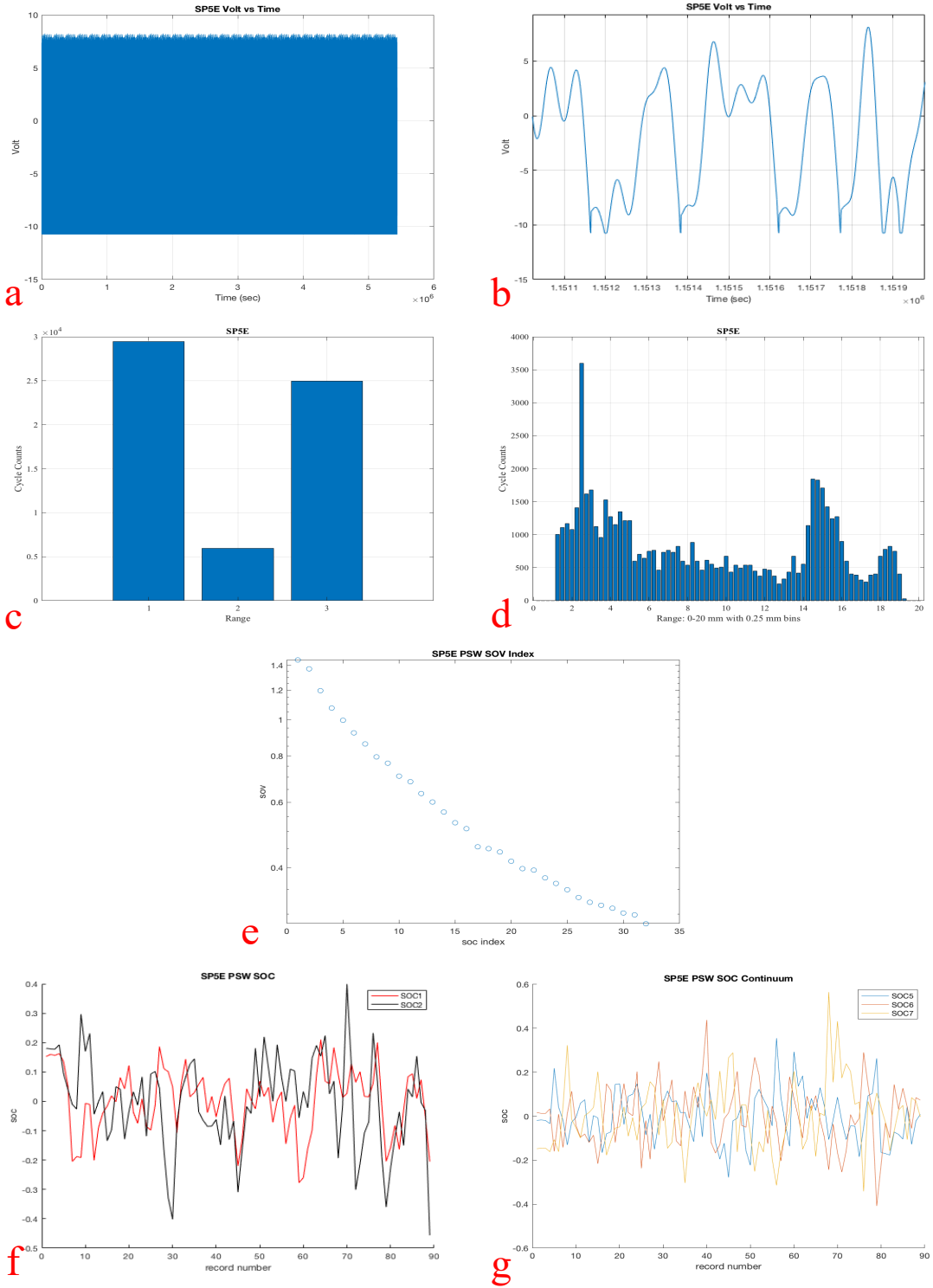


Figure D.14 – Specimen 5E plots. a) voltage vs. time b) zoomed time series c) three bin histogram of cycle count d) 0.25mm bin cycle count histogram e) SOC index f) SOM of eigenvalue g) SOC continuum

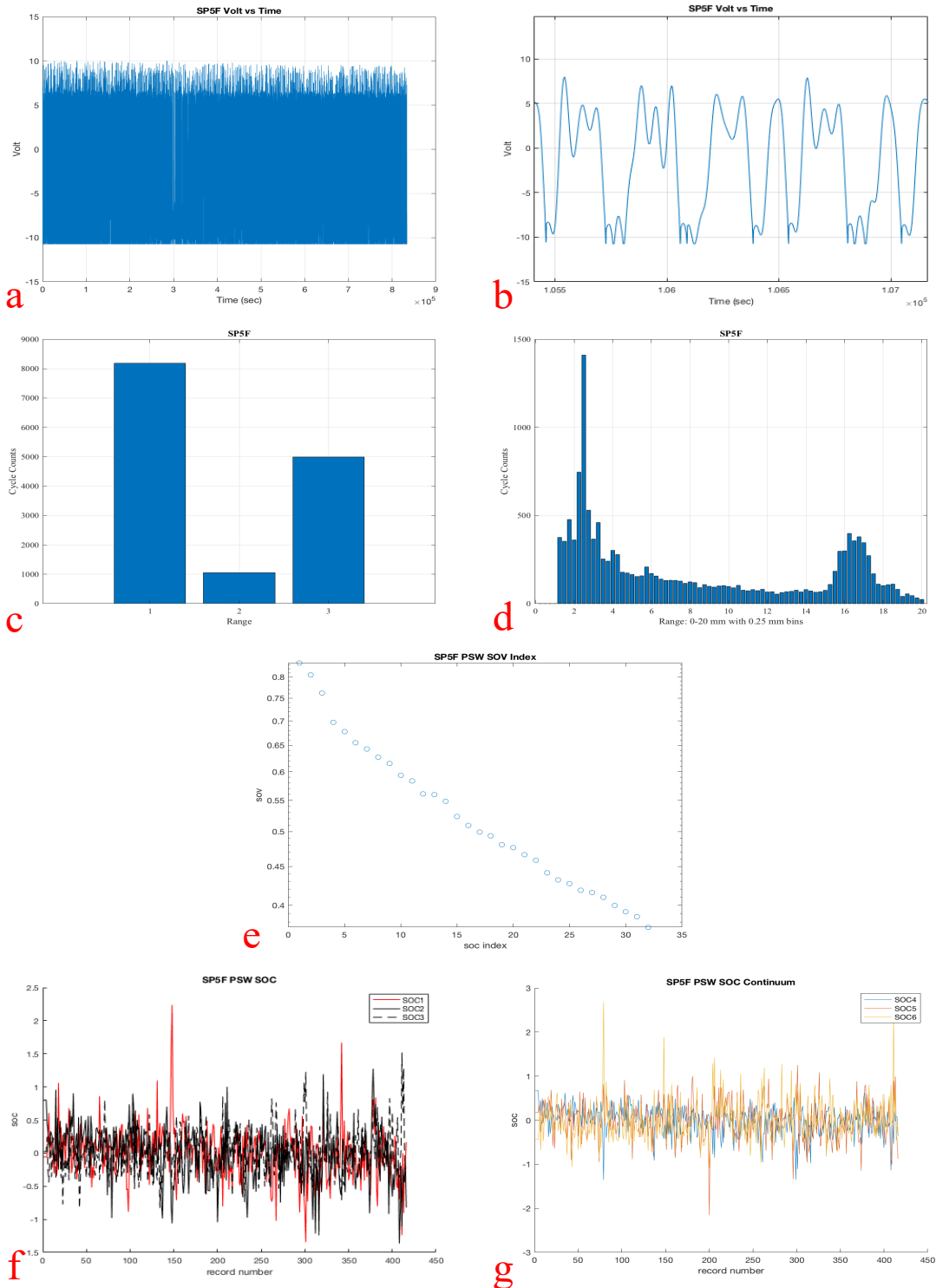


Figure D.15 – Specimen 5F plots. a) voltage vs. time b) zoomed time series c) three bin histogram of cycle count d) 0.25mm bin cycle count histogram e) SOC index f) SOM of eigenvalue g) SOC continuum

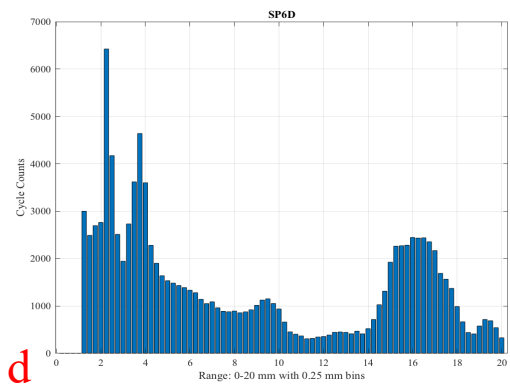
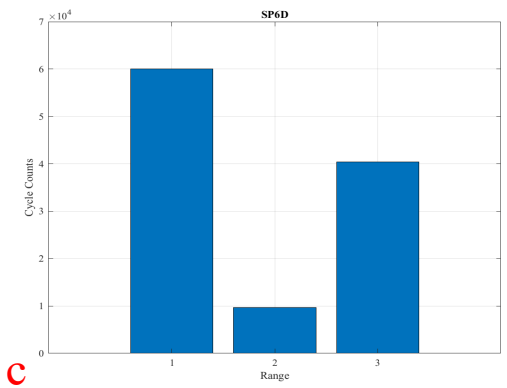
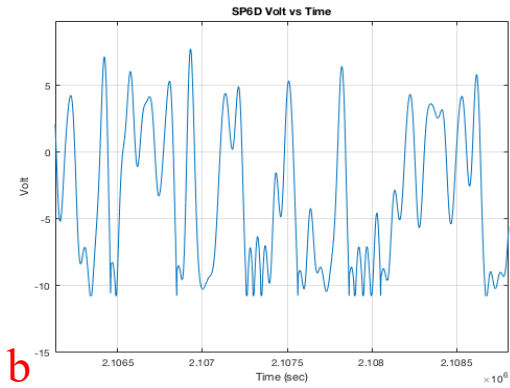
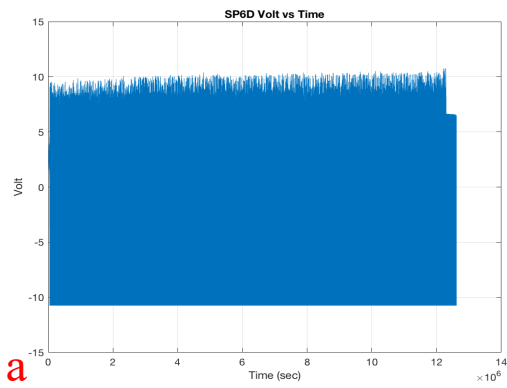


Figure D.16 – Specimen 6D plots. a) voltage vs. time b) zoomed time series c) three bin histogram of cycle count d) 0.25mm bin cycle count histogram. There was no PSW data.

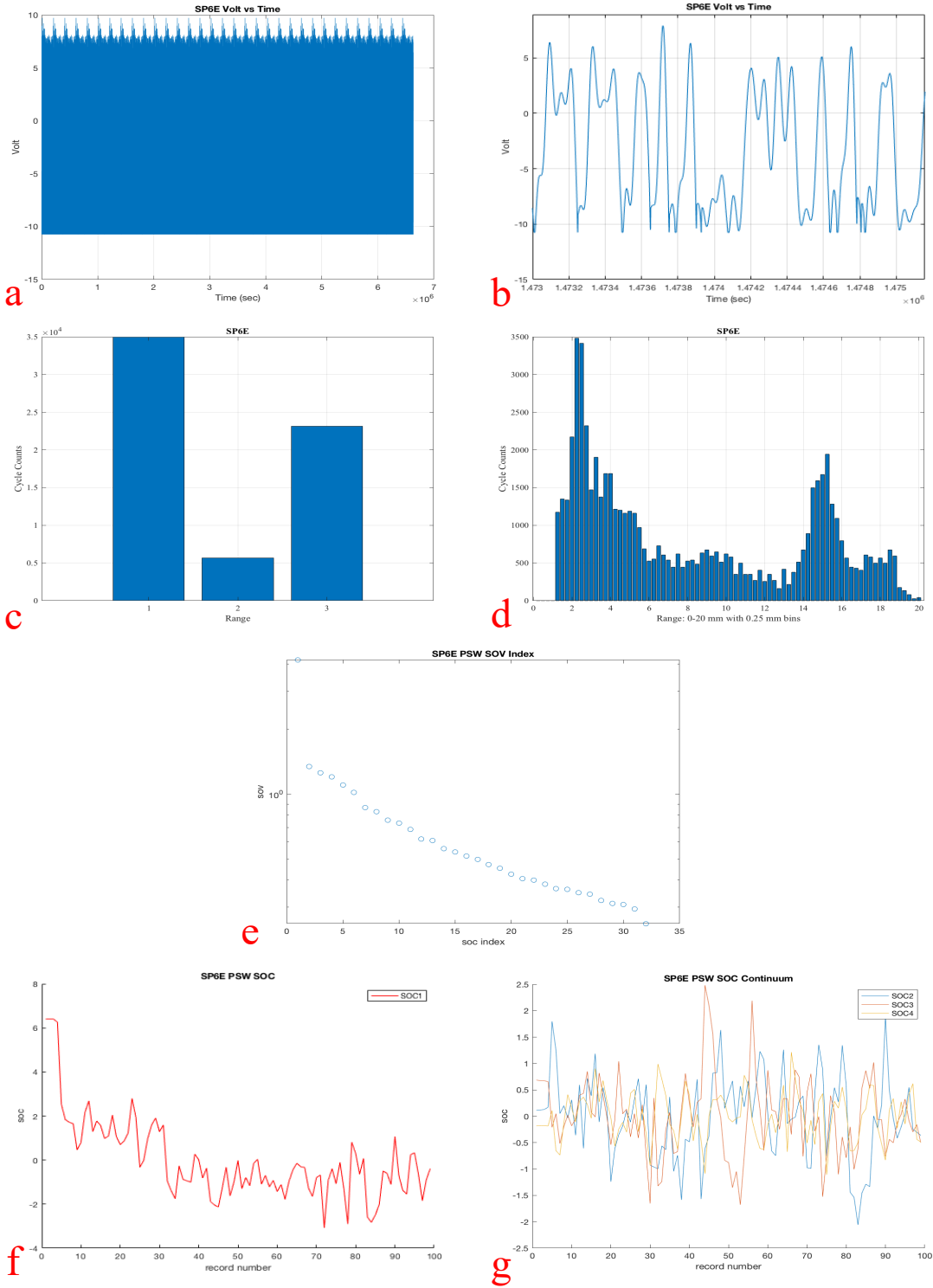


Figure D.17 – Specimen 6E plots. a) voltage vs. time b) zoomed time series c) three bin histogram of cycle count d) 0.25mm bin cycle count histogram e) SOC index f) SOM of eigenvalue g) SOC continuum

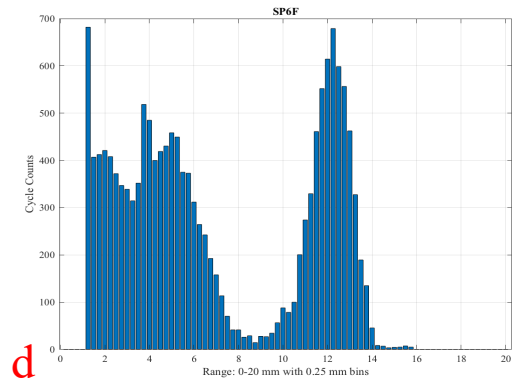
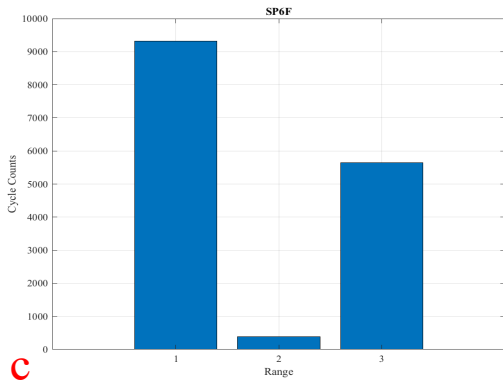
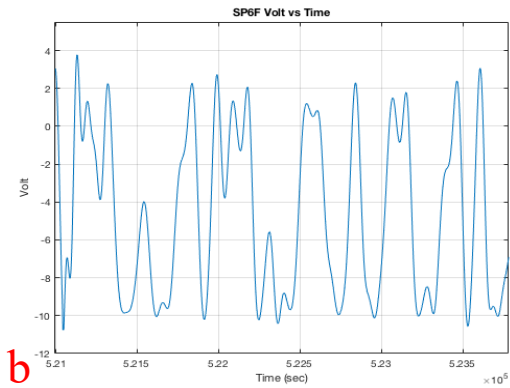
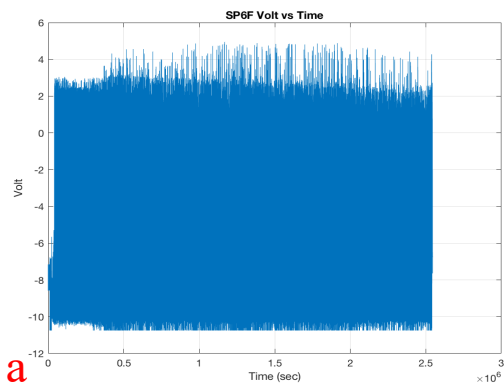


Figure D.18 – Specimen 6F plots. a) voltage vs. time b) zoomed time series c) three bin histogram of cycle count d) 0.25mm bin cycle count histogram. There was no PSW data.

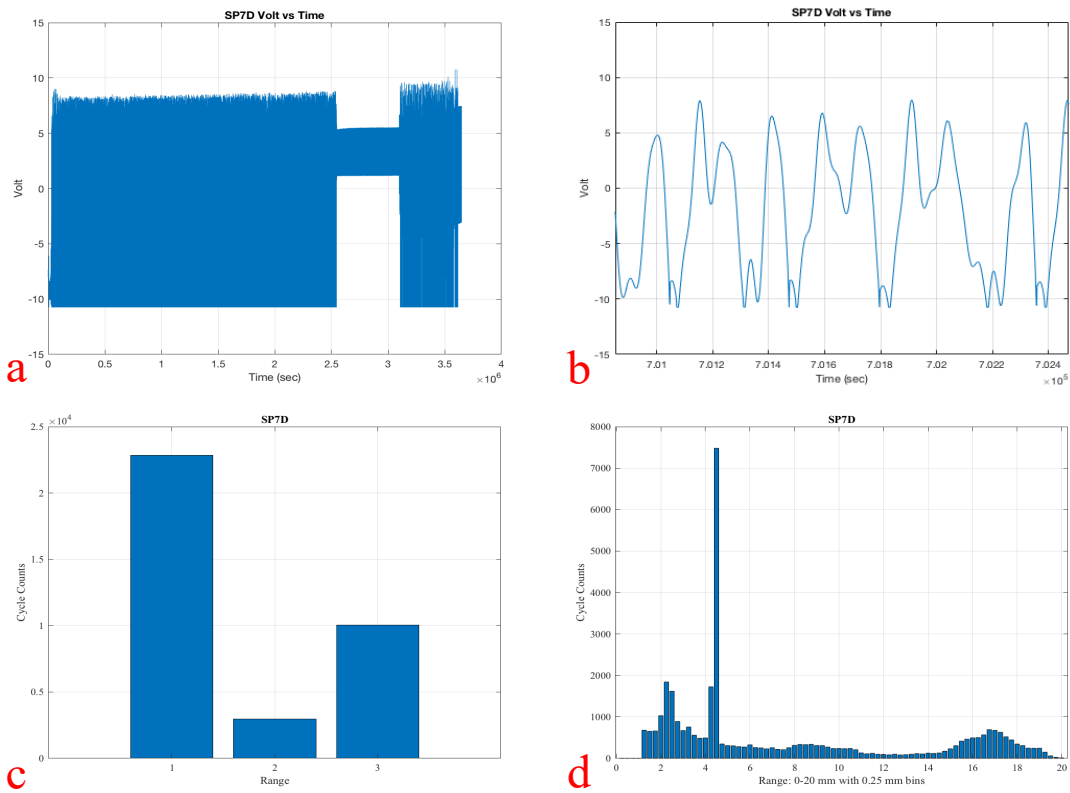


Figure D.19 – Specimen 7D plots. a) voltage vs. time b) zoomed time series c) three bin histogram of cycle count d) 0.25mm bin cycle count histogram. There was no PSW data.

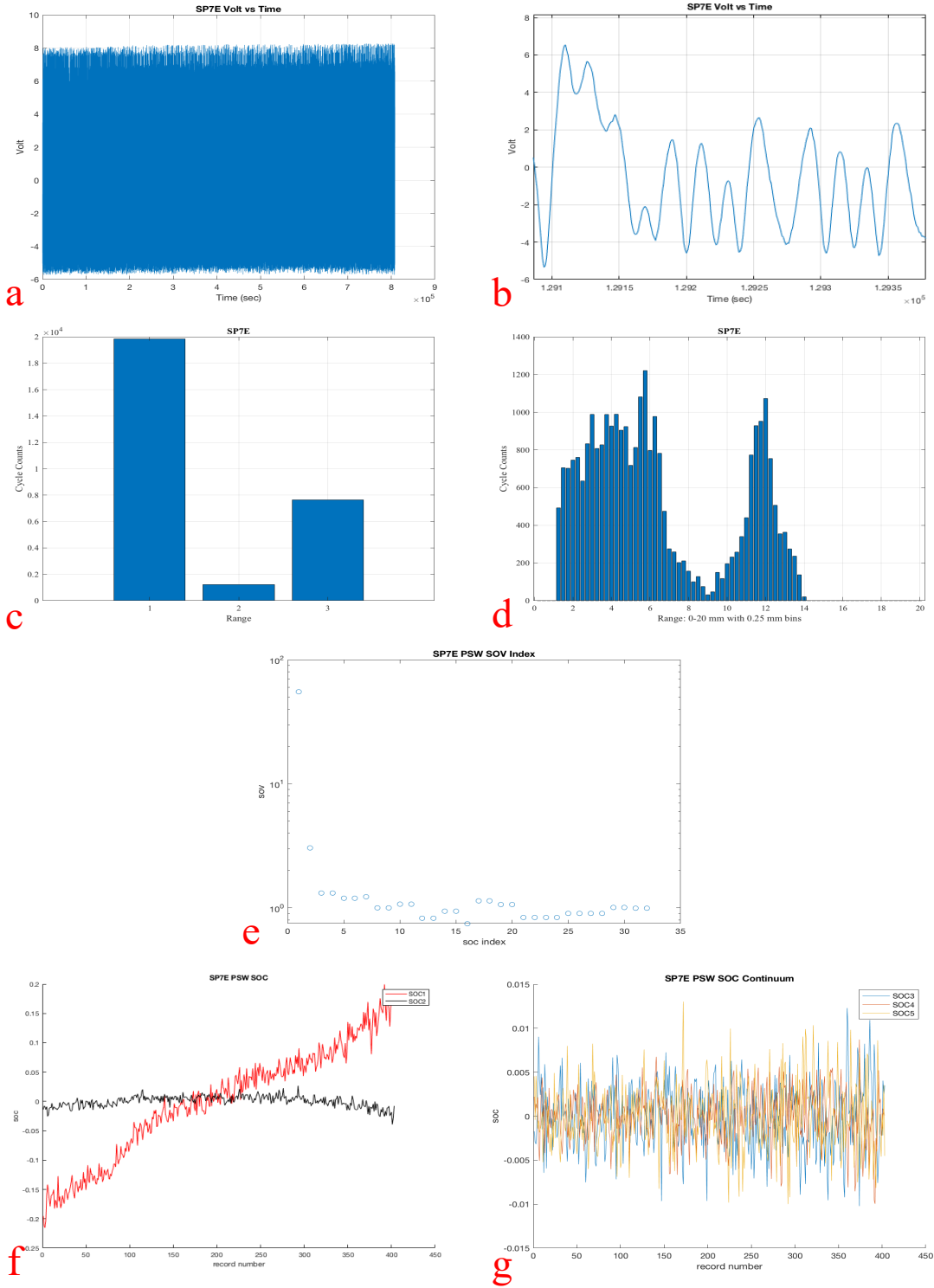


Figure D.20 – Specimen 7E plots. a) voltage vs. time b) zoomed time series c) three bin histogram of cycle count d) 0.25mm bin cycle count histogram e) SOC index f) SOM of eigenvalue g) SOC continuum

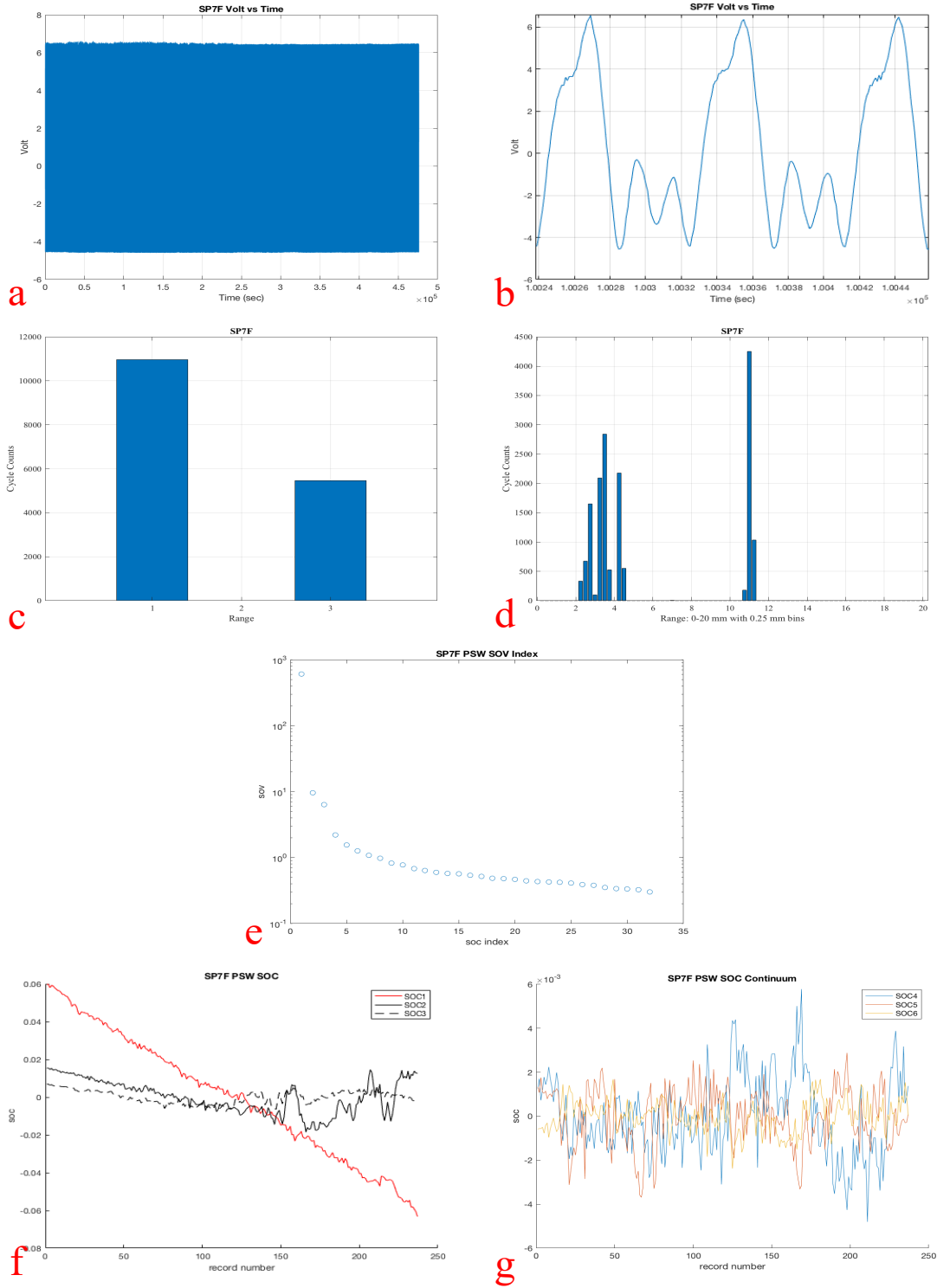


Figure D.21 – Specimen 7F plots. a) voltage vs. time b) zoomed time series c) three bin histogram of cycle count d) 0.25mm bin cycle count histogram e) SOC index f) SOM of eigenvalue g) SOC continuum

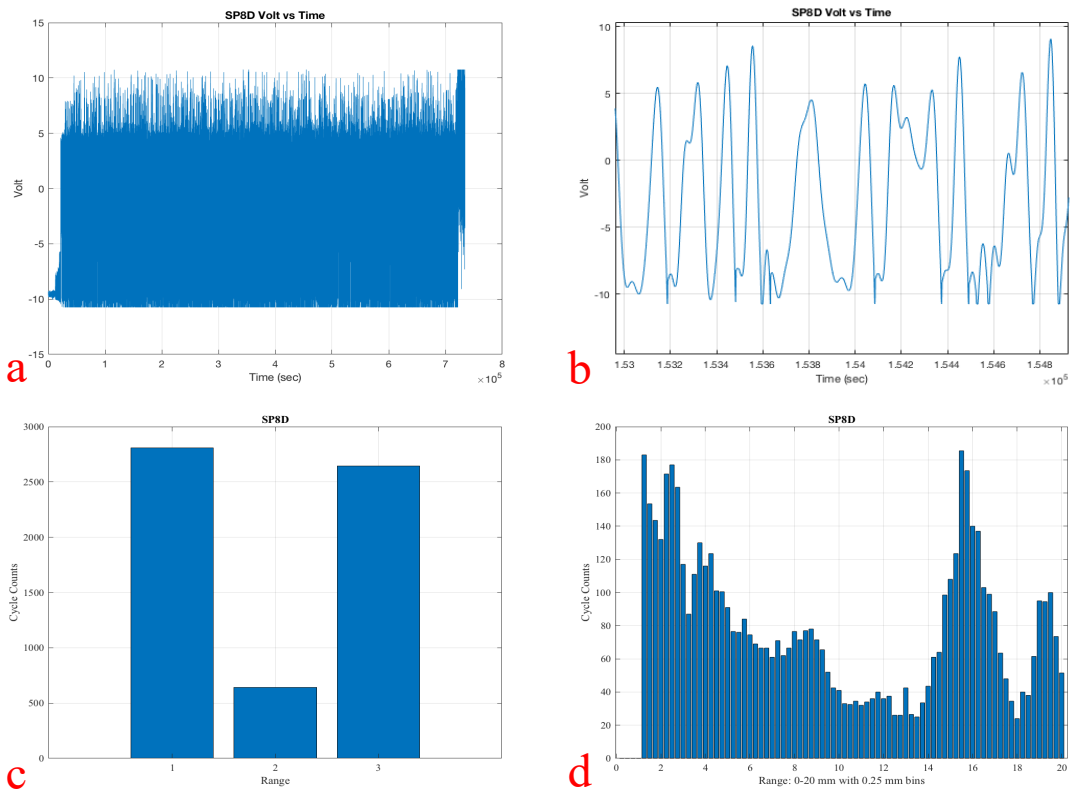


Figure D.22 – Specimen 8D plots. a) voltage vs. time b) zoomed time series c) three bin histogram of cycle count d) 0.25mm bin cycle count histogram. There was no PSW data.

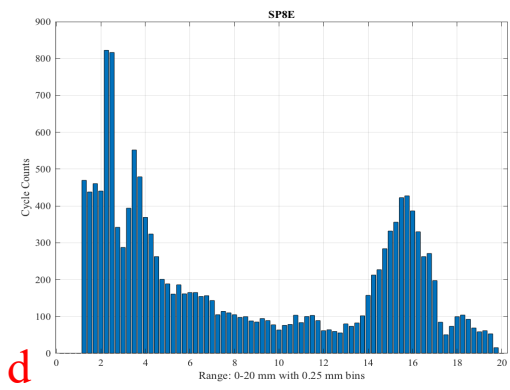
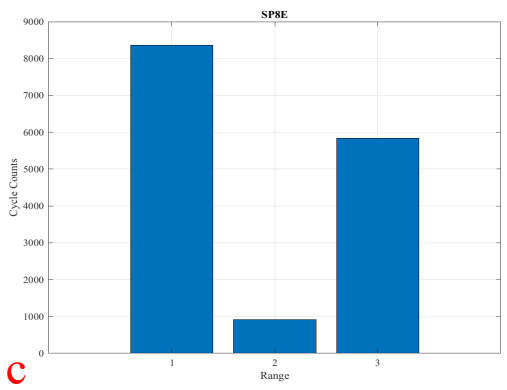
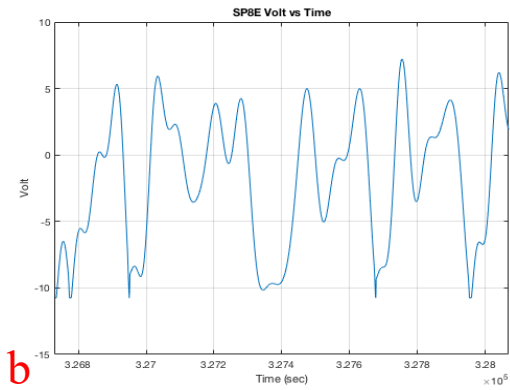
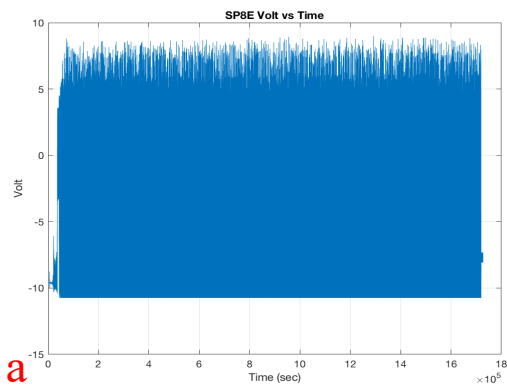


Figure D.23 – Specimen 8E plots. a) voltage vs. time b) zoomed time series c) three bin histogram of cycle count d) 0.25mm bin cycle count histogram. There was no PSW data.

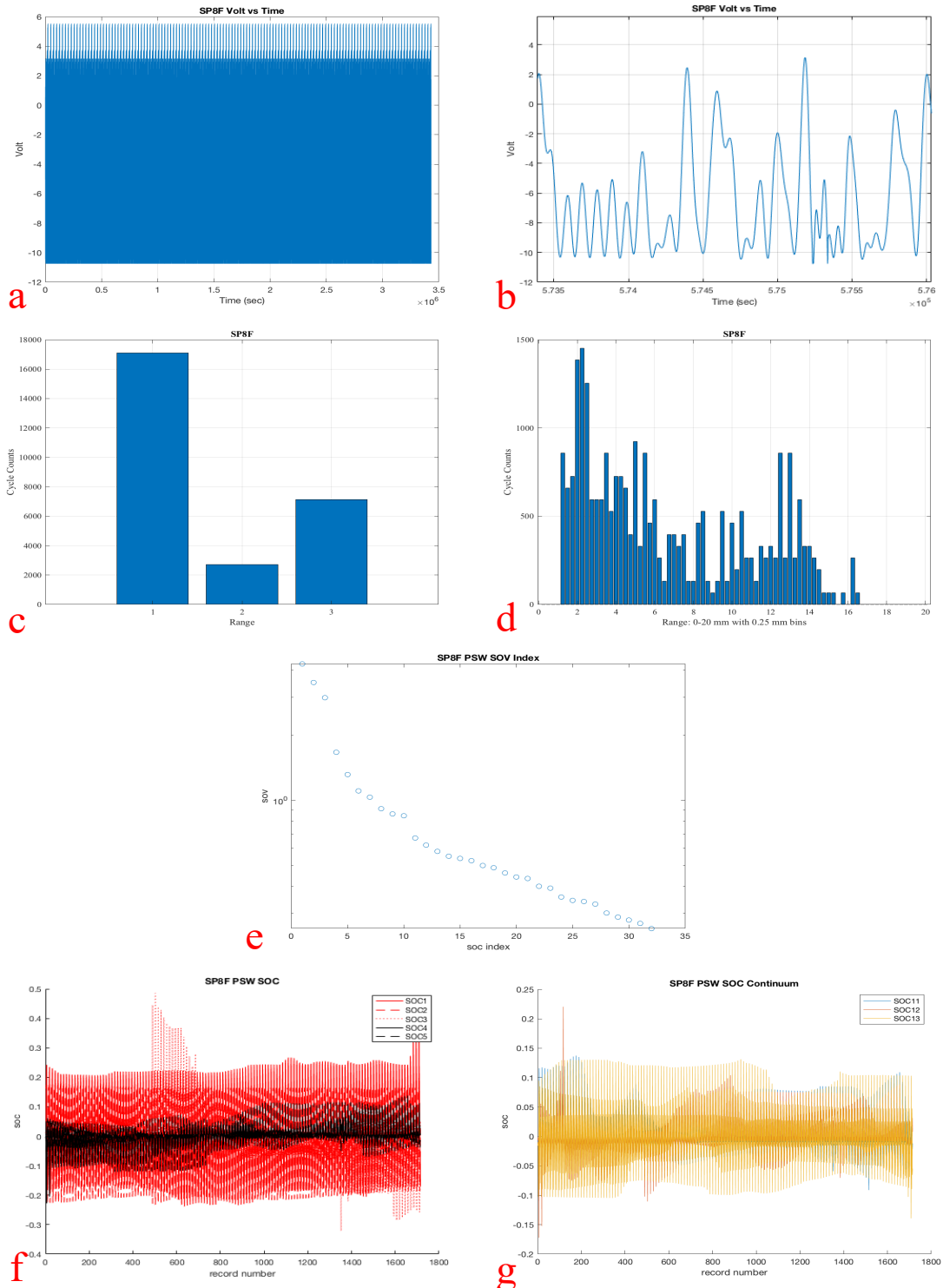
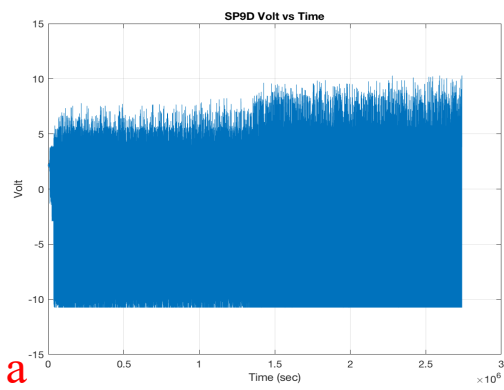
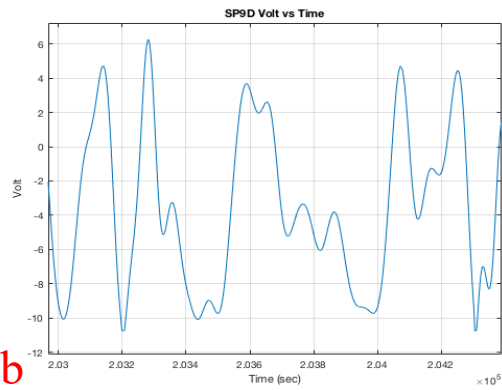


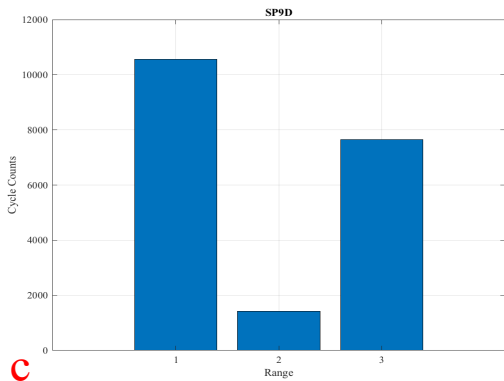
Figure D.24 – Specimen 8F plots. a) voltage vs. time b) zoomed time series c) three bin histogram of cycle count d) 0.25mm bin cycle count histogram e) SOC index f) SOM of eigenvalue g) SOC continuum



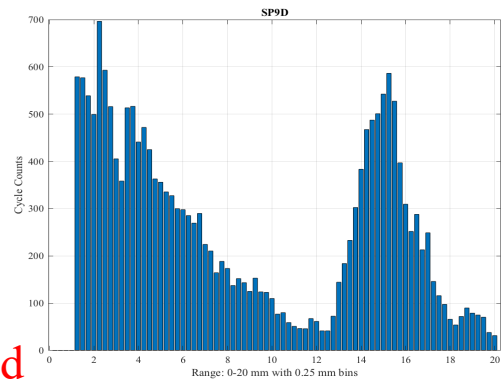
a



b



c



d

Figure D.25 – Specimen 9D plots. a) voltage vs. time b) zoomed time series c) three bin histogram of cycle count d) 0.25mm bin cycle count histogram. There was no PSW data.

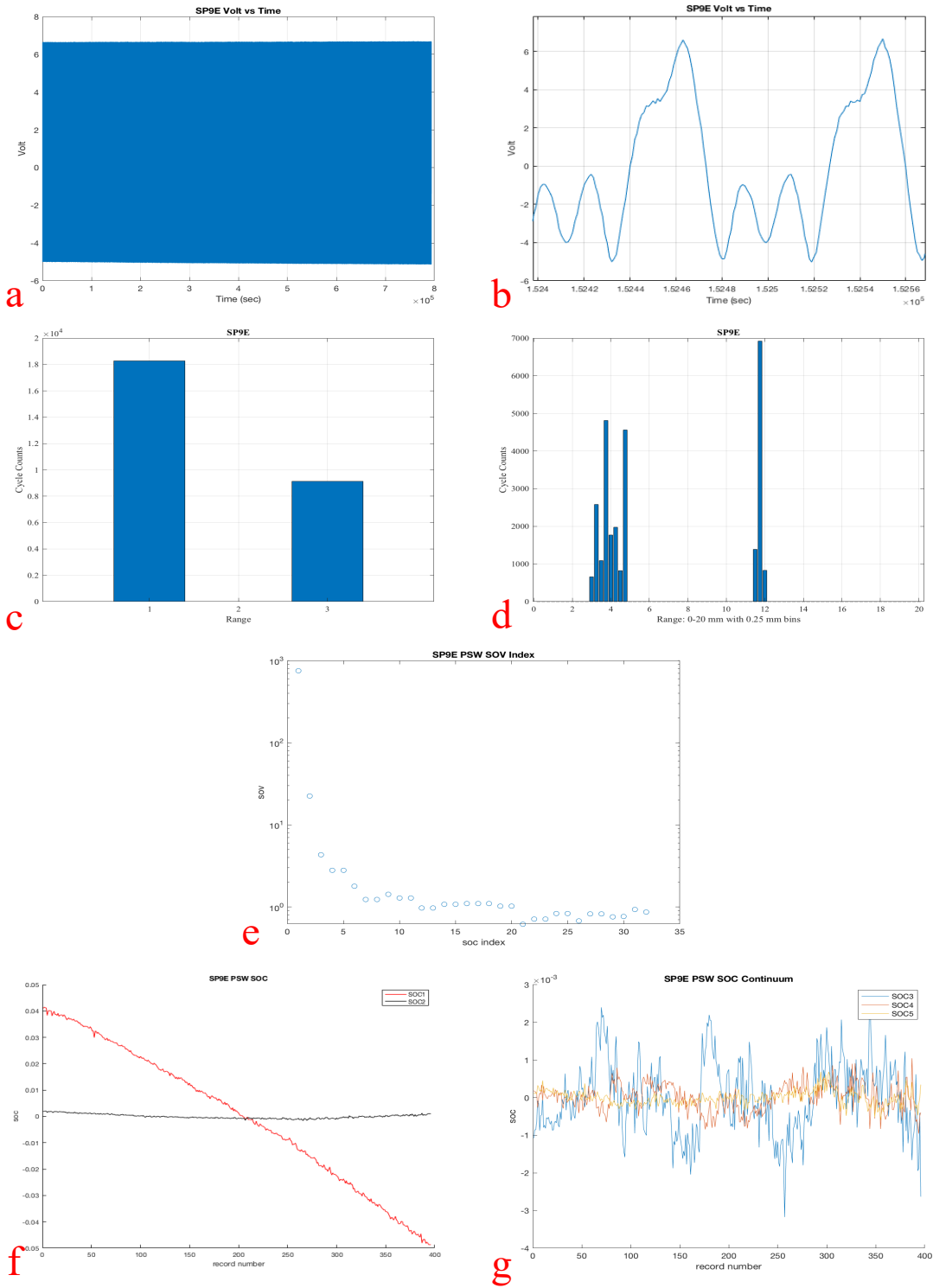


Figure D.26 – Specimen 9E plots. a) voltage vs. time b) zoomed time series c) three bin histogram of cycle count d) 0.25mm bin cycle count histogram e) SOC index f) SOM of eigenvalue g) SOC continuum

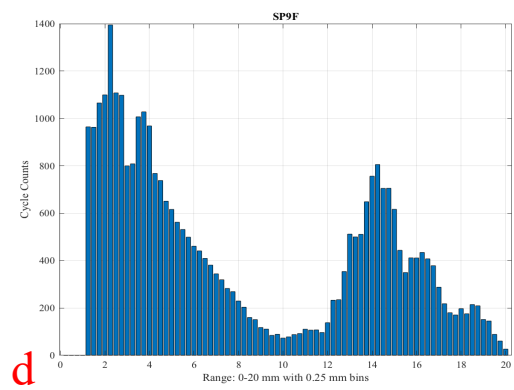
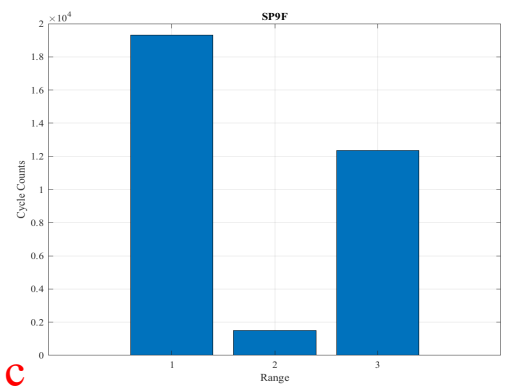
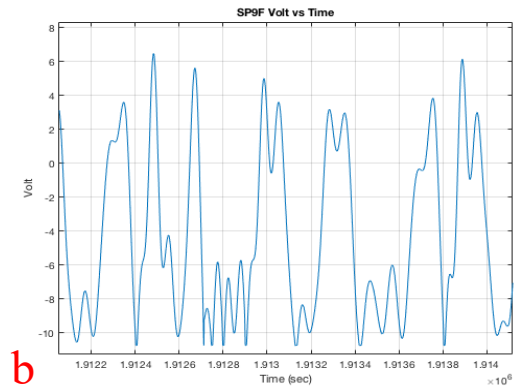
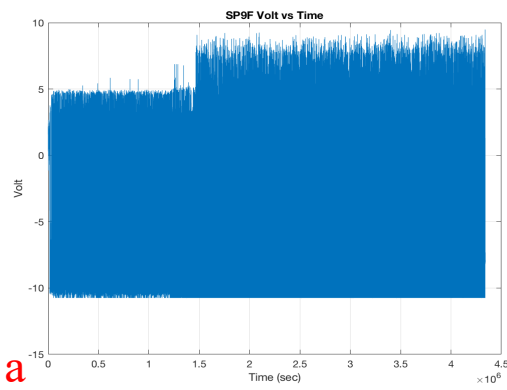


Figure D.27 – Specimen 9F plots. a) voltage vs. time b) zoomed time series c) three bin histogram of cycle count d) 0.25mm bin cycle count histogram. There was no PSW data.

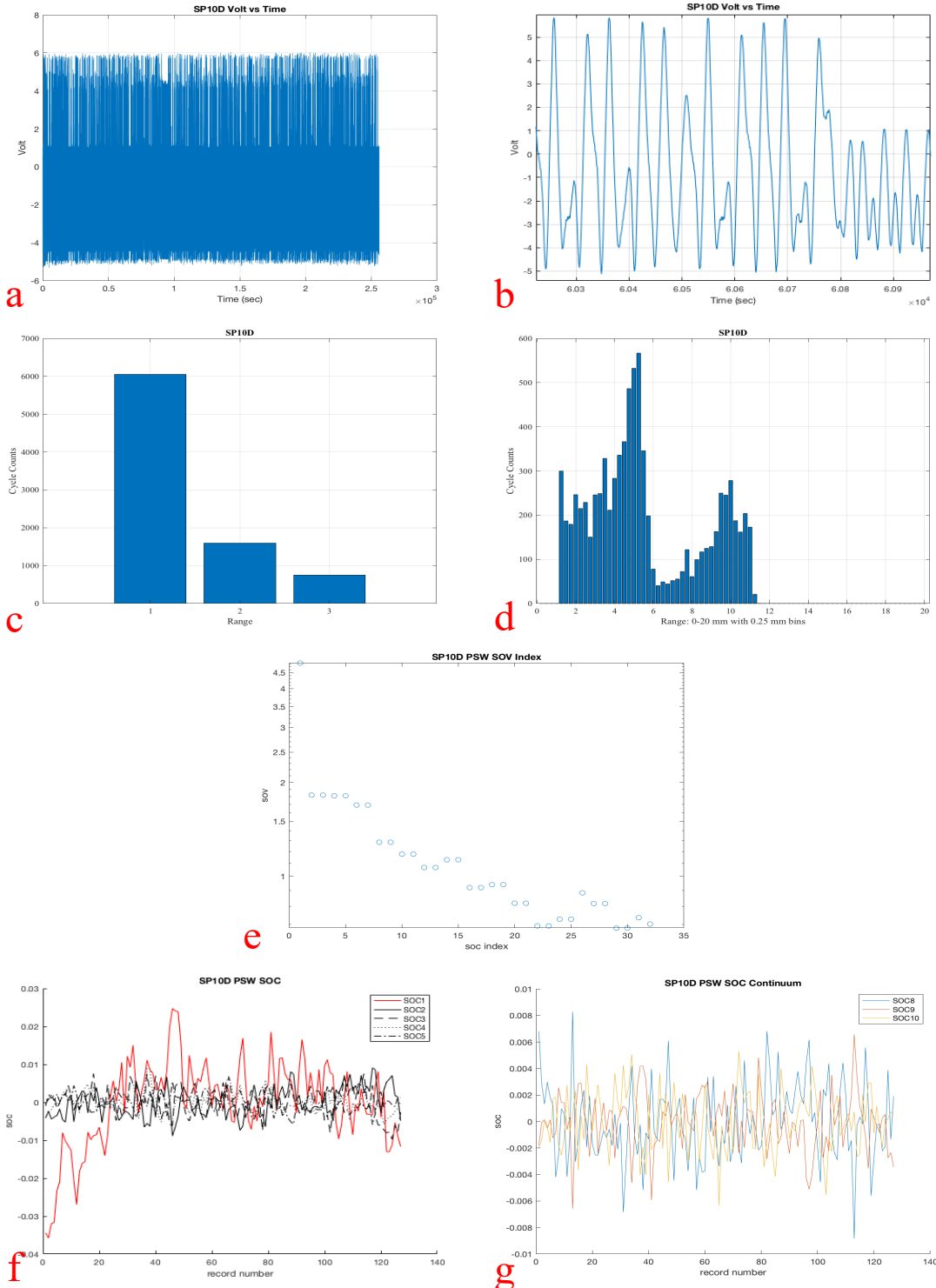


Figure D.28 – Specimen 10D plots. a) voltage vs. time b) zoomed time series c) three bin histogram of cycle count d) 0.25mm bin cycle count histogram e) SOC index f) SOM of eigenvalue g) SOC continuum

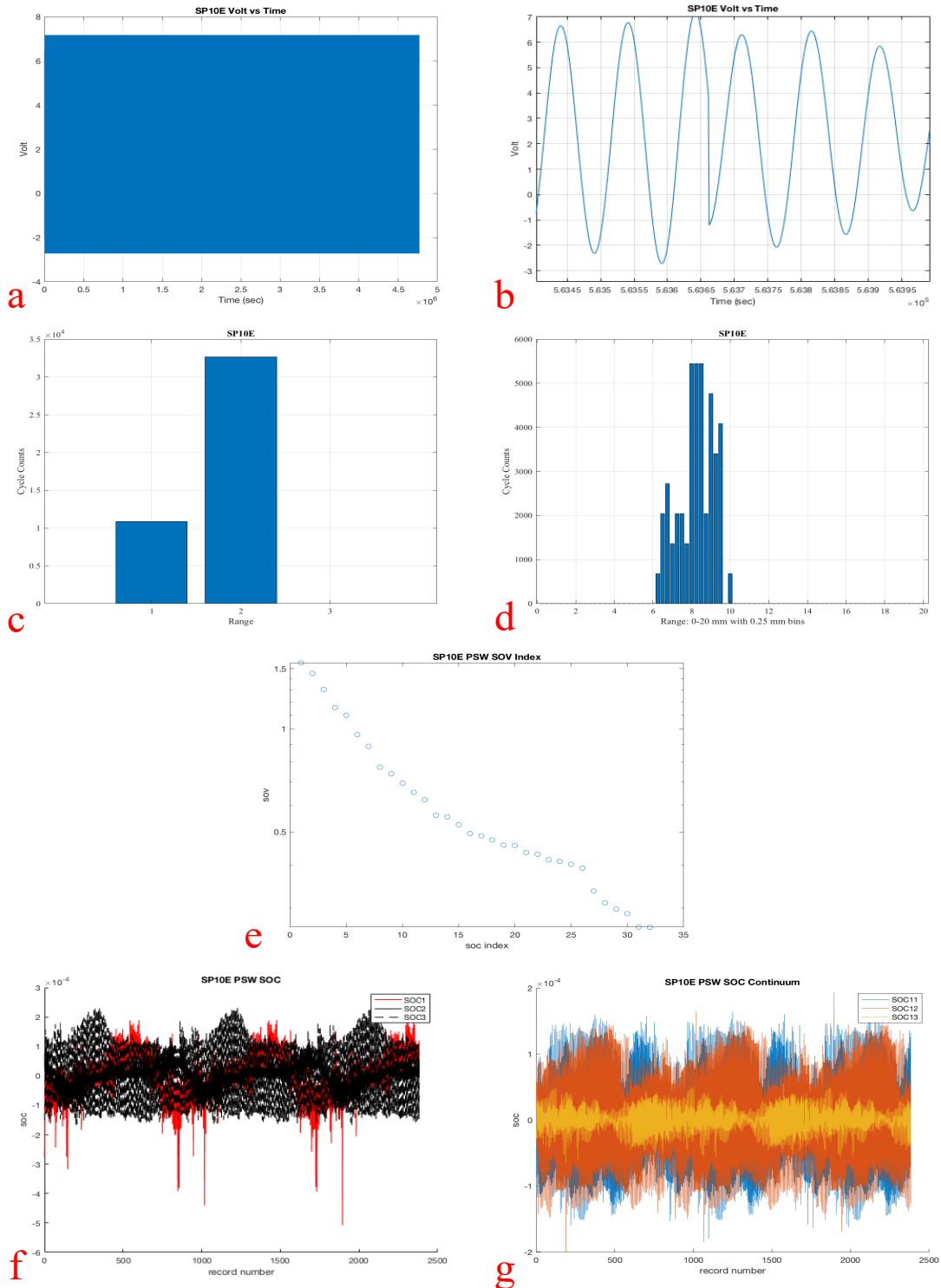


Figure D.29 – Specimen 10E plots. a) voltage vs. time b) zoomed time series c) three bin histogram of cycle count d) 0.25mm bin cycle count histogram e) SOC index f) SOM of eigenvalue g) SOC continuum

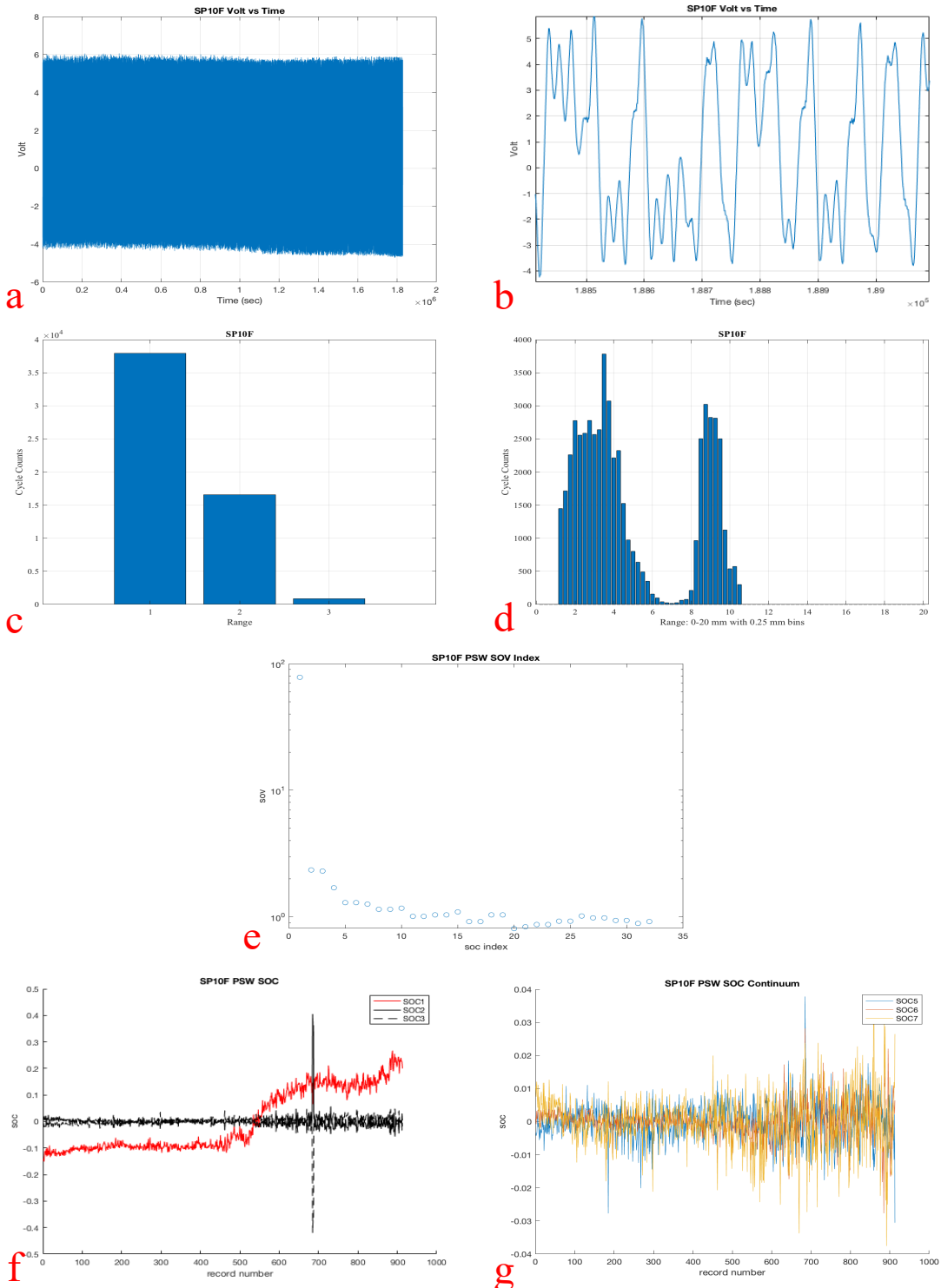


Figure D.30 – Specimen 10F plots. a) voltage vs. time b) zoomed time series c) three bin histogram of cycle count d) 0.25mm bin cycle count histogram e) SOC index f) SOM of eigenvalue g) SOC continuum

Variable Amplitude Test

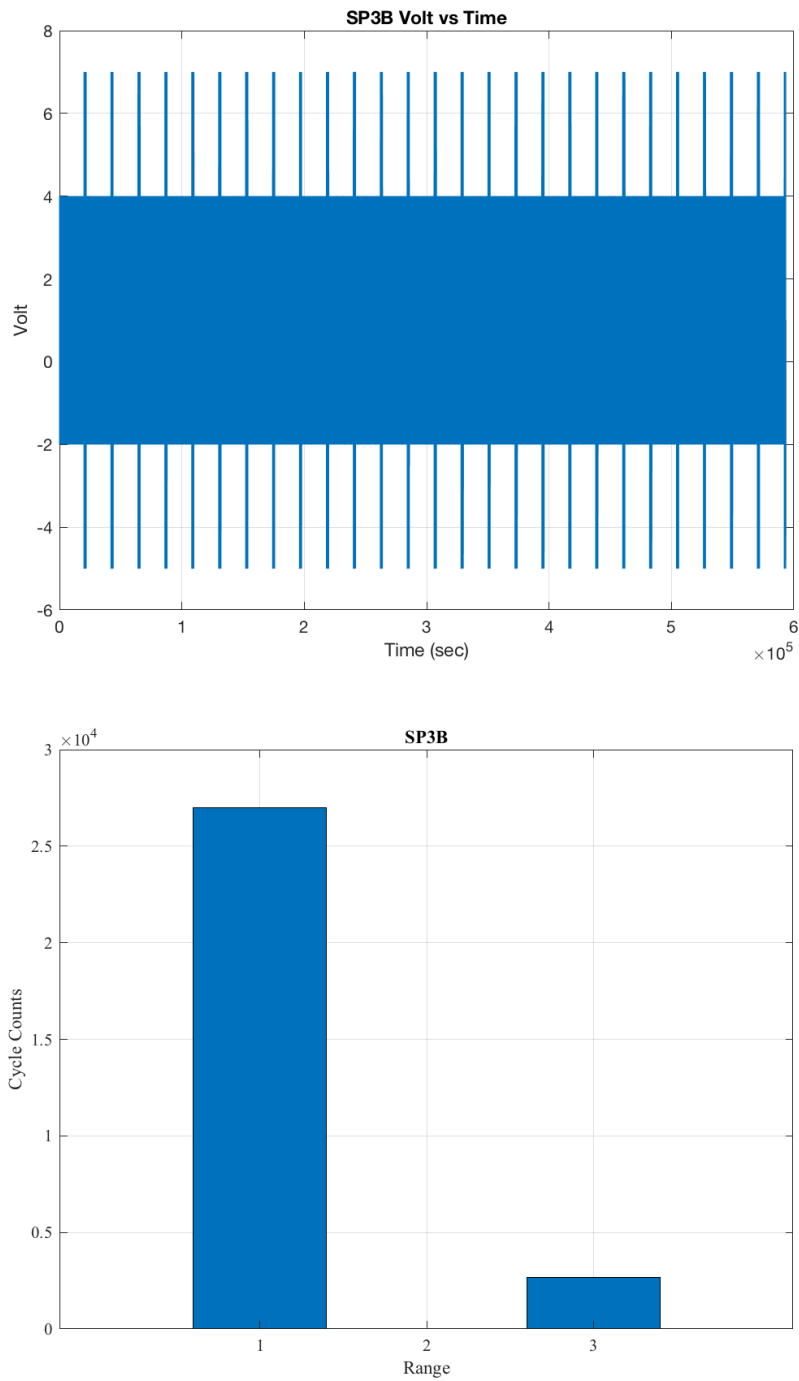


Figure D.31 – Specimen 3B plots. Top plot is of the specimen time series. The bottom plot shows the three bin histogram of the cycle

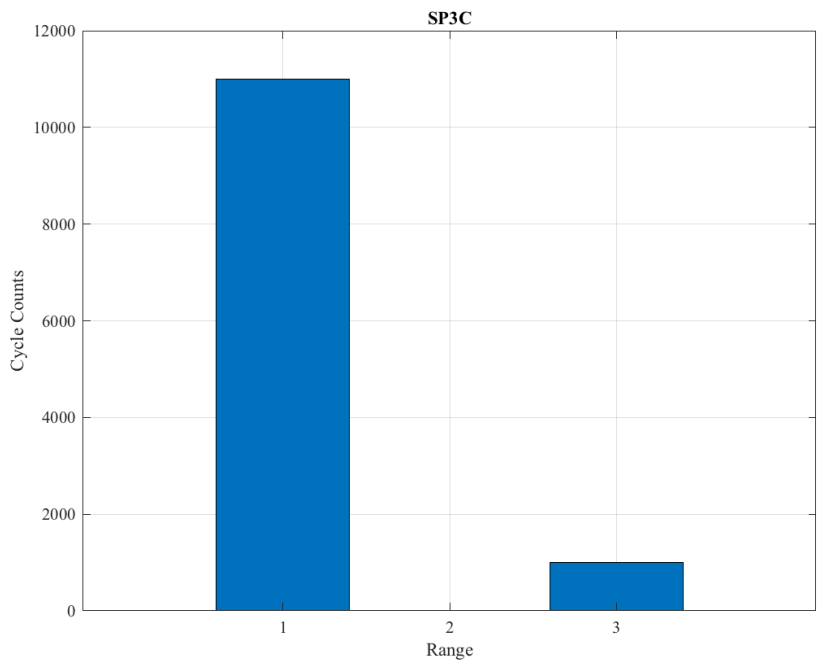
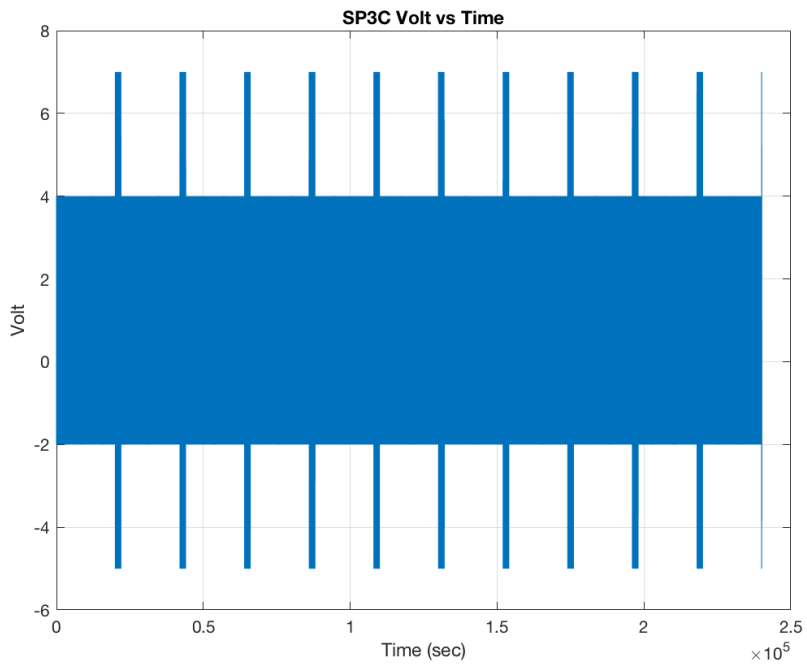


Figure D.32 – Specimen 3C plots. Top plot is of the specimen time series. The bottom plot shows the three bin histogram of the cycle

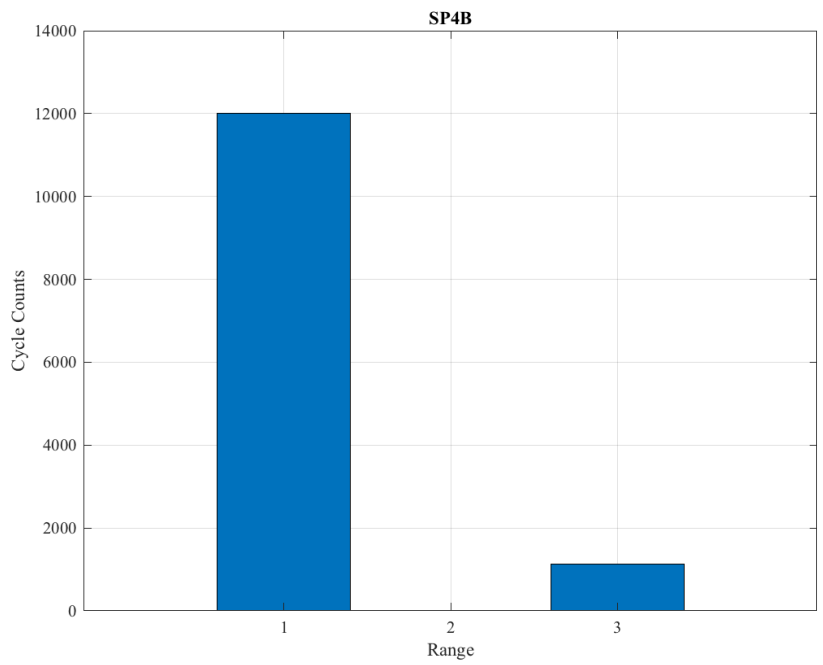
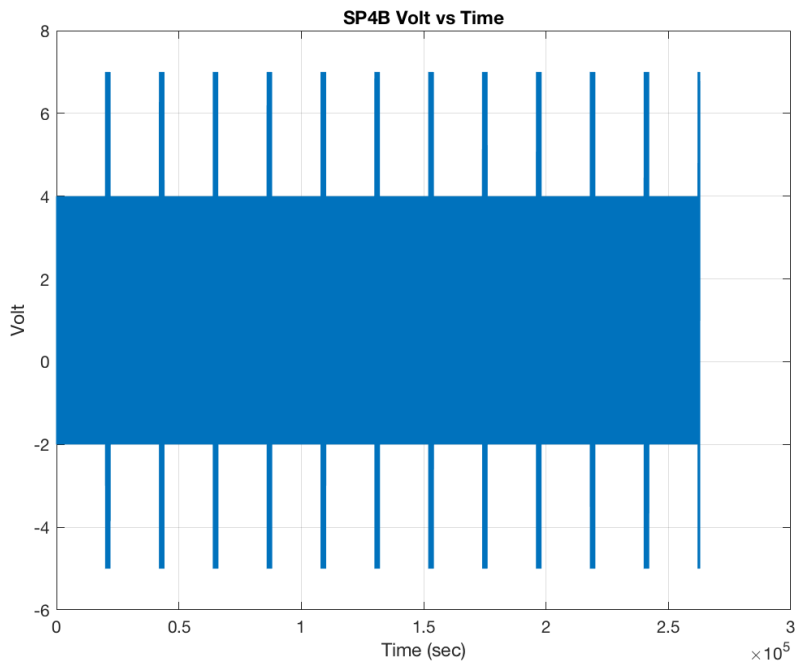


Figure D.33 – Specimen 4B plots. Top plot is of the specimen time series. The bottom plot shows the three bin histogram of the cycle

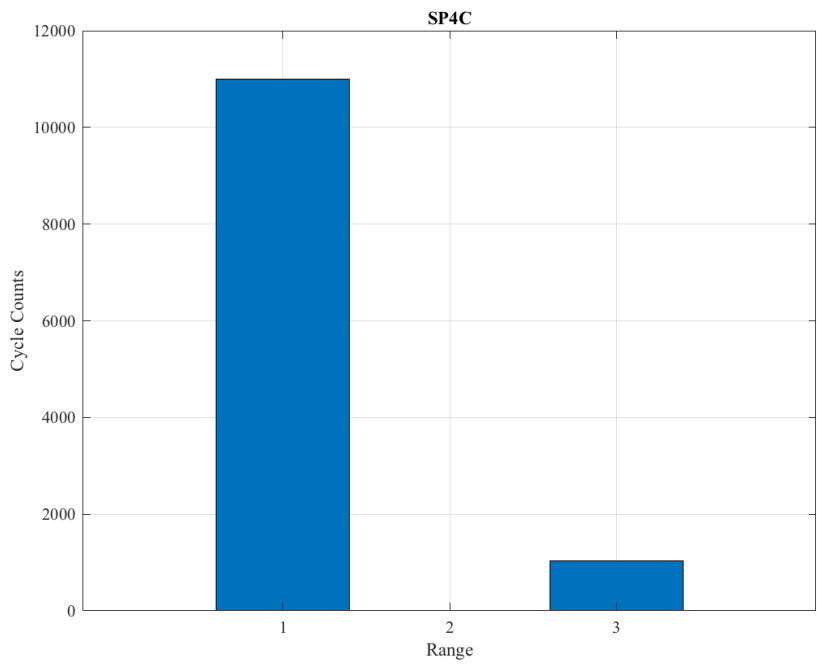
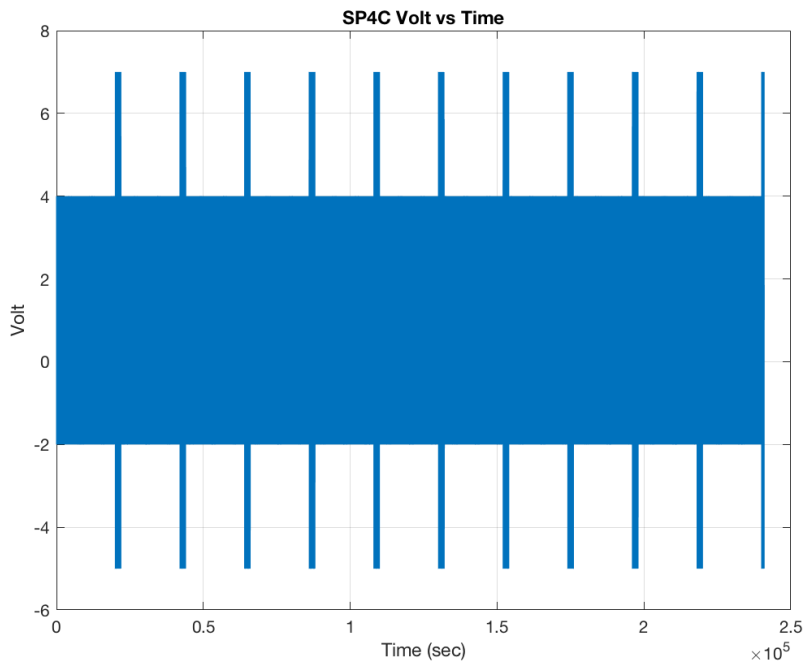


Figure D.34 – Specimen 4C plots. Top plot is of the specimen time series. The bottom plot shows the three bin histogram of the cycle

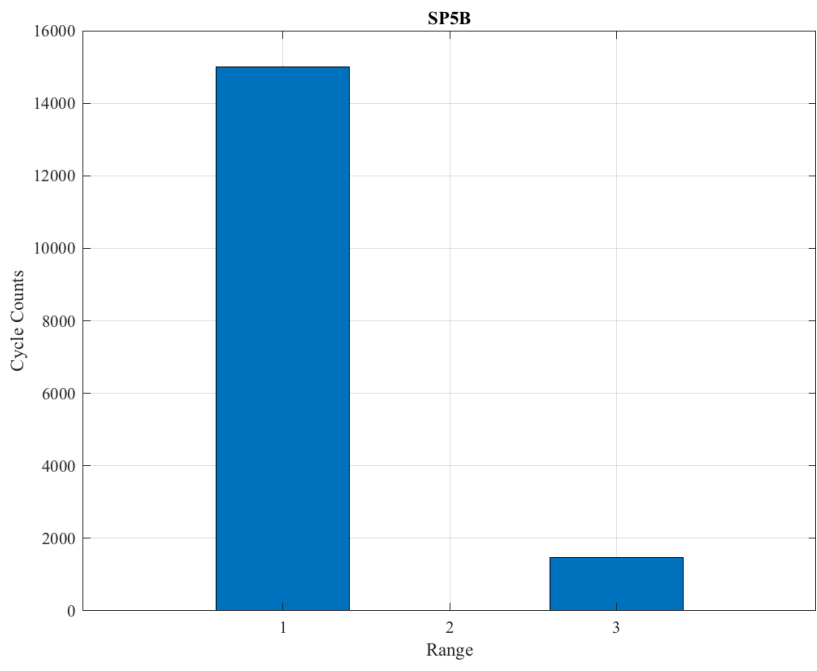
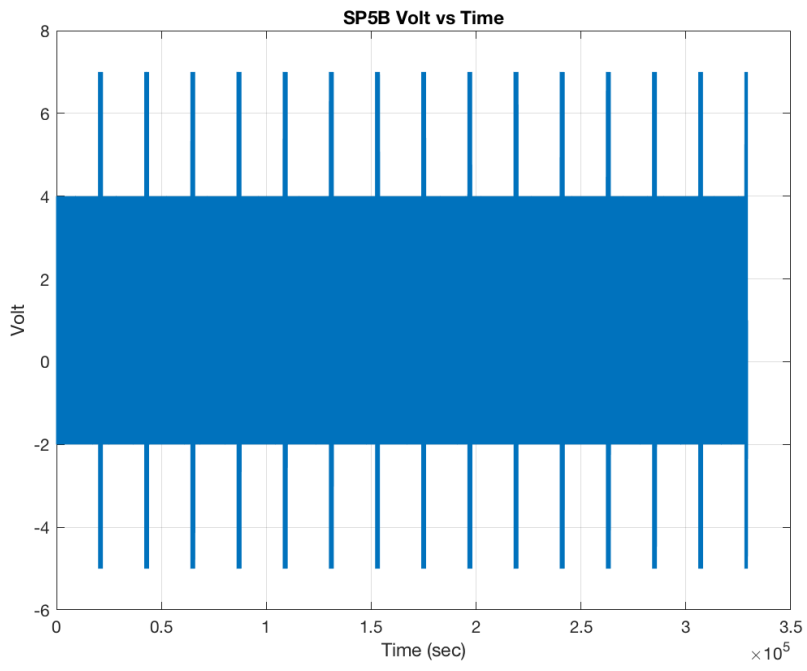


Figure D.35 – Specimen 5B plots. Top plot is of the specimen time series. The bottom plot shows the three bin histogram of the cycle

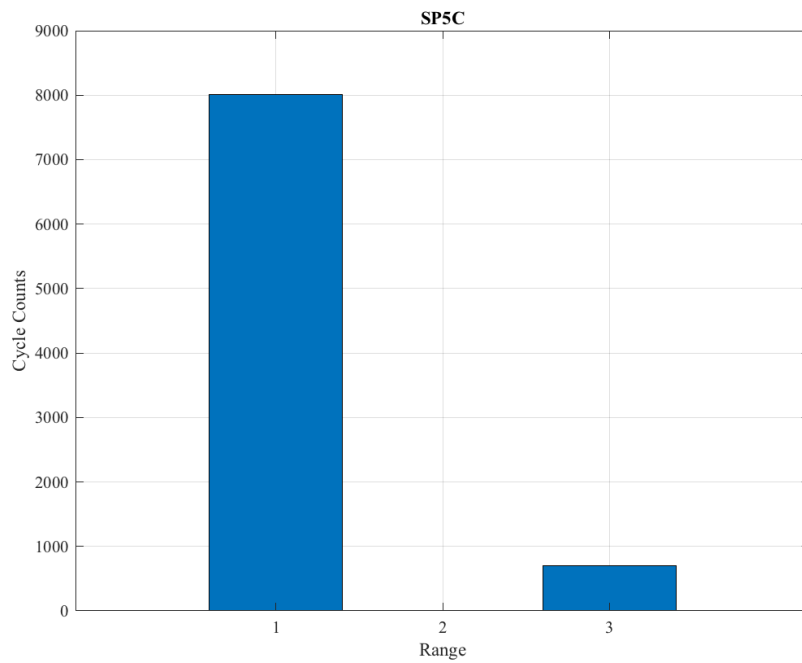
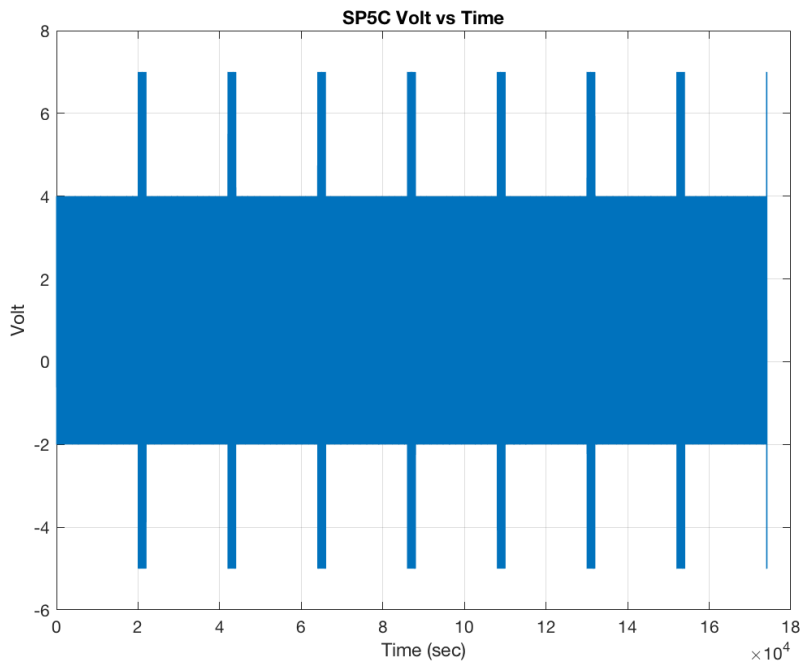


Figure D.36 – Specimen 5C plots. Top plot is of the specimen time series. The bottom plot shows the three bin histogram of the cycle

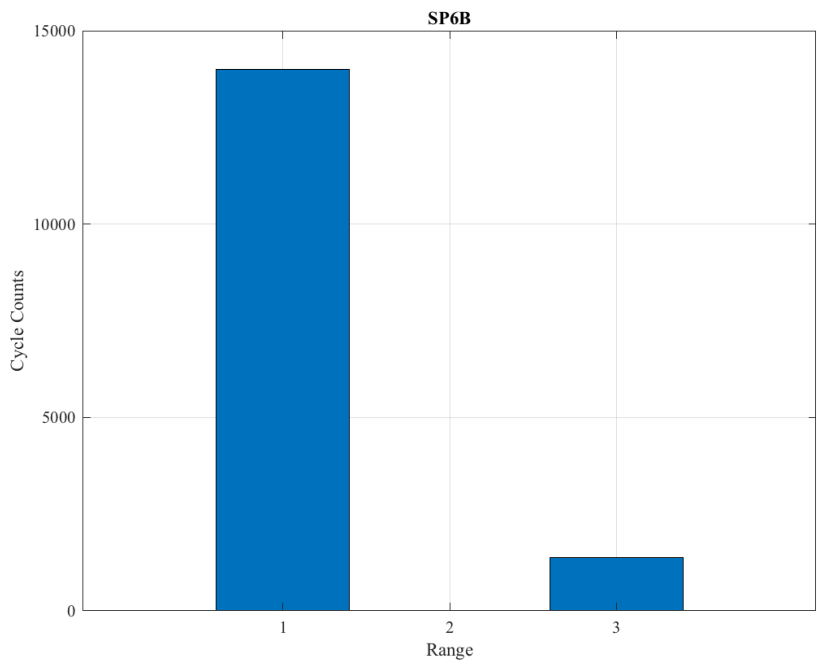
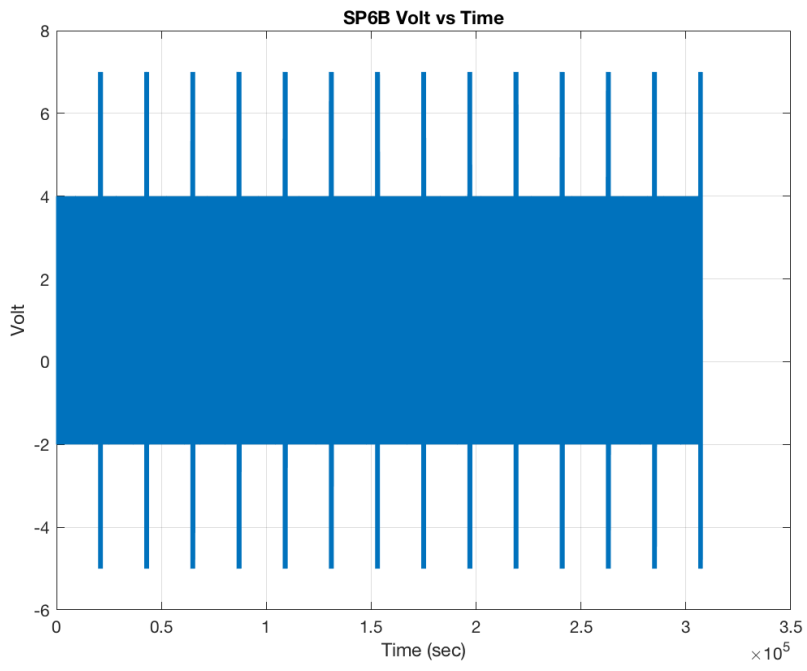


Figure D.37 – Specimen 6B plots. Top plot is of the specimen time series. The bottom plot shows the three bin histogram of the cycle

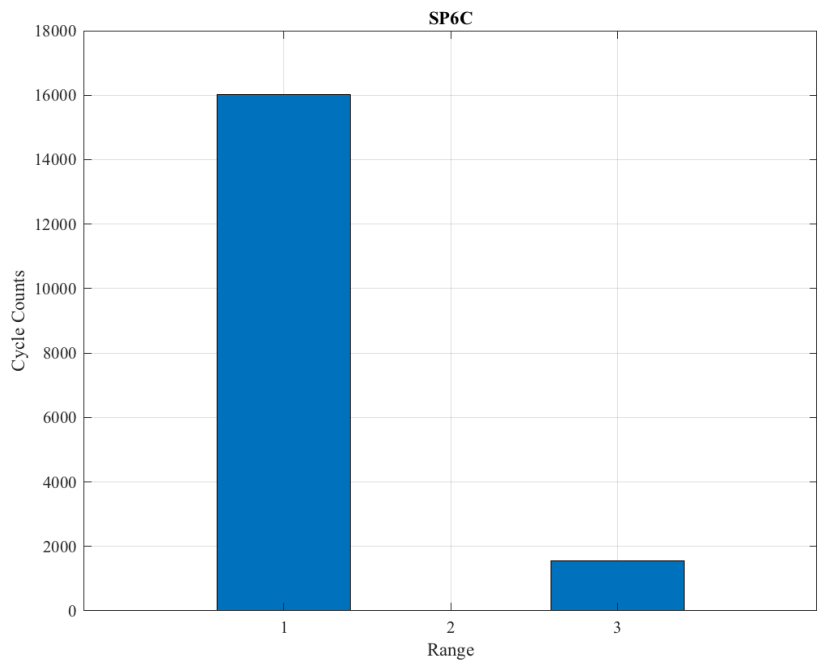
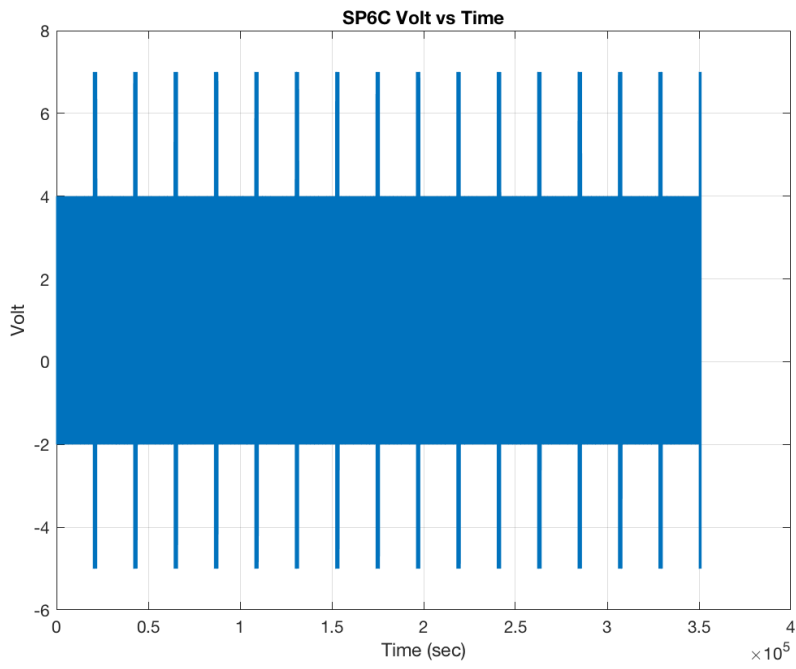


Figure D.38 – Specimen 6C plots. Top plot is of the specimen time series. The bottom plot shows the three bin histogram of the cycle

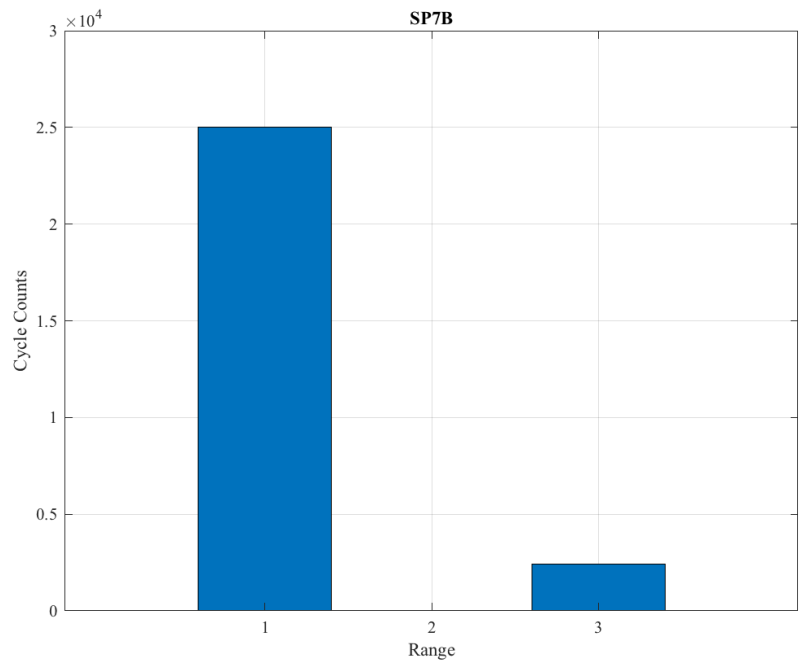
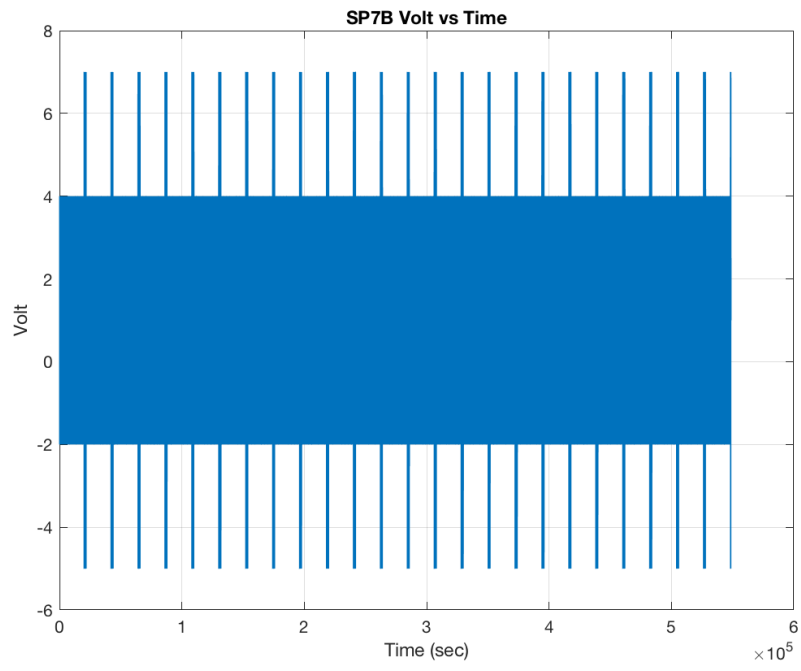


Figure D.39 – Specimen 7B plots. Top plot is of the specimen time series. The bottom plot shows the three bin histogram of the cycle

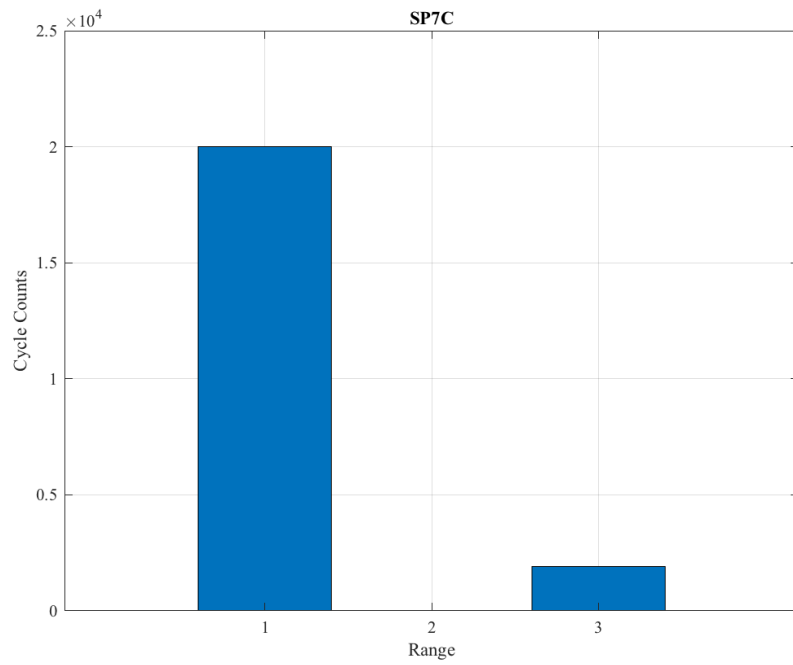
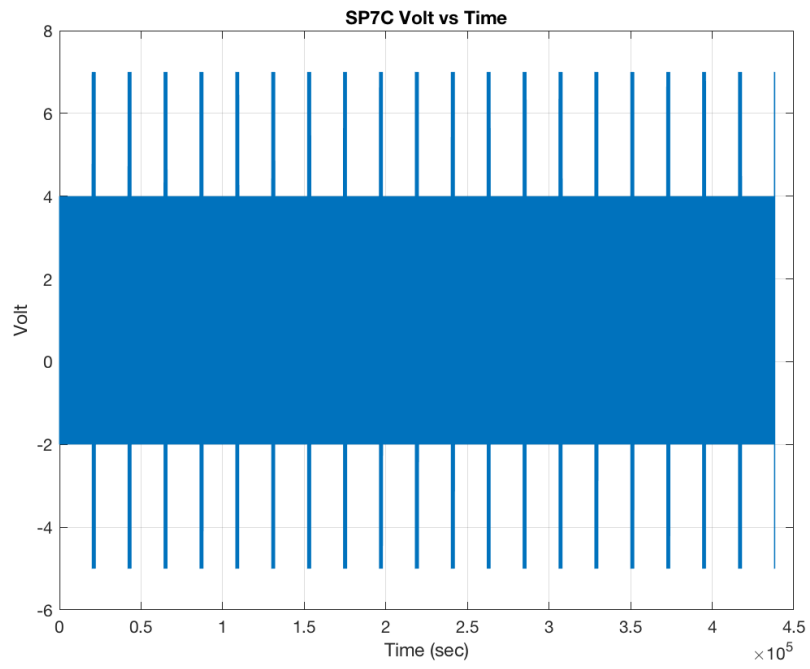


Figure D.40 – Specimen 7C plots. Top plot is of the specimen time series. The bottom plot shows the three bin histogram of the cycle

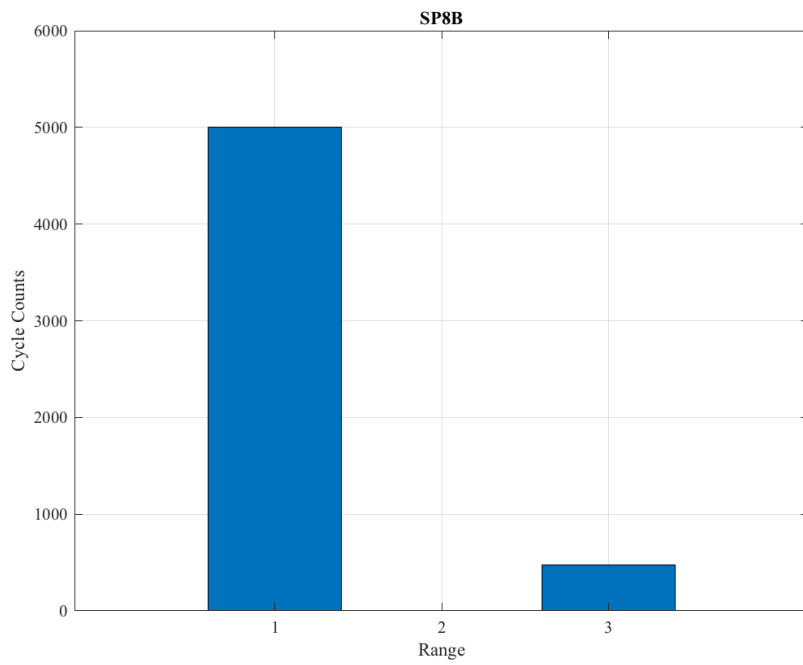
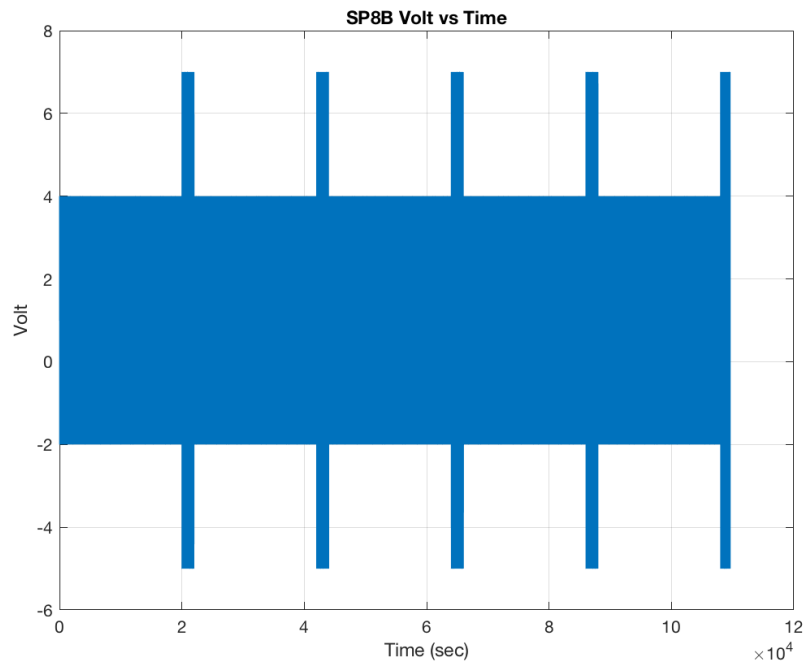


Figure D.41 – Specimen 8B plots. Top plot is of the specimen time series. The bottom plot shows the three bin histogram of the cycle

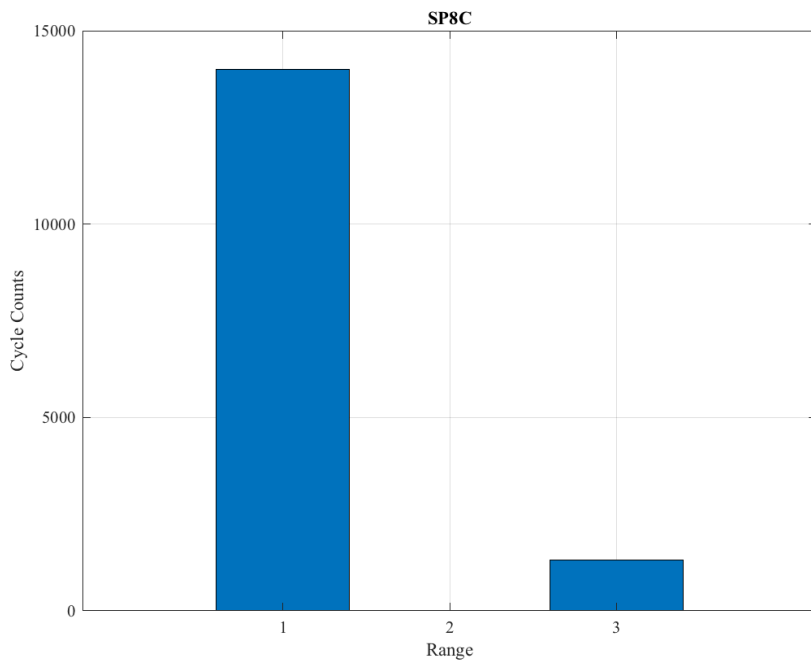
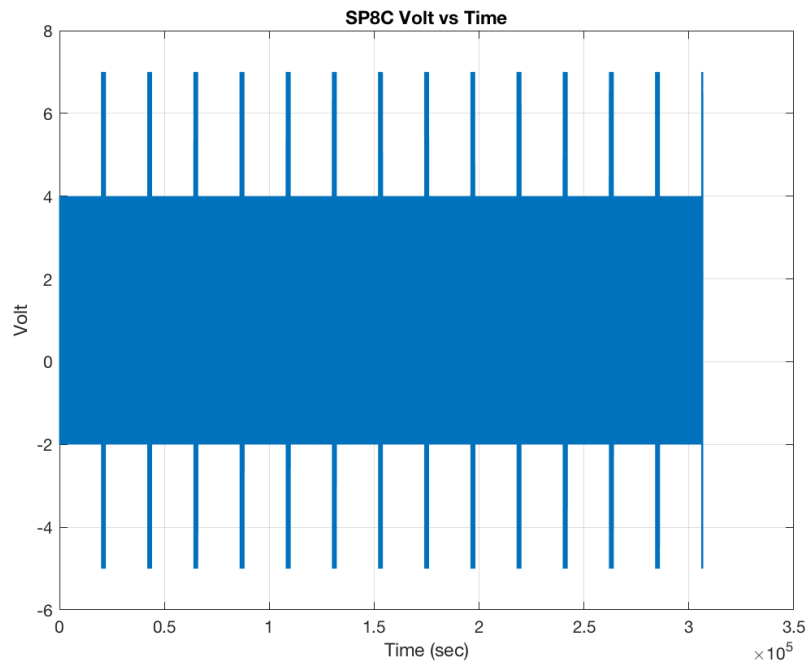


Figure D.42 – Specimen 8C plots. Top plot is of the specimen time series. The bottom plot shows the three bin histogram of the cycle

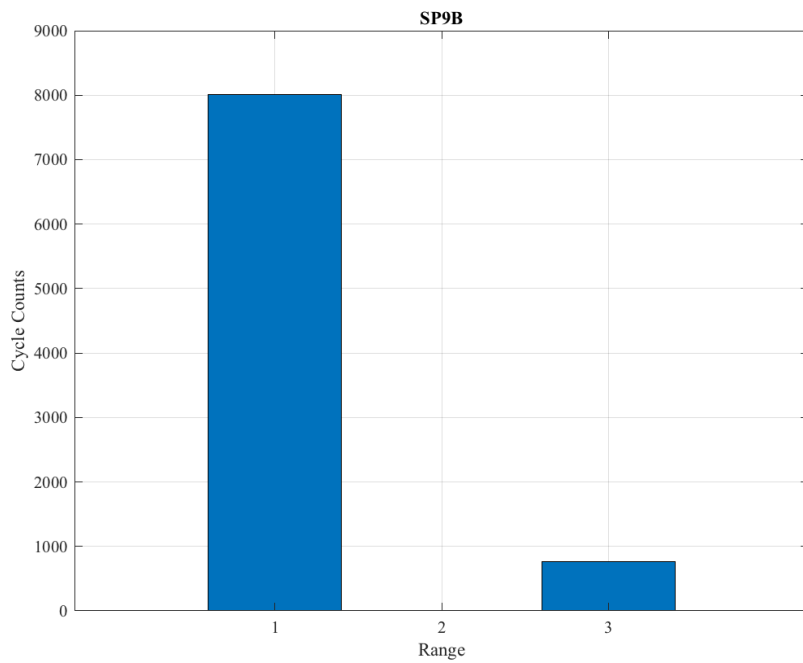
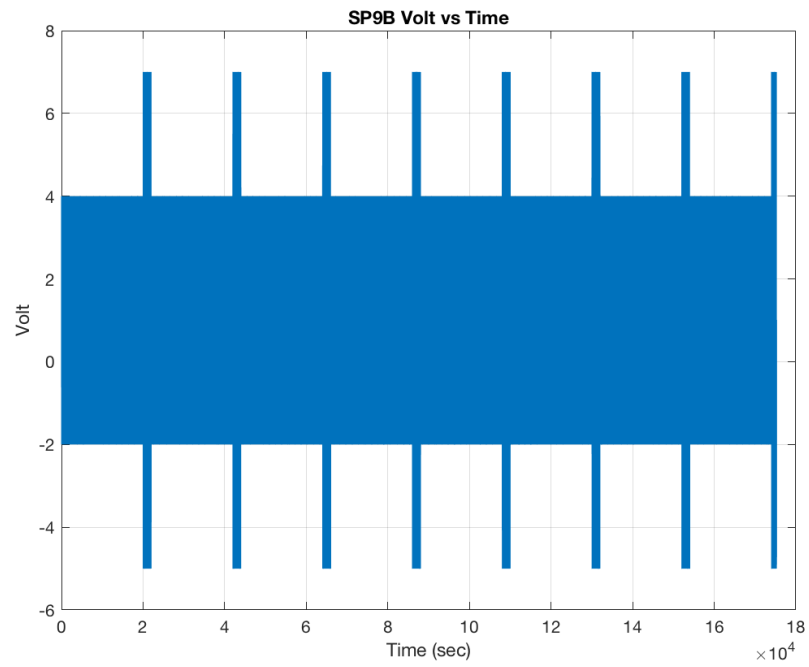


Figure D.43 – Specimen 9B plots. Top plot is of the specimen time series. The bottom plot shows the three bin histogram of the cycle

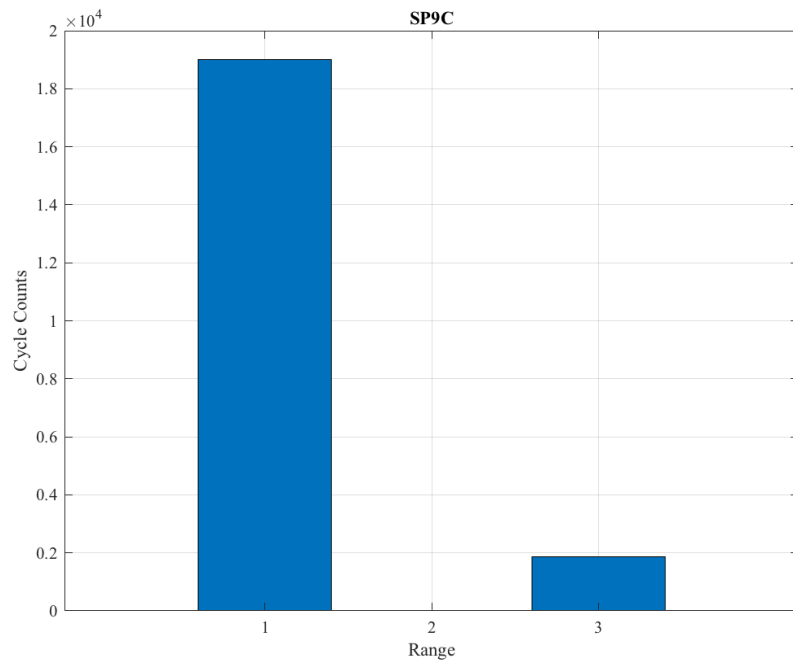
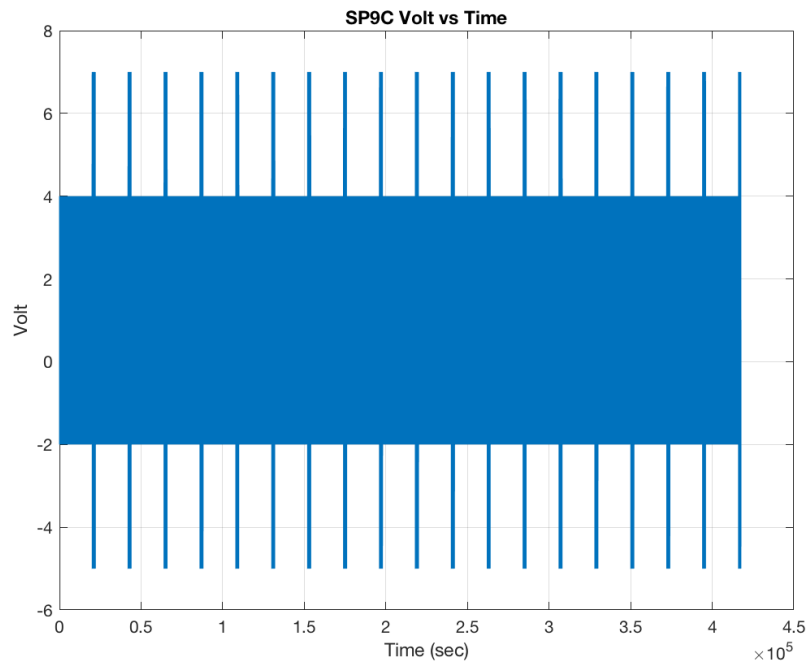


Figure D.44 – Specimen 9C plots. Top plot is of the specimen time series. The bottom plot shows the three bin histogram of the cycle

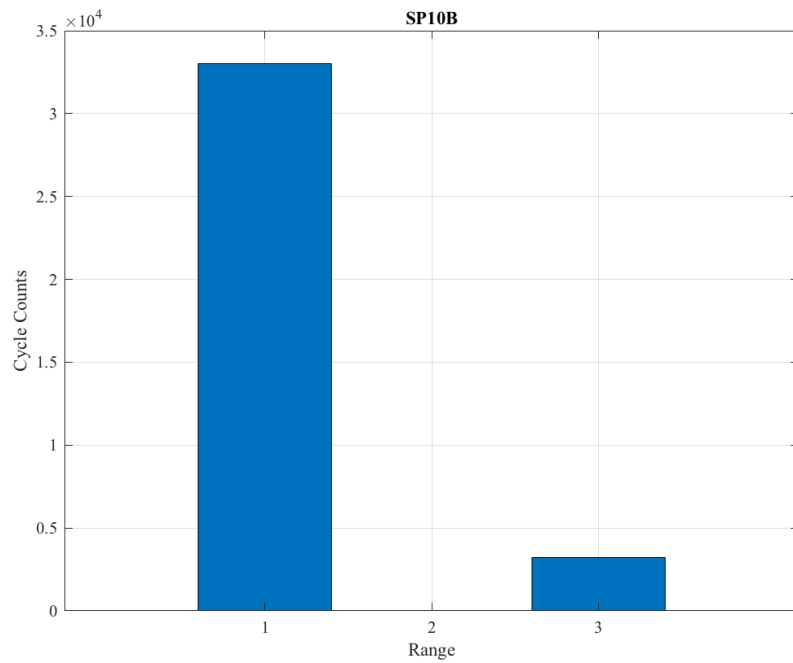
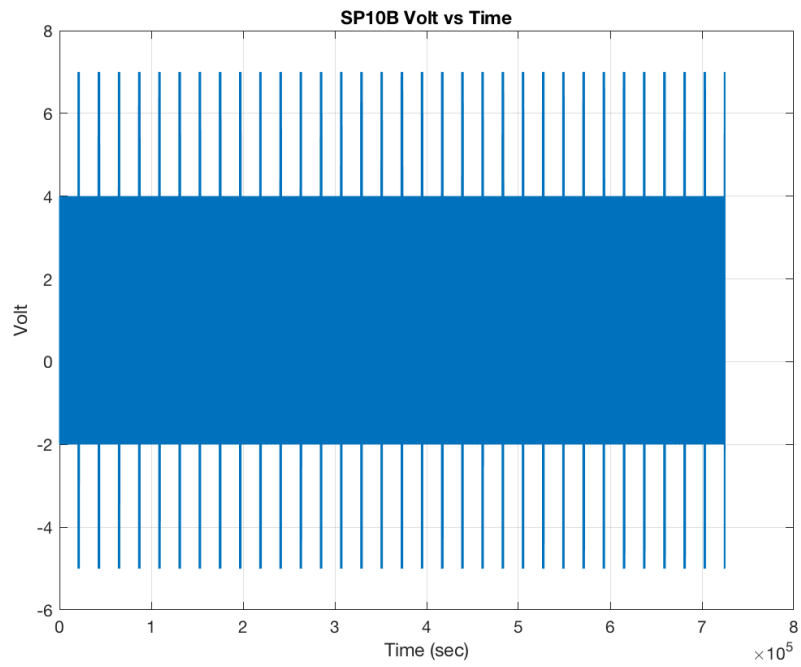


Figure D.45 – Specimen 10B plots. Top plot is of the specimen time series. The bottom plot shows the three bin histogram of the cycle

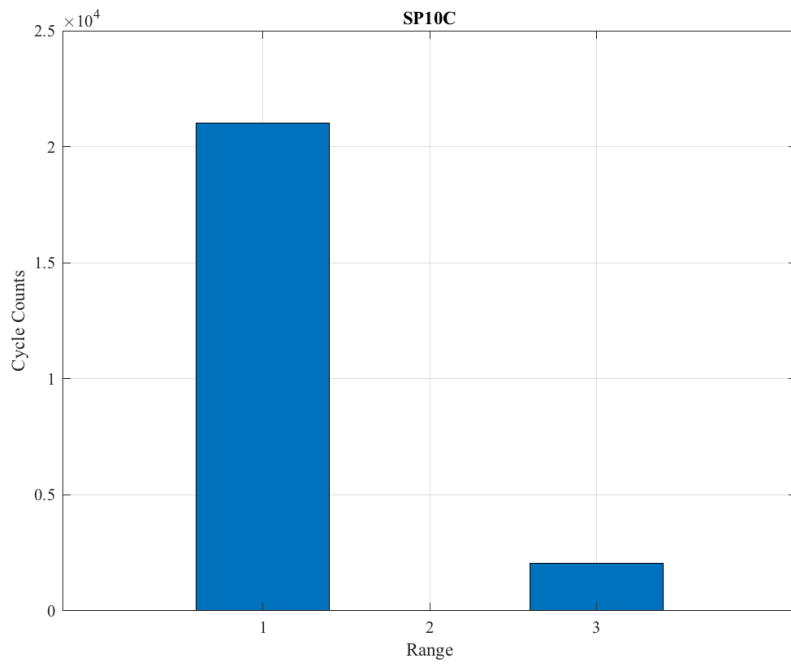
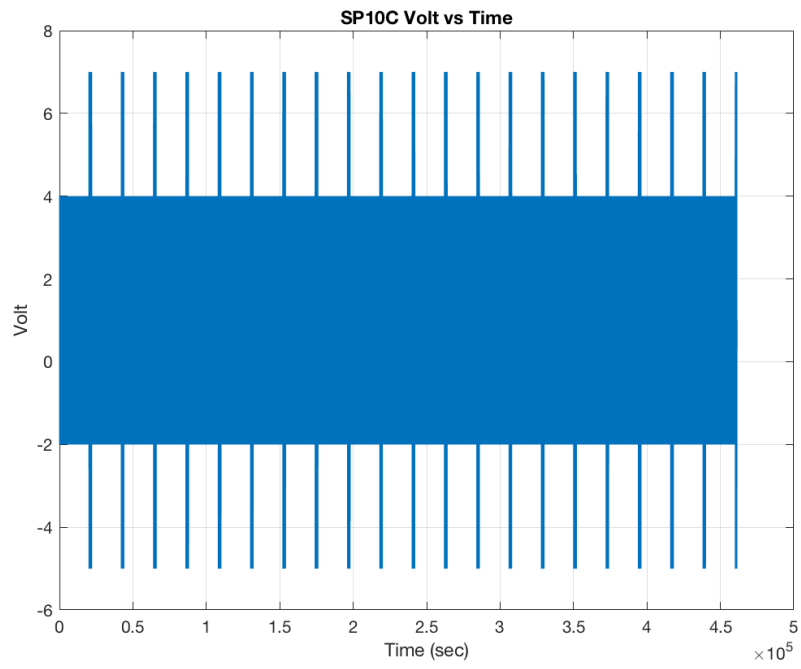


Figure D.46 – Specimen 10C plots. Top plot is of the specimen time series. The bottom plot shows the three bin histogram of the cycle

Four-Point Bend Test

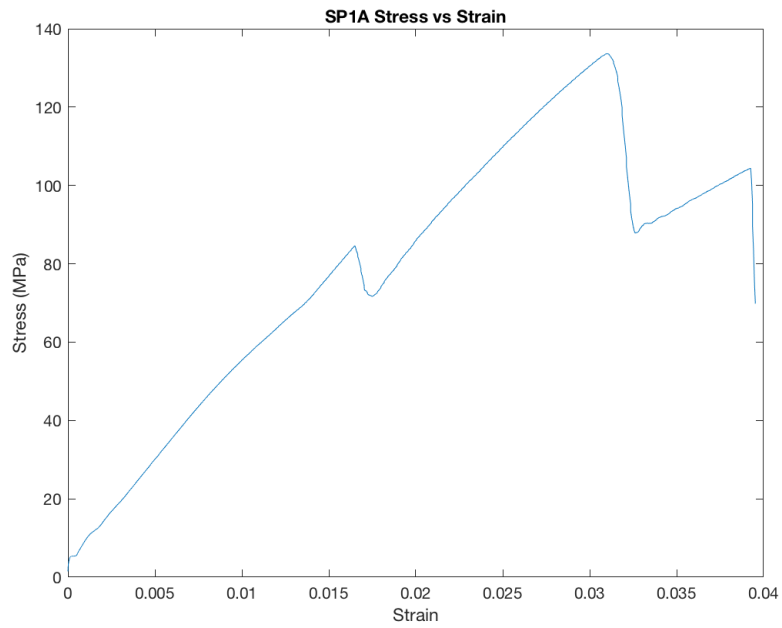


Figure D.47 – Stress vs. Strain plot for specimen 1A

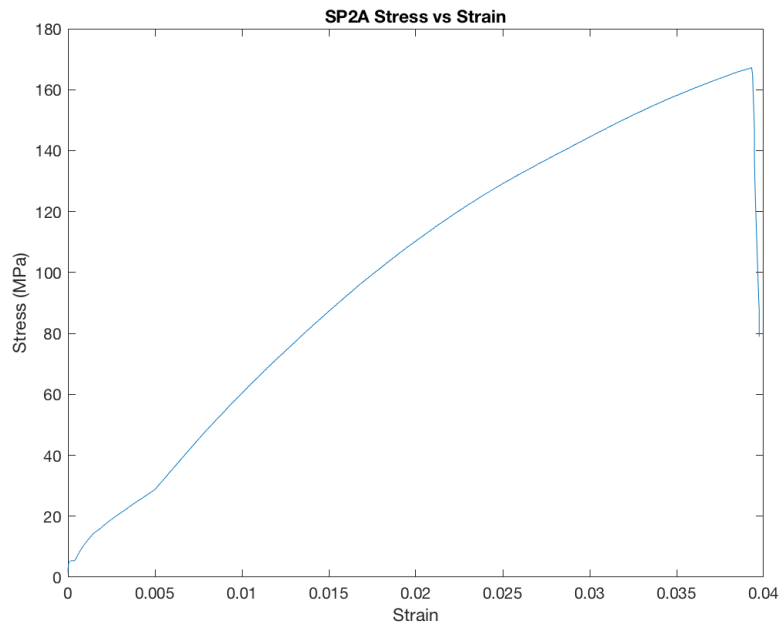


Figure D.48 – Stress vs. Strain plot for specimen 2A

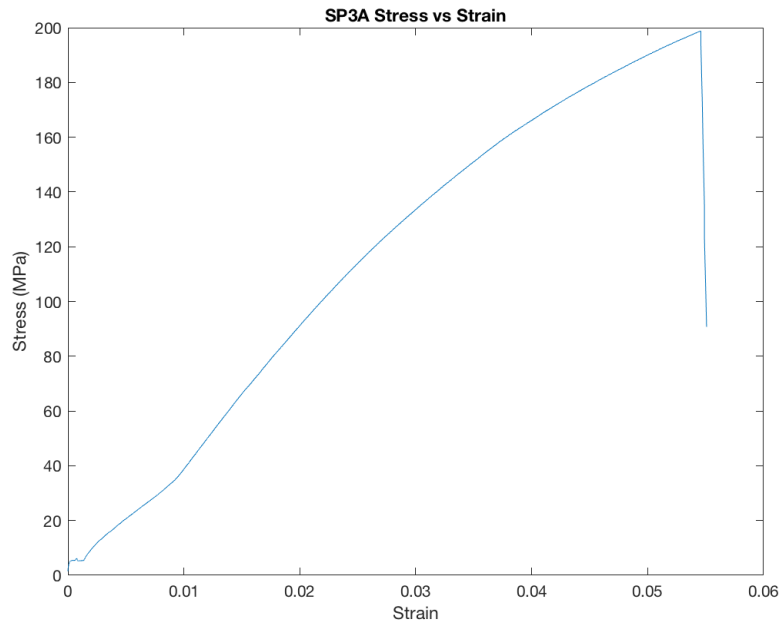


Figure D.49 – Stress vs. Strain plot for specimen 3A

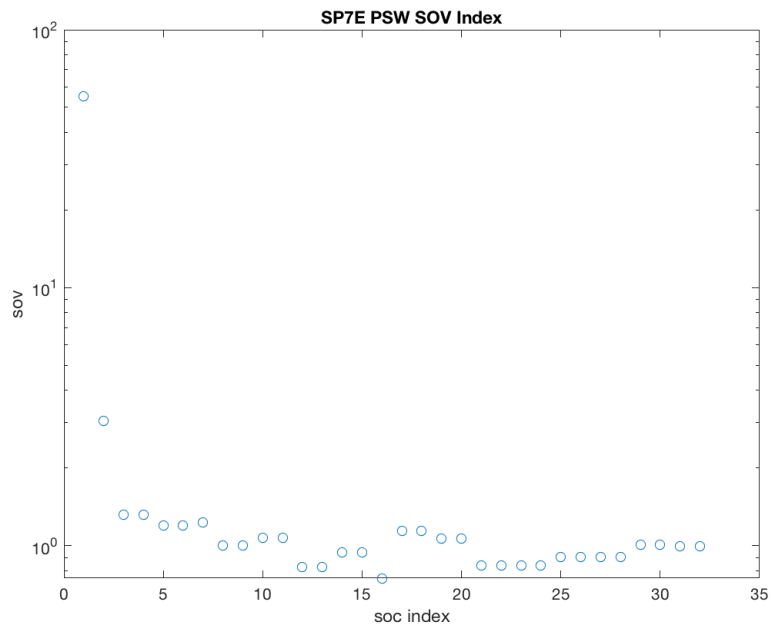


Figure D.50 – Stress vs. Strain plot for specimen 4A

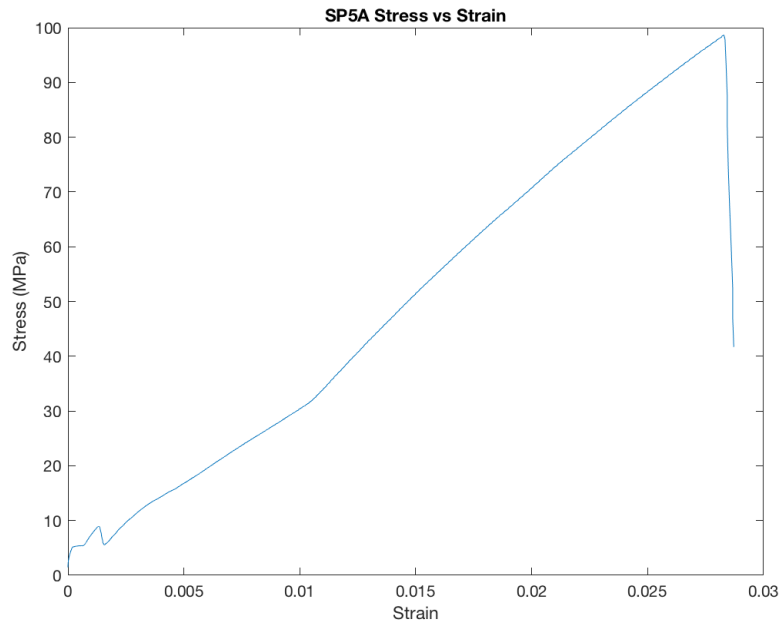


Figure D.51 – Stress vs. Strain plot for specimen 5A

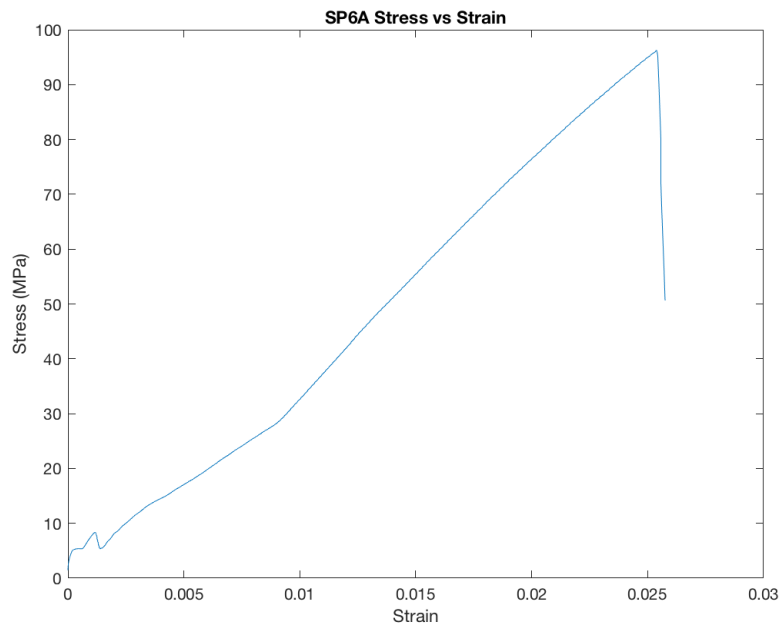


Figure D.52 – Stress vs. Strain plot for specimen 6A

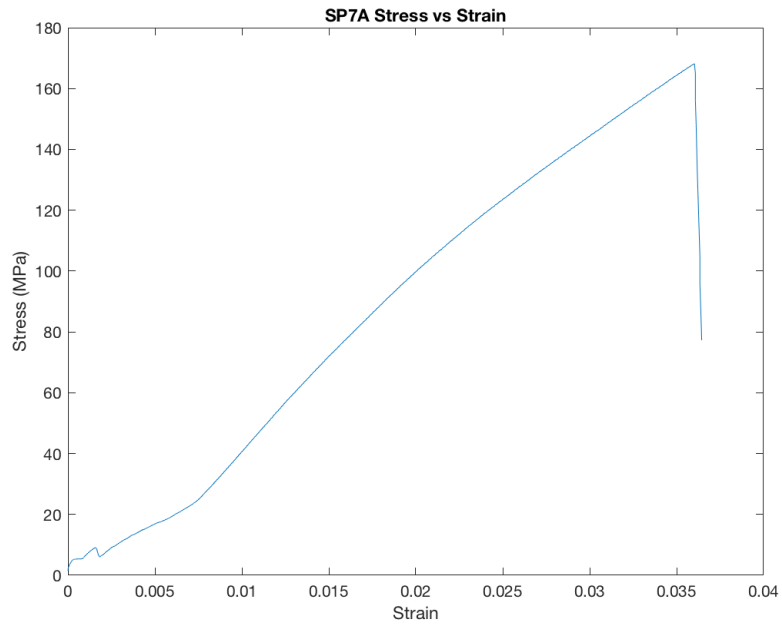


Figure D.53 – Stress vs. Strain plot for specimen 7A

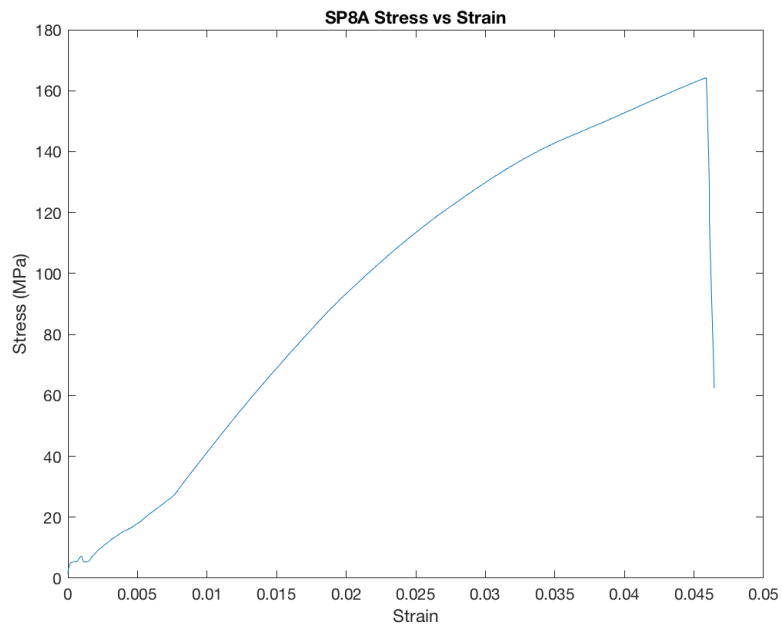


Figure D.54 – Stress vs. Strain plot for specimen 8A

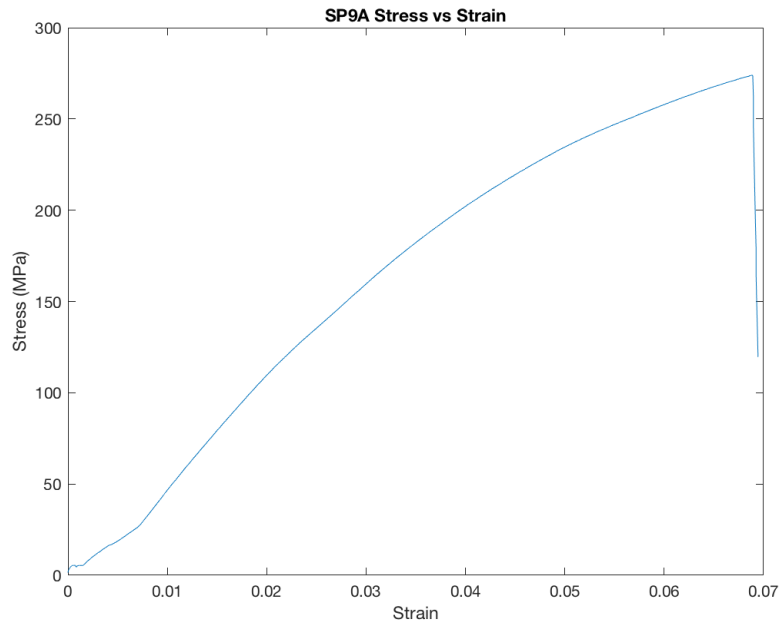


Figure D.55 – Stress vs. Strain plot for specimen 9A

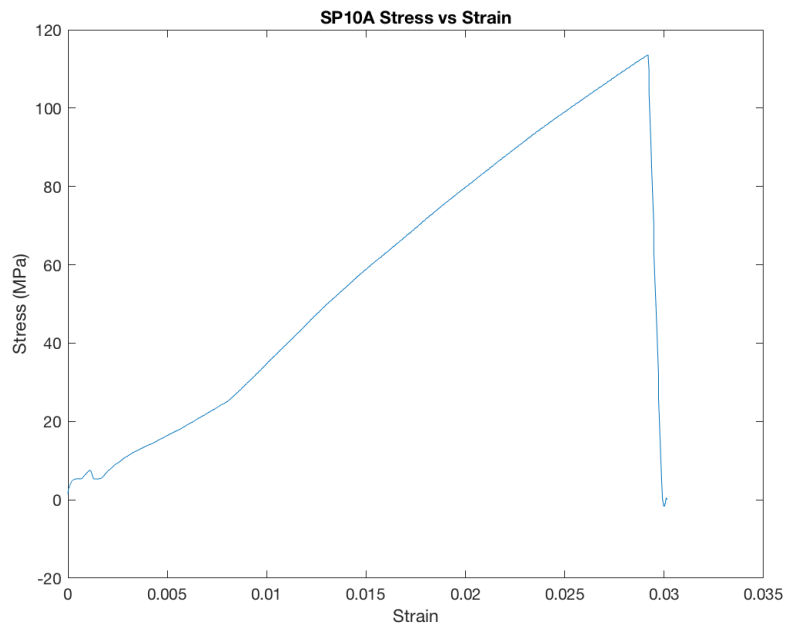


Figure D.56 – Stress vs. Strain plot for specimen 10A

Statistical Analysis

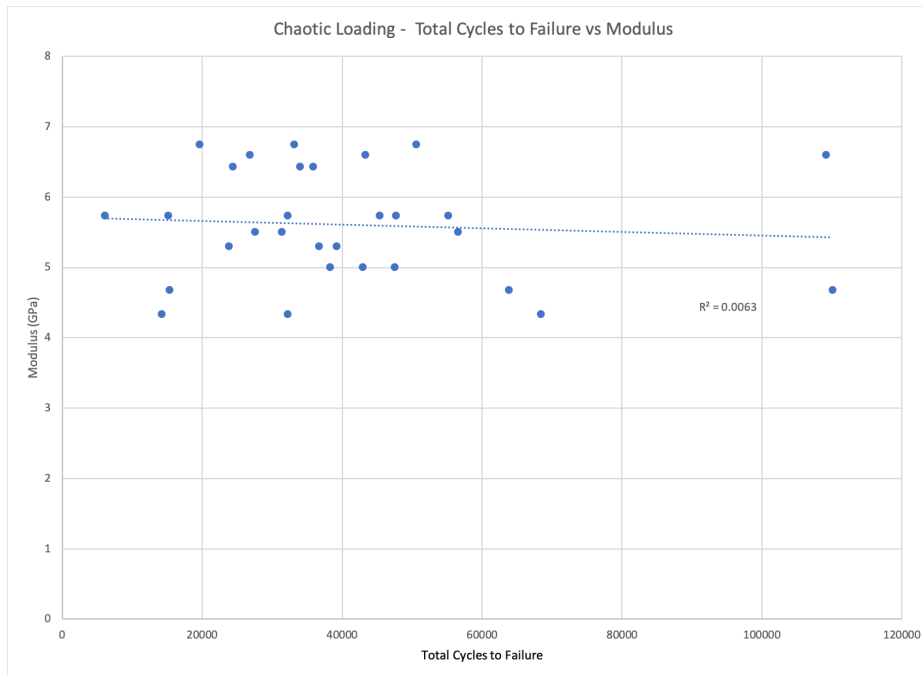


Figure D.57 – Chaotic loading total cycles to failure vs. modulus.

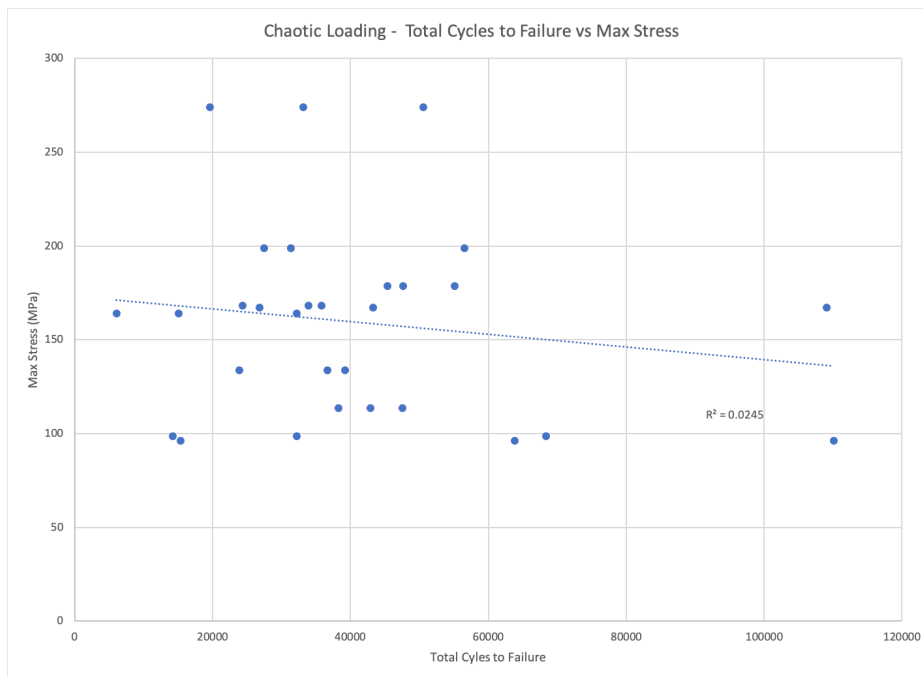


Figure D.58 – Chaotic loading total cycles to failure vs. max stress

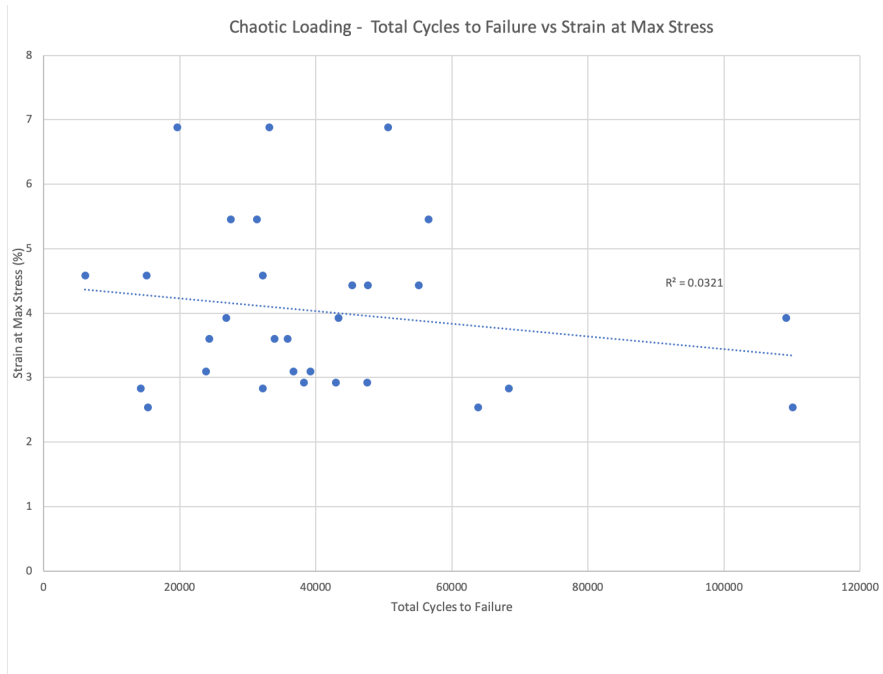


Figure D.59 – Chaotic loading total cycles to failure vs. strain at max stress.

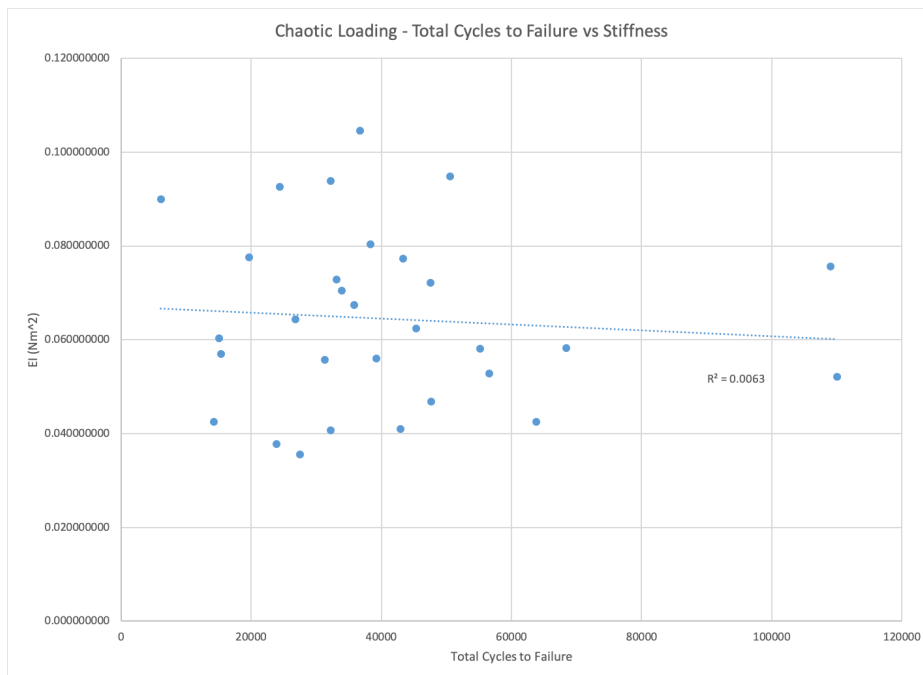


Figure D.60 – Chaotic loading total cycles to failure vs. stiffness.

Table D.1 – Data table from chaotic loading correlations.

| Chaotic Loading Comparisons | | | | |
|-----------------------------|-------------------------|---------------|------------------|--------------------------|
| Specimen | Total Cycles to Failure | Modulus (GPa) | Max Stress (MPa) | Strain at Max Stress (%) |
| 1D | 23858.5 | 5.30 | 133.61 | 3.10 |
| 1E | 36704.0 | 5.30 | 133.61 | 3.10 |
| 1F | 39241.0 | 5.30 | 133.61 | 3.10 |
| 2D | 26843.5 | 6.60 | 167.24 | 3.93 |
| 2E | 43303.5 | 6.60 | 167.24 | 3.93 |
| 2F | 109103.0 | 6.60 | 167.24 | 3.93 |
| 3D | 56547.0 | 5.51 | 198.77 | 5.46 |
| 3E | 31330.0 | 5.51 | 198.77 | 5.46 |
| 3F | 27524.5 | 5.51 | 198.77 | 5.46 |
| 4D | 55154.5 | 5.74 | 178.75 | 4.43 |
| 4E | 45370.0 | 5.74 | 178.75 | 4.43 |
| 4F | 47650.0 | 5.74 | 178.75 | 4.43 |
| 5D | 32174.0 | 4.34 | 98.66 | 2.83 |
| 5E | 68418.5 | 4.34 | 98.66 | 2.83 |
| 5F | 14237.0 | 4.34 | 98.66 | 2.83 |
| 6D | 110087.0 | 4.68 | 96.26 | 2.54 |
| 6E | 63827.5 | 4.68 | 96.26 | 2.54 |
| 6F | 15349.0 | 4.68 | 96.26 | 2.54 |
| 7D | 35836.0 | 6.43 | 168.17 | 3.60 |
| 7E | 24359.5 | 6.43 | 168.17 | 3.60 |
| 7F | 33950.0 | 6.43 | 168.17 | 3.60 |
| 8D | 6094.0 | 5.74 | 164.22 | 4.58 |
| 8E | 15109.0 | 5.74 | 164.22 | 4.58 |
| 8F | 32195.0 | 5.74 | 164.22 | 4.58 |
| 9D | 19634.5 | 6.75 | 273.97 | 6.88 |
| 9E | 50591.0 | 6.75 | 273.97 | 6.88 |
| 9F | 33156.0 | 6.75 | 273.97 | 6.88 |
| 10D | 47541.0 | 5.01 | 113.57 | 2.92 |
| 10E | 42958.5 | 5.01 | 113.57 | 2.92 |
| 10F | 38285.5 | 5.01 | 113.57 | 2.92 |

Table D.2 – Data table from chaotic loading stiffness correlation.

| Chaotic Loading Stiffness Comparison | | | | | | | | |
|--------------------------------------|-------------------------|---------------|--------------|----------------|------------|-----------------------|----------------------|-----------------------|
| Specimen | Total Cycles to Failure | Modulus (Gpa) | Modulus (Pa) | Thickness (in) | Width (in) | Ix (in ⁴) | Ix (m ⁴) | EI (Nm ²) |
| 1D | 23858.5 | 5.30 | 5.30E+09 | 0.0840 | 0.3472 | 1.71E-05 | 7.14E-12 | 0.038 |
| 1E | 36704.0 | 5.30 | 5.30E+09 | 0.1180 | 0.3464 | 4.74E-05 | 1.97E-11 | 0.105 |
| 1F | 39241.0 | 5.30 | 5.30E+09 | 0.0960 | 0.3445 | 2.54E-05 | 1.06E-11 | 0.056 |
| 2D | 26843.5 | 6.60 | 6.60E+09 | 0.0950 | 0.3278 | 2.34E-05 | 9.75E-12 | 0.064 |
| 2E | 43303.5 | 6.60 | 6.60E+09 | 0.1000 | 0.3378 | 2.82E-05 | 1.17E-11 | 0.077 |
| 2F | 109103.0 | 6.60 | 6.60E+09 | 0.1010 | 0.3207 | 2.75E-05 | 1.15E-11 | 0.076 |
| 3D | 56547.0 | 5.51 | 5.51E+09 | 0.0940 | 0.3328 | 2.30E-05 | 9.59E-12 | 0.053 |
| 3E | 31330.0 | 5.51 | 5.51E+09 | 0.0960 | 0.3294 | 2.43E-05 | 1.01E-11 | 0.056 |
| 3F | 27524.5 | 5.51 | 5.51E+09 | 0.0830 | 0.3248 | 1.55E-05 | 6.44E-12 | 0.035 |
| 4D | 55154.5 | 5.74 | 5.74E+09 | 0.0964 | 0.3254 | 2.43E-05 | 1.01E-11 | 0.058 |
| 4E | 45370.0 | 5.74 | 5.74E+09 | 0.0980 | 0.3327 | 2.61E-05 | 1.09E-11 | 0.062 |
| 4F | 47650.0 | 5.74 | 5.74E+09 | 0.0900 | 0.3228 | 1.96E-05 | 8.16E-12 | 0.047 |
| 5D | 32174.0 | 4.34 | 4.34E+09 | 0.0928 | 0.3380 | 2.25E-05 | 9.37E-12 | 0.041 |
| 5E | 68418.5 | 4.34 | 4.34E+09 | 0.1050 | 0.3341 | 3.22E-05 | 1.34E-11 | 0.058 |
| 5F | 14237.0 | 4.34 | 4.34E+09 | 0.0939 | 0.3409 | 2.35E-05 | 9.79E-12 | 0.042 |
| 6D | 110087.0 | 4.68 | 4.68E+09 | 0.0980 | 0.3410 | 2.67E-05 | 1.11E-11 | 0.052 |
| 6E | 63827.5 | 4.68 | 4.68E+09 | 0.0917 | 0.3392 | 2.18E-05 | 9.07E-12 | 0.042 |
| 6F | 15349.0 | 4.68 | 4.68E+09 | 0.1030 | 0.3210 | 2.92E-05 | 1.22E-11 | 0.057 |
| 7D | 35836.0 | 6.43 | 6.43E+09 | 0.0979 | 0.3221 | 2.52E-05 | 1.05E-11 | 0.067 |
| 7E | 24359.5 | 6.43 | 6.43E+09 | 0.1080 | 0.3296 | 3.46E-05 | 1.44E-11 | 0.093 |
| 7F | 33950.0 | 6.43 | 6.43E+09 | 0.0980 | 0.3359 | 2.63E-05 | 1.10E-11 | 0.071 |
| 8D | 6094.0 | 5.74 | 5.74E+09 | 0.1100 | 0.3396 | 3.77E-05 | 1.57E-11 | 0.090 |
| 8E | 15109.0 | 5.74 | 5.74E+09 | 0.0970 | 0.3322 | 2.53E-05 | 1.05E-11 | 0.060 |
| 8F | 32195.0 | 5.74 | 5.74E+09 | 0.1110 | 0.3446 | 3.93E-05 | 1.63E-11 | 0.094 |
| 9D | 19634.5 | 6.75 | 6.75E+09 | 0.0990 | 0.3416 | 2.76E-05 | 1.15E-11 | 0.078 |
| 9E | 50591.0 | 6.75 | 6.75E+09 | 0.1051 | 0.3491 | 3.38E-05 | 1.41E-11 | 0.095 |
| 9F | 33156.0 | 6.75 | 6.75E+09 | 0.0975 | 0.3359 | 2.59E-05 | 1.08E-11 | 0.073 |
| 10D | 47541.0 | 5.01 | 5.01E+09 | 0.1080 | 0.3298 | 3.46E-05 | 1.44E-11 | 0.072 |
| 10E | 42958.5 | 5.01 | 5.01E+09 | 0.0900 | 0.3232 | 1.96E-05 | 8.17E-12 | 0.041 |
| 10F | 38285.5 | 5.01 | 5.01E+09 | 0.1110 | 0.3383 | 3.86E-05 | 1.60E-11 | 0.080 |

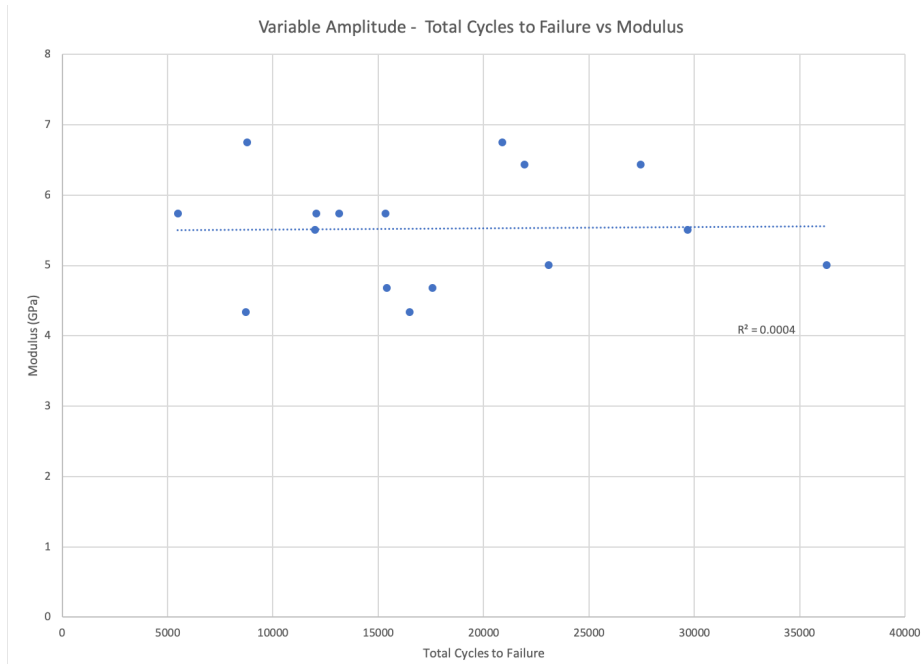


Figure D.61 – Variable amplitude total cycles to failure vs. modulus.

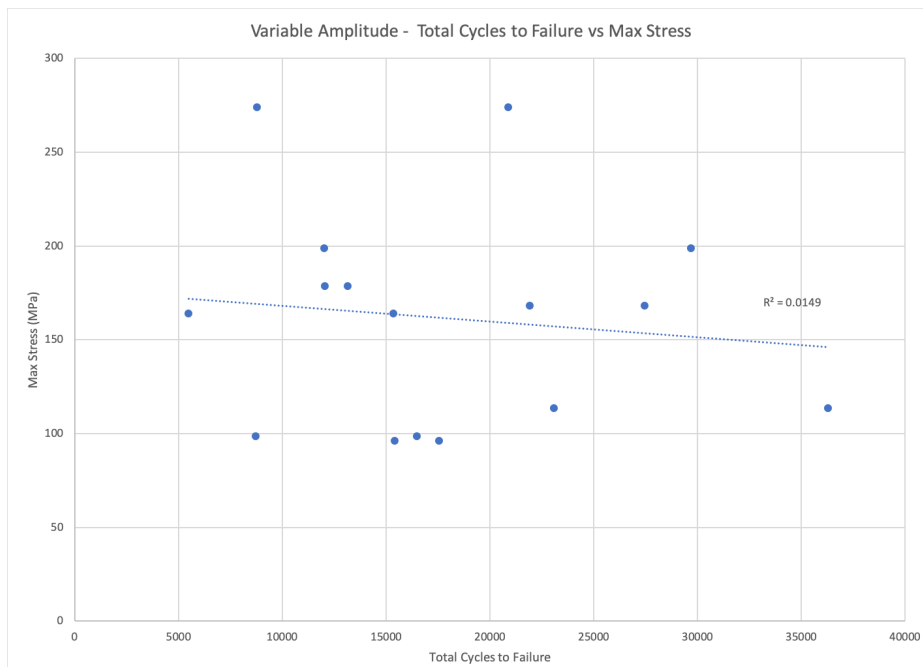


Figure D.62 – Variable amplitude total cycles to failure vs. max stress.

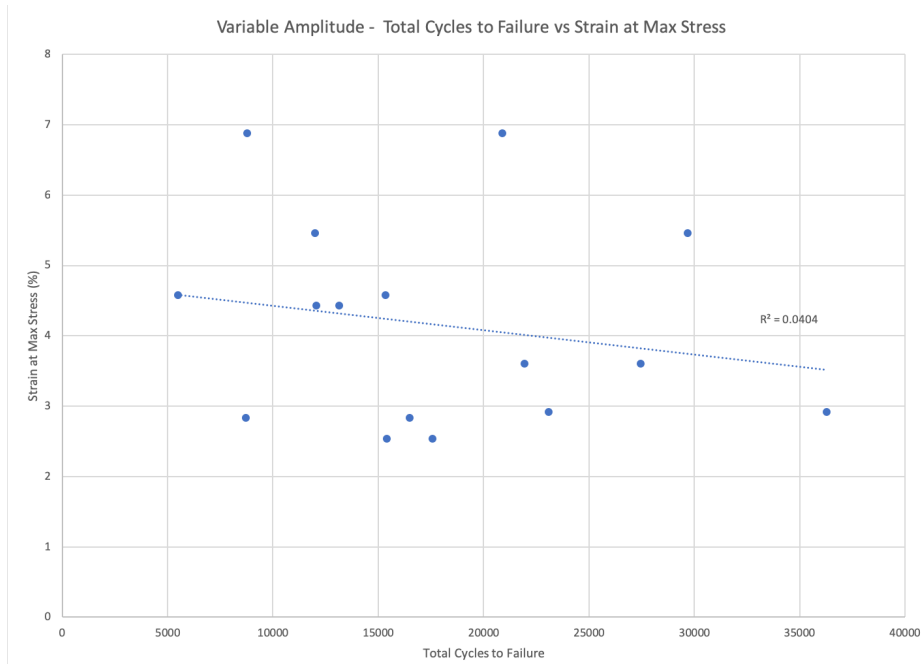


Figure D.63 – Variable amplitude total cycles to failure vs. strain at max stress

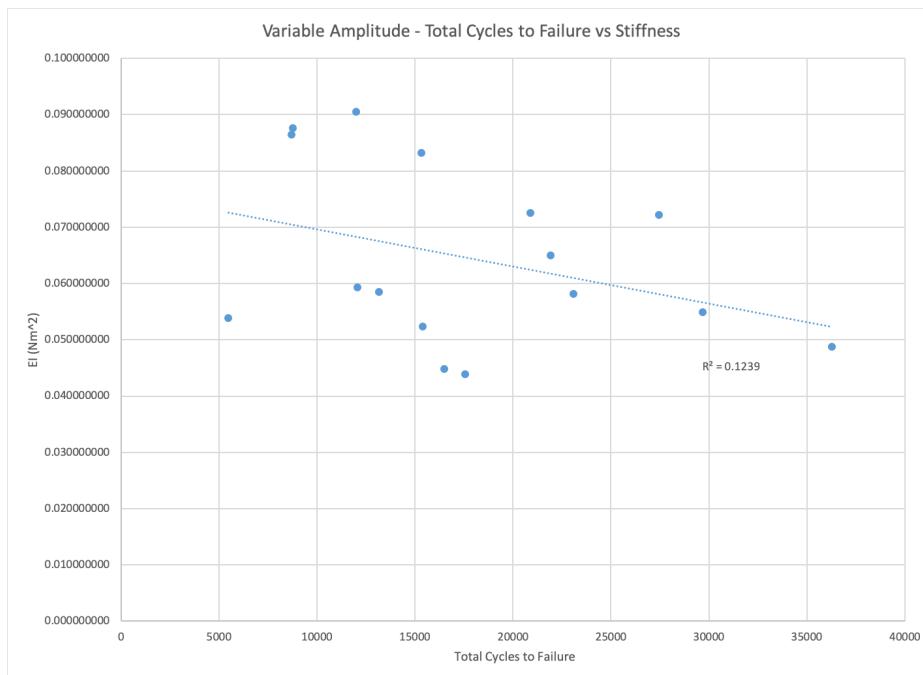


Figure D.64 – Variable amplitude total cycles to failure vs. stiffness.

Table D.3 – Data table from variable amplitude correlations.

| Variable Amplitude Comparisons | | | | |
|--------------------------------|-------------------------|---------------|------------------|--------------------------|
| Specimen | Total Cycles to Failure | Modulus (GPa) | Max Stress (MPa) | Strain at Max Stress (%) |
| 3B | 29690 | 5.51 | 198.77 | 5.46 |
| 3C | 12011 | 5.51 | 198.77 | 5.46 |
| 4B | 13149 | 5.74 | 178.75 | 4.43 |
| 4C | 12052 | 5.74 | 178.75 | 4.43 |
| 5B | 16479 | 4.34 | 98.66 | 2.83 |
| 5C | 8713 | 4.34 | 98.66 | 2.83 |
| 6B | 15402 | 4.68 | 96.26 | 2.54 |
| 6C | 17565 | 4.68 | 96.26 | 2.54 |
| 7B | 27448 | 6.43 | 168.17 | 3.60 |
| 7C | 21925 | 6.43 | 168.17 | 3.60 |
| 8B | 5483 | 5.74 | 164.22 | 4.58 |
| 8C | 15341 | 5.74 | 164.22 | 4.58 |
| 9B | 8769 | 6.75 | 273.97 | 6.88 |
| 9C | 20889 | 6.75 | 273.97 | 6.88 |
| 10B | 36271 | 5.01 | 113.57 | 2.92 |
| 10C | 23077 | 5.01 | 113.57 | 2.92 |

Table D.4 – Data table from variable amplitude stiffness correlation.

| Variable Amplitude Stiffness Comparison | | | | | | | | |
|---|-------------------------|---------------|--------------|----------------|------------|-----------------------------------|----------------------------------|-----------------------|
| Specimen | Total Cycles to Failure | Modulus (GPa) | Modulus (Pa) | Thickness (in) | Width (in) | I _x (in ⁴) | I _x (m ⁴) | EI (Nm ²) |
| 3B | 29690.0 | 5.51 | 5.51E+09 | 0.0950 | 0.3354 | 2.40E-05 | 9.97E-12 | 0.055 |
| 3C | 12011.0 | 5.51 | 5.51E+09 | 0.1110 | 0.3465 | 3.95E-05 | 1.64E-11 | 0.091 |
| 4B | 13149.0 | 5.74 | 5.74E+09 | 0.0955 | 0.3376 | 2.45E-05 | 1.02E-11 | 0.059 |
| 4C | 12052.0 | 5.74 | 5.74E+09 | 0.0972 | 0.3246 | 2.48E-05 | 1.03E-11 | 0.059 |
| 5B | 16479.0 | 4.34 | 4.34E+09 | 0.0970 | 0.3260 | 2.48E-05 | 1.03E-11 | 0.045 |
| 5C | 8713.0 | 4.34 | 4.34E+09 | 0.1200 | 0.3322 | 4.78E-05 | 1.99E-11 | 0.086 |
| 6B | 15402.0 | 4.68 | 4.68E+09 | 0.0980 | 0.3425 | 2.69E-05 | 1.12E-11 | 0.052 |
| 6C | 17565.0 | 4.68 | 4.68E+09 | 0.0922 | 0.3448 | 2.25E-05 | 9.37E-12 | 0.044 |
| 7B | 27448.0 | 6.43 | 6.43E+09 | 0.0980 | 0.3437 | 2.70E-05 | 1.12E-11 | 0.072 |
| 7C | 21925.0 | 6.43 | 6.43E+09 | 0.0960 | 0.3296 | 2.43E-05 | 1.01E-11 | 0.065 |
| 8B | 5483.0 | 5.74 | 5.74E+09 | 0.0930 | 0.3360 | 2.25E-05 | 9.37E-12 | 0.054 |
| 8C | 15341.0 | 5.74 | 5.74E+09 | 0.1090 | 0.3227 | 3.48E-05 | 1.45E-11 | 0.083 |
| 9B | 8769.0 | 6.75 | 6.75E+09 | 0.1050 | 0.3234 | 3.12E-05 | 1.30E-11 | 0.088 |
| 9C | 20889.0 | 6.75 | 6.75E+09 | 0.0985 | 0.3241 | 2.58E-05 | 1.07E-11 | 0.073 |
| 10B | 36271.0 | 5.01 | 5.01E+09 | 0.0938 | 0.3404 | 2.34E-05 | 9.74E-12 | 0.049 |
| 10C | 23077.0 | 5.01 | 5.01E+09 | 0.1000 | 0.3349 | 2.79E-05 | 1.16E-11 | 0.058 |

APPENDIX E

MATLAB Code

ResonantFrequencyLVM.m

```
%This program plots the frequency of the .lvm file outputted by LabView  
%It uses the 'RFreadColData.m' file to call in the data file
```

```
clear clc
```

```
%Define file you want to call
```

```
fname=input('Laser Data File Name ');
```

```
%Call text and dat files%LTo is the Laser original time, Volt is the  
laser voltage [labels,LTo,Volt] = readColData(fname,2,0,0);
```

```
Fs=200;t=0:1/Fs;x=Volt;figure pwelch(x,[],[],[],Fs,'onesided');
```

LaserLabViewCUTv2.m

```
clc
close all

%Gets file you want to call
[fn,~]=uigetfile('*.');
A = strsplit(fn, '.');
fname = A(1,1);
%Name .txt file from original and convert to str
filename = strcat(fname, '.txt');
filename = filename{1};

A = importdata(fn);

%LTo is the Laser original time, Volt is the laser voltage
LTo = A(:,1);
Volt = A(:,2);

%Set Laser actual time (LT)
%LT is the Laser zeroed time
LT = zeros(length(LTo),1);

for x=1:length(LTo)
    LT(x)=LTo(x)-LTo(1);
end

%Zero the voltage outputted by the laser
V = zeros(length(Volt),1);

for x=1:length(Volt)
    V(x)=Volt(x)-Volt(1);
end

VV=reshape(V,length(V),1);

%Graph all figures
figure;
%Plot
plot(LT,VV, 'r');
xlabel('Time (sec)');
ylabel('Volt');
title('Volt vs Time');
axis tight;

%What needs to be trimmed?
Dbefore = input('Delete data before time ');
Dafter = input('Delete data after time ');

%Trim using index
[~,idxDb] = ismember(Dbefore,LTo); [~,idxDa] = ismember(Dafter,LTo);
LT = LTTo(idxDb:idxDa)';
TVolt = Volt(idxDb:idxDa)';
```

```
Data = [LT; TVolt];  
  
%Save as .txt file  
fid=fopen(filename, 'w');  
fprintf(fid, '%12.3f %12.6f\r\n', Data);  
fclose(fid);
```

rainflow_bins_mod3.m

```
% This code creates the histogram with 0.25 mm bin sizes
%Creator info
%
% rainflow_bins.m ver 2.1 September 20, 2013
% by Tom Irvine Email: tom@vibrationdata.com
% ASTM E 1049-85 (2005) Rainflow Counting Method
%
% What follows is a modified version of Mr. Irvine's code
% Updated: Marcus Hurtado (2018)
%
close all;
clear all;
%
%To know how long the code took to run
tic
%
fig_num=1;
%
%Define file you want to call
[fname,~]=uigetfile('*.');
A = strsplit(fname, '.');
fname2 = A(1,1);

%Call .lvm file

A = importdata(fname);
LTo = A(:,1);
Volt = A(:,2);

%LTo is the Laser original time, Volt is the laser voltage
%
y=double(Volt);
m=length(y)-1;
a=zeros(m,1); % max and mins
t=zeros(m,1); % loc a
a(1)=y(1);
t(1)=1;
k=2;
%
%Slope calculation
% TO SPEED UP MAYBE CHANGE TO DIFF( <-----
-----
slope1=(y(2)-y(1));
for i=2:m
    slope2=(y(i+1)-y(i));
    if((slope1*slope2)<=0)
        a(k)=y(i);
        t(k)=i;
        k=k+1;
    end
    slope1=slope2;
end
%
a(k)=y(m+1);
```

```

t(k)=t(k-1)+1;
k=k+1;
%
clear temp;
temp(1:k-1)=a(1:k-1);
clear a;
a=temp;
%
clear temp;
temp(1:k-1)=t(1:k-1);
clear t;
t=temp;
%
% ensuring column vector
sza=size(a);
if(sza(2)>sza(1))
    a=a';
end
szt=size(t);
if(szt(2)>szt(1))
    t=t';
end
aa=[t a];
%
%%%%%%%%%%%%%%%%%%%%%%%%%%%%%%%%%%%%%%%%%%%%%%%%%%%%%%%%%%%%%%%%%%%%%%%%
%%
% Rules for this method are as follows: let X denote
% range under consideration; Y, previous range adjacent to X
%%%%%%%%%%%%%%%%%%%%%%%%%%%%%%%%%%%%%%%%%%%%%%%%%%%%%%%%%%%%%%%%%%%%%%%%
%%
%
n=1;
i=1;
j=2;
%
aamax=0;
B=zeros(m,4);
a_mean=zeros(m,2);
kv=1;
msa_orig=max(size(aa));
% matrix of cycles
while(1)
    msa=max(size(aa)); % # rows in aa (continually
decreasing)...
%
    if((j+1)>=msa)
        break; % 1 value at start or at the
end --> exit loop
end
    if((i+1)>=msa)
        break;
end
%
    Y=(abs(aa(i,2)-aa(i+1,2))); % Prev. R
    X=(abs(aa(j,2)-aa(j+1,2))); % Consider
%
    if(Y<=1)
        aa(i,:)=[]; % clear noise

```

```

        i=1;
        j=2;
    else
        if(X<=1)
            aa(j:j+1,:)=[];
            i=1;
            j=2;
        else
            % create matrix for bin sorting
            B(kv,2)=0.5;
            am=[aa(i,2) aa(i+1,2)];
            B(kv,3)=am(1);
            B(kv,4)=am(2);
            aa(1,:)=[];
            B(kv,1)=Y;
            if(Y>aamax)
                p1=aa(i,2);
                p2=aa(i+1,2);
                tp1=aa(i,1);
                tp2=aa(i+1,1);
                aamax=Y;
            end
            kv=kv+1;
            i=1;
            j=2;
        end
    end
end
%
% Count each range that has not been previously counted
%
N=max(size(aa));
disp(' ');
for i=(N-1)
    Y=(abs(aa(i,2)-aa(i+1,2)));
    %
    if(Y>1)
        B(kv,1)=Y;
        B(kv,2)=0.5;
        am=[aa(i,2) aa(i+1,2)];
        B(kv,3)=am(1);
        B(kv,4)=am(2);
        if(Y>aamax)
            p1=aa(i,2);
            p2=aa(i+1,2);
            tp1=aa(i,1);
            tp2=aa(i+1,1);
            aamax=Y;
        end
        kv=kv+1;
    end
end
end
%
%Bin sorting
% aamax=max(B(:,1));
% recall, 1 V = 1 mm
L = [0:0.25:20];
%
num=max(size(L))-1;

```

```

C=zeros(num,1);
%
AverageMean=zeros(num,1);
MaxMean=ones(num,1);
MinMean=ones(num,1);
%
MaxPeak=ones(num,1);
MinValley=ones(num,1);
%
MaxAmp=zeros(num,1);
AverageAmp=zeros(num,1);
%
kvn=kv-1;
%
for i=1:kvn
    for ijk=1:num
        Y=B(i,1);
        if(Y>=L(ijk) && Y<=L(ijk+1))
            C(ijk)=C(ijk)+B(i,2);
            bm=(B(i,3)+B(i,4))/2;
            if(B(i,3)>MaxPeak(ijk))
                MaxPeak(ijk)=B(i,3);
            end
            if(B(i,4)>MaxPeak(ijk))
                MaxPeak(ijk)=B(i,4);
            end
            if(B(i,3)<MinValley(ijk))
                MinValley(ijk)=B(i,3);
            end
            if(B(i,4)<MinValley(ijk))
                MinValley(ijk)=B(i,4);
            end
        end
        %
        AverageAmp(ijk)=AverageAmp(ijk)+B(i,1)*B(i,2);
        AverageMean(ijk)=AverageMean(ijk)+bm*B(i,2);
        %
        if( bm > MaxMean(ijk))
            MaxMean(ijk)=bm;
        end
        if( bm < MinMean(ijk))
            MinMean(ijk)=bm;
        end
        %
        if(B(i,1)>MaxAmp(ijk))
            MaxAmp(ijk)=B(i,1);
        end
    end
end
end
for ijk=1:num
    if( C(ijk)>0)
        AverageAmp(ijk)=AverageAmp(ijk)/C(ijk);
        AverageMean(ijk)=AverageMean(ijk)/C(ijk);
    end
end
%
N=max(size(C));
BIG=zeros(N,10);

```

```

disp(' ');
disp('      Range = (peak-valley) ');
disp('  Amplitude = (peak-valley)/2 ');
disp(' ');
disp('      Range Limits      Cycle      Average      Max
Min  Average  Max  Min      Max ');
disp('      (units)      Counts      Amp      Amp
Mean  Mean      Mean Valley Peak');
%
MaxAmp=MaxAmp/2;
AverageAmp=AverageAmp/2;
%
for i=1:N
    j=N+1-i;
%
    if(C(j)==0)
        AverageAmp(j)=0.;
        MaxAmp(j)=0.;
        MinMean(j)=0.;
        AverageMean(j)=0.;
        MaxMean(j)=0.;
        MinValley(j)=0.;
        MaxPeak(j)=0.;
    end
%
    out1=sprintf('\t %7.4g to %7.4g \t %g \t %6.3g \t %6.3g \t
%6.3g\t %6.3g\t %6.3g\t %6.3g\t
%6.3g',L(j),L(j+1),C(j),AverageAmp(j),MaxAmp(j),MinMean(j),AverageMean(
j),MaxMean(j),MinValley(j),MaxPeak(j));
%
    disp(out1);
    BIG(i,1)=L(j);
    BIG(i,2)=L(j+1);
    BIG(i,3)=C(j);
    BIG(i,4)=AverageAmp(j);
    BIG(i,5)=MaxAmp(j);
    BIG(i,6)=MinMean(j);
    BIG(i,7)=AverageMean(j);
    BIG(i,8)=MaxMean(j);
    BIG(i,9)=MinValley(j);
    BIG(i,10)=MaxPeak(j);
end
%
out1=sprintf('\n  Max Range=%6.3g ',aamax);
disp(out1);
%
TC=sum(C);
%
out1=sprintf('\n Total Cycles =%g \n',TC);
disp(out1);
disp(' ');
%
fig_num=1;
figure(fig_num);
fig_num=fig_num+1;
plot(y);
grid on;
%

```

```
figure(fig_num);
fig_num=fig_num+1;
h=bar(C);
grid on;
title(fname2);
ylabel('Cycle Counts');
xlabel('Range: 0-20 mm with 0.25 mm bins');
set(gca, 'FontName', 'Times New Roman');
%
toc
```

rainflow_bins_mod4.m

```
% This code creates the histogram with 3 bins
%Creator info
%
% rainflow_bins.m ver 2.1 September 20, 2013
% by Tom Irvine Email: tom@vibrationdata.com
% ASTM E 1049-85 (2005) Rainflow Counting Method
%
% What follows is a modified version of Mr. Irvine's code
% Updated: Marcus Hurtado (2018)

close all;
clear all;
%
%To know how long the code took to run
tic
%
fig_num=1;
%
%Define file you want to call

[fname,~]=uigetfile('*.');
A = strsplit(fname, '.');
fname2 = A(1,1);
filename = fname2;

%Call .lvm file

A = importdata(fname);
LTo = A(:,1);
Volt = A(:,2);

%LTo is the Laser original time, Volt is the laser voltage
%
y=double(Volt);
m=length(y)-1;
a=zeros(m,1); % for max and mins
t=zeros(m,1); % for loc a
a(1)=y(1);
t(1)=1;
k=2;
%
%Slope calculation
% TO SPEED UP MAYBE CHANGE TO DIFF( <-----
-----
slope1=(y(2)-y(1));
for i=2:m
    slope2=(y(i+1)-y(i));
    if((slope1*slope2)<=0)
        a(k)=y(i); % max and mins
        t(k)=i; % loc a
        k=k+1;
    end
    slope1=slope2;
end
end
```

```

%
a(k)=y(m+1);
t(k)=t(k-1)+1;
k=k+1;
%
clear temp;
temp(1:k-1)=a(1:k-1);
clear a;
a=temp;
%
clear temp;
temp(1:k-1)=t(1:k-1);
clear t;
t=temp;
%
% ensuring column vector
sza=size(a);
if(sza(2)>sza(1))
    a=a';
end
szt=size(t);
if(szt(2)>szt(1))
    t=t';
end
aa=[t a];
%
%{
%%%%%%%%%%%%%%%%%%%%%%%%%%%%%%%%%%%%%%%%%%%%%%%%%%%%%%%%%%%%%%%%%%%%%%%%
%%%%
figure(fig_num);
fig_num=fig_num+1;
hold on;
%plot(y);
% temp figure to check how the code is working!!!
plot(a, '-o');
hold off;
grid on;
%%%%%%%%%%%%%%%%%%%%%%%%%%%%%%%%%%%%%%%%%%%%%%%%%%%%%%%%%%%%%%%%%%%%%%%%
%%%%
%}
%
% Rules for this method are as follows: let X denote
% range under consideration; Y, previous range adjacent to X
%
n=1;
i=1;
j=2;
%
aamax=0;
B=zeros(m,4);
a_mean=zeros(m,2);
kv=1;
msa_orig=max(size(aa));
% matrix of cycles
while (1)
    msa=max(size(aa));
    decreasing)...
    % # rows in aa (continually
%

```

```

        if((j+1)>=msa)
            break; % 1 value at start or at the
end --> exit loop
end
if((i+1)>=msa)
    break;
end
%
Y=(abs(aa(i,2)-aa(i+1,2))); % Prev. R
X=(abs(aa(j,2)-aa(j+1,2))); % Consider
%
if Y<=1
    aa(i+1,:)=[]; % clear noise
    i=1;
    j=2;
else
    if X<=1
        aa(j:j+1,:)=[];
        i=1;
        j=2;
    else % create matrix for bin sorting
        B(kv,2)=0.5;
        am=[aa(i,2) aa(i+1,2)];
        B(kv,3)=am(1);
        B(kv,4)=am(2);
        aa(1,:)=[];
        B(kv,1)=Y;
        if(Y>aamax)
            p1=aa(i,2);
            p2=aa(i+1,2);
            tp1=aa(i,1);
            tp2=aa(i+1,1);
            aamax=Y;
        end
        kv=kv+1;
        i=1;
        j=2;
    end
end
end
%
%
% Count each range that has not been previously counted
%
N=max(size(aa));
disp(' ');
for i=(N-1)
    Y=(abs(aa(i,2)-aa(i+1,2)));
    %
    if(Y>1)
        B(kv,1)=Y;
        B(kv,2)=0.5;
        am=[aa(i,2) aa(i+1,2)];
        B(kv,3)=am(1);
        B(kv,4)=am(2);
        if(Y>aamax)
            p1=aa(i,2);
            p2=aa(i+1,2);

```

```

        tp1=aa(i,1);
        tp2=aa(i+1,1);
        aamax=Y;
    end
    kv=kv+1;
end
end
%}
%
%Bin sorting
% aamax=max(B(:,1));
% recall, 1 V = 1 mm
L = [1 7.5 10 20];
%
num=max(size(L))-1;
C=zeros(num,1);
%
AverageMean=zeros(num,1);
MaxMean=ones(num,1);
MinMean=ones(num,1);
%
MaxPeak=ones(num,1);
MinValley=ones(num,1);
%
MaxAmp=zeros(num,1);
AverageAmp=zeros(num,1);
%
kvn=kv-1;
%
for i=1:kvn
    for ijk=1:num
        Y=B(i,1);
        if(Y>=L(ijk) && Y<=L(ijk+1))
            C(ijk)=C(ijk)+B(i,2);
            bm=(B(i,3)+B(i,4))/2;
            if(B(i,3)>MaxPeak(ijk))
                MaxPeak(ijk)=B(i,3);
            end
            if(B(i,4)>MaxPeak(ijk))
                MaxPeak(ijk)=B(i,4);
            end
            if(B(i,3)<MinValley(ijk))
                MinValley(ijk)=B(i,3);
            end
            if(B(i,4)<MinValley(ijk))
                MinValley(ijk)=B(i,4);
            end
        end
        %
        AverageAmp(ijk)=AverageAmp(ijk)+B(i,1)*B(i,2);
        AverageMean(ijk)=AverageMean(ijk)+bm*B(i,2);
        %
        if( bm > MaxMean(ijk))
            MaxMean(ijk)=bm;
        end
        if( bm < MinMean(ijk))
            MinMean(ijk)=bm;
        end
    end
end
%

```

```

                if(B(i,1)>MaxAmp(ijk))
                    MaxAmp(ijk)=B(i,1);
                end
            end
        end
    end
    for ijk=1:num
        if( C(ijk)>0)
            AverageAmp(ijk)=AverageAmp(ijk)/C(ijk);
            AverageMean(ijk)=AverageMean(ijk)/C(ijk);
        end
    end
    end
    %
    N=max(size(C));
    BIG=zeros(N,10);
    disp(' ');
    disp('      Range = (peak-valley) ');
    disp('  Amplitude = (peak-valley)/2 ');
    disp(' ');
    disp('      Range Limits      Cycle      Average      Max
Min   Average   Max   Min   Max ');
    disp('      (units)      Counts      Amp      Amp
Mean   Mean   Mean   Valley   Peak');
    %
    MaxAmp=MaxAmp/2;
    AverageAmp=AverageAmp/2;
    %
    for i=1:N
        j=N+1-i;
        %
        if(C(j)==0)
            AverageAmp(j)=0.;
            MaxAmp(j)=0.;
            MinMean(j)=0.;
            AverageMean(j)=0.;
            MaxMean(j)=0.;
            MinValley(j)=0.;
            MaxPeak(j)=0.;
        end
        %
        out1=sprintf('\t %7.4g to %7.4g \t %g \t %6.3g \t %6.3g \t
%6.3g\t %6.3g\t %6.3g\t %6.3g\t
%6.3g',L(j),L(j+1),C(j),AverageAmp(j),MaxAmp(j),MinMean(j),AverageMean(
j),MaxMean(j),MinValley(j),MaxPeak(j));
        %
        disp(out1);
        BIG(i,1)=L(j);
        BIG(i,2)=L(j+1);
        BIG(i,3)=C(j);
        BIG(i,4)=AverageAmp(j);
        BIG(i,5)=MaxAmp(j);
        BIG(i,6)=MinMean(j);
        BIG(i,7)=AverageMean(j);
        BIG(i,8)=MaxMean(j);
        BIG(i,9)=MinValley(j);
        BIG(i,10)=MaxPeak(j);
    end
    %

```

```

out1=sprintf('\n Max Range=%6.3g ',aamax);
disp(out1);
%
TC=sum(C);
%
out1=sprintf('\n Total Cycles =%g \n',TC);
disp(out1);
disp(' ');
%
figure(fig_num);
fig_num=fig_num+1;
plot(y);
title(filename);
xlabel('Time');
ylabel('Volts');
set(gca, 'FontName', 'Times New Roman');
grid on;
%
figure(fig_num);
fig_num=fig_num+1;
h=bar(C);
grid on;
title(filename);
ylabel('Cycle Counts');
xlabel('Range');
set(gca, 'FontName', 'Times New Roman');
%
toc

```

SpeedPMR.m

```
% Speed Funtion by MH 2018

function [EnduranceLimit,Dapredict,Da,delDa,T] = SpeedPMR(cycles)

[r,~] = size(cycles);
n1=cycles(:,1);
n2=cycles(:,2);
n3=cycles(:,3);

% n1 = large amp
% n2 = medium amp
% n3 = small amp

%Cycles to failure at different amplitudes determined via CAL tests
%N1=Number of cycles to failure under S1
N1=9970;
%N2=Number of cycles to failure under S2
N2=39632;
%N3=Number of cycles to failure under S3
N3=138021;

%initializing for speed
Da = zeros(r,1);
EnduranceLimit = zeros(r,1);
delDa = zeros(r,1);
Dapredict = zeros(r,1);
n1u = zeros(r,1);
n2u = zeros(r,1);
n3u = zeros(r,1);

for i = 1:r
%Da=sumation of ni/Ni---At the average Endurance Limit
Da(i) = (n1(i)/N1)+(n2(i)/N2)+(n3(i)/N3);
EnduranceLimit(i) = (n1(i)+n2(i)+n3(i));

% Uncertainty
n1u(i) = (n1(i)/N1)*(4527/N1);
n2u(i) = (n2(i)/N2)*(14517/N2);
n3u(i) = (n3(i)/N3)*(18686/N3);
delDa(i) = sqrt(n1u(i).^2+n2u(i).^2+n3u(i).^3);

Dapredict(i) = EnduranceLimit(i)./Da(i);
end

% figure out if it went outside of limit of 1
xlow = Da-delDa;
xhigh = Da+delDa;

% Allocating for speed
T = zeros(r,1);
```

```
for i=1:r
    if xlow(i)<1 && xhigh(i)>1
        T(i)=1; %T = 1 means true
    elseif xlow(i)==1 || xhigh(i)==1
        T(i)=1;
    else
        T(i)=0; %T = 0 means false
    end
end
T=T';

end
```

PSW_protocool2v2.m

```
% protocol
%%
% load data and assign it to x
% Define file you want to call
% slight edits by MH 2018

close all
clear all
clc

[fname,~]=uigetfile('*.');
A = strsplit(fname, '.');
fname2 = A(1,1);
filename = strcat(fname2, ' PSW');
filename = filename{1};
% Call .lvm file
A = importdata(fname);

LTo = A(:,1);
Volt = A(:,2);

% remove mean
x1 = Volt-mean(Volt);
% filter signal
d = designfilt('lowpassfir', 'FilterOrder', 100, ...
    'CutoffFrequency', 15, 'SampleRate', 200, ...
    'Window', 'hamming');
x = filtfilt(d,x1);
%
% average mutual information to get delay time
figure
ami(x,8000,60,32); % get delay time
disp(' ')
disp('Assign delay.') % determined from 1st minimum in ami
m = input('enter 1st minimum value ');
disp(' ')
%
% false nearest neighbors search to get embedding dimension
figure
nn = false_neighbors_kd(x, m, 6, 8000); % get embedding dimension
plot_false_neighbors(nn,10,0.5)
disp(' ')
disp('Assign embedding dimension.')
d = input('enter dimension when fnns=0 ');
disp(' ')
%
%%
%%%%%%%%%%%%%%%%%%%%%%%%%%%%%%%%%%%%%%%%%%%%%%%%%%%%%%%%%%%%%%%%%%%%%%%%%% Where do these values come
from???
nm = 8000; % decide the reference model size
nb = 32; % decide how many boxes you need in the phase space
nn = 20; % decide how many points to use for local linear model
step = 1; % model prediction time
mtr = 0; % use scalar tracking metric
```

```

r1 = 2000; % decide how many points you need in each record
n = length(x); % total number of points in your data set (reconstructed
phase space)
nr = floor(n/r1); % decide how many records you need overall
%%
prpr = 1; % 0 if no preprocessing needed, otherwise 1
%%
%
% now get the tracking matrix
Y = psw_cont(x, m, d, nm, nb, nn, step, mtr, r1, nr, prpr);
%
% now analyze tracking matrix using new method
DY = diff(Y);
Y = Y(1:end-1,:);
for k = 1:size(Y,2)
    Y(:,k) = Y(:,k) - mean(Y(:,k));
    DY(:,k) = DY(:,k) - mean(DY(:,k));
end
Syy = Y.'*Y/(size(Y,1)-1);
Sydy = Y.'*DY/(size(Y,1)-1);
[P,E] = eig(Syy,Sydy);
ev = diag(E);
k = 1;
Pn = P;
while k < size(E,2)
    if ~isreal(ev(k))
        Pn(:,k) = (P(:,k) + P(:,k+1))/2;
        Pn(:,k+1) = (P(:,k) - P(:,k+1))/2/1i;
        k = k + 2;
    else
        k = k + 1;
    end
end
roc = Y*Pn;
figure
semilogy(abs(ev),'o'), xlabel('ev index'), ylabel('ev')
filename2 = strcat(filename, ' ev index');
% filename2 = filename2{1};
saveas(gcf,filename2,'png')

figure
for i = 1:16
    subplot(4,4,i)
    plot(roc(:,i)), xlabel('record number'), ylabel(['roc '
num2str(i)])
    axis tight
end
filename3 = strcat(filename, ' roc');
% filename3 = filename3{1};
saveas(gcf,filename3,'png')

% old analysis
[U,V,X,C,S] = gsvd(Y,DY);
soc = fliplr(U*C);
sov = flipud(diag(C'*C)./diag(S'*S));

```

```

figure
semilogy(sov,'o'), xlabel('soc index'), ylabel('sov')
filename4 = strcat(filename,' soc index');
% filename4 = filename4{1};
saveas(gcf,filename4,'png')

figure
for i = 1:16
    subplot(4,4,i)
    plot(soc(:,i)), xlabel('record number'), ylabel(['soc '
num2str(i)])
    axis tight
end
filename5 = strcat(filename,' soc');
% filename5 = filename5{1};
saveas(gcf,filename5,'png')

%% Its Done!!!

load train
sound(y,Fs)
%}

```

PSW Code Set

The PSW codes were developed by Dr. Chelidze at the University of Rhode Island. His complete catalog of codes may be found at <http://egr.uri.edu/nld/software/>

Four_Point_Bend_Analysis.m

```
% Plot Stress vs Strain
% Find max stress
% Find strain at max stress
% Determine modulus

%% Load in data

%Gets file you want to call
[fn,~]=uigetfile('*.');
A = strsplit(fn, '.');
fname = A(1,1);
%Name .txt file from original and convert to str
filename = strcat(fname, '.mat');
filename = filename{1};

A = importdata(fn);

% Desired Variables
Strain = A(:,1);
Stress = A(:,2); % MPa

%% Plot
plot(Strain,Stress)

figure(1)
xlabel('Strain');
ylabel('Stress (MPa)');
filename1 = strcat(fname, ' Stress vs Strain');
filename1 = filename1{1};
title(filename1);
saveas(gcf,filename1, 'png')

%% Find maximums

[max_stress,I] = max(Stress);
strain_at_max_stress = Strain(I,1);

fprintf('\nmax stress value: %6.4f',max_stress)
fprintf('\nstrain at max stress: %6.4f\n\n',strain_at_max_stress)

%% Find Modulus
```

```

Dbefore = input('Delete data before time ');
Dafter = input('Delete data after time ');

%Trim using index

start = find(Strain<Dbefore,1,'last');
final = find(Strain<Dafter,1,'last');

Strain2 = Strain(start:final);
Stress2 = Stress(start:final);

% linear fit
xl=Strain2; % linearizing
yl=Stress2;

N=length(Strain2);
xo=linspace(min(xl),max(xl));

z=[ones(N,1),xl]; % solving
B=(z'*z)\(z'*yl);
A=[B(1),B(2)]; % drawing out a0 and a1
fl=A(1)+xo*A(2); % linear fit

St = sum((sum(yl)/N - yl).^2);
Sr = sum((yl - (B(1)+B(2)*xl)).^2);
r2l = (St-Sr)/St; % r^2 value linear

fprintf('\nslope value: %6.4f',A(2))
fprintf('\nr^2 value linear fit: %6.4f\n\n',r2l)

figure(2)
plot(Strain,Stress)
hold on
plot(Strain2,Stress2,'ro','MarkerSize',12)
plot(xo,fl,'k','LineWidth',4)
xlabel('Strain');
ylabel('Stress (MPa)');
filename2 = strcat(fname,' Stress vs Strain Linear Regression');
filename2 = filename2{1};
title(filename2);
% saveas(gcf,filename2,'png')

%% Save data
Data(:,1) = Strain;
Data(:,2) = Stress;
Data(1,3) = A(2);
Data(1,4) = max_stress;
Data(1,5) = strain_at_max_stress;

save(filename,'Data')

```

NI LabVIEW VI Programs

WaveGeneration.vi

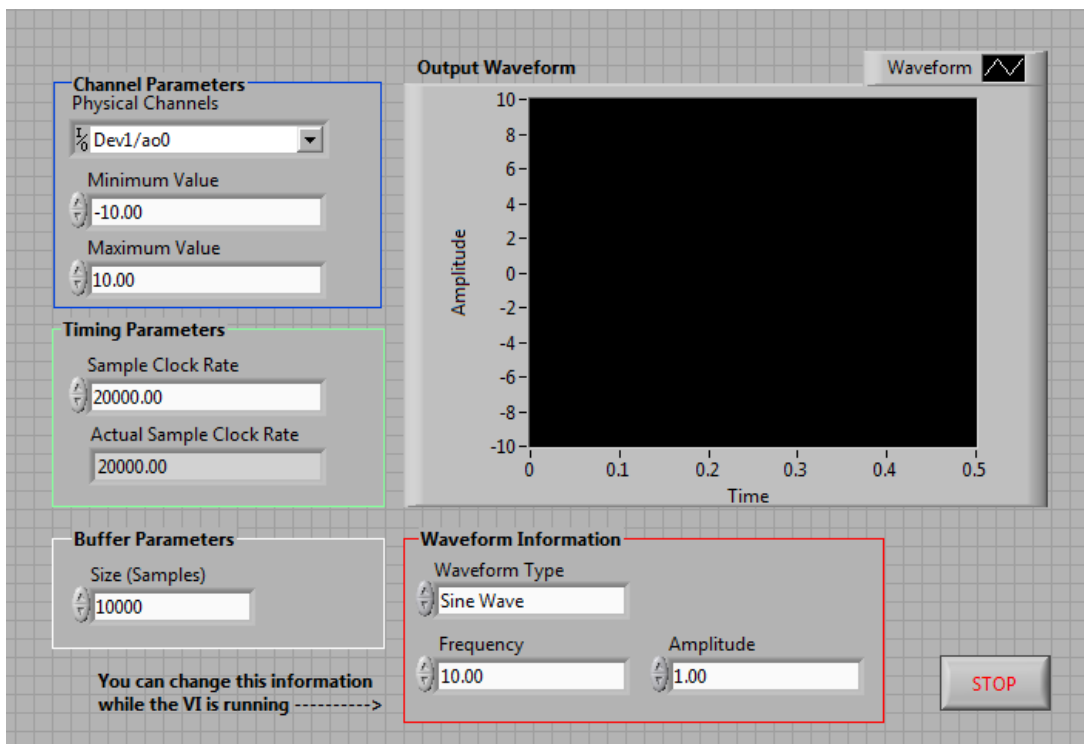


Figure E.1. – GUI interface of WaveGeneration.vi

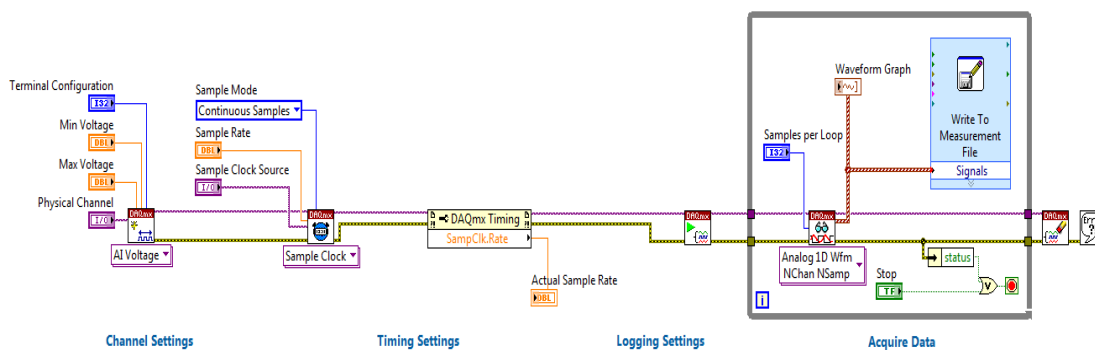


Figure E.2. – Block code of WaveGeneration.vi

Variable AmplitudeWaveGeneration-VoltageOutput.vi

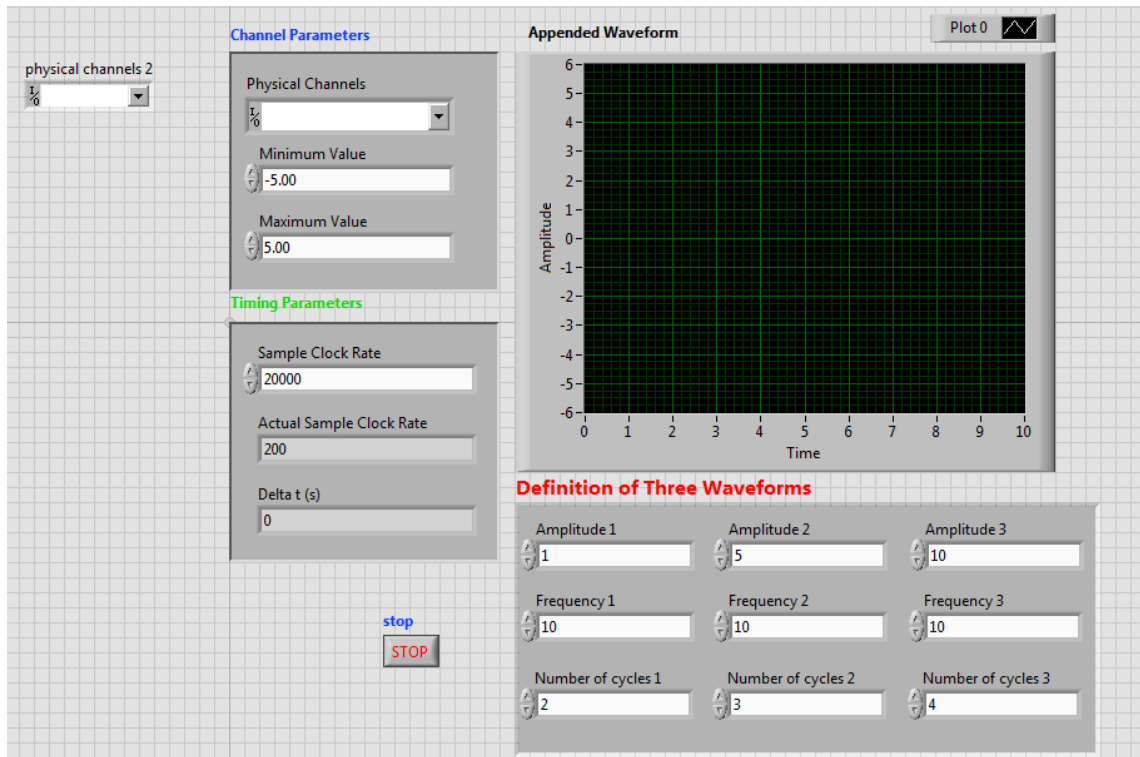


Figure E.3. – GUI of VariableAmplitudeWaveGeneration-VoltageOutput.vi

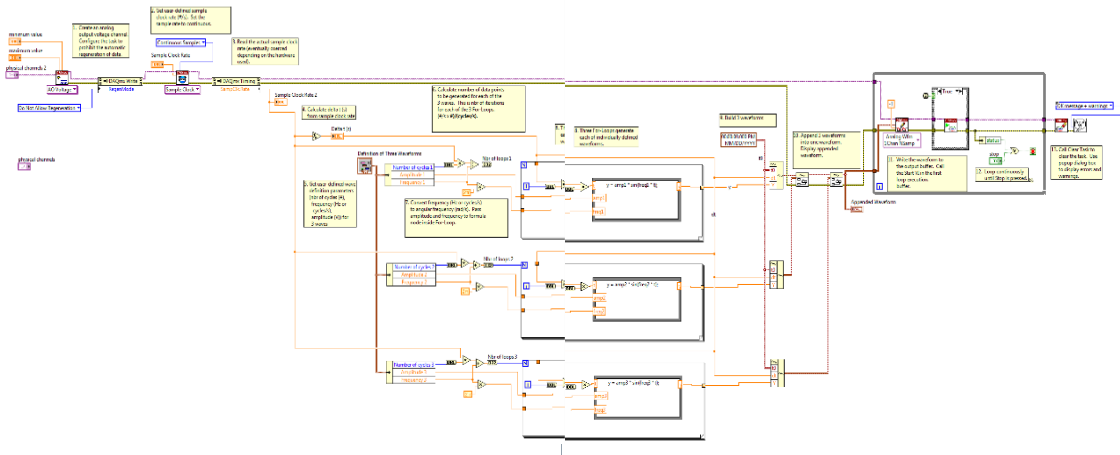


Figure E.4. – Block code of VariableAmplitudeWaveGeneration-VoltageOutput.vi

LASER-Voltage-ContinuousInput.vi

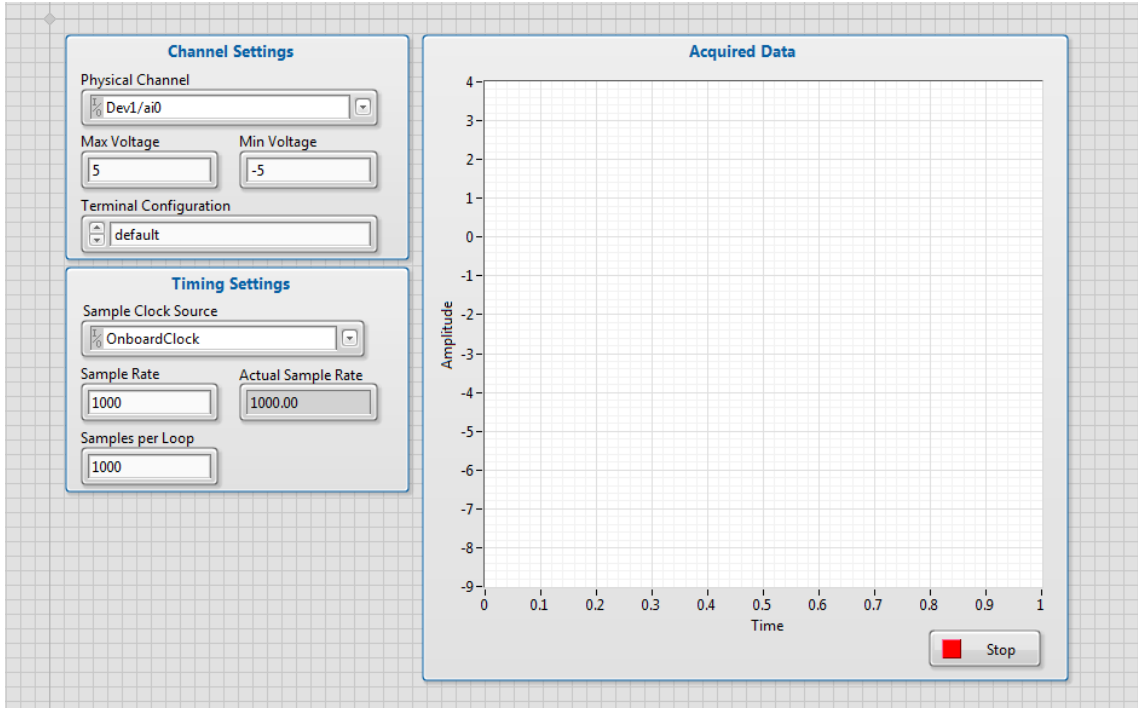


Figure E.5. – GUI of LASER-Voltage-ContinuousInput.vi

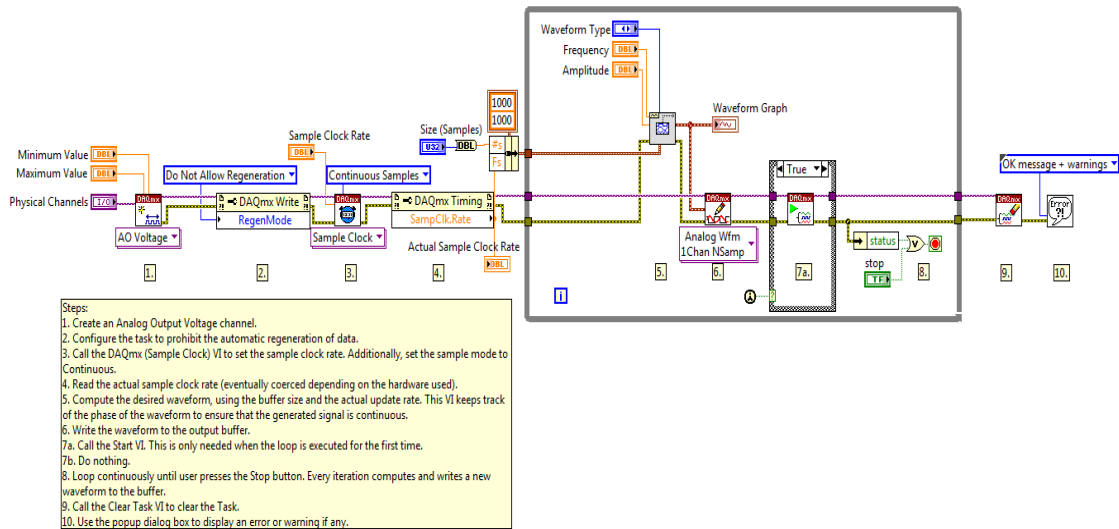


Figure E.6. – Block code of LASER-Voltage-ContinuousInput.vi

APPENDIX F

Four Point Bend Jig Diagram

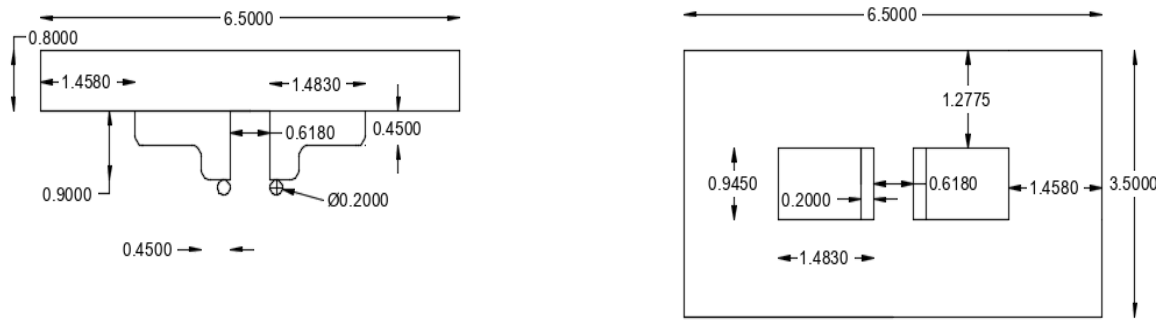


Figure F.1 – Top half of four-point bend jig.

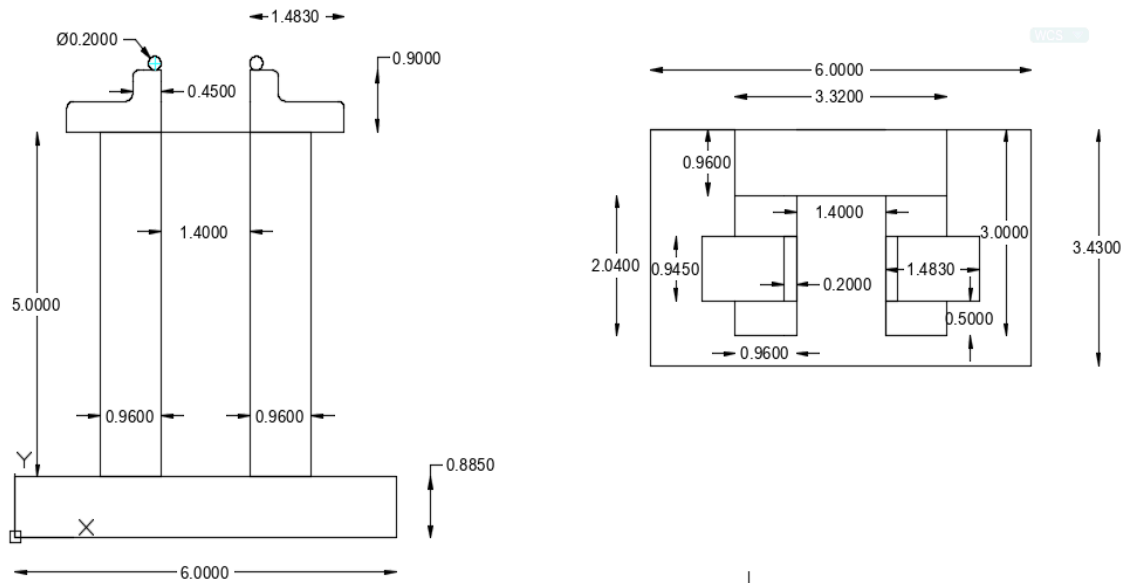


Figure F.2 – Bottom half of four-point bend jig.

APPENDIX G

Specifications

Amplifier

XTi 2 Series



XTi 1002, 2002, 4002



XTi 6002

Power Matrix

| Model | Channels | 2Ω Dual | 4Ω Dual | 8Ω Dual | 4Ω Bridged | 8Ω Bridged |
|-------|----------|---------|---------|---------|------------|------------|
| 1002 | 2 | 700W | 500W | 275W | 1400W | 1000W |
| 2002 | 2 | 1000W | 800W | 475W | 2000W | 1600W |
| 4002 | 2 | 1600W | 1200W | 650W | 3200W | 2400W |
| 6002 | 2 | 3000W | 2100W | 1200W | 6000W | 4200W |

*1kHz, 20ms burst, both channels driven

Figure G.1 – Amplifier specifications part 1

| Amplifier Performance Specifications | XTi 1002 | XTi 2002 | XTi 4002 | XTi 6002 |
|--|--------------------------------|------------------------|------------------------|------------------------|
| Sensitivity (for full rated power at 4Ω) | 1.4V | | | |
| Rated Power Output (per Channel at 4Ω) | 500W Stereo | 800W Stereo | 1200W Stereo | 2100W Stereo |
| Signal to Noise Ratio (below rated 1 kHz power at 8Ω) | 100 dB (A Weighted) | 100 dB (A Weighted) | 100 dB (A Weighted) | 103 dB (A Weighted) |
| Total Harmonic Distortion | <0.5% | | | |
| Damping Factor 20 Hz to 1 kHz | >500 | | | |
| Frequency Response (at 1W, 20 Hz to 20 kHz) | +0 dB, -1 dB | | | |
| Crosstalk (below rated power) 20 Hz to 1 kHz | >70 dB | | | |
| Input Impedance | 20kΩ balanced, 10kΩ unbalanced | | | |
| Physical Specifications | | | | |
| Width | 19 in. (48.3cm) | | | |
| Height | 3.5 in. (8.9cm) | | | |
| Depth | 12.25 in. (31.1 cm) | 12.25 in. (31.1 cm) | 12.25 in. (31.1 cm) | 16.2 in. (41.1 cm) |
| Net Weight | 18.5 lbs (8.4kg) | 18.5 lbs (8.4kg) | 18.5 lbs (8.4kg) | 24 lbs (10.9kg) |
| Shipping Weight | 21.5 lbs (9.75kg) | 21.5 lbs (9.75kg) | 21.5 lbs (9.75kg) | 30 lbs (13.6kg) |

Figure G.2 – Amplifier specifications part 2

Low-pass filter

SR600 Series Specifications

Filter

| | |
|----------------------|--------------------------------------|
| Frequency range | 1 Hz to 100 kHz (3-digit resolution) |
| Type | 8-pole, 6-zero elliptic |
| Rolloff | 115 dB/octave |
| Passband ripple | 0.1 dB peak to peak (typ.) |
| Stopband attenuation | 80 dB (typ.) |

Transfer Function (Bi-Quad Cascade)

| | |
|------------|----------|
| Stage 1 | |
| ω_p | 0.634752 |
| Q | 0.543939 |
| ω_z | n/a |
| Stage 2 | |
| ω_p | 0.805995 |
| Q | 0.950701 |
| ω_z | 1.675935 |
| Stage 3 | |
| ω_p | 0.985073 |
| Q | 2.095314 |
| ω_z | 1.935978 |
| Stage 4 | |
| ω_p | 1.076768 |
| Q | 7.375143 |
| ω_z | 2.883197 |

Input

| | |
|-------------------|--|
| Impedance | 1 M Ω // 15 pF |
| Configuration | Single-ended (A or B) or differential (A-B) |
| CMRR | >85 dB at 100 Hz (input gain >20 dB) |
| Coupling | AC or DC |
| Input noise | 6 nV/ $\sqrt{\text{Hz}}$ at 1 kHz (with 60 dB input gain) |
| Gain | 0, 10, 20, 30, 40, 50, 60 dB \pm 0.2 dB |
| Max. input signal | 10 V _{pp} (overload) 5 V _{pp} (no distortion) |

Output

| | |
|--|---|
| Impedance | <1 Ω |
| Full-scale output signal | 10 V _{pp} into >300 Ω |
| Option 01 | 10 V _{pp} into 50 Ω |
| DC offset | Adjustable to 0 V |
| Gain | 0, 10, 20 dB \pm 0.5 dB |
| Harmonic distortion (<1 V _{pp} output) | <-80 dB below full scale at 100 Hz <-50 dB below full scale at 1 kHz |
| Spurious components | <-80 dB below full scale (with input source <50 Ω) |
| Channel crosstalk | <-110 dB below full scale (with input source <50 Ω) |
| Phase match | \pm 0.75° (DC to f_c , typ.) |

General

| | |
|-----------------|---|
| Interfaces | GPIB and RS-232 standard. All instrument functions can be controlled and read through the interfaces. |
| Stored settings | Nine complete dual-channel instrument configurations may be stored in non-volatile memory. |
| Power | 45 W, 100/120/220/240 VAC, 50/60 Hz |
| Dimensions | 15.7" \times 3.0" \times 14.0" (WHD) |
| Weight | 12 lbs. |
| Warranty | One year parts and labor on defects in materials and workmanship |

Figure G.3 – Low-pass filter specifications part 1



SR640 rear panel

Ordering Information

| | | |
|-----------|--|--------|
| SR640 | Two-channel low pass filter with RS-232, GPIB and rack mount kit | \$3295 |
| SR645 | Two-channel high pass filter with RS-232, GPIB and rack mount kit | \$3295 |
| SR650 | One high, one low pass filter with RS-232, GPIB and rack mount kit | \$3295 |
| Option 01 | High current output | \$200 |

Figure G.4 – Low-pass filter specifications part 2

Laser Vibrometer

Table G.1 – Laser vibrometer specifications

| | | | |
|---|---------------------------------------|--|--------------|
| Model | | LJ-V7300 | |
| Light source | Type | Blue semiconductor laser | |
| | Wavelength | 405 nm (visible beam) | |
| | Laser class | Class 2 Laser Product (IEC60825-1, FDA(CDRH) Part 1040.10 ^{*1}) | |
| | Output | 4.8 mW | |
| Measuring range | Z-axis (Height) | | |
| | ±145 mm 5.71" (F.S.=290 mm 11.42") | | |
| | X-axis (Width) | Near | 110 mm 4.33" |
| | | Reference distance | 180 mm 7.09" |
| Far | | 240 mm 9.45" | |
| Repeatability | Z-axis (Height) | 5 µm 0.000197" | |
| | X-axis (Width) | 60 µm 0.002363" | |
| Profile data interval | | 300 µm 0.012" | |
| Linearity Z-axis (Height) | | ±0.05 to ² ±0.15% of F.S. | |
| Mounting conditions | | Diffuse reflection | |
| Reference distance | | 300 mm 11.81" | |
| Spot shape (at reference distance) | | Approx 240 mm x 610 µm 9.45" x 0.024016" | |
| Sampling cycle (trigger interval) | | Top speed: 16 µs (high-speed mode) Top speed: 32 µs (advanced function mode) | |
| Temperature characteristics | | 0.01% of F.S./°C | |
| Enclosure rating | | IP67 (IEC60529) | |
| Environmental resistance | Operating ambient luminance | Incandescent lamp: 10000 lux max | |
| | Operating temperature range | 0 to +45°C 32 to 113°F | |
| | Operating ambient humidity | 20 to 85% RH (No condensation) | |
| | Shock resistance | 15 G/6 msec | |
| | Vibration | 10 to 57 Hz, 1.5 mm 0.06" double amplitude in X, Y, and Z directions, 3 hours respectively | |
| Material | | Aluminum | |
| Weight | | Approx 1000 g | |
| ^{*1} The laser classification for FDA(CDRH) is implemented based on IEC60825-1 in accordance with the requirements of Laser Notice No. 50. ^{*2} The linearity will differ depending on the measurement area. | | | |

Linear Guide

A custom slide was ordered. In addition to the specifications listed below, the slide is made of nonmagnetic materials. The model name is SI-4AC0NMS.

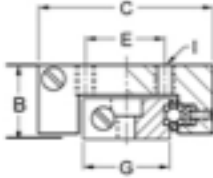
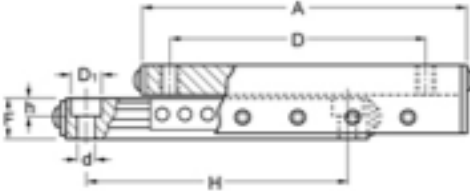


Anti-Creep Linear Slides - Inch
 Family: S1-AC
 Model: S1-4AC
 Price: \$ 144.00

The standard finish is a clear anodize carriage and black anodize base. Other finishes are available on request.

Add to cart

| | |
|--------------------------|--------------------|
| Carriage 4 Holes (I) | 6-32 UNC-2B Thread |
| Base Hole d | .157 |
| Base Hole D ₁ | .244 |
| Base Hole h | .150 |
| Counter Bore Screw Size | #6 |

Custom slides available. Please call to learn more.

| All dimensions in inches unless otherwise specified | | | | | | | | | | | | | | |
|---|----------|--------|------------|-------------|----------|----------|---------|-----------------------|-------|-----------------|-------|-------|-------|----------------------------|
| Model | Price \$ | Travel | Load (lbs) | Weight (oz) | Length A | Height B | Width C | Carriage Hole Spacing | | Base Dimensions | | | | Accuracy (in/in of travel) |
| | | | | | | | | D | E | F | G | H | | |
| S1-4AC | 144.00 | 4 | 35 | 8.2 | 6.00 | 0.62 | 1.50 | 5.375 | 0.625 | 0.340 | 0.750 | 4.000 | .0005 | |

https://www.deltron.com/search/Slides_Ball_Crossed_Roller_Model.aspx?pkid=3023

Figure G.5 – Linear guide specifications

Shaker



PERMANENT MAGNET SHAKER SYSTEMS

| Small Permanent Magnet Systems | VTS 40 | VTS 65 | VTS 80 | VTS 100 | VTS 150 |
|--|--|---------------------|----------------------|----------------------|----------------------|
| LOW COST, LOW FORCE VIBRATION SYSTEMS | | | | | |
| Peak Sine | 40 lbf | 65 lbf | 80 lbf | 100 lbf | 150 lbf |
| Amplifier Cooling Fan | INCLUDED | | | | |
| Vibrator Cooling Fan | N/A | INCLUDED | | | |
| Stroke (p-p) | .75" | .75" | .75" | .75" | 1.0" |
| Velocity | 35 ips | 70 ips | 80 ips | 100 ips | 70 ips |
| Max. Acceleration (bare table) | 60g | 100g | 115g | 150g | 210g |
| Armature Weight | .66 lbs | .66 lbs | .70 lbs | .66 lbs | .71 lbs |
| Suspension Stiffness | 40 lbs./in (options available for larger payloads) | | | | |
| First Major Resonance | 4500 Hz | 4500 Hz | 7000 Hz | 4500 Hz | 5400 Hz |
| Frequency Range | 2-6500 Hz | | | | 2-8500 Hz |
| Nominal Impedance | 6 Ohms | | | | |
| Power Requirements | 4A/120V 2A/240V | 14A/120V 8A/240V | 18A/120V 10A/240V | 18A/120V 10A/240V | 28A/120V 15A/240V |

Figure G.6 – Shaker specifications

TESTRESOURCE Machine



Project No: 1508055-03
Customer: Baylor University
Product: 100Q1000-12

Ship Date: November 9, 2015
Warranty Period: 1 year; November 9, 2016

Load Frame: **Model: 100 Series Frame**
P/N: 20046101
S/N: 1508055-03F

Actuator: **Model: DG.1000.12**
P/N: 20064411-02
S/N: 1508055-03A

Controller: **Model: Q-Controller**
P/N: 20028804
S/N: 1508055-03C
Assy No: 150911-694
Power: 110V; 4A Max

Position Cal: Pulses/inch: 3,077,671; Max Speed: 5 in/min
Gains: Load: P -> 30, I -> 1, D -> 0; Position: P -> 1500, I -> 20, D -> 0;

Load Cells: **Model: SM-1000-294**
Channel: 0
S/N: 752722
Output: 3.17787
Shunt: 183.404 lbs.

Strain Gauges: **Model: E3542-025M-025-ST** **Model: E3540-100T-ST**
Gauge: 25.0000 mm Gauge: N/A
Travel: 6.2500 mm Travel: 1.0000 in
Channel: 0 Channel: 1
S/N: E96406 S/N: E96414
P/N: 23003542-32 P/N: 23003540-05
Shunt: 2.8005 mm Shunt: 0.454 in

Figure G.7 – TESTRESOURCES specifications part 1



| | | | | |
|--------------|--|--------------------------|---------------|---------------------|
| Accessories: | Model: | G240G Grips | Model: | J240GBP Jaws |
| | P/N: | 20031201 | P/N: | 20008601 |
| | Quantity: | 2 | Quantity: | 2 |
| | Model: | G327-159 Grips | | |
| | P/N: | 20002701 | | |
| | Quantity: | 1 | | |
| Cabling: | Model: | I/O Cable P, Q, R | Model: | USB Cable |
| | P/N: | 20044832 | P/N: | 20052601 |
| Manual: | Q-controller Operators, Xy Software, 300 Series Frame Manual | | | |
| Firmware: | 0.3L-2098 | | | |
| Software: | Version: | Xy Plot | | |
| | S/N: | 150911-926 | | |
| | P/N: | 20003809 | | |

Figure G.8 – TESTRESOURCES specifications part 1

APPENDIX H

Bill of Materials

Table H.1 – Bill of Materials

| Division of Work/Machine | Name of Item | Company Purchased From | Location |
|---|---|--|--|
| Specimens and prep | Bovine bone-4 Feml 0s | Animbal Technologies | Tyler, TX |
| | Bandsaw | Craftsman | |
| | IsoMet 1000 Precision Saw | Buehler | 41 Waukegan Road, Lake Bluff, |
| | 114276 : IsoMet Wafering Blades - 15 LC, 6 X | Buehler | Illinois 60044 |
| | 0.020 in | | |
| | 106001: Cool 3 | Buehler | |
| | Ziploc bags (gallon) | N/A | |
| | File for notches | Lowes | |
| | 13" Drill press-11/64" bit | Central Machinery | |
| SP6001 : Scout Pro Digital Scale | Ohaus Corporation | 7 Campus Drive, Suite 310, Parsippany, NJ 07054 | |
| Machine - Pendulum Assembly | Aluminum Plate (Spacer); 5" x 1/2" x 1/8" | Lowes | |
| | Weldable Flat Bar | | |
| | Magnetic Plates (2); 9 1/4" x 1/2" x 1/8" | Lowes | |
| | Weldable Flat Bar | | |
| | Attachment Piece to Shaker; Multipurpose 6061 | McMaster-Carr | 6100 Fulton Industrial Blvd. SW, |
| | Aluminum Alloy; Rectangular Bar, 1/8" x 2-1/2", | | Atlanta, GA 30336-2853 |
| | 6" Long | | |
| | Bottom Arm; Multipurpose 6061 Aluminum | McMaster-Carr | |
| | Alloy; Tube, 1/8" Wall Thickness, 1" x 1-1/2", 1' | | |
| | Length | | |
| | Top Arm & Fastener Cap, Vertical Bar; | McMaster-Carr | |
| | Multipurpose 6061 Aluminum Alloy; 1" Thick, 1- | | |
| 1/2" Width, 3' Length | | | |
| Linear Guide Conversion Piece; 0.875" Thick, 3" | N/A | | |
| Wide and 6" Long | | | |
| Nexus Vibration Isolation Table | Thorlabs | 56 Sparta Ave., Newton, NJ 07860 | |
| Anticreep, non-magnetic, linear slide; S1-4AC- | Del-Tron Precision, Inc. | 5 Trowbridge Dr., P.O. Box 505, | |
| NMS | | Bethel, CT 06801 | |
| Cam Followers (2)- 3/4" diameter | MSC Industrial Suppy Co. | 75 Maxess Road, Melville, NY | |
| 5/8"x5/8" Cylinders - 2 Neodymium Rare Earth | | 157 RMX Way, Petersburg, WV | |
| Magnets | Apex Magnets | 26847 | |
| Machine - Laser Stand | Base Plate-Aluminum 1/2" Thick, 5" Width, 4" | N/A | |
| | Length | | |
| | Beam-Aluminum 3/4" Diameter, 16-1/2" Length | N/A | |
| | Stage-Aluminum 1" Thick, 6-3/4" Width, 5-1/2" | N/A | |
| | Length | | |
| Machine-linear guide, shaker, blower, laser vibrometer, amplifier | VTS-100 | Vibration Test Systems, Inc. | 10246 Clipper Cove, Aurora, OH |
| | VTS blower | Vibration Test Systems, Inc. | 44202 |
| | VTS shaker-blower hose | Vibration Test Systems, Inc. | |
| | Laser vibrometer: LJ-V7300 | Keyence | 1100 North Arlington Heights |
| | Laser vibrometer: DC24V Power source | Keyence | Road, Suite210, Itasca, IL 60143 |
| | Laser vibrometer: Controllor | Keyence | |
| | Laser vibrometer: Head cable | Keyence | |
| | 2002 XTISeries Amplifier | Crown Audio | 1718 W. Mishawaka Road, Elkhart, IN 46517 |
| Electrical - DAQ Related | 9205 32-Channel +/-10 V, 250 kS/s, 16-Bit | National Instruments | 11500 N Mopac Expwy, Austin, |
| | Analog Input Module | Corporation | TX 78759-3504 |
| | NI 9201 Screw Terminal, +/- 10 V, 12-Bit, 500 | National Instruments | |
| KS/S , 8-CH, AI C Series Module | Corporation | | |

Table H.2 – Bill of Materials continued

| | | | |
|-----------|--|--|---|
| | 9263 Screw Terminal, +/-10V, 16-Bit, 100 bS/s/ch, 4-ch, Simult AO C Series Module cDAQ-9174, CompactDAQ chassis (4 slot USB) | National Instruments Corporation National Instruments Corporation | |
| | Power Cord, AC, US, 120 VAC, 2.3 meters | National Instruments Corporation | |
| Black box | Black felt Black thread Velcro Fabric glue XE25W3 : Quick corner cube for 25 mm Rails XE25A90 : Right-Angle Bracket for 25 mm Rails | JoAnns Fabric JoAnns Fabric JoAnns Fabric JoAnns Fabric Thorlabs, Inc. Thorlabs, Inc. | 4633 Jack Kuitgen Fwy #104, Waco, TX 76706 56 Sparta Ave., Newton, NJ 07860 |
| | SH25LP38 : 1/4"-20 Low-Profile Channel Screws (100 Screws/Box) XE25T1 : Drop-In T-Nut, 1/4"-20 Tapped Hole, Qty: 10 XE25L48 : 25 mm Construction Rail, L = 48" XE25L24 : 25 mm Construction Rail, L = 24" XE25L28 : 25 mm Construction Rail, L = 28" | Thorlabs, Inc. Thorlabs, Inc. Thorlabs, Inc. Thorlabs, Inc. Thorlabs, Inc. | |
| Fasteners | Round-Head Machine Screw Phillips (4) #10-32 x 3/4" Round-Head Combo Machine Screw (2) #10-24 tpi x 1" Socket Head Cap Screw (22) 1/4" - 20 tpi x 1" Hex head bolts (3) | N/A Home Depot N/A Keyence | 1100 North Arlington Heights Road, Suite210, Itasca, IL 60143 |

REFERENCES

- [1] Meardon, S. A., Willson, J. D., Gries, S. R., Kernozek, T. W., and Derrick, T. R., 2015, "Bone Stress in Runners with Tibial Stress Fracture," *Clin. Biomech.*, **30**(9), pp. 895–902.
- [2] Pohl, M. B., Mullineaux, D. R., Milner, C. E., Hamill, J., and Davis, I. S., 2008, "Biomechanical Predictors of Retrospective Tibial Stress Fractures in Runners," *J. Biomech.*, **41**(6), pp. 1160–1165.
- [3] Milner, C. E., Davis, I. S., and Hamill, J., 2006, "Free Moment as a Predictor of Tibial Stress Fracture in Distance Runners," *J. Biomech.*, **39**(15), pp. 2819–2825.
- [4] Magness, S., Ambegaonkar, J. P., Jones, M. T., and Caswell, S. V., 2011, "Lower Extremity Stress Fracture in Runners: Risk Factors and Prevention," *Int. J. Athl. Ther. Train.*, **16**(4), pp. 11–15.
- [5] Whitton, R. C., Mirams, M., Mackie, E. J., Anderson, G. A., and Seeman, E., 2013, "Exercise-Induced Inhibition of Remodelling Is Focally Offset with Fatigue Fracture in Racehorses," *Osteoporos. Int.*, **24**(7), pp. 2043–2048.
- [6] "Fractographic Examination of Racing Greyhound Central (Navicular) Tarsal Bone Failure Surfaces Using Scanning Electron Microscopy | SpringerLink" [Online]. Available: <https://link-springer-com.ezproxy.baylor.edu/article/10.1007%2Fs002230001129>. [Accessed: 28-Feb-2018].
- [7] Kozinc, Z., and Sarabon, N., 2017, "Common Running Overuse Injuries and Prevention," *Montenegrin J. Sports Sci. Med.*, **6**(2), pp. 67–74.
- [8] Warden, S. J., Hurst, J. A., Sanders, M. S., Turner, C. H., Burr, D. B., and Li, J., 2005, "Bone Adaptation to a Mechanical Loading Program Significantly Increases Skeletal Fatigue Resistance," *J. Bone Miner. Res.*, **20**(5), pp. 809–816.
- [9] Patel, D. S., Roth, M., and Kapil, N., 2011, "Stress Fractures: Diagnosis, Treatment, and Prevention," *Am. Fam. Physician*, **83**(1), pp. 39–46.
- [10] Whipple, T. J., and Eckhardt, R. B., 2011, *The Endurance Paradox: Bone Health for the Endurance Athlete*, Walnut Creek: Taylor and Francis.
- [11] Clarke, B., 2008, "Normal Bone Anatomy and Physiology," *Clin. J. Am. Soc. Nephrol. CJASN*, **3**(Suppl 3), pp. S131–S139.
- [12] 1989, *On Biomineralization*, Oxford University Press, Oxford, New York.

- [13] Reznikov, N., Shahar, R., and Weiner, S., 2014, “Bone Hierarchical Structure in Three Dimensions,” *Acta Biomater.*, **10**(9), pp. 3815–3826.
- [14] Warshaw, J., Bromage, T. G., Terranova, C. J., and Enlow, D. H., 2017, “Collagen Fiber Orientation in Primate Long Bones,” *Anat. Rec.*, **300**(7), pp. 1189–1207.
- [15] Rho, J.-Y., Kuhn-Spearing, L., and Zioupos, P., 1998, “Mechanical Properties and the Hierarchical Structure of Bone,” *Med. Eng. Phys.*, **20**(2), pp. 92–102.
- [16] Downey, P. A., and Siegel, M. I., 2006, “Bone Biology and the Clinical Implications for Osteoporosis,” *Phys. Ther.*, **88**(1), p. 77.
- [17] Florencio-Silva, R., Sasso, G. R. da S., Sasso-Cerri, E., Simões, M. J., and Cerri, P. S., 2015, “Biology of Bone Tissue: Structure, Function, and Factors That Influence Bone Cells,” *Biomed Res. Int.*, **2015**, pp. 421746–421746.
- [18] Kirchner, H. O. K., and Lazar, M., 2008, “The Thermodynamic Driving Force for Bone Growth and Remodelling: A Hypothesis,” *J. R. Soc. Interface*, **5**(19), pp. 183–193.
- [19] Murphy, W., and Black, J., 2016, *Handbook of Biomaterial Properties*, Springer, Boston, MA.
- [20] Pal, S., 2014, *Design of Artificial Human Joints & Organs*, Springer, Boston, MA.
- [21] Mow, V. C., and Hayes, W. C., 1997, *Basic Orthopaedic Biomechanics*, Lippincott-Raven Publishers, Philadelphia, PA.
- [22] Burstein, A. H., Currey, J. D., Frankel, V. H., and Reilly, D. T., 1972, “The Ultimate Properties of Bone Tissue: The Effects of Yielding,” *J. Biomech.*, **5**(1), pp. 35–44.
- [23] Yin, L., Venkatesan, S., Webb, D., Kalyanasundaram, S., and Qin, Q.-H., 2012, “2D and 3D Mapping of Microindentations in Hydrated and Dehydrated Cortical Bones Using Confocal Laser Scanning Microscopy,” *J. Mater. Sci.*, **47**(10), pp. 4432–4438.
- [24] Yan, J., Daga, A., Kumar, R., and Mecholsky, J. J., 2008, “Fracture Toughness and Work of Fracture of Hydrated, Dehydrated, and Ashed Bovine Bone,” *J. Biomech. Kidlington*, **41**(9), pp. 1929–1936.
- [25] Samuel, J., Sinha, D., Zhao, J. C.-G., and Wang, X., 2014, “Water Residing in Small Ultrastructural Spaces Plays a Critical Role in the Mechanical Behavior of Bone,” *Bone*, **59**(Supplement C), pp. 199–206.
- [26] Riis, B. J., Hansen, M. A., Jensen, A. M., Overgaard, K., and Christiansen, C., 1996, “Low Bone Mass and Fast Rate of Bone Loss at Menopause: Equal Risk Factors for Future Fracture: A 15-Year Follow-up Study,” *Bone*, **19**(1), pp. 9–12.

- [27] “Increasing Sex Difference in Bone Strength in Old Age: The Age, Gene/Environment Susceptibility-Reykjavik Study (AGES-REYKJAVIK) - ScienceDirect” [Online]. Available: <http://www.sciencedirect.com.ezproxy.baylor.edu/science/article/pii/S8756328206003784>. [Accessed: 10-Nov-2017].
- [28] Wallace, I. J., 2015, “Osteoporosis,” *Evol. Med. Public Health*.
- [29] Marcus, R., Feldman, D., and Kelsey, J., 2001, *Osteoporosis, Two-Volume Set*, Academic Press.
- [30] Ulbrich, C., Wehland, M., Pietsch, J., Aleshcheva, G., Wise, P., Loon, J. van, Magnusson, N., Infanger, M., Grosse, J., Eilles, C., Sundaresan, A., and Grimm, D., 2014, “The Impact of Simulated and Real Microgravity on Bone Cells and Mesenchymal Stem Cells,” *BioMed Res. Int.*, **2014**.
- [31] Sambandam, Y., Baird, K. L., Stroebel, M., Kowal, E., Balasubramanian, S., and Reddy, S. V., 2016, “Microgravity Induction of TRAIL Expression in Preosteoclast Cells Enhances Osteoclast Differentiation,” *Sci. Rep. Nat. Publ. Group Lond.*, **6**, p. 25143.
- [32] Iwamoto, J., Takeda, T., and Sato, Y., 2005, “Interventions to Prevent Bone Loss in Astronauts during Space Flight,” *Keio J. Med.*, **54**(2), pp. 55–59.
- [33] Lang, T. F., Leblanc, A. D., Evans, H. J., and Lu, Y., 2006, “Adaptation of the Proximal Femur to Skeletal Reloading after Long-Duration Spaceflight,” *J. Bone Miner. Res. Off. J. Am. Soc. Bone Miner. Res.*, **21**(8), pp. 1224–1230.
- [34] Herman, B. C., Cardoso, L., Majeska, R. J., Jepsen, K. J., and Schaffler, M. B., 2010, “Activation of Bone Remodeling after Fatigue: Differential Response to Linear Microcracks and Diffuse Damage,” *Bone*, **47**(4), pp. 766–772.
- [35] Varvani-Farahani, A., and Najmi, H., 2010, “A Damage Assessment Model for Cadaveric Cortical Bone Subjected to Fatigue Cycles,” *Int. J. Fatigue*, **32**(2), pp. 420–427.
- [36] Gibson, V. A., Stover, S. M., Martin, R. B., Gibeling, J. C., Willits, N. H., Gustafson, M. B., and Griffin, L. V., 1995, “Fatigue Behavior of the Equine Third Metacarpus: Mechanical Property Analysis,” *J. Orthop. Res. Off. Publ. Orthop. Res. Soc.*, **13**(6), pp. 861–868.
- [37] Guo, X. E., Liang, L. C., and Goldstein, S. A., 1998, “Micromechanics of Osteonal Cortical Bone Fracture,” *J. Biomech. Eng.*, **120**(1), pp. 112–117.
- [38] Alto, A., and Pope, M. H., 1979, “On the Fracture Toughness of Equine Metacarpi,” *J. Biomech.*, **12**(6), pp. 415–421.

- [39] Martin, R. B., Gibson, V. A., Stover, S. M., Gibeling, J. C., and Griffin, L. V., 1996, "Osteonal Structure in the Equine Third Metacarpus," *Bone*, **19**(2), pp. 165–171.
- [40] Bell, K. L., Loveridge, N., Power, J., Garrahan, N., Meggitt, B. F., and Reeve, J., 1999, "Regional Differences in Cortical Porosity in the Fractured Femoral Neck," *Bone*, **24**(1), pp. 57–64.
- [41] Arcos, D., and Vallet-Regí, M., 2010, "Sol–Gel Silica-Based Biomaterials and Bone Tissue Regeneration," *Acta Biomater.*, **6**(8), pp. 2874–2888.
- [42] Fatihhi, S. J., Harun, M. N., Kadir, M. R. A., Abdullah, J., Kamarul, T., Öchsner, A., and Syahrom, A., 2015, "Uniaxial and Multiaxial Fatigue Life Prediction of the Trabecular Bone Based on Physiological Loading: A Comparative Study," *Ann. Biomed. Eng.*, **43**(10), pp. 2487–2502.
- [43] Moyle, D. D., Welborn, J. W., and Cooke, F. W., 1978, "Work to Fracture of Canine Femoral Bone," *J. Biomech.*, **11**(10), pp. 435–440.
- [44] Campbell, A. M., Cler, M. L., Skurla, C. P., and Kuehl, 2016, "Damage Accumulation of Bovine Bone under Variable Amplitude Loads," Baylor University.
- [45] Cler, M. L., Skurla, C., and Kuehl, J., 2016, "Damage Accumulation of Bovine Bone Under Chaotic Loading," Baylor University.
- [46] Gupta, H. S., and Zioupos, P., 2008, "Fracture of Bone Tissue: The 'Hows' and the 'Whys,'" *Med. Eng. Phys.*, **30**(10), pp. 1209–1226.
- [47] Burr, D. B., 2011, "Why Bones Bend but Don't Break," *J. Musculoskelet. Neuronal Interact.*, **11**(4), pp. 270–285.
- [48] Plotkin, L. I., Gortazar, A. R., Davis, H. M., Condon, K. W., Gabilondo, H., Maycas, M., Allen, M. R., and Bellido, T., 2015, "Inhibition of Osteocyte Apoptosis Prevents the Increase in Osteocytic Receptor Activator of Nuclear Factor KB Ligand (RANKL) but Does Not Stop Bone Resorption or the Loss of Bone Induced by Unloading," *J. Biol. Chem.*, **290**(31), pp. 18934–18942.
- [49] Cheung, W.-Y., Simmons, C. A., and You, L., 2012, "Osteocyte Apoptosis Regulates Osteoclast Precursor Adhesion via Osteocytic IL-6 Secretion and Endothelial ICAM-1 Expression," *Bone*, **50**(1), pp. 104–110.
- [50] Hertzberg, R. W., Vinci, R. P., and Hertzberg, J. L., 2012, *Deformation and Fracture Mechanics of Engineering Materials, 5th Edition*, Wiley Global Education.
- [51] Ritchie, R. O., Buehler, M. J., and Hansma, P., 20090601, "Plasticity and Toughness in Bone," *Phys. Today*.

- [52] Hiller, L. P., Stover, S. M., Gibson, V. A., Gibeling, J. C., Prater, C. S., Hazelwood, S. J., Yeh, O. C., and Martin, R. B., 2003, "Osteon Pullout in the Equine Third Metacarpal Bone: Effects of Ex Vivo Fatigue," *J. Orthop. Res.*, **21**(3), pp. 481–488.
- [53] Evans, A. g., and Faber, K. t., 1984, "Crack-Growth Resistance of Microcracking Brittle Materials," *J. Am. Ceram. Soc.*, **67**(4), pp. 255–260.
- [54] Hutchinson, J. W., 1987, "Crack Tip Shielding by Micro-Cracking in Brittle Solids," *Acta Metall.*, **35**(7), pp. 1605–1619.
- [55] Sigl, L. S., 1996, "Microcrack Toughening in Brittle Materials Containing Weak and Strong Interfaces," *Acta Mater.*, **44**(9), pp. 3599–3609.
- [56] Nalla, R. K., Kruzic, J. J., and Ritchie, R. O., 2004, "On the Origin of the Toughness of Mineralized Tissue: Microcracking or Crack Bridging?," *Bone*, **34**(5), pp. 790–798.
- [57] Pezzotti, G., and Sakakura, S., 2003, "Study of the Toughening Mechanisms in Bone and Biomimetic Hydroxyapatite Materials Using Raman Microprobe Spectroscopy," *J. Biomed. Mater. Res. A*, **65**(2), pp. 229–236.
- [58] Kruzic, J. J., Nalla, R. K., Kinney, J. H., and Ritchie, R. O., 2003, "Crack Blunting, Crack Bridging and Resistance-Curve Fracture Mechanics in Dentin: Effect of Hydration," *Biomaterials*, **24**(28), pp. 5209–5221.
- [59] Nalla, R. K., Kinney, J. H., and Ritchie, R. O., 2003, "Mechanistic Fracture Criteria for the Failure of Human Cortical Bone," *Nat. Mater.*, **2**(3), pp. 164–168.
- [60] Currey, J., 2001, "Biomaterials: Sacrificial Bonds Heal Bone," *Nature*, **414**(6865), p. 414699a.
- [61] Wang, W., and Elbanna, A., 2014, "Crack Propagation in Bone on the Scale of Mineralized Collagen Fibrils: Role of Polymers with Sacrificial Bonds and Hidden Length," *Bone*, **68**(Supplement C), pp. 20–31.
- [62] Yeni, Y. N., Kim, D.-G., Dong, X. N., Turner, A. S., Les, C. M., and Fyhrie, D. P., 2006, "Do Sacrificial Bonds Affect the Viscoelastic and Fracture Properties of Bone?," *Clin. Orthop.*, **443**, pp. 101–108.
- [63] Fantner, G. E., Hassenkam, T., Kindt, J. H., Weaver, J. C., Birkedal, H., Pechenik, L., Cutroni, J. A., Cidade, G. A. G., Stucky, G. D., Morse, D. E., and Hansma, P. K., 2005, "Sacrificial Bonds and Hidden Length Dissipate Energy as Mineralized Fibrils Separate during Bone Fracture," *Nat. Mater. Lond.*, **4**(8), pp. 612–6.
- [64] Lieou, C. K. C., Elbanna, A. E., and Carlson, J. M., 2013, "Sacrificial Bonds and Hidden Length in Biomaterials: A Kinetic Constitutive Description of Strength and Toughness in Bone," *Phys. Rev. E*, **88**(1), p. 012703.

- [65] Bathias, C., 2013, “Introduction on Very High Cycle Fatigue,” *Fatigue Limits in Metals*, John Wiley & Sons, Incorporated.
- [66] Todinov, M. T., 2001, “Necessary and Sufficient Condition for Additivity in the Sense of the Palmgren–Miner Rule,” *Comput. Mater. Sci.*, **21**(1), pp. 101–110.
- [67] McEvily, A., Ishihara, S., and Endo, M., 2004, “On the Causes of Deviation from the Palmgren–Miner Rule,” *J. ASTM Int.*, **1**(8), p. 19025.
- [68] Chen, N.-Z., Wang, G., and Guedes Soares, C., 2011, “Palmgren–Miner’s Rule and Fracture Mechanics-Based Inspection Planning,” *Eng. Fract. Mech.*, **78**(18), pp. 3166–3182.
- [69] Suhir, E., Ghaffarian, R., and Yi, S., 2017, “Probabilistic Palmgren–Miner Rule, with Application to Solder Materials Experiencing Elastic Deformations,” *J. Mater. Sci. Mater. Electron.*, **28**(3), pp. 2680–2685.
- [70] Carpinteri, A., Vantadori, S., Łagoda, T., Karolczuk, A., Kurek, M., and Ronchei, C., 2018, “Fatigue Assessment of Metallic Components under Uniaxial and Multiaxial Variable Amplitude Loading,” *Fatigue Fract. Eng. Mater. Struct.*, **41**(6), pp. 1306–1317.
- [71] Shamsaei, N., Fatemi, A., and Socie, D. F., 2011, “Multiaxial Fatigue Evaluation Using Discriminating Strain Paths,” *Int. J. Fatigue*, **33**(4), pp. 597–609.
- [72] Wang, C., and Brown, M., 1993, “A Path-Independent Parameter for Fatigue Under Proportional and Nonproportional Loading,” *Fatigue Fract. Eng. Mater. Struct.*, **16**(12), pp. 1285–1298.
- [73] Anthes, R. J., 1997, “Modified Rainflow Counting Keeping the Load Sequence,” *Int. J. Fatigue*, **19**(7), pp. 529–535.
- [74] Cusumano, J. P., Chelidze, D., and Chatterjee, A., 2002, “A Dynamical Systems Approach to Damage Evolution Tracking, Part 2: Model-Based Validation and Physical Interpretation,” *J. Vib. Acoust.*, **124**(2), p. 258.
- [75] Yung, M., Bigelow, P. L., Hastings, D. M., and Wells, R. P., 2014, “Detecting Within- and between-Day Manifestations of Neuromuscular Fatigue at Work: An Exploratory Study,” *Ergonomics*, **57**(10), pp. 1562–1573.
- [76] Alwasel, A., Yung, M., Abdel-Rahman, E. M., Wells, R. P., and Haas, C. T., 2017, “Fatigue Detection Using Phase-Space Warping,” *J. Biomech. Eng.*, **139**(3), pp. 031001-031001–9.
- [77] Cusumano, J. P., Chelidze, D., and Chatterjee, A., 2002, “A Dynamical Systems Approach to Damage Evolution Tracking, Part 2: Model-Based Validation and Physical Interpretation,” *J. Vib. Acoust.*, **124**(2), pp. 258–264.

- [78] Chelidze, D., and Liu, M., 2005, “Dynamical Systems Approach to Fatigue Damage Identification,” *J. Sound Vib.*, **281**(3), pp. 887–904.
- [79] Chelidze, D., and Cusumano, J. P., 2006, “Phase Space Warping: Nonlinear Time-Series Analysis for Slowly Drifting Systems,” *Philos. Transact. A Math. Phys. Eng. Sci.*, **364**(1846), pp. 2495–2513.
- [80] Chelidze, D., and Liu, M., 2008, “Reconstructing Slow-Time Dynamics from Fast-Time Measurements,” *Philos. Trans. R. Soc. Lond. Math. Phys. Eng. Sci.*, **366**(1866), pp. 729–745.
- [81] Chelidze, D., and Zhou, W., 2006, “Smooth Orthogonal Decomposition-Based Vibration Mode Identification,” *J. Sound Vib.*, **292**(3), pp. 461–473.
- [82] Liu, M., 2005, “Multidimensional Damage State Identification Using Phase Space Warping,” Ph.D., University of Rhode Island.
- [83] Chelidze, D., Cusumano, J. P., and Chatterjee, A., 2002, “A Dynamical Systems Approach to Damage Evolution Tracking, Part 1: Description and Experimental Application,” *J. Vib. Acoust.*, **124**(2), pp. 250–257.
- [84] “Delay Coordinate Embedding” [Online]. Available: <http://cs.brown.edu/research/ai/dynamics/tutorial/Documents/DelayCoordinateEmbedding.html>. [Accessed: 23-May-2018].
- [85] Thomas, R. D., Moses, N. C., Semple, E. A., and Strang, A. J., 2014, “An Efficient Algorithm for the Computation of Average Mutual Information: Validation and Implementation in Matlab,” *J. Math. Psychol.*, **61**, pp. 45–59.
- [86] Xie, D. Y., “Lecture 2: Entropy and Mutual Information,” *Inf. Theory*, p. 19.
- [87] Chelidze, D., “Chapter 7: Delay Coordinate Embedding.”
- [88] Chelidze, D., 2017, “Reliable Estimation of Minimum Embedding Dimension Through Statistical Analysis of Nearest Neighbors,” *J. Comput. Nonlinear Dyn.*, **12**(5), p. 051024.
- [89] Kuehl, J. J., DiMarco, S. F., Spencer, L. J., and Guinasso, N. L., 2014, “Application of the Smooth Orthogonal Decomposition to Oceanographic Data Sets,” *Geophys. Res. Lett.*, **41**(11), pp. 3966–3971.
- [90] Farooq, U., and Feeny, B. F., 2008, “Smooth Orthogonal Decomposition for Modal Analysis of Randomly Excited Systems,” *J. Sound Vib.*, **316**(1–5), pp. 137–146.
- [91] Chelidze, D., 2014, “Smooth Local Subspace Projection for Nonlinear Noise Reduction,” *Chaos Interdiscip. J. Nonlinear Sci.*, **24**(1), p. 013121.

- [92] Hai Nguyen, S., and Chelidze, D., 2016, “Dynamic Model for Fatigue Evolution in a Cracked Beam Subjected to Irregular Loading,” *J. Vib. Acoust.*, **139**(1), p. 014502.
- [93] Zioupos, P., and Casinos, A., 1998, “Cumulative Damage and the Response of Human Bone in Two-Step Loading Fatigue,” *J. Biomech.*, **31**(9), pp. 825–833.
- [94] Novitskaya, E., Chen, P.-Y., Lee, S., Castro-Ceseña, A., Hirata, G., Lubarda, V. A., and McKittrick, J., 2011, “Anisotropy in the Compressive Mechanical Properties of Bovine Cortical Bone and the Mineral and Protein Constituents,” *Acta Biomater.*, **7**(8), pp. 3170–3177.
- [95] Ferreira, F., Vaz, M. A., and Simões, J. A., 2006, “Mechanical Properties of Bovine Cortical Bone at High Strain Rate,” *Mater. Charact.*, **57**(2), pp. 71–79.
- [96] Diskin, M. G., and Kenny, D. A., 2014, “Optimising Reproductive Performance of Beef Cows and Replacement Heifers,” *Anim. Int. J. Anim. Biosci. Camb.*, **8**(s1), pp. 27–39.
- [97] Leonard, M. B., Elmi, A., Mostoufi-Moab, S., Shults, J., Burnham, J. M., Thayu, M., Kibe, L., Wetzsteon, R. J., and Zemel, B. S., 2010, “Effects of Sex, Race, and Puberty on Cortical Bone and the Functional Muscle Bone Unit in Children, Adolescents, and Young Adults,” *J. Clin. Endocrinol. Metab.*, **95**(4), pp. 1681–1689.
- [98] Pettinato, A. A., Loud, K. J., Bristol, S. K., Feldman, H. A., and Gordon, C. M., 2006, “Effects of Nutrition, Puberty, and Gender on Bone Ultrasound Measurements in Adolescents and Young Adults,” *J. Adolesc. Health*, **39**(6), pp. 828–834.
- [99] Larson, R. L., 2007, “Heifer Development: Reproduction and Nutrition,” *Vet. Clin. North Am. Food Anim. Pract.*, **23**(1), p. 53.
- [100] Engelken, T. J., 2008, “Developing Replacement Beef Heifers,” *Theriogenology*, **70**(3), pp. 569–572.